UNIVERSITY OF CALIFORNIA, IRVINE

Fundamental Studies of CO_2 Substitution in Methane Hydrate

DISSERTATION

submitted in partial satisfaction of the requirements
for the degree of

DOCTOR OF PHILOSOPHY

in Civil and Environmental Engineering

by

Navid Saeidi

Dissertation Committee:
Professor Derek Dunn-Rankin, Chair
Associate Project Scientist Yu-Chien Chien, Co-Chair
Associate Professor Russell Detwiler
Assistant Professor Mohammad Javad Abdolhosseini Qomi

2022

DEDICATION

To

My parents and wife. A special feeling of gratitude to my loving parents, Hassan and Efat whose words of encouragement and push for tenacity ring in my ears. My wife Nadi has never left my side and supported me throughout the process.

TABLE OF CONTENTS

LIST OF FIGURES vii

LIST OF TABLES xii

ACKNOWLEDGEMENTS xiii

VITA xiv

LIST OF PUBLICATIONS AND CONTRIBUTIONS xiv

ABSTRACT OF THE DISSERTATION xvi

CHAPTER 1: GENERAL BACKGROUND OF HYDRATES 1

1.1 Important aspects of natural gas hydrates 4

1.2 A brief history of gas hydrates and current technologies 8

1.3 Strategies for gas production from hydrates 13

1.3.1 Overall strategies and background 13

1.3.2 CO_2 injection 15

1.3.2.1 CO_2 hydrate and spontaneous reaction 15

1.3.2.2 CO_2 substitution mechanisms 15

1.3.2.3 Promoters assisting the process 16

1.3.3 Research motivation and objective 19

CHAPTER 2: THEORY OF DISSOCIATION AND GROWTH OF GAS HYDRATES ... 20

2.1 Hydrate formation, dissociation, and stability limits 20

2.2 Hydrate nucleation from various phases 28

CHAPTER 3: COMPUTATIONAL MODELING OF DISSOCIATION AND GROWTH OF GAS HYDRATES 36

3.1 Residual thermodynamics approach 36

3.2 Heterogeneous hydrate nucleation on water/gas interface 42

3.3 Homogeneous hydrate nucleation from dissolved hydrate formers in water 44

3.4 Enthalpy calculations 47

3.5 Gas production from hydrate 49

3.5.1 Pressure reduction 49

3.5.2 Thermal stimulation 51

3.5.3 Injection of CO_2 51

CHAPTER 4: EXPERIMENT METHODS OF DISSOCIATION AND GROWTH OF GAS HYDRATES 55

4.1 Experimental apparatus 56

4.1.2 Test section 59

4.1.3 Main chilling system 61

4.1.4 Auxiliary chilling system 62

4.1.5 Vacuum pump 65

4.1.6 Data-acquisition system 65

4.1.7 Halo H_2O injection system 66

4.1.8 CO_2 injection system 67

4.1.9 CH_4 injection system 68

4.1.10 N_2 injection system 69

4.1.11 Surfactant injection system 71

4.2 Experimental principal, method and procedures 72

4.2.1 CH_4 hydrate formation process 73

4.2.2 CO_2 and CH_4 hydrates exchange process 75

4.2.3 CO_2/CH_4 exchange and sampling 77

CHAPTER 5: EXPERIMENT RESULTS OF DISSOCIATION AND GROWTH OF GAS HYDRATES 79

5.1 Results and discussions 79

5.1.1 Capillary rise of water in porous media/sediment 79

5.1.2 Methane hydrate molar conversion and Z factor 83

5.1.3 Measured P and T with time for methane and exchange hydrates 90

5.1.4 Kinetic rate of hydrate exchange 95

5.1.5 Sample gas condensation and composition analysis 102

CHAPTER 6: CONCLUSION AND FUTURE WORK 110

6.1 Conclusion 110

6.2 Future work 111

BIBLIOGRAPHY 113

APPENDIX A: EXTRA CALCULATIONS 120

APPENDIX B: STANDARD OPERATING PROCEDURES..... 183

LIST OF FIGURES

Page

Figure 1.1 Schematic of gas hydrate research topics (modified from [1]). 2

Figure 1.2 Idealized phase diagrams illustrating where methane hydrate is stable in marine and permafrost settings [15]. 5

Figure 1.3 Phase diagram for a water/hydrocarbon system [17]. 6

Figure 1.4 Gas hydrate structure illustration at the center of gas hydrate research from Herriot-Watt University [19]. 7

Figure 1.5 locations where gas hydrate has been recovered, where gas hydrate is inferred to be present on the basis of seismic data, and where gas hydrate drilling expeditions have been completed in permafrost or deep marine environments, also leading to recovery of gas hydrate [23]. 8

Figure 1.6 Schematic illustration of carbon sequestration in deep-ocean sediments [31]. 12

Figure 1.7 Overall look at the cycle of CO_2-CH_4 hydrate exchange. 18

Figure 1.8 Single layer of surfactant at the water-gas interface. 18

Figure 2.1 a) System can reach to equilibrium. b) System cannot reach to equilibrium (when there is hydrate film at the interface). 21

Figure 2.2 a) Limits of CH_4 hydrate formation in the pressure temperature projection. No hydrate for any pressure below the curve. The contour graph above the Pressure Temperature projection are limits of CH_4 hydrate stability as function of mole-fraction CH_4 in surrounding water. b) Hydrate stability limits as function of mole fraction water in CH_4 phase. 28

Figure 3.1 a) Solubility of CH_4 in H_2O. b) Solubility of H_2O in CH_4. 41

Figure 3.2 a) Calculated critical radius as function of pressure for a temperature of 274 K (solid), 280 K (dashed), 284 K (dash-dot). Equilibrium pressures for the three temperatures are 24.5 bar for 274 K, 48.5 bar for 280 K and 76.9 bar for 284 K. b) Nucleation times for three temperatures as function of pressure. The solid is at 274 K, dashed is 280 K and dash-dot is 284 K..... 43
Figure 3.3 Natural logarithm of nucleation time as a function of various pressures with different diffusion coefficients at 274 K..... 44
Figure 3.4 Homogeneous nucleation of CH_4 hydrate from dissolved CH_4 in water at 274 K and 100 bars. Minimum mole-fraction CH_4 in water for hydrate stability at 274 K and 100 bars from Figure 2.2 a) is $9.84 \cdot 10^{-4}$. a) Free energy difference for the phase transition as function of mole-fraction CH_4 in water in between solubility, figure 3.1 and hydrate stability limit, figure 2.2. b) Critical radius as function of mole-fraction of CH_4. 46
Figure 3.5 a) Calculated nucleation times for 274 K and 100 bars pressure, as function of mole fraction CH_4 in water. b) Calculated nucleation times for 284 K and 200 bars pressure, as function of mole fraction CH_4 in water. Minimum mole-fraction CH_4 in water for hydrate stability is $1.74 \cdot 10^{-3}$ [50]..... 46
Figure 3.6 Isothermal free energy changes for dissociation pressure reduction from equilibrium pressures [75]. The lowest curve is for 40 bars reduction from the equilibrium pressures, 30 bars reduction, 20 bars reduction and upper curve for 10 bars reduction from equilibrium pressures [76]..... 49
Figure 3.7 Enthalpy change in hydrate formation for the same range of the temperature and pressure stability limits as in figure 3.6 [76]. 50
Figure 3.8 a) Enthalpy of hydrate formation mixtures. Black curve is pure CO_2 hydrate, and red curve is 30 moles% CO_2 and 70 moles% N_2. Solid blue is 5 moles% CH_4 with 27.5 moles% N_2 and 67.5 moles% CO_2. Dashed blue is 10 moles% CH_4 with 25 moles% N_2 and 65 moles% CO_2. Dashed-dot blue is 20 moles% CH_4 with 20 moles% N_2 and 60 moles% CO_2. Solid green curve is pure methane hydrate, b) Equilibrium curves for all mixtures [60]..... 52

Figure 4.1 Schematic diagram of experiment of CH_4 production by CO_2 substitution. 56
Figure 4.2 a) High-pressure vessel fully assembled, b) shown all injection lines, burst disk, and thermocouples probe at the top of the vessel. 59
Figure 4.3 a) Bottom view of basket with 6 spacers, b) basket's structure (fully stands). c) Basket filled with glass beads without lid and water injection, and d) basket with lid and halo water drip line. 61
Figure 4.4 a) Main cooling system, b) Inlet and outlet lines from chiller. 62
Figure 4.5 a) A hand-held 4 channel temperature display with K-type thermocouples. b) Auxiliary chilling system. 63
Figure 4.6 Magnetic drive centrifugal water pump and cooling bath. 64
Figure 4.7 Vacuum pump. 65
Figure 4.8 a) Two pressure transducers are located on top and bottom of high-pressure vessel, b) Data acquisition module. 66
Figure 4.9 a) H_2O HPLC pump, and water reservoir is on the scale, b) Halo water drip line, c) The head of high-pressure vessel with water line that it attached to the halo water drip. 67
Figure 4.10 a) CO_2 aluminum storage tank is on the scale and attached to the syringe pump. b) Heat exchanger (ice bath) for CO_2. 68
Figure 4.11 a) CH_4 injection system, b) CH_4 aluminum storage tank. C) Heat exchanger (ice bath) for CH_4. 69
Figure 4.12 a) Digital mass flow meter, b) Shown mixing nitrogen gas and CO2 at 90 degrees mixture section with include of 0.5 microns stainless steel filter. 70
Figure 4.13 a) Empty CO_2 supply aluminum tank with stainless-steel plumbing fixture scaled to hold the required amount of surfactant. b) Roller system for mixing CO_2 liquid and surfactant. 71
Figure 4.14 Qualitative illustration of methane hydrate formation in porous media. a) Macroscopic view of dry glass beads representing sediments, b) methane gas and liquid water were introduced inside the glass beads while the temperature is reduced for hydrate formation, c) methane hydrate formed in the porous media after 48 hours [55]. 74

Figure 4.15 Animated macroscopic CO_2 and CH_4 hydrate exchange process in porous media. a) Injection of CO_2 liquid from the bottom of vessel into the media bed, section B. b) Nuclei CO_2 hydrate with residual water around the methane hydrate. c) New CO_2 hydrate formation in porous media and the heat released will dissociate CH_4 hydrate [55]. (Note: N_2 gas molecules are not illustrated in this figure)..... 76
Figure 4.16 The full schematic of the sample gas condensation setup. The 50 ml stainless steel sample bottle with pressure transducer, thermocouple, and a ball valve for receiving gas in and out of the sample bottle. 77

Figure 5.1 Capillary rise [82]. 80
Figure 5.2 Three types of hydrate morphologies. (a) matrix-supporting; (b) Hydrate growth everywhere and (c) pore-filling. (Note: blue spheres represent sediment grains and the yellow refer to hydrates)..... 81
Figure 5.3 Bulk flow (gas molecules) moves through the space between particles and react with liquid water for forming gas hydrate. (Note: brown color represents sediment and blue color is water, gray color is bulk flow). 81
Figure 5.4 Water and slightly polar components adsorb directly on mineral surfaces (rust surface) and generate efficient conditions for hydrate nucleation. 82
Figure 5.5 a) Simultaneous variations in measured temperatures and pressures as a function of time and compared to CH_4 temperature-pressure hydrate stability limits and CO_2 temperature-pressure hydrate stability limits. The figure shows that the conditions are always inside in the equilibrium hydrate formation domain. b) Free energy of CH_4 hydrate along the pressure-temperature hydrate stability limits. Similar curve for hydrate from pure CO_2 and water. 84
Figure 5.6 Time histories of methane hydrate and CO_2/CH_4 hydrate exchange process. 94
Figure 5.7 a) Moles of methane released by substitution of CO_2 from lowest to the highest methane hydrate production level. b) Shows the average slope of each condition from 0-6 hours, and 6-15 hours. 99
Figure 5.8 The pressure versus N_t at the constant temperature for cond#12, 14 and15..... 100

Figure 5.9 The temperature results of the condensation process and the various cases of calculated temperatures along the time (left), and the concluded compositions with the error (right). The standard deviation of experiments is marked (around 4.66 for all the conditions). 107

LIST OF TABLES

Page

Table 3.1 Parameters for dimensionless chemical potential functions in the equation. 39

Table 3.2 Parameters for equation (46). 40

Table 5.1 Experimental injection composition (mole%) 87

Table 5.2 Calculated from SRK (Soave-Redlich-Kwong) equation of state (described in 5.1.4 with more details) [95,96] to find the compressibility factor (Z), moles of CH_4 (N_{CH4}), and mole fraction of water in hydrate ($x_{H_2O}^{H}$) at the end of CH_4 formation under high pressure (t_e) and after pressure reduction prior to CO_2 injection (t_0) for all of the experimental conditions. 87

Table 5.3 Moles of methane released from hydrate structure by substitution of CO_2 for each condition. . 98

Table 5.4 Number of moles/mole fraction of other gases released during the exchange process. 102

ACKNOWLEDGEMENTS

I am extremely grateful to my supervisors, Professor Derek Dunn-Rankin and Dr. Yu-Chien Chien for their invaluable advice, continuous support, and patience during my PhD study. Their immense knowledge and plentiful experience have encouraged me throughout my academic research and daily life.

I would like to thank my committee members, Professor Russell Detwiler and Professor Mohammad Javad Abdolhosseini Qomi for joining my PhD dissertation committees.

In addition, I am thankful to Professor Bjørn Kvamme from University of Bergen, who introduced me to gas hydrate formation and dissociation in non-equilibrium situations and who gave me a great opportunity for taking his course and doing numerical research with him and his group to better understanding the fundamental concepts behind the hydrate formation.

A special feeling of gratitude to my loving wife (Nadi) who has never left my side and supported me throughout the process.

At the end, I am really appreciative of Robert Smith's (Smitty) support in providing expertise and consultancy for the details of experimental designs on CO_2 sequestration and methane hydrate formation.

VITA

Navid Saeidi

2013 B.S. in Mechanical and Aerospace Engineering, University of California, Irvine

2014 M.S. in Mechanical and Aerospace Engineering, University of California, Irvine

2016-2021 Ph.D. in Civil and Environmental Engineering, University of California, Irvine

2016-2021 Research Assistant, Program in Environmental Engineering, University of California, Irvine

2016-2021 Teaching Assistant, Graduate School of Engineering (MAE Department), University of California, Irvine

FIELD OF STUDY

Substitution Kinetics in Gas Hydrates.

LIST OF PUBLICATIONS AND CONTRIBUTIONS

PUBLICATIONS

1. Kvamme B, Wei N, Zhao J, Zhou S, Zhang K, Sun W, and **Saeidi N**. Alcohols for hydrate inhibition – different alcohols and different mechanisms. Petroleum. 2021.

2. Kvamme B, Wei N, Zhao J, Zhou S, Zhang L, Sun W, and **Saeidi N**. Routes to hydrate formation from water dissolved in gas and impact of mineral surfaces. Petroleum. 2021;7(4):385-401.

3. **Saeidi N**, Dunn-Rankin D, Kvamme B, Chien Y. Experimental studies on combined production of CH4 and safe long-term storage of CO2 in the form of solid hydrate in sediment. Physical Chemistry Chemical Physics. 2021;23(40):23313-23324.

4. Kvamme B, **Saeidi N**. A zero-emission scheme for producing energy from natural gas hydrates and conventional natural gas. Petroleum. 2021;7(4):364-384.

5. Kvamme B, Zhao J, Wei N, Sun W, Zarifi M, **Saeidi N** et al. Why should we use residual thermodynamics for calculation of hydrate phase transitions? Energies. 2020;13(16):4135.

6. Kvamme B, Zhao J, Wei N, **Saeidi N**. Hydrate—A mysterious phase or just misunderstood? Energies. 2020;13(4):880.

7. Kvamme B, Zhao J, Wei N, Sun W, **Saeidi N**, Pei J et al. Hydrate production philosophy and thermodynamic calculations. Energies. 2020;13(3):672.

8. Kvamme B, Aromada S, **Saeidi N**, Hustache-Marmou T, Gjerstad P. Hydrate nucleation, growth, and induction. ACS Omega. 2020;5(6):2603-2619.

9. Aromada S, Kvamme B, Wei N, **Saeidi N**. Enthalpies of hydrate formation and dissociation from residual thermodynamics. Energies. 2019;12(24):4726.

10. Kvamme B, Coffin R, Zhao J, Wei N, Zhou S, Li Q, **Saeidi N** et al. Stages in the dynamics of hydrate formation and consequences for design of experiments for hydrate formation in sediments. Energies. 2019;12(17):3399.

11. Kvamme B, Aromada S, **Saeidi N**. Heterogeneous and homogeneous hydrate nucleation in CO2/water systems. Journal of Crystal Growth. 2019; 522:160-174.

12. Kvamme B, Selvåg J, **Saeidi N**, Kuznetsova T. Methanol as a hydrate inhibitor and hydrate activator. Physical Chemistry Chemical Physics. 2018;20(34):21968-21987.

13. Kvamme B, Zhao J, Wei N, Li Q, **Saeidi N**, Sun W et al. Thermodynamics of hydrate systems using a uniform reference state. Asia-Pacific Journal of Chemical Engineering. 2021;16(6).

INTERNATIONAL/DOMESTIC CONFERENCES

1. **Navid Saeidi***, Bjørn Kvamme, Derek Dunn-Rankin, "Strategies for Energy Production from Natural Gas Hydrates and Safe Long Terms Storage of CO_2". Presented at: 12th International Methane Hydrate Research and Development Conference, Chengdu Shi, Sichuan Sheng China, Oct 31, 2018 - Nov 3, 2018, Poster Presentation.

2. **Navid Saeidi***, Bjørn Kvamme, Yu-Chien Chien, Derek Dunn-Rankin, "Fundamental Study of CO_2 Substitution in Methane Hydrates for Energy Production and Long-Term Sequestration". Presented at: Gas Hydrates – From Potential Geohazard to Carbon-Efficient Fuel? AAPG, Geosciences Technology Workshop; Auckland, New Zealand 15-17 April 2019, Oral Presentation.

3. **Navid Saeidi***, Bjørn Kvamme, Derek Dunn-Rankin, Yu-Chien Chien, "Strategies for Energy Production from Natural Gas Hydrates and Safe Long Terms Storage of CO_2". Presented at: Finding the Good News on Energy and Environment, University of California, Irvine, March 10th, 2020, Oral Presentation.

4. **Navid Saeidi***, Derek Dunn-Rankin, Yu-Chien Chien, Bjørn Kvamme, "Zero emission Energy generation from *in situ* CH_4 hydrates by substitution with CO_2". Submitted Abstract to: 10th International Conference on Gas hydrate (ICGH 10), July 6th-11th, 2022, Singapore.

ABSTRACT OF THE DISSERTATION

Fundamental Studies of CO_2 Substitution in Methane Hydrate

by

Navid Saeidi

Doctor of Philosophy in Civil and Environmental Engineering

University of California, Irvine, 2022

Professor Derek Dunn-Rankin, Chair

The enormous energy reserve of methane gas stored in gas hydrate structures is substantially more than all known fossil fuel reserves around the world. Efficient extraction of methane from the hydrate cavity structures is still a technological challenge but the use of CO_2 injection and substitution is a potentially viable approach. Gas hydrates in sediments are in a state of stationary balance with their surroundings. They are not in thermodynamic equilibrium and competing phase transitions of hydrate dissociation and hydrate reformation determines the stationary situation. The specific objective of this research is to dictate the phase transition conditions that enhance the growth rate of CO_2 hydrate and increase the dissociation rate of methane hydrate in porous media by understanding the behavior of surfactants in promoting the growth rate of CO_2 hydrate experimentally. In addition, the investigation explores the addition of a small amount of nitrogen gas to increase permeability following dissociation of CH_4 hydrate. The CO_2-CH_4 gas exchange concept is theoretically more efficient than any other methods for extracting methane from gas hydrate reservoirs but the theory has not previously been demonstrated experimentally. Furthermore, due to increased concerns regarding carbon dioxide

emissions as a driver of global warming, CO_2 hydrate formation may be a promising form of CO_2 storage as well as an efficient strategy for CH_4 recovery. New CO_2 hydrate forms from injected CO_2 and free liquid water in the porous media. When the CO_2 hydrate forms, the released heat from this formation is directed through the water phase and causes CH_4 hydrate to dissociate.

The experimental results illustrate that 20 moles% N_2 and 1 mole% NFM (N-formylmorpholine) with CO_2 liquid injection is the most effective of the conditions tested for conversion between CO_2/CH_4 hydrates. Maximum conversion in this study was 88 moles% of CO_2, and 2 moles% N_2 taking the place of methane hydrate in large and small cavities.

This research work also uses theoretical modeling to evaluate efficient production schemes in order to develop a feasible method for future practical implementation. It is known that a critical element in the dynamics of hydrate phase transitions is the mass transport, as the hydrate forms across a thin interface layer between liquid water and the interacting gas phase. An efficient production scheme needs to be able to break the water hydrogen bonds in this interface. On the other hand, the kinetic rate of hydrate growth also depends strongly on hydrate formation at the interface. This study shows how the balance of film barrier and hydrate growth at the interface can be affected by a judicious selection of surfactants.

CHAPTER 1: GENERAL BACKGROUND OF HYDRATES

The fundamental and applied topics associated with gas hydrates are wide-ranging, and each topic has an immense research (and in some cases commercial) literature attached to it. The breadth and depth of hydrate science and technology makes it critical that the ambit of the current research topic be carefully delineated. This chapter sets the baseline knowledge framework of gas hydrates necessary for motivating the specific research contribution of the dissertation. The diagram in Figure 1.1 provides the recent taxonomy of knowledge surrounding gas hydrates and the different topics of research interest [1]. Figure 1.1 shows that the research of gas hydrates is divided into three categories: 1) Understanding natural hydrates in space and earth (estimation of the amount, resources, environmental and climate effects), 2) Understanding the theory and physics of hydrates (formation condition, structure, morphology, composition and kinetics), and 3) Technological aspects in utilization and fighting hydrates (storage of gas, transport of natural gas, energy production, water desalinization, fire extinction, food industries, preventing in pipelines, depressurizing,…etc.). The technological aspect of storage of gas and fuel is the focus of this dissertation.

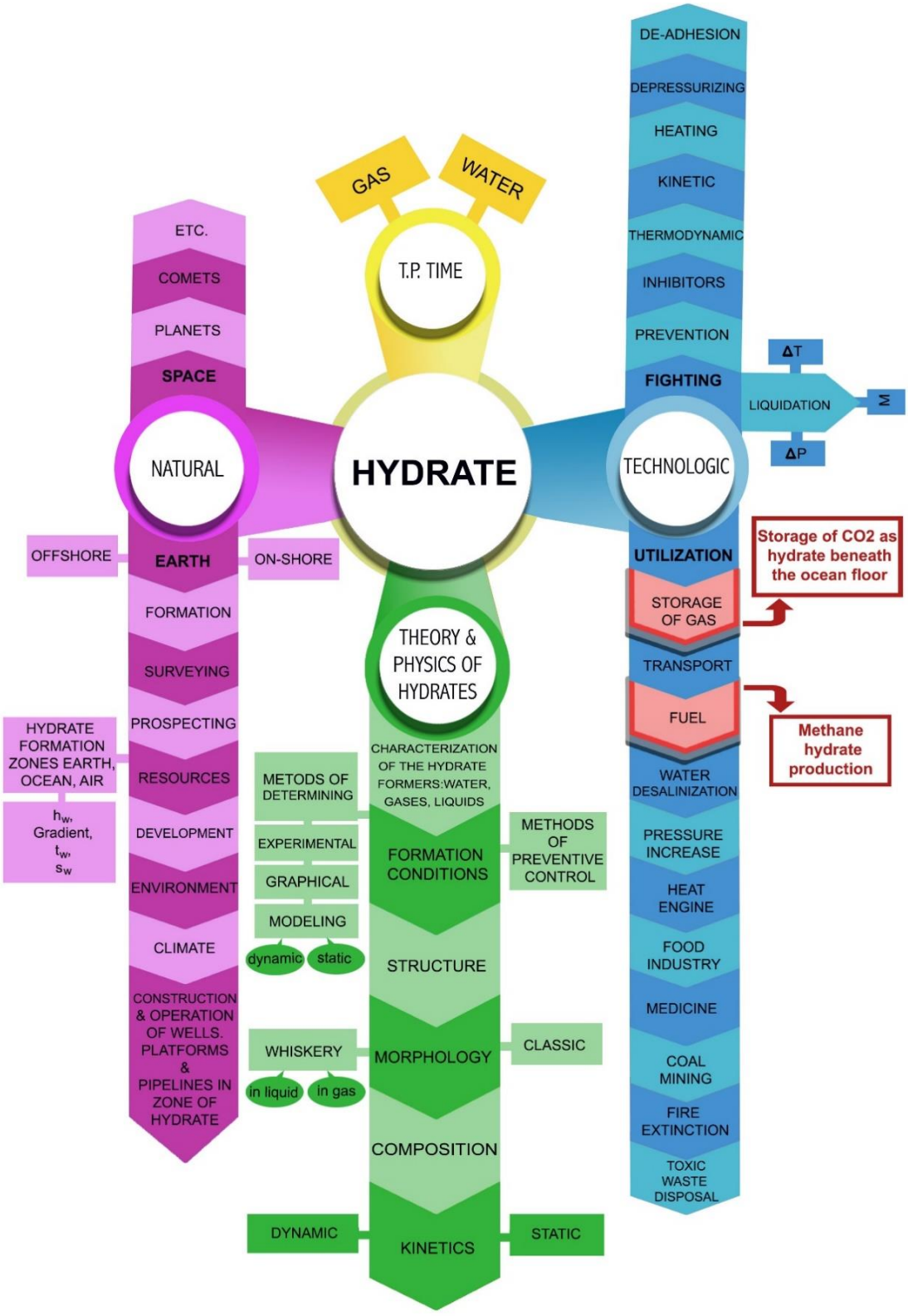

Figure 1.1 Schematic of gas hydrate research topics (modified from [1]).

Natural gas hydrates are central in two major domains: (1) flow assurance, where hydrate formation in fossil fuel pipelines can create solid plugs that cause major damage – including, for example, the well-known failure to capture gas issuing from the Deepwater Horizon well; and (2) the enormous storehouse of natural gas in the form of hydrates in permafrost and deep ocean continental shelves. Both of these domains have Nation-level efforts to prevent hydrate formation in domain (1) [1,2] and to map and potentially extract energy from existing hydrate fields in domain (2) [3,4]. In addition to these two dominant hydrate themes, there are ancillary research and development efforts in topics such as energy transport [5], gas separation [6-8], CO_2 sequestration, and water purification [9-12].

Although hydrate technology is wide-ranging, the core science and understanding needed for many of the technologies rests in the formation and dissolution of the hydrate structure under changing conditions of temperature, pressure, and surrounding chemical composition. There is a reasonably good practical knowledge base regarding the prevention and dissolution of hydrates based in the flow assurance literature [2]. Similarly, the thermodynamic understanding of extracting methane from a hydrate by changing temperature and pressure is well-developed [3,4]. However, the dynamics of extracting methane gas from a hydrate and simultaneously sequestering CO_2 in a substitution hydrate remains lightly studied. Furthermore, most of the studies that do exist are computational/theoretical in nature. There are currently no well-controlled experimental results documenting the substitution performance and potential performance enhancement of CO_2 into a sediment-bearing methane hydrate structure. Remediating this lack of experimentally verified understanding of hydrate substitution dynamics is the principal focus of this dissertation.

To guide the study, there are two basic hypotheses being evaluated that are addressed more fully in Section 1.3:

Hypothesis 1 – CO_2 can replace methane in hydrate without depressurization or external heating; the dissociation energy is provided entirely by the heat released when the more stable CO_2 hydrate forms.

Hypothesis 2 – Properly constructed surfactants in combination with nitrogen in the substitution gas mix can enhance the hydrate substitution performance.

The introductory chapter provides the basics of the relevant hydrate structures important in this work and describes in some detail the significance of understanding substitution dynamics as relevant to the major environmental impacts associated with natural gas hydrate extraction and the potential for simultaneously segregating carbon dioxide in the process.

1.1 Important aspects of natural gas hydrates

Natural gas hydrates are non-stoichiometric compounds of water and caged gas guest molecules. These clathrate hydrates are ice-like structures in which the gas (mostly methane) is surrounded by hydrogen bonded water molecules. In contrast with ordinary pure water ice, gas hydrates have significant energy and environmental consequence. They are widely distributed and naturally occurring, two features that make these crystal structures attractive as a future energy source with high worldwide geographic potential. Natural gas or methane hydrate is formed under conditions of low temperatures and high pressure and in locations lower than the ocean floor or in frozen areas of the earth [13]. Since hydrates have metastable states, variation in pressure, temperature, water salinity and the porous medium characteristics affect hydrate stability [14]. Because of the above unique thermodynamic features exhibited in natural gas hydrates, scientists continue to study how gas hydrates are composed and formed. Figure 1.2 demonstrates the generally accepted gas hydrate stability boundary with respect to temperature, pressure, and depth.

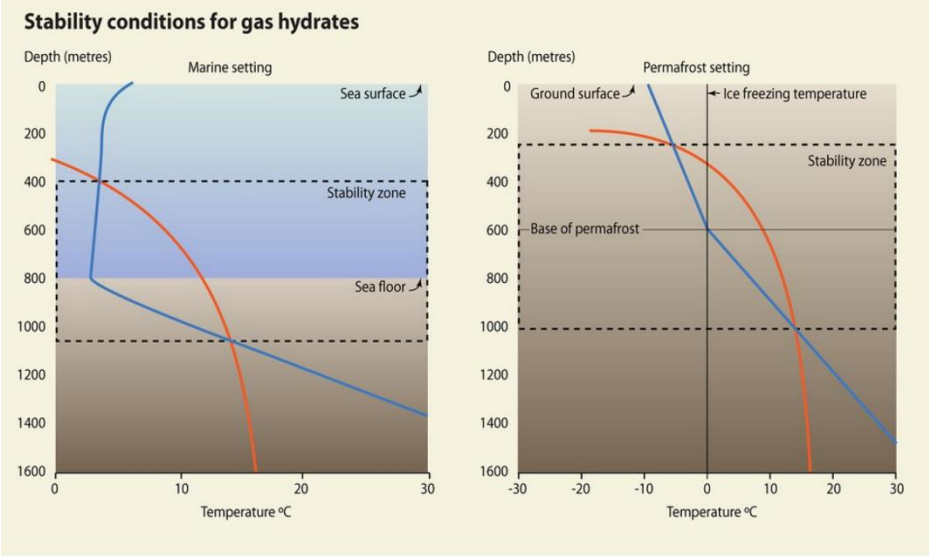

Figure 1.2 Idealized phase diagrams illustrating where methane hydrate is stable in marine and permafrost settings [15].

Figure 1.2 shows that hydrates can exist at depths where the temperature (blue curve) is less than the maximum stability temperature for gas hydrate (orange curve). Pressure and temperature both increase with depth in the Earth. The temperature falls with depth in the ocean but rises with depth in the ocean floor. Although hydrates can exist at warmer temperatures when the pressure is high (orange curve), the temperature at depth (blue curve) is too hot for hydrate to be stable, limiting hydrate stability to the upper ~1km or less of sediment. The presence of salt, a gas hydrate inhibitor, shifts the gas hydrate stability curve (orange) to lower temperatures, decreasing the depth range of the gas hydrate stability zone. For seawater, this decrease is approximately 1.1°C [15]. Gas hydrate formation and dissociation is not a chemical reaction, it is a phase transition phenomenon [16]. Figure 1.3 illustrates the equilibrium phase diagram for gas hydrate.

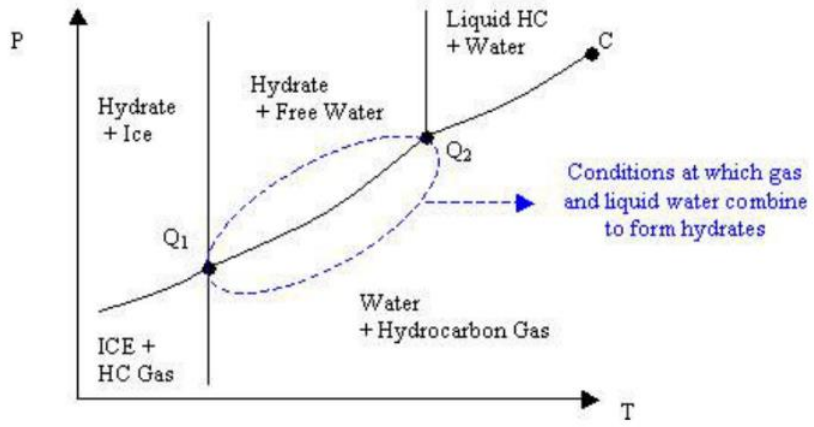

Figure 1.3 Phase diagram for a water/hydrocarbon system [17].

Gas hydrates have three classified crystal structures. They are structure I (SI), structure II (SII), and structure H (SH), which consist of various cages with different sizes and shapes [13]. SI is a cubic structure with 12.01 Å sides in each face. The unit cell of structure I consists of 46 water molecules with two small and six larges of cavities. The small cavity has the shape of a pentagonal dodecahedron (5^{12}) and the large one is tetradecahedron with a hexagonal truncated trapezohedron ($5^{12}6^2$). Guest molecules in SI have diameters in the range of between 4.2 and 6 Å. SII is a cubic structure with 17.3 Å sides in each face. The unit cell of structure II consists of 136 water molecules with sixteen small and eight large cavities. The small cavity has the shape of a pentagonal dodecahedron (5^{12}), and the large one is a hexadecahedron ($5^{12}6^4$). Guest molecules in SII have diameters in the range of between 6 to 7 Å. The unit cell of structure H consists of 34 water molecules and three small cavities (5^{12}), two medium cavities ($4^3 5^6 6^3$), and one large cavity ($5^{12}6^8$). Small cages in SH have a similar shape and configuration as SI and SII. Medium cages have three squares, six pentagonal and three hexagonal structures. Large cages are composed of 12 pentagonal and 8 hexagonal structures [13]. Hydrate structure I and II can be formed through single guest molecules in small or large cavities, but in structure H, guest molecules should occupy both large

and small cavities in order to maintain hydrate stability [18]. Figure 1.4 demonstrates the difference between these three types of gas hydrate molecule structures [19].

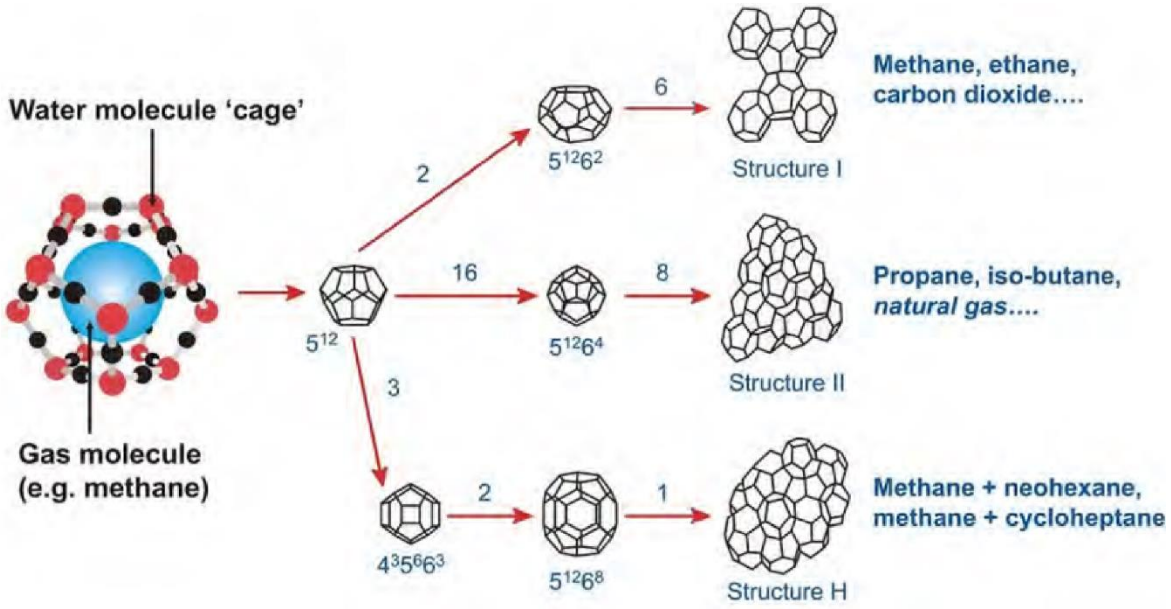

Figure 1.4 Gas hydrate structure illustration at the center of gas hydrate research from Herriot-Watt University [19].

With its cage-like structure allowing gas molecules such as methane to be stored inside, several field experiments have been conducted on the production of energy from hydrate sources and their results reveal the possibility of producing energy from hydrate sources [20,21]. This is because natural gas, being composed almost entirely of low-carbon methane is the cleanest of fossil fuels, and it has been identified as a strong candidate for future energy resources compared to oil and coal. Natural gas hydrates as a source of methane are estimated to contain twice the carbon-based fuel energy of all other fossil fuels combined. In addition, hydrates are distributed around the world, making them accessible to nations without terrestrial sources of fossil fuels. Based on the U.S. Geological Survey, "global stocks of gas hydrates account for at least 10 times the supply of conventional natural gas deposits in land and offshore, with between 10,000 and 300,000 trillion cubic feet of gas yet to be discovered" [20].

These values are not confirmed, but because these hydrates form along continental fault lines, scientists strongly infer locations where huge sources of natural gas hydrates will almost certainly be found. Therefore, any attempt to touch this energy source is predicated on knowing exactly where it is, something that energy providers expect in order to plan to explore and exploit the resources [13,22,23]. The desire for this planning knowledge means that most of studies of natural gas hydrates have been focused on the amount of gas reserves around the world. There remains little known about the depth, location, and amount of technically or economically recoverable gas hydrates available, but Figure 1.5 demonstrates locations where gas hydrate has been recovered or can be inferred to exist.

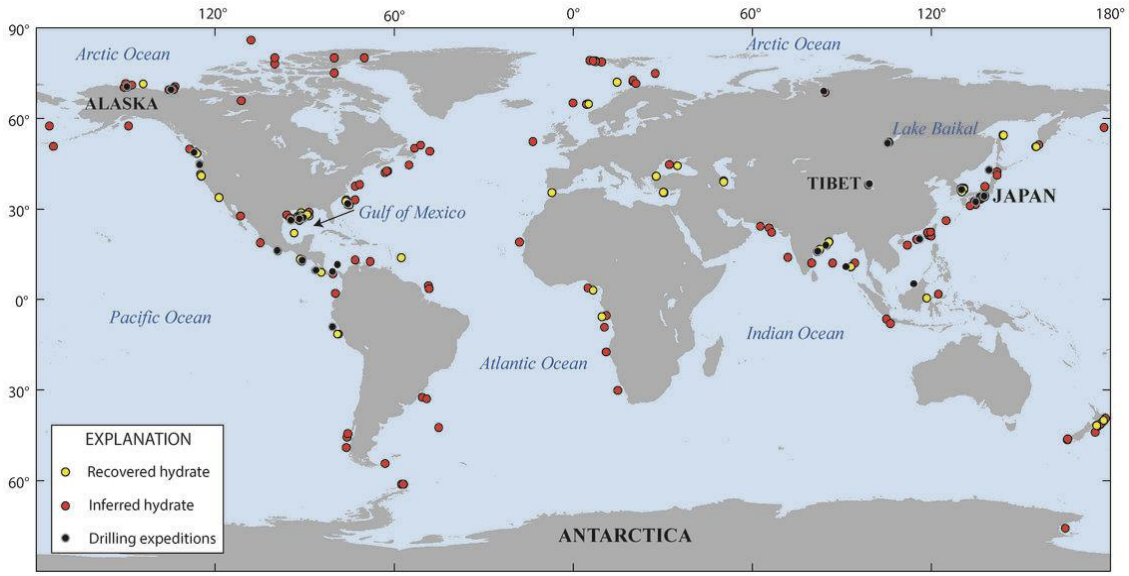

Figure 1.5 locations where gas hydrate has been recovered, where gas hydrate is inferred to be present on the basis of seismic data, and where gas hydrate drilling expeditions have been completed in permafrost or deep marine environments, also leading to recovery of gas hydrate [23].

1.2 A brief history of gas hydrates and current technologies

From a historical point of view, the studies of gas hydrates have been initiated at three different times:

- Hydrate discovery is first documented from 1810. Gas hydrates were studied as an new scientific phenomenon, in which water and gas are transferred into a solid network.
- From 1934, there were studies from the gas transfer industry reviewing the phenomenon of gas hydrate formation.
- From the 1960's, the focus started with the discovery of underground hydrate resources in the depth of oceans and frozen areas particularly in the permafrost.

Sir Humphrey Davy, in 1811, was the first to document experiments with cooling a water solution full of Chlorine at minus 40 degrees Fahrenheit (-40F). He noticed the formation of Chlorine hydrates [13]. From 1810 to 1934, the studies on hydrates were done on the below two axes:

1- Identifying all compounds that could form hydrates.
2- Describing compounds from the percentage of composition and physical properties.

In the first century since the discovery of hydrates, the number of items published was reported as around 40 publications, whereas in 2000 alone, the publication rate had reached to 400. This shows the importance and rising attention to this matter [13,14]. From 1934 onwards, the studies on hydrates had been channeled into finding ways to prevent hydrate from forming in gas transmission lines. In that time, Hammerschmidt [18] realized that the blockage in the gas pipeline/transmission lines was caused by formation of hydrates and not by being frozen. The importance of hydrates increased after their discovery in a natural state in areas of Alaska, Siberia, and Canada [13]. These mineral deposits of hydrates have been recognized as an untapped source of energy, and they were noticed because of the vast amount of stored gases in them. Storing and transmitting natural gas with the hydrate method was first proposed by Benesh in 1942 [13]. After that it was also suggested by Miller & Strong in 1946 [18], Parent in 1948 [13], and Dubinin & Zhidenko in 1979 [13]. In 1982, McIver was first to suggest that there is a connection between gas

hydrates and landslides [24]. Landslides are the most important type of marine geohazard, and hydrates help stabilize the seafloor sediment. The strength of hydrates in sediments is a function of temperature, strain rate, density and cage occupancy. When the gas hydrate burial depth increases, the temperature of the gas hydrate changes, which can cause dissociation of the gas hydrate. In addition, if the hydrate decomposes rapidly, it has been suggested that the released CH_4 from the hydrate will transfer to the air and add significantly to the greenhouse effect [3]. There is some controversy over this last point, however, since the methane released from the Deep-Water Horizon spill never reached the ocean surface [25], though it is possible that in a much larger release that the methane gas would reach the atmosphere.

Lately, these discovered hydrate properties have given rise to numerous applications in broad areas of exploration not only focusing on the potential of the enormous energy resource situated at the bottom of the ocean but also considering the connection with carbon dioxide anthropogenically produced every day. In recent decades, scientists have devoted substantial effort in CO_2 capture or separation from combustion of natural gas/oil in power plants, a process which leads to an exhaust gas product typically containing 3 to 13 percent CO_2. It is because carbon dioxide from combustion sources is among the most significant greenhouse gases in our lifetime that efforts toward sequestration are so important. Direct radiative absorption by CO_2 per molecule is less than methane and nitric oxide, but its concentration is high, and it is more potent than water vapor per molecule. The increase in atmospheric carbon dioxide is responsible for two-thirds of the total energy mismatch that causes the Earth's temperature to rise [26,27]. Following this trend, concerns about carbon dioxide emissions and climate change are expected to grow significantly and will be the focus of attention in the coming decades. This greenhouse gas mitigation demand drives interest in the above-mentioned CO_2 capture/separation, in combination with gas hydrate

extraction and sequestration technology development potential. Studies indicate that the hydrate-based approaches can bring a lower cost of energy production and in a more environmentally friendly manner, as compared to other existing CO_2 reduction techniques, such as absorption, adsorption, or membrane methods [6,7,8]. Research has shown that storing carbon dioxide in the deep ocean is more thermodynamically stable and safer than other methods [9,10], and there is significant space under the seafloor available as storage for carbon dioxide that would otherwise be emitted into the atmosphere. The major concept of CO_2 sequestration below the ocean is pumping carbon dioxide 3 kilometers down where it is injected directly under the seabed. Prior research of accumulating CO_2 underground brought concerns about possible leakage and potential safety issues to the environment [9,10,28,29]. The key advantage of sequestration by injecting carbon dioxide at the depth of 3,000 meters with the surrounding natural environment conditions of high pressure and low temperature is that the carbon dioxide will convert into the liquid phase which is more compressed in volume than the surrounding water, so it will continue to sink downwards. Experiments [9,10] have shown that this injected CO_2 will ultimately form ice-like compounds (hydrates), as there are water molecule cages trapping carbon dioxide molecules inside. Any ocean disposal of CO_2 has to be deep enough to avoid CO_2 getting into the shallow water regions. Shallow water, less than 200-300 meters, are significantly affected by ocean waves and temperature variations between day and night. Any ocean disposal of CO_2 has to be deep enough to avoid CO_2 getting into those regions and potentially leaking into the atmosphere due to water circulation generated transport [28,29]. However, at depths greater than 3 km, the dense liquid CO_2 would sink to the ocean floor where it would form a lake of cold CO_2. This location would then convert to a hydrate structure strong enough that even in most severe eartquakes, CO_2 will not release from the hydrate.

Despite its promise, deep ocean hydrate sequestration of CO_2 (Figure 1.6) research has been stopped because of concerns that the hydrates will dissolve into the surrounding unsaturated seawater, producing a deep ocean acidification. Some proof of concept tests from USGS and Monterey Bay Aquarium show this dissolving process [30]. However, tests have not been done at the deep ocean conditions described above, and particularly when there are sediments also involved. Hence, understanding CO_2 hydrate stability in an unsaturated environment remains an area of active research.

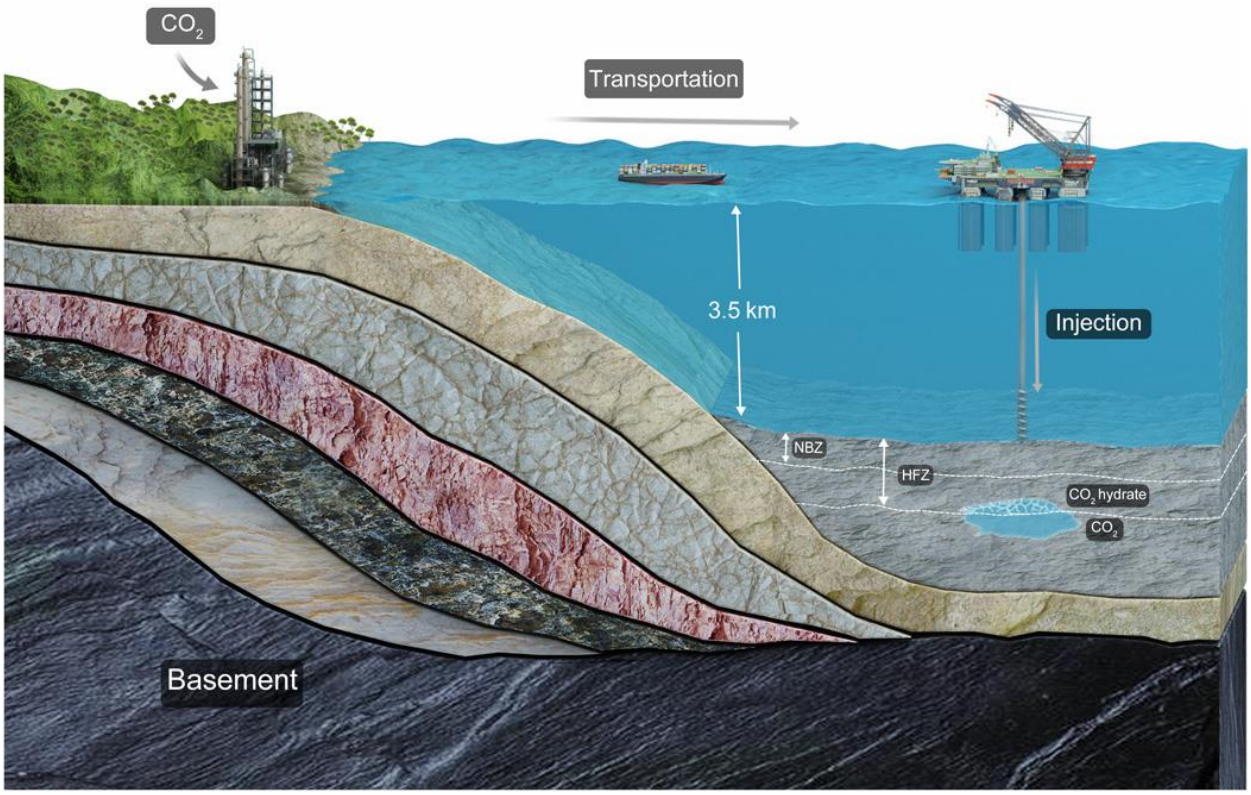

Figure 1.6 Schematic illustration of carbon sequestration in deep-ocean sediments [31].

In addition to the extensive research and development of CO_2 sequestration, another gas hydrate utilization opportunity is desalination of seawater. The conventional desalination process requires a large amount of energy to separate salts from seawater but the novel method of hydrate-based desalination can have lower energy cost than other technologies, and perhaps more importantly the hydrate method is not limited to low salt concentration conditions [11,12,32].

Natural gas hydrate can also be a stable gas storage method, and hydrates can then serve as a form for energy transportation. Transportation of natural gas has been essential for production fields to the place of use, including pipeline natural gas (PNG), liquified natural gas (LNG), compressed natural gas (CNG), and gas to liquid (GTL) conversion. Transportation of natural gas in the form of gas hydrates may have an economic advantage under some conditions because of its lower investment in infrastructure and equipment [5]. Hydrate can be transported either as slurry or solid blocks depending on the location of target or destination; the slurry form of transporting hydrate is usually a better option for distance of approximately 2500 miles or less while the solid form is suitable for distances of 3500 miles or more. Transportation costs for gas hydrates are much lower than LNG for low transportation distances [33]. One of the keys of natural gas hydrate storage and transportation relies on an enhanced kinetic rate of hydrate formation, or, on the other hand, a reduced induction time. Preliminary findings indicate that including surfactants, stirring, and nearby solid surfaces, might all enhance hydrate formation rate. Finally, one other hydrate utilization technique that has been studied is using the high latent heat provided by the gas hydrate during dissociation to apply towards refrigerator applications [7].

It is clear from the above that gas hydrates have both natural and technological significance in a wide range of applications. But these applications are only in nascent stages, whereas the most significant hydrate-based area for study, as described briefly next, is the extraction of methane gas from naturally occurring hydrate beds.

1.3 Strategies for gas production from hydrates

1.3.1 Overall strategies and background

Natural gas combustion produces the lowest amount of CO_2 per unit of energy in comparison to other fossil fuels. There are increased numbers of research studies focusing on the

potential of replacing coal and oil with natural gas as a primary energy source to reduce CO_2 emissions in the foreseeable future as a bridging preventive measure to reduce greenhouse emission [34]. Scientists have been dedicated in exploring methods or strategies for reliable production of natural gas hydrates from the deep ocean. There are three major approaches: 1) thermal stimulation, 2) depressurization, and 3) the addition of inhibitors into the hydrates [35]. While the production strategy depends heavily on the geological structure of the hydrate deposits and their accumulation state [4,36], both depressurization and thermal stimulation involve reducing local pressure and increasing local temperature to cause the hydrate to move away from steady stable conditions and to start dissociating. Thermal stimulation is to inject steam or hot water to the location of the gas hydrate, but this technique is not yet economically feasible due to the large energy costs driven by heat losses during the deep injection. The method of pressure reduction still requires introducing heat to make up for the phase change latent heat, and the heat that can be supplied from the surroundings of typical hydrate deposits are limited. The depressurization strategy for acquiring gas from hydrate may not be sufficient for commercial production rates. Several tentative gas hydrate production trials have been initiated but the challenge remains. One example is the world's first offshore pilot test in Nankai Trough in 2013, which was planned for 2 weeks of production, but was hindered by freezing problems occurring during the process, as well as the appearance of sand and water [37-40]. The latest pilot scale test offshore in Japan was planned for 6 months production, but the freezing issue occurred again after 24 days [38,40]. The strategy of addition of inhibitor into the hydrate is to inject compounds that cause hydrate to dissociate by changing the hydrate stability conditions. These inhibitors can be methanol, salt or any chemical compound that is useful to break the hydrogen bond between water molecules, as well as weakening Van der Waals forces between water molecules and guest

molecules of the hydrate structure. This promising approach underwent experiments [38,41,42], and researchers found that some of the inhibitors are dissolved into the water and lost during the process. This method, therefore, is not efficient and is expensive.

1.3.2 CO_2 injection

Besides the above-mentioned inhibitors, which can cause dissolution during the injection and production, the latest and perhaps the only feasible potential method is to inject CO_2 into the methane hydrate as a win-win situation. That is, this method might sequester CO_2 and eject methane simultaneously. It is this simultaneous strategy that is the focus of the present research.

1.3.2.1 CO_2 hydrate and spontaneous reaction

CO_2, originally produced from fossil fuel combustion, has low cost as an injection species compared to the other methods because the carbon dioxide can be found easily anywhere. It can also be naturally trapped in the deep ocean within solid CO_2 hydrates [43-45]. Hence, CH_4–CO_2 replacement in naturally occurring gas hydrates has been indicated as a potentially effective method of both CO_2 sequestration and CH_4 recovery [45-47]. It is important to recognize that due to climate change, when the temperature increases, gas production can affect geo-mechanical stability of the sediment zone in which the hydrate is dissociated [48,49]. The replacement of CH_4 with CO_2 in gas hydrates is a thermodynamically spontaneous reaction and does not then lead to the potential geo-mechanical hazards that might occur during a strict removal-only methane hydrate production process [24,38,47].

1.3.2.2 CO_2 substitution mechanisms

Injection of CO_2 into the methane hydrate to produce the methane gas from hydrate structure is expected to be a safe and geophysically inconsequential method. There are two primary

mechanisms for substitution of CO_2 into the methane hydrate. One is a solid-state conversion mechanism which is an extremely slow process that may require several years for any significant conversion. Because it has high limitations of mass transport relative to the observation time scale, solid state conversion is not practically feasible [45,47]. The diffusivity for CO_2 involved in the conversion is uncertain but various molecular dynamic simulation studies indicate that the value is in the range of 10^{-12} m^2/s to 10^{-17} m^2/s [50]. Another exchange mechanism is forming a new hydrate from the injected CO_2 and the free liquid water in the porous media. The heat released during the formation process will be directed through the liquid water phase and will cause in situ CH_4 hydrate to dissociate. Since this is a fluid transport-controlled mechanism, the kinetic rates are several orders of magnitude faster than would be possible with solid-state conversion [47,50].

1.3.2.3 Promoters assisting the process

The nucleation process is one of the major reaction steps of hydrate formation. Nucleation happens extremely rapidly at the interface between CO_2 and pore water [50]. When the hydrate nucleation occurs at the interface, with only pure compounds CO_2 and water, the formed hydrate will block the pore space and prevent further transport [41,47]. Researchers, however, identified that adding surfactant to the injected CO_2 will reduce hydrate formation at the interface and thus make it possible to control combined CH_4 production and CO_2 storage [47,51]. Surfactants are either manufactured or exhibited in nature. There are bio-surfactants which are decomposed from microorganisms produced by Pseudomonas aeruginosa and synthetic-surfactants produced from petroleum/vegetable-bases [52]. Surfactants contain both hydrophilic “head” and lipophilic “tail” character. When dissolved in water, the head sits inside the water and the tail points out of the water (hydrophobic). Surfactants should stay at the water-gas interface, and after a hydrate film forms rapidly, the surfactant remains very close to the hydrate film and causes it to dissociate or

at least keeps holes open through the film (Figure 1.8). It thereby holds open the hydrate interface for mass transport from gas to liquid water instead of mass transport through the hydrate film. Without surfactant there are no holes in the hydrate film, and this layer will continue to thicken and grow upward [51,53] so mass transport through the hydrate will be very slow. Low molecular weight surfactants constructed on the basis of physical solvents for CO_2 are attractive because they enhance the interface thickness and dynamics without making very stable emulsions that could partly trap hydrate particles and clog pore space [53]. On the other hand, surfactants are surface-active agents that can increase the volume of gas trapped in the hydrate network by changing the thermodynamic condition of hydrate formation, and at the same time they can improve the rate of hydrate growth by reducing surface tension to enhance the mass transfer from gas phase into the liquid water phase [51]. Another strategy to promote the CO_2 hydrate formation process is introducing nitrogen along with CO_2/surfactant during injection. This increases permeability, and N_2 can also fill the small cavities of the hydrate. CO_2 molecules only penetrate to the large cavities in hydrate structure I, they do not fit into the small cavities due to size and stronger attraction energy to the water molecules [41,47]. As an example, in the Ignik Sikumi Gas Hydrate Exchange field trial on the Alaska North Slope during 2011 and 2012, both nitrogen and carbon dioxide were injected into a natural hydrate field. In this project, a mixture of 23% CO_2 and 77% N_2 by volume were injected into the methane hydrate but the problem was that an extremely slow and inefficient exchange process was observed [41,54]. The main difficulty was that the hydrate film slowed down hydrate growth. Results like this one often lead to a typical misunderstanding that CO_2 is not efficient for producing hydrates [38,55]. In fact, however, it is the tuning of the surfactant and CO_2 mixture ratio that makes the difference. Adding large amounts of nitrogen in the CO_2 is not a good solution, because nitrogen reduces the thermodynamic driving force for making new CO_2

hydrate [38]. A limited amount of N_2 can be useful for increasing the permeability of the injection gas. It is the above set of findings that motivates the current research. A primary objective of the work is to determine the feasibility of a direct exchange of CO_2 into a methane hydrate with surfactants to promote the rate (see Figure 1.7).

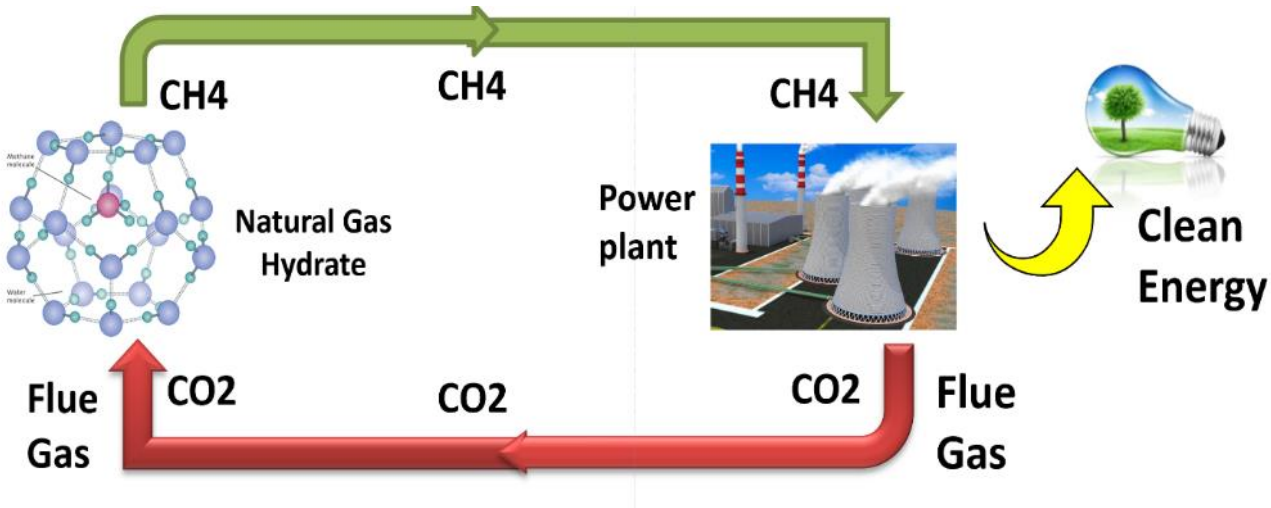

Figure 1.7 Overall look at the cycle of CO_2-CH_4 hydrate exchange.

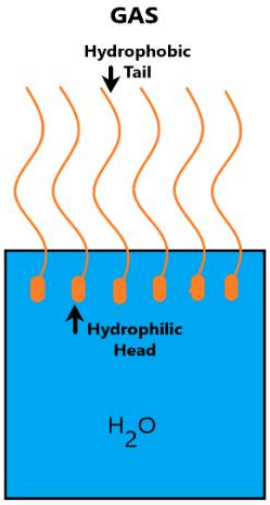

Figure 1.8 Single layer of surfactant at the water-gas interface.

1.3.3 Research motivation and objective

The motivations of this research are addressed in the above-mentioned details of CH_4, and CO_2 hydrate in nature, along with the attractive potential of sequestering CO_2 in the deep ocean to help mitigate global climate change, and also the chance of using gas hydrates as a clean future energy source which helps meet the increasing energy demands. Natural gas hydrates can be environmentally friendly because the exhaust emission from direct combustion creates less carbon dioxide than does the combustion of other heavier, more carbon rich fossil fuels [56].

The specific objective of this research is to determine the kinetic rate of new CO_2 hydrate formation and dissociation of methane hydrate in porous media computationally and experimentally, and also to develop an understanding of the potential role of surfactants to promote the hydrate substitution and growth rate.

CHAPTER 2: THEORY OF DISSOCIATION AND GROWTH OF GAS HYDRATES

Hydrate formation has been a complicated research topic because even in the simplest system with one hydrate former, for instance CH_4, the water surrounding the guest molecule will not reach a full thermodynamic equilibrium no matter if it is in natural surroundings or in industrial applications. Most of the existing experiments are, however, dedicated to hydrate equilibrium measurements. These equilibrium measurements and calculations are useful bounds on the formation behavior, but they do not capture the kinetic rate information that is needed practically for a realistic formation process. This chapter outlines the fundamentals of hydrate thermodynamics and particularly discusses the likely situation that hydrates do not reach equilibrium in any realistic configuration. This non-equilibrium hypothesis has been documented and widely distributed by the group of Kvamme, et al. [1,38,41,47,50,57], but it still seems to be relatively unaccepted by the broader hydrate research community. One reason for the hesitancy in adopting the non-equilibrium viewpoint is the more complex analysis required, and it is conceivable that the additional insight is not warranted by the increased complexity. The current research is meant to shed some light on this non-equilibrium view as part of the practical understanding necessary to create hydrate technologies of relevance.

2.1 Hydrate formation, dissociation, and stability limits

With three co-existing phases, liquid water (or ice), gas and hydrate film, the full formation process distributes the mass of the two components, host and guest molecules, over a total of 12 independent thermodynamic properties. The hydrate formation and dissociation process involve

classic statistical thermodynamics and has been studied extensively [50,57]. Among the above mentioned 12 thermodynamic properties, temperature and pressure are the two key physical properties shared among all three phases (this represents 6 independent variables). The mole-fraction of the two chemical components (host and guest) changing among each phase are the 6 additional independent variables. There are also species conservation laws, as well as physical and chemical equilibrium as functions of volume among these three phases. The species conservation equations are from the sum of mole-fractions in the three phases. In addition, there are the equilibrium equations for temperature and pressure, and finally there are four independent equations of chemical equilibrium. In order to illustrate this set of equations and constraints governing the hydrate system, it is convenient to recall some basic thermodynamics. Figure 2.1 shows the equilibrium and non-equilibrium conditions in closed system.

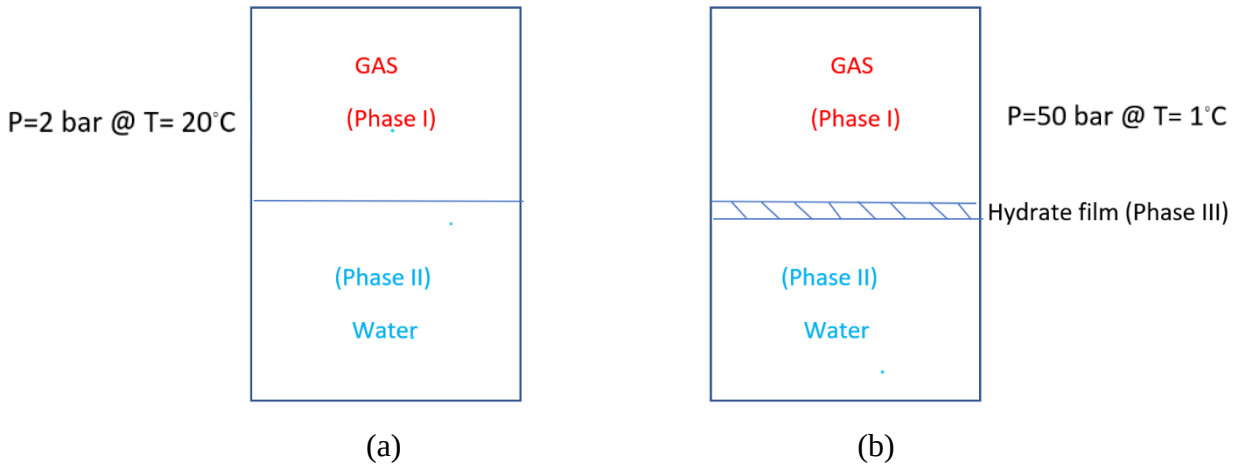

Figure 2.1 a) System can reach equilibrium. b) System cannot reach equilibrium (when there is hydrate film at the interface).

If water and CH_4 are totally isolated at constant volume, and are at conditions outside of hydrate stability, then the first law for the composite system of these two phases is:

$$d\underline{U}^{(aq)} = dQ^{(aq)} - P^{(aq)} d\underline{V}^{(aq)} + \sum_{i=1}^{n} \mu_i^{(aq)} dN_i^{(aq)} \quad (1)$$

$$d\underline{U}^{(gas)} = dQ^{(gas)} - P^{(gas)} d\underline{V}^{(gas)} + \sum_{i=1}^{n} \mu_i^{(gas)} dN_i^{(gas)} \quad (2)$$

The liquid phase is denoted as *aq (aqueous solution)* and the gas/vapor phase is denoted as *gas*. U is internal energy and the line under denote extensive energy in Joules. The line under the volume *V* denotes extensive volume in m^3. *N* is number of moles and index *i* is a counter on components. In this case, *i* is either CH_4 or water. The two first terms are the added heat and the delivered mechanical work while the last term is frequently denoted as the chemical work. Basically, this is the work needed to release (negative dN_i) molecules from the phase. The chemical potential $\mu_i^{(aq)}$ is the driving force for this release and represents the necessary energy to release the molecules from attractions to surrounding molecules, along with an entropy contribution related to rearrangements of the remaining molecules. And since the system is isolated then:

$$d\underline{U}^{(aq)} + d\underline{U}^{(gas)} = 0 \quad (3)$$

$$dQ^{(aq)} + dQ^{(gas)} = 0 \quad (4)$$

$$d\underline{V}^{(gas)} + d\underline{V}^{(aq)} = 0 \quad (5)$$

$$dN_i^{(gas)} + dN_i^{(aq)} = 0 \quad (6)$$

The second law of thermodynamics for the system is:

$$d\underline{S} = d\underline{S}^{(gas)} + d\underline{S}^{(aq)} \geq 0 \quad (7)$$

$$\frac{dQ^{(aq)}}{T^{(aq)}} = d\underline{S}^{(aq)} \quad (8)$$

$$\frac{dQ^{(gas)}}{T^{(gas)}} = d\underline{S}^{(gas)} \quad (9)$$

Combining equations (1), (4), (7) and (8) gives:

$$d\underline{U}^{(aq)} \leq T^{(gas)} d\underline{S}^{(aq)} - P^{(aq)} d\underline{V}^{(aq)} + \sum_{i=1}^{n} \mu_i^{(aq)} dN_i^{(aq)} \quad (10)$$

Combining equations (2), (4), (7) and (9) gives:

$$d\underline{U}^{(gas)} \leq T^{(aq)} d\underline{S}^{(gas)} - P^{(gas)} d\underline{V}^{(gas)} + \sum_{i=1}^{n} \mu_i^{(gas)} dN_i^{(gas)} \quad (11)$$

(7), (10) and (11) using (3), (5) and (6) gives:

$$d\underline{S}^{total} \geq d\underline{U}^{(gas)}\left[\frac{1}{T^{(aq)}}-\frac{1}{T^{(gas)}}\right]-d\underline{V}^{(gas)}\left[\frac{P^{(gas)}}{T^{(aq)}}-\frac{P^{(aq)}}{T^{(gas)}}\right] \quad (12)$$
$$+\sum\left[\frac{\mu_j^{(gas)}}{T^{(aq)}}-\frac{\mu_j^{(aq)}}{T^{(gas)}}\right]dN_i^{(gas)} \geq 0$$

And the only absolute solutions that make stability possible for the system is when the entropy change approaches unconditionally zero when all the terms in the brackets in (12) approach zero.

$$T^{(aq)} = T^{(gas)} \quad (13)$$

$$P^{(aq)} = P^{(gas)} \quad (14)$$

$$\mu_i^{(aq)}(T^{(aq)}, P^{(aq)}, \vec{x}^{(aq)}) = \mu_i^{(gas)}(T^{(gas)}, P^{(gas)}, \vec{y}^{(gas)}) \quad (15)$$

The independent thermodynamic variables in this system are the two temperatures (water and gas), two pressures, and the two chemical potentials for water and CH_4 in each of the two phases; in total 8 variables. The two species conservation laws are the sum of mole-fractions in each of the two phases. Conditions of equilibrium; equations (13) and (14), plus equation (15) for water and CH_4 gives 4 conditions. In total there are 6 constraints on the 8 independent thermodynamic variables. Fixing temperature and pressure then gives the necessary completion of balance between the number independent variables and the constraints on the system.

Heat transport through condensed water phases is 2 – 3 orders of magnitude faster than mass transport. Thermal stability, equation (13) in the simple system and similar for other phases in the more complex hydrate system, is therefore often in place even for non-equilibrium systems.

Mechanical stability is also assumed to be fulfilled for all phases. Chemical stability, however, is quite another case. The combined first and second law of thermodynamics is therefore more conveniently expressed in terms of Gibbs free energy through a Legendre transform of (10), (11) for the simple system and with a similar equation for hydrate:

$$\begin{aligned} d\underline{G}^{total} \le & -\underline{S}^{(aq)}\, dT^{(gas)} + \underline{V}^{(aq)}\, dP^{(aq)} + \sum_{i=1}^{n} \mu_i^{(aq)} dN_i^{(aq)} \\ & -\underline{S}^{(gas)}\, dT^{(aq)} - \underline{V}^{(gas)}\, dP^{(gas)} + \sum_{i=1}^{n} \mu_i^{(gas)} dN_i^{(gas)} \\ & -\underline{S}^{(H)}\, dT^{(aq)} - \underline{V}^{(H)}\, dP^{(H)} + \sum_{i=1}^{n} \mu_i^{(H)} dN_i^{(H)} \end{aligned} \qquad (16)$$

where superscript H now denotes hydrate. Since the 3-phase system is mathematically over determined, the minimization of (16), under constraints of mass and heat transport gives the local distribution of masses over the co-existing phases. None of the phases (and associated compositions) are unconditionally stable. If one of the phases found should be stable, then the additional conditions have to be fulfilled:

$$\left[\frac{\partial \underline{G}^{(m)}}{\partial M}\right]_{K \neq M} \delta M \le 0 \qquad \text{for any possible range of changes of independent variable M} \quad (17)$$

The first law is needed for the energy balance involved, and for the heat transport:

$$d\underline{H}^{total} \le \sum_{m=1}^{phases} dQ^{(m)} + \underline{V}^{(m)}\, dP^{(m)} + \sum_{i=1}^{n.m} \mu_i^{(m)} dN_i^{(m)} \qquad (18)$$

Since a non-equilibrium system does not have unique criteria for stability, except for local minima in (16), it is important to discuss stability limits rather than using the expression "equilibrium curves". Figure 2.2 illustrates this for CH_4. Figure 2.2 a) is the most important one since it illustrates the limited stability window for hydrates in nature and in industrial settings. Even if hydrate is at forming conditions in the temperature-pressure projection, the hydrate will dissociate if the surrounding water contains less CH_4 than the contours above. Figure 2.2 b) illustrates the limit for hydrate sublimation. If the water content in the CH_4 gas is less than the concentration contour, then hydrate will sublime. The phase transition involved in Figure 2.2 also sets the stability limits in this case. Hydrate can grow from dissolved CH_4 in water from the concentrations in Figure 2.2 a), and down to the concentration contour in Figure 2.2 a). This will be discussed in the next section as part of a discussion on hydrate nucleation from various phases. The thermodynamic basis for the curves in Figure 2.2 is, however, needed in this section. The derivation of chemical potential for water in hydrate from the semi grand canonical ensemble [50,57], is similar to that of van der Waal & Platteeuw [58] except for the approximation of a rigid lattice in [58], which is not needed. The final result is:

$$\mu_{H_2O}^{H} = \mu_{H_2O}^{O,H} - \sum_{k=1,2} RT\nu_k \ln\left(1+\sum_i h_{ki}\right) \quad (19)$$

$\mu_{H_2O}^{O,H}$ is the chemical potential for water in an empty clathrate. The number of cavities is ν, with subscript k indexing for large and small cavities. For structure I, which is the main focus here, $\nu_{large}=3/24$ and $\nu_{small}=1/24$.

$$h_{ki} = e^{\beta a_{ki}} \quad (20)$$

Beta is the inverse of Boltzmann constant times temperature ($1/k_BT$) in molecular units, and the inverse of the universal gas constant times temperature in molar units. The rigid water lattice version of this derivation is:

$$a_{ki} = \beta\left[\mu_{ki} + \beta^{-1}\ln b_{ki}\right] \quad (21)$$

$$b_{ki} = \left[\frac{m_i}{\beta 2\pi\hbar}\right]\int_{V_k} e^{\beta[w_{ki}(V_k)]}dV_k \quad (22)$$

m_i is the molecular mass of guest molecule i, $\hbar$ is the Plank-Dirac constant. $w_{ki}(V_k)$ is the interaction energy between guest molecule i in the cavity of type *k* and all surrounding molecules. Frequently all water molecules are limited to surrounding water molecules (see for instance [13] and references in that book) while guest interactions with guest molecules in neighbouring cavities may also have a significant impact on the integral [59]. Slightly polar molecules, in which the average partial charge (when rotating the molecule around the center of mass inside the cavity) is positive outwards to cavity walls, will have extra coulombic force stabilization effects [59,60]. A typical example is H_2S, which forms hydrates at low pressures. The opposite effect occurs for molecules in which the average charge is pointing outwards, like for instance CO_2. Large molecules relative to available space for movements inside the cavity will significantly interact with the water vibrational movements relative to minimum energy positions. For this purpose, a harmonic oscillator approach gives a more accurate description since it will specifically also incorporate destabilization of the water lattice due to specific ranges of frequencies of guest movements, which interferes with water movement frequencies. The harmonic oscillator

formulation is:

$$a_{ki} = \beta\left[\mu_{ki} - \Delta g_{ki}\right] \quad (23)$$

The second term inside the brackets is the free energy of inclusion, which is evaluated based on samplings of fluctuations from the energy minimum in the cavity of type k [13,57].

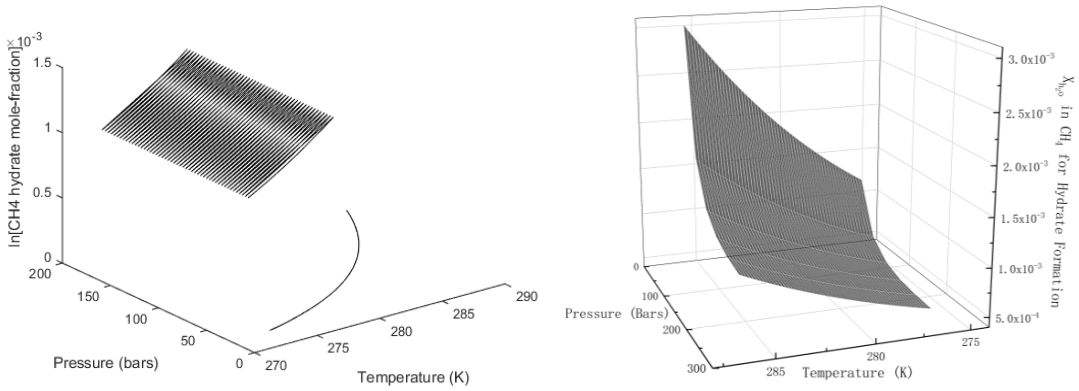

(a) (b)

Figure 2.2 a) Limits of CH_4 hydrate formation in the pressure temperature projection. No hydrate for any pressure below the curve. The contour graph above the Pressure Temperature projection are limits of CH_4 hydrate stability as function of mole-fraction CH_4 in surrounding water. b) Hydrate stability limits as function of mole fraction water in CH_4 phase.

2.2 Hydrate nucleation from various phases

Hydrate formation is a multiscale process since any phase transition is a nano scale rearrangement of molecules into a new phase that can continue to grow, and the bulk phase is at a larger scale. The necessary mass needed has to be supplied from a larger surrounding on a meso scale level, and any released heat needs to be carried away. Hydrate formation in a pipeline nucleation can happen towards rusty surfaces or on water/gas interfaces [50]. A meso scale layer

will typically be the layer which is significantly affected by the solid wall in terms of friction. On the average this layer can be slowed to laminar flow but with special flow features very close to the roughness of the surface [61]. On top of the nano and meso scales there is the "bulk" flow in the pipeline which exchanges mass and heat with the finer scale levels. For hydrates in sediment, the similar level will be that of the local nucleation through diffusional mass transport across interfaces on the order of 1-2 nm. These nanoscale processes are connected to fluid mechanical flow in the pores. And then at the larger scale, all pores are connected to the reservoir scale models. The typical problem in many modelling efforts is that they must frequently skip the nano level scale, despite the fact that this may the dynamic bottleneck of the problem. Reducing pressure on a block of ice at the triple point does not result in fast dissociation of ice. A similar reduction of pressure on a block of CH_4 hydrate will be slightly faster but is still dynamically limited by the slow breaking of the hydrogen bonds. How to couple the various levels of dynamics is another story. One possible way is to use a meso scale model which also incorporates the nano scale and then extracts the most important results/effects over to a simplified model that can be numerically handled efficiently by a macro model, like for instance a hydrate reservoir simulator [62-64].

Classical Nucleation Theory (CNT) is simple enough numerically to be used in various macro models like pipeline flow simulators or hydrate reservoir simulators. The original version of CNT is, however, of limited use since it contains a homogeneous mass transport term originally written for one component. A combination CNT approach, with a mass transport term derived from Fick's law and results from molecular dynamics simulations, produces a very simple formalism while still maintaining many nanoscales transport details. The first step in this development was published by Kvamme et al. [50]. In this first study, a simple logarithmic profile

for diffusivities were utilized in Fick's law for the mass transport. Classical Nucleation Theory (CNT) can be expressed as:

$$J = J_0 e^{-\beta \Delta G^{Total}} \quad (24)$$

where J_0 is the mass transport flux supplying building block for the hydrate growth. The meaning of J_0 will be the limiting mass transport flux through the interface between the old phase and the new phases. In the case of hydrate nucleation and growth, a hydrate core will always be covered with water. For heterogeneous nucleation on a liquid water/gas interface the capillary waves, as well as capillary forces between hydrate water and liquid water will ensure that the hydrate core during nucleation is covered by liquid water. The actual rate limiting transport in J_0 is therefore the transport of hydrate forming molecules across an interface of gradually more structured water from the liquid side towards the hydrate side. The units of J_0 will be moles/m^{3}s for homogeneous hydrate formation, and moles/m^{2}s for heterogeneous hydrate formation. Heterogeneous formation is normally faster if the mass is available during the process. The first order Fick's law provides the limiting flux across the interface (as shown below):

$$J_0 = -D_{CH_4}^{interface}(R)\frac{\partial C_{CH_4}^{interface}}{\partial R} \quad (25)$$

J in equation (24) has the same units as J_0. β is the inverse of the gas constant times temperature and ΔG^{Total} is the molar free energy change of the phase transition. This molar free energy consists of two contributions. The phase transition free energy and the penalty work of pushing aside old

phases in order to give room for the new phase. Since the molar densities of liquid water and hydrate are reasonably close, it is a fair approximation to multiply the molar free energy of the phase transition with the molar density of hydrate times the volume of the hydrate core. The push work penalty term is simply the interface free energy times the surface area of the hydrate crystal. Using lines below symbols to indicate extensive properties (in Joules):

$$\Delta \underline{G}^{Total} = \Delta \underline{G}^{Phasetransition} + \Delta \underline{G}^{Pushwork} \quad (26)$$

The exponential term in (24) contains the thermodynamic control of the phase transition. A simple spherical model for hydrate is sufficient for illustration, and is also accurate enough for many systems in which other uncertainties are larger.

$$\Delta \underline{G}^{\text{Total}} = \frac{4}{3}\pi R^3 \rho_N^H \Delta G^{\text{Phase transition}} + 4\pi R^2 \gamma \quad (27)$$

where ρ_N^H is the molar density of the hydrate and γ is the interface free energy (interfacial tension) between hydrate and the surrounding phase. We have used $30 \cdot 10^{-6}$ kJ/m^2 for this interfacial energy. Even if the hydrate core growing on the surface of water is assumed to be floating, one will still expect the small crystals to be covered by water on the gas side as well because of capillary forces facilitating transport and adsorption of water molecules from the liquid water side. The hydrate density is given by the filling fractions of the various cavities and the sizes of the unit crystal. For structure I hydrate the smallest symmetrical unit cell is 12.01Å on a side and contains 46 water molecules, 6 large cavities, and two small cavities.

The mole fractions of the equilibrium hydrate comes directly from the statistical mechanics first as filling fractions and then recalculated to the corresponding mole-fractions.

$$\theta_{ki} = \frac{h_{ki}}{1 + \sum_j h_{ki}} \quad (28)$$

θ_{ki} is the filling fraction of component *I* in cavity type *k*. Also:

$$x^H_{i,large} = \frac{\theta_{large,i}\nu_{large}}{1 + \theta_{large,i}\nu_{large} + \theta_{small,i}\nu_{small}} \quad (29)$$

$$x^H_{i,small} = \frac{\theta_{small,i}\nu_{small}}{1 + \theta_{large,i}\nu_{large} + \theta_{small,i}\nu_{small}} \quad (30)$$

where ν is the fraction of cavity per water for the actual cavity type, as indicated by subscripts. The corresponding mole-fraction water is then given by:

$$x^H_{H_2O} = 1 - \sum_i x^H_{i,large} - \sum_i x^H_{i,small} \quad (31)$$

and the associated hydrate free energy is then:

$$G^{(H)} = x^{H}_{H_2O}\mu^{H}_{H_2O} + \sum_i x^{H}_i \mu^{H}_i \quad (32)$$

The associated heat transport related to the phase transition dynamics is linked to the enthalpy change for the phase transition. In order to make this link thermodynamically consistent the enthalpy change has to be related to the free energy change through the fundamental relationship:

$$\frac{\partial\left[\frac{\Delta G^{Total}}{RT}\right]_{P,\vec{N}}}{\partial T} = -\left[\frac{\Delta H^{Total}}{RT^2}\right] \quad (33)$$

$$\dot{Q} \sim \Delta H^{Total} \quad (34)$$

Heat transport mechanism (conduction, convection, radiation) for the related heat transport $\dot{Q}$ (units are Joule/s). As mentioned earlier, heat transport through water systems is typically 2–3 orders of magnitudes faster than mass transport [50], and in many cases of hydrate phase transitions in porous media a simple approximate heat conductivity model is used.

Transport of CH_4 inside liquid water is several orders of magnitudes faster than the diffusion through structured water close to the hydrate surface. This interface (1.2 nm) will continuously be renewed due to water hydrogen entropy optimization. With reference to the discussion above note that the total free energy change, equation (27) is used in these calculations up to critical size while the penalty work is approximately omitted for the growth regime above critical radius.

$$R^* = -\frac{2\gamma}{\rho_N^H \Delta G^{\text{Phase transition}}} \quad (35)$$

$$t(R) - t(o) = \int_{C_{CH_4}(R=0)}^{C_{CH_4}(R=12)} \frac{\partial C_{CH_4}(z)}{\left[-D_{CH_4}(z)\frac{\partial^2 C_{CH_4}(z)}{\partial z^2}\right]} \quad (36)$$

To summarize the main findings of theory and concept of hydrate in this chapter:

- Hydrate in nature and industries are not in equilibrium because there are too many co-existing phases, and the chemical potential of hydrate formers are not the same in all phases.
- It is possible to accurately capture the non-equilibrium behavior with fairly standard statistical thermodynamic models.
- In this model, the heat transport rate is much faster compared to the transport of mass needed to create the hydrate. When liquid water is present then heat transport is three orders of magnitude faster. Hence, heat released disappears instantly and normally spreads into the large volume of water, so temperature change is damped to zero almost (isothermal phase transition).
- The substitution kinetics described, modeled, and experimentally verified in this research will take into account the true non-equilibrium nature of the interface dynamics inherent in hydrates – it does not assume standard equilibrium conditions.

- Hydrate formation is a multi-scale process since the nucleation occurs at the nanoscale, but the formation structure requires transport that occurs at the mesoscale; modeling the entire process is difficult for this reason.

The next chapter shows this modeling in more detail.

CHAPTER 3: COMPUTATIONAL MODELING OF DISSOCIATION AND GROWTH OF GAS HYDRATES

As demonstrated in this chapter, a residual thermodynamic approach for the description of hydrate has been available for 25 years, but only recently has it been used for more detailed analysis of phase transition kinetics and various hydrate production scenarios. Less than two years ago, a model for enthalpy calculations was derived from the same concept. This chapter will give a brief overview of modeling of heterogeneous and homogeneous hydrate nucleation, and based on this modeling will discuss some possible hydrate production methods from the residual thermodynamic point of view. In this chapter, and in the previous chapter, all figures are calculated by running the "Khuram code" that was developed and exercised in collaboration with within Kvamme's group in Norway (now emeritus Professor Bjorn Kvamme from the University of Bergen). This code has a non-equilibrium thermodynamic package to calculate differences in free energies of hydrates and hydrate formers. Gibb's free energy minimization was employed to consider competing hydrate phase transitions. Hydrate formation, dissociation, and reformation were analyzed by considering undersaturation or supersaturation with respect to independent thermodynamic variables, such as temperature, pressure and concentration. Some of these graphs are already published in the journal papers listed in the CV at the start of this dissertation.

3.1 Residual thermodynamics approach

In order to solve equations (13) to (15) from the previous chapter, as well as species conservation, we need thermodynamic models:

$$\mu_i^{(m)}(T^{(m)},P^{(m)},\vec{x}^{(m)}) = \mu_i^{(pure,m,reference)}(T^{(m)},P^{(m)}) + \Delta\mu_i^{(m,reference,idealmix)}(T^{(m)},P^{(m)},\vec{x}^{(m)}) + \Delta\mu_i^{(m,non-ideal)}(T^{(m)},P^{(m)},\vec{x}^{(m)}) \quad (37)$$

For a gas phase model, the ideal gas approach is the natural choice. The first term on the right-hand side of (37) is available from statistical mechanics using molecular mass and rotational momentum for rigid molecules. Contributions from intramolecular rotations and vibrations in non-linear molecules require some integrations if these contributions are significant enough. The second term on the right-hand side comes from the entropy change when a number of molecules, all at the same T and P are mixed into a volume, the so-called entropy of mixing. The last term is the residual contribution. In statistical mechanics this is the configurational contribution. Any model that describes pressure as a function of volume, temperature and composition can provide this contribution through a derivation using Helmholtz free energy. The details are not needed here and can be found in chemical engineering thermodynamics textbooks. Formally this residual for a component i in phase m is expressed as:

$$\ln\phi_i^m = \frac{\mu_i^{m,real} - \mu_i^{m,ideal\,gas,mix}}{RT} \quad (38)$$

ϕ_i^m is the fugacity coefficient for molecule *i* in phase *m*. Superscript *real* means the actual property while superscript *ideal gas, mix* represents ideal gas, and is in the first two terms in equation (37). Equation (37) for residual thermodynamics is then:

$$\mu_i^{(m)}(T^{(m)},P^{(m)},\vec{x}^{(m)}) = \mu_i^{(pure,m,ideal\,gas)}(T^{(m)},P^{(m)}) + RT\ln x_i^m + RT\ln\phi_i^m(T^{(m)},P^{(m)},\vec{x}^{(m)}) \quad (39)$$

For complex liquid state mixtures, a more convenient reference state is pure liquid chemical potential and the similar equation to (39) is:

$$\mu_i^{(m)}(T^{(m)}, P^{(m)}, \vec{x}^{(m)}) = \mu_i^{(pure,m,pureliquid)}(T^{(m)}, P^{(m)}) + RT \ln x_i^m + RT \ln \gamma_i^m (T^{(m)}, P^{(m)}, \vec{x}^{(m)}) \quad (40)$$

where superscript *pure liquid* means pure liquid state for component *i* in phase m. γ_i^m is the activity coefficient for component *i* in phase m. The mathematical form of this expression is similar to equation (38) except for the difference between the real mixture and ideal liquid mixture.

Equation (40) can also be linked to residual thermodynamics since the chemical potential of pure liquid water can be calculated using molecular dynamics simulations for model molecules. In computational chemistry, the water model is created with various types of forcefield potentials depending on the point of interactions and physical conditions being solved. The simplest water model is TIP3P which contains 3-sites as transferrable intermolecular potential while TIP4P is a four-point rigid water model extension (of the traditional three-point model) by adding an additional site for interaction at a fixed distance [65-69]. Kvamme & Tanaka [57] utilized the TIP4P [70] interaction model for water to calculate chemical potential for ice and then utilized the following relationship:

$$\frac{\partial \left[\frac{\Delta \mu_{H_2O}(T,P)}{RT} \right]_{P,\vec{N}}}{\partial T} = -\left[\frac{\Delta H_{H_2O}(T,P)}{RT^2} \right] \quad (41)$$

to calculate chemical potential for liquid water using the experimental enthalpy for ice dissociation to derive chemical potentials for liquid water based on the TIP4P calculated chemical potentials for water as ice below 273.15 K. Experimental data for the specific heat capacity of liquid water were utilized for higher temperatures. In addition to the ice and liquid water, also water in empty hydrate clathrate I and II were calculated and are listed in Table 3.1 below.

Table 3.1 Parameters for dimensionless chemical potential functions in the equation.

$$\frac{\mu_{H_2O}^m}{RT} = a_0^m + a_1^m \left[\left(\frac{273.15}{T} \right) - 1 \right] \quad (42)$$

Water phase, m	a_0	a_1
Empty structure I	-21.333	-18.246
Empty structure II	-21.374	-18.186
Ice (T < 273.15 K)	-21.690	-19.051
Liquid water (T>273.15 K)	-21.690	-16.080

Equation (40) is called symmetric excess since the activity coefficients approach unity when the mole fraction approaches unity for a component. Components of low solubility in water are closer to infinite dilution and asymmetric excess is then more appropriate, defined as:

$$\mu_i^{(m)}(T^{(m)}, P^{(m)}, \vec{x}^{(m)}) = \mu_i^{(\infty,m,liquid)}(T^{(m)}, P^{(m)}) + RT \ln x_i^m + RT \ln \gamma_i^{\infty,m}(T^{(m)}, P^{(m)}, \vec{x}^{(m)}) \quad (43)$$

The infinity symbol on the chemical potential in the first term on the right-hand side denotes infinite dilution chemical potential in the solvent liquid. Equation (43) is called the asymmetric excess convention since the activity coefficient with the infinite superscript goes to unity when the mole-fraction approaches zero. Obviously then the model for the activity coefficient must ensure that mole-fraction times activity coefficient approaches unity as a

mathematical limit to prevent any singularity. A model for CH_4 dissolved in water is given by equations (44) and (45) below. The ideal gas contribution to (44) is available from statistical mechanics using experimental values for partial molar volume of CH_4 at infinite dilution in water (see Table 3.2).

$$\mu_{CH_4}^{\infty,\text{Residual}} = 3.665 + \frac{40.667}{T_R} - \frac{48.860}{T_R^2} \quad (44)$$

$$\ln \gamma_{CH_4}^{\infty}(T,P,\vec{x}) = \sum_{i=1,2}^{39} \left[a_0(i) + \frac{a_1(i+1)}{T_R} \right] (x_{CH_4})^{\left[0.05+\frac{i-1}{40}\right]} \quad (45)$$

Table 3.2 Parameters for equation (46).

I	a_0	a_1	*I*	a_0	a_1	*i*	a_0	a_1
1	1.360608	3.796962	15	-11.580192	16.384626	29	-23.855418	31.720767
3	.033630	-.703216	17	-.087295	13.171333	31	-35.125907	37.064849
5	.656974	-12.441339	19	-.558793	13.556732	33	-33.675110	41.544360
7	1.763890	-21.119318	21	-23.753020	16.573197	35	-27.027285	57.609882
9	5.337858	-33.298760	23	-10.128675	13.591099	37	-19.026786	54.961702
11	-.024750	12.387276	25	-41.212178	5.060082	39	-37.872252	57.204781
13	48.353808	17.261174	27	-31.279868	31.289978			

Using residual thermodynamics for CH_4 in the gas phase and the Soave-Redlich-Kwong (SRK) [61] equation of state for the fugacity coefficient in the gas phase, and equations (44) and (45) for CH_4 dissolved in liquid water, the solubility of CH_4 in liquid water is found from the solution of the equation:

$$\begin{aligned} &\mu_{CH_4}^{(CH_4,gas,ideal\,gas)}(T^{(gas)},P^{(gas)}) + RT\ln y_{CH_4}^{gas} + RT\ln \phi_{CH_4}^{gas}(T^{(gas)},P^{(gas)},\vec{y}^{(gas)}) \\ &= \mu_{CH_4}^{(\infty,water,liquid)}(T^{(water)},P^{(water)}) + RT\ln x_{CH_4}^{water} + RT\ln \gamma_{CH_4}^{\infty,water}(T^{(water)},P^{(water)},\vec{x}^{(water)}) \end{aligned} \quad (46)$$

With symmetric excess for liquid water, equation (40), and residual thermodynamics for water dissolved in gas, the solubility of water into the CH_4 gas is given by:

$$\mu_{H_2O}^{(gas,ideal\,gas)}(T^{(gas)},P^{(gas)})+RT\ln y_{H_2O}^{gas}+RT\ln\phi_{H_2O}^{gas}(T^{(gas)},P^{(gas)},\vec{y}^{(gas)})$$
$$=\mu_{H_2O}^{(pue,water,liquid)}(T^{(water)},P^{(water)})+RT\ln x_{H_2O}^{water}+RT\ln\gamma_{H_2O}^{water}(T^{(water)},P^{(water)},\vec{x}^{(water)}) \quad (47)$$

The thermal and mechanical equilibrium, equations (13) and (14) from the previous chapter, and temperature and pressure equations (45) and (46), along with species conservation, leaves two equations in two unknown mole-fractions. The solutions are plotted in Figure 3.1 below.

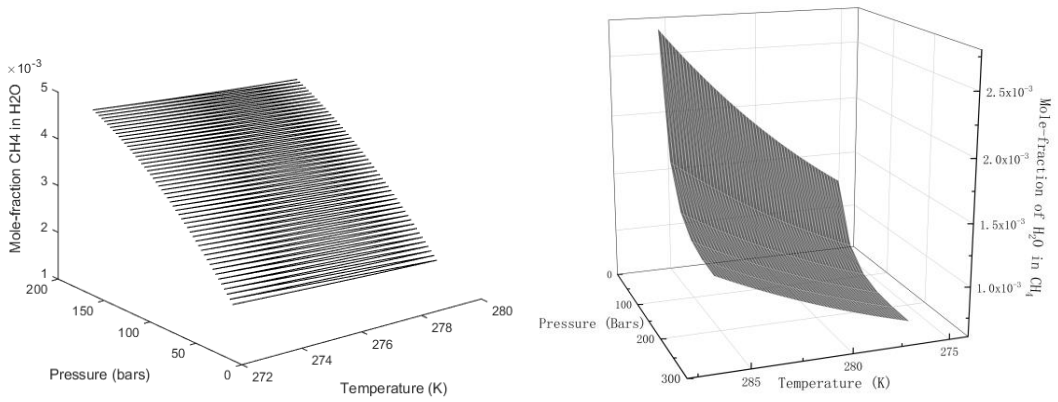

(a) (b)

Figure 3.1 a) Solubility of CH_4 in H_2O. b) Solubility of H_2O in CH_4.

If the two-component system is now transferred into hydrate forming conditions, the number of independent thermodynamic variables increases to 12. Conservation of mole-fractions in each phase is now 3 and equilibrium conditions are 8. Equilibrium cannot therefore be achieved if only 1 independent thermodynamic variable is defined. This has been well known since systematic hydrate equilibrium experiments started more than 80 years ago. Some find it surprising that only the pressure and temperature projection of the hydrate stability window is used in many

papers related to hydrate formation risk analysis, or analysis of hydrate production from offshore or permafrost hydrate deposits when in reality the phase interactions are always significant.

3.2 Heterogeneous hydrate nucleation on water/gas interface

As described in chapter 2, heterogeneous hydrate formation occurs on the interface between two phases. It can be between liquid water and a separate hydrate former phase, but it can also result from nucleation towards a solid surface containing adsorbed water and hydrate formers. Hydrate nucleation is the process of unstable agglomeration of molecules into small hydrate particles. After nucleation, these particles grow or decay depending on the competition between the free energy benefit of the phase transition and the penalty of pushing away the old phases. The latter penalty is proportional to the interface free energy times the surface area of particles. On the basis of molecular dynamics (MD) studies from various groups around the world, the thickness of the interface between hydrate and liquid water is roughly 1.2 nm. The critical size of a spherical hydrate nuclei is the radius of the particle at which the sum of free energy for the transition and the penalty work reaches a maximum turning point so that the free energy starts to dominate the phase transition. After that point, the hydrate will grow without decay. The exception is the situation of limited new mass available for growing the hydrate. In this mass-limited case more stable particles will consume less stable hydrate particles in the vicinity. Kinetically the growth is normally limited by mass transport across the thin liquid/hydrate interface because of the very slow diffusion of guest molecules through structured hydrogen-bonded water. Heat transport is rarely a limitation since it is 2 to 3 orders of magnitudes faster than mass transport through the water phase or interface. This context, which is generally provided in [60-64], is used to describe the overall phenomenon rather than the mathematical and parameter details of the current work.

Figure 3.2 comes from calculating hydrate nucleation based on temperature and pressure [50]. The critical nucleus radius for the three temperatures as a function of pressure for CH_4 hydrate is plotted in Figure 3.2 a) along with corresponding nucleation times in Figure 3.2 b).

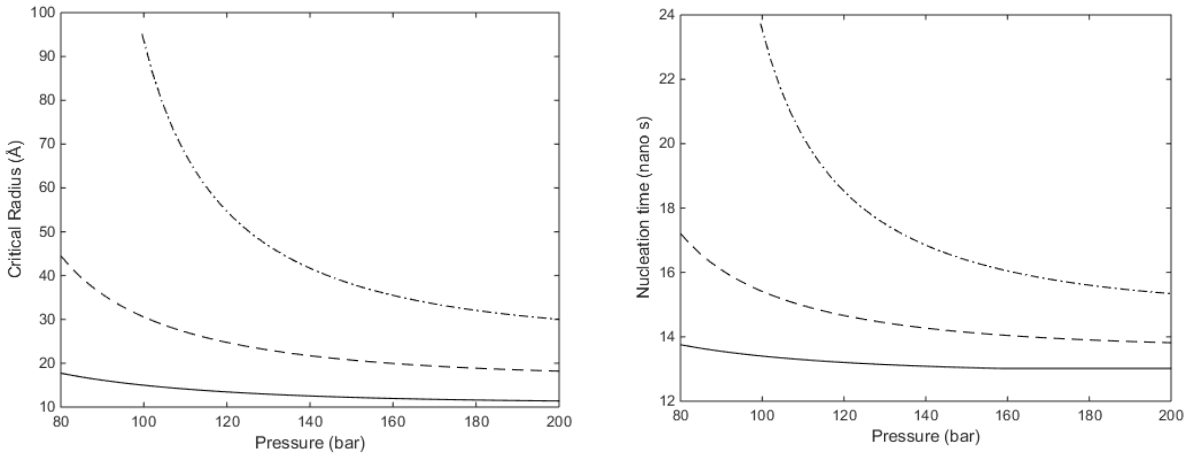

(a) (b)

Figure 3.2 a) Calculated critical radius as function of pressure for a temperature of 274 K (solid), 280 K (dashed), 284 K (dash-dot). Equilibrium pressures for the three temperatures are 24.5 bar for 274 K, 48.5 bar for 280 K and 76.9 bar for 284 K. b) Nucleation times for three temperatures as function of pressure. The solid is at 274 K, dashed is 280 K and dash-dot is 284 K.

The key finding demonstrated by Figure 3.2 is that nucleation, even with relatively modest hydrate formation driving force (modest pressure and warm temperature), is extremely rapid (on the order of tens of nanoseconds). Hence, it is not nucleation delay that is responsible for slow hydrate formation. Figure 3.3 illustrates nucleation time as function of pressure with different diffusion coefficients of mass transport through the hydrate film [50]. The Figure shows that the nucleation time is highly dependent on the rate of mass diffusion.

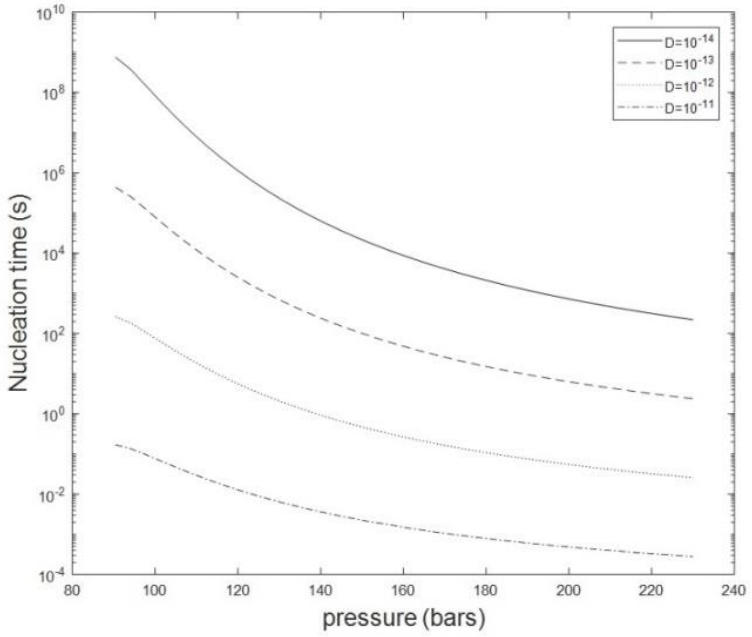

Figure 3.3 Natural logarithm of nucleation time as a function of various pressures with different diffusion coefficients at 274 K.

3.3 Homogeneous hydrate nucleation from dissolved hydrate formers in water

When the hydrate forms under specific temperature and pressure conditions, it also implies that the hydrate is a more stable phase and preferred format than a liquid phase combination of water molecules and gas molecules as dissolved solute. Hydrate can therefore form from dissolved guest molecules in water. This is possible when the solution concentration to form and maintain stable hydrate is in a window between the liquid water solubility and the lowest limit of guest molecule concentration in water. Any guest molecule concentration in surrounding water below that concentration limit leads to hydrate dissociation. That is, the chemical potential dissolves the hydrate to try and saturate the surrounding liquid. This is the reason that the CO_2 hydrates carried to the deep ocean dissolved even though the temperature and pressure conditions were in the stable hydrate zone [30]. Heat transport during hydrate nucleation from dissolved CH_4, through surrounding liquid water, is similar to the example for heterogeneous nucleation discussed in

section 3.2. Isothermal nucleation is therefore accurate also in this case. Hydrate can grow from solution between the concentration contours for CH_4 solubility in liquid water, Figure 3.1, and the necessary concentration of CH_4 in water needed to keep the hydrate stable, Figure 2.2.

An example is plotted in Figure 3.4 with the change of total free energy and critical nuclei size as a function of mole-fraction of CH_4 in water. The nucleation time is plotted in Figure 3.5 a) is at 274 K and 100 bar while b) shows the conditions of 284 K and 200 bar.

Thermodynamically it will be favorable for hydrate to grow from dissolved CH_4 towards an existing hydrate film, which may have been formed heterogeneously (see section 3.2). The mass transport through the hydrate/liquid water interface, as film, is expected to be the same in this case. The chemical potentials for CH_4 trapped in water structured by the hydrate might be slightly different than occurs in pure liquid water, but it is not expected to produce a difference particularly in the nucleation times [50], as demonstrated in Figure 3.5.

With reference to (Figure 3.4 a)) it is important to keep in mind that each point on this curve corresponds to one CH_4 chemical potential. This also implies that each point on this curve will result in a specific composition and density, which means that it is, by thermodynamic definition, a unique phase since the canonical partition function for the cavities will be different for every concentration. Practically this means that many hydrates will form, and the non-equilibrium nature of the system increases. Over time, and with limitations in access to the new mass of hydrate formers, these hydrates will reorganize into fewer particles due to the first and second laws of thermodynamics. The model demonstrates that the hydrate particles of lowest free energy survive and grow at the cost of less stable hydrate particles.

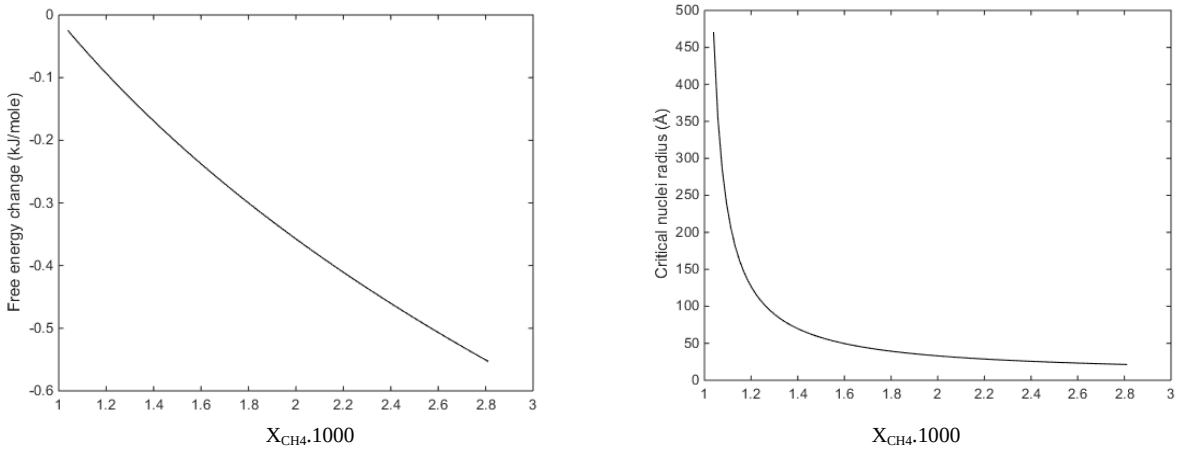

(a) (b)

Figure 3.4 Homogeneous nucleation of CH_4 hydrate from dissolved CH_4 in water at 274 K and 100 bars. Minimum mole-fraction CH_4 in water for hydrate stability at 274 K and 100 bars from Figure 2.2 a) is $9.84 \cdot 10^{-4}$. a) Free energy difference for the phase transition as function of mole-fraction CH_4 in water in between solubility, figure 3.1 and hydrate stability limit, figure 2.2. b) Critical radius as function of mole-fraction of CH_4.

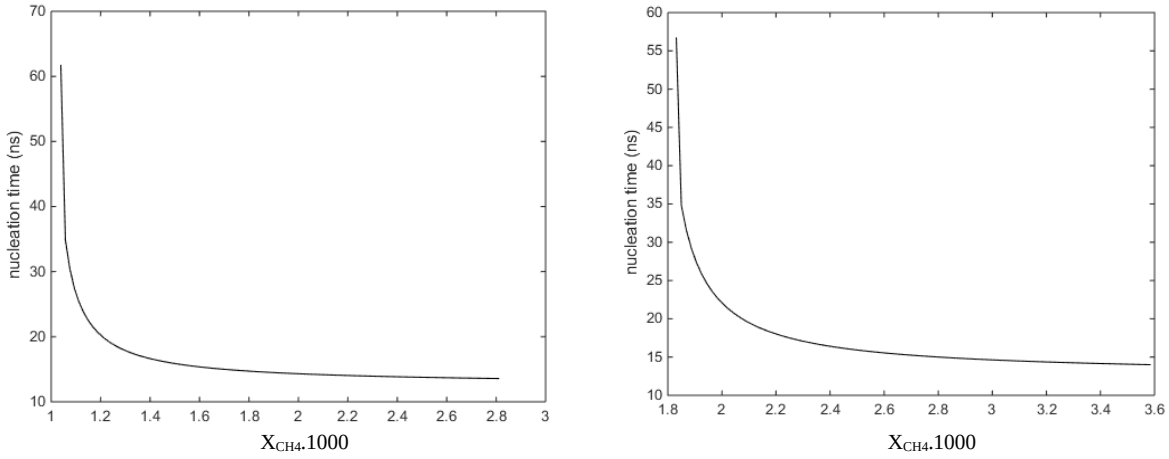

(a) (b)

Figure 3.5 a) Calculated nucleation times for 274 K and 100 bars pressure, as function of mole fraction CH_4 in water. b) Calculated nucleation times for 284 K and 200 bars pressure, as function of mole fraction CH_4 in water. Minimum mole-fraction CH_4 in water for hydrate stability is $1.74 \cdot 10^{-3}$ [50].

3.4 Enthalpy calculations

Measurements of enthalpies of hydrate dissociation are complicated for several reasons. One reason is that a level of heating above dissociation temperature is needed. How this heat is distributed in terms of the energy consumed in heating the hydrate sample and energy consumed by the dissociation process can be hard to trace experimentally and numerically. Another challenge is that the concentration ratio of liquid water to hydrate former solution is frequently missing. The conversion of measured enthalpies of hydrate dissociation to a value per mass hydrate former is therefore uncertain. Complete evaluation is challenging when lacking some critical information on hydrate number, no indication of pressure, and the degree of superheating. For these reasons there are substantial differences in values for heats of dissociation between different publications. Review by Kvamme et.al. [60,71-73], shows some experimental data regarding enthalpies of hydrate formation and explains their differences. However, thermodynamically it is very important to maintain consistency between calculated enthalpies and calculated free energies of the phase transitions because otherwise related quantities may be inconsistent. That is, if Gibbs free energy is not consistent with how enthalpy is calculated then entropy may be wrong and the phase incorrect. This is the motivation behind the approach used here and by Kvamme [74], and it is also demonstrated for hydrate formation from a liquid water solution [74]. Briefly the theory is based on the use of equation (13) with (19), from chapter 2 for water in hydrate, equation (40) for water in liquid state, and gas enthalpy from a real gas equation of state (Soave-Redlich-Kwong was used in [74]). The only missing piece is the enthalpy of the guest molecules inside the hydrate, which was calculated using model molecules which are verified to be representative for relevant properties.

Differentiation of equation (13) from chapter 2 gives the following results for the partial molar enthalpy of water in hydrate:

$$\bar{H}^{H}_{H_2O} = -RT^2 \frac{\partial\left[\frac{\mu^{0,H}_{H_2O}}{RT}\right]_{P,\vec{N}}}{\partial T} + \left[\sum_{k=1,2} v_k \frac{\sum_i h_{ki}\left[(\mu_{ki} - \Delta g_{ki}) - T(\frac{\partial \mu_{ki}}{\partial T} - \frac{\partial \Delta g_{ki}}{\partial T})\right]}{\left(1 + \sum_i h_{ki}\right)}\right] \quad (48)$$

And from equation (40):

$$\bar{H}^{water}_{H_2O} = -RT^2 \frac{\partial\left[\frac{\mu^{pure,H_2O}_{H_2O}}{RT}\right]_{P,\vec{N}}}{\partial T} - -RT^2 x^{water}_{H_2O} \left.\frac{\partial \ln \gamma^{water}_{H_2O}}{\partial T}\right|_{P,\vec{N}} \quad (49)$$

The enthalpy of hydrate formation is then:

$$\Delta\bar{H}^{(H_1),Phasetransition}_{H_2O} = x^{(H_1)}_{H_2O}\left[\bar{H}^{H_1}_{H_2O} - \bar{H}^{water}_{H_2O}\right] + \sum_{i=1}^{n} x_i^{(H_1)}\left[\bar{H}^{H_1}_{i} - \bar{H}^{gas}_{i}\right] \quad (50)$$

$\bar{H}^{H_1}_{i}$ was calculated from sampled interaction energies and active volumes for various guest molecules using a Monte Carlo approach [57,59].

Having now a consistent thermodynamic understanding of hydrate formation and dissociation, it is possible to evaluate accurately the potential for different methods of removing methane from natural gas hydrates.

3.5 Gas production from hydrate

There are several methods, that have existed for three decades, to stimulate dissociation of natural gas hydrate.

3.5.1 Pressure reduction

Pressure reduction is one method for encouraging gas release from hydrate. Figure 3.6 shows the free energy change for methane hydrate when reducing pressure 40, 30, 20, and 10 bars below the stability limit curve. These results are verified by pressure and temperature hydrate stability limits [75]. The chemical potential of methane and liquid water are used in the calculation as the basis of free energies along the equilibrium curve. This figure is sufficient illustration of the magnitude of free energy changes related to pressure reduction for gas production.

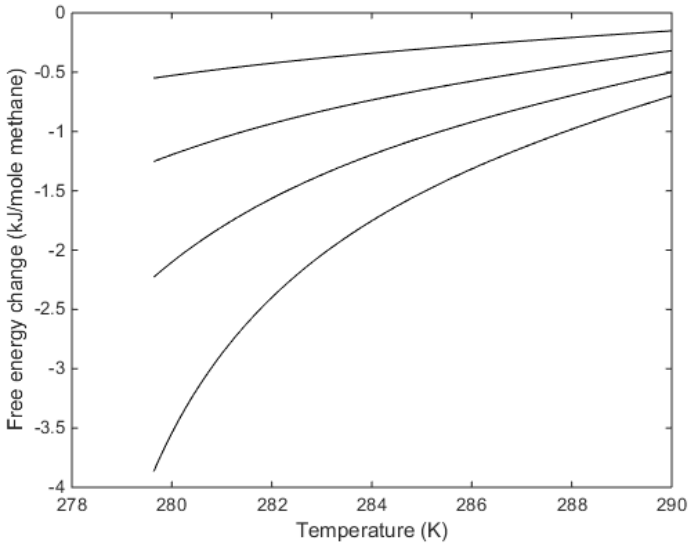

Figure 3.6 Isothermal free energy changes for dissociation pressure reduction from equilibrium pressures [75]. The lowest curve is for 40 bars reduction from the equilibrium pressures, 30 bars reduction, 20 bars reduction and upper curve for 10 bars reduction from equilibrium pressures [76].

The major question is whether the temperature change related to the pressure reduction is able to set up a sufficient temperature gradient towards the surrounding formation to drive

sufficient thermal transport for dissociation. That is, since the pressure reduction forces the system to dissociate, the dissolution enthalpy must be provided. This means that some mechanism must be provided to support that heat requirement if commercial hydrate gas production is to be feasible. In addition, pressure reduction will cool the released gas, so more heat may be needed but this is very individual for every case of hydrate saturation and other factors such as sand production during real processes. For an example, sand production results in the reduction of hydrocarbon production rates and sand production can cause erosion and wear components which can be time consuming for repairs and replacement of well and production facilities [77]. The combination of the unfavourable demand for heat and the potential challenge of sand production if a loose sediment result makes the pressure reduction method not ideal. Figure 3.7 illustrates the enthalpy change in hydrate formation at the stability limits.

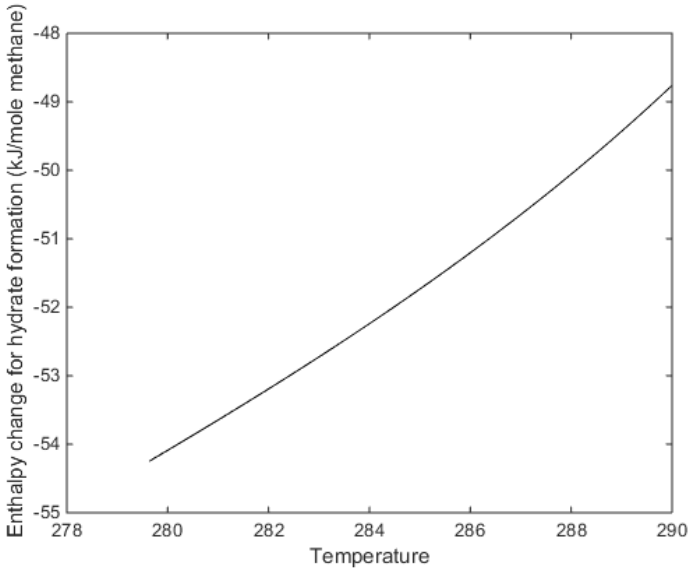

Figure 3.7 Enthalpy change in hydrate formation for the same range of the temperature and pressure stability limits as in figure 3.6 [76].

In addition, the mechanism of hydrate formation and dissociation are different because the hydrate growth is limited by the transport barrier created as the hydrate film forms rapidly at the

interface between liquid water and the hydrate former. Dissociation, however, requires that the hydrogen bonds in the interface be broken thermally, so pure pressure reduction is not feasible unless there is a large heat supply from the surroundings, which is rare.

3.5.2 Thermal stimulation

Thermal stimulation is an extremely rapid process for gas release from hydrate, but thermal stimulation alone is likely not economical feasible because it has large energy costs. This method will not be discussed in detail here, but some challenges include identifying critical regions for possibility re-freezing and limited local thermal stimulation methods [78,79]. Thermal stimulation in the form of steam or hot water can be technically accomplished although heat is lost to mineral and sections of the reservoir for production. Even heat sources of 50°C in temperature difference may have little effect on the water hydrogen bonding structure in the hydrate and on the interface between hydrate and surrounding water [80]. It is still a challenge to add heat efficiently at the right location. Furthermore, thermal stimulation and pressure reduction will result in the dissociation of hydrates and the production of a large amount of water which can increase overburden stress, as well as affect the geomechanically stability of hydrate-bearing sands, potentially creating landslides in the hydrate dissociated region [81].

3.5.3 Injection of CO_2

The core subject of the current research is to examine if the injection of CO_2 into the methane hydrate filled sediments is a preferable approach for methane release from hydrates, and if it will result in a win-win situation, in which CO_2 replaces methane in hydrate. There are two primary mechanisms that make this exchange possible. As addressed in section 1.3.2b, the solid-state mechanism has been proven for the water ice range [45], but this is an extremely slow process, and it may not even be practically achievable in a lifetime. However, any new CO_2 hydrate created

from injected CO_2 and free water in sediment pores [38,41,47,60,72] releases heat during hydrate formation of about 10 kJ/mole higher than that needed to dissociate CH_4 hydrate [47,60]. Hence, it is at least energetically feasible to use the excess heat as part of an in-situ methane hydrate dissociation and gas release.

In addition, and as mentioned in the literature [38,41,47], the impact of the first law and the second law of thermodynamics, as well as different gas components dissolved in liquid water, can have the result of enhanced CO_2 hydrate formation when a small amount of nitrogen is included in the guest gas mixture. More nitrogen gas increases permeability of CO_2/N_2 into the methane hydrate, but we need to pay attention to the situation with limited amounts of nitrogen [41,76]. Figure 3.8 a) demonstrates the enthalpy of CO_2 hydrate formation with a mixture of N_2 and CH_4 with respect to the temperature-pressure, and 3.8 b) shows the hydrate stability limits of different hydrate formations. These plots are also generated by the "Khuram code" already referenced.

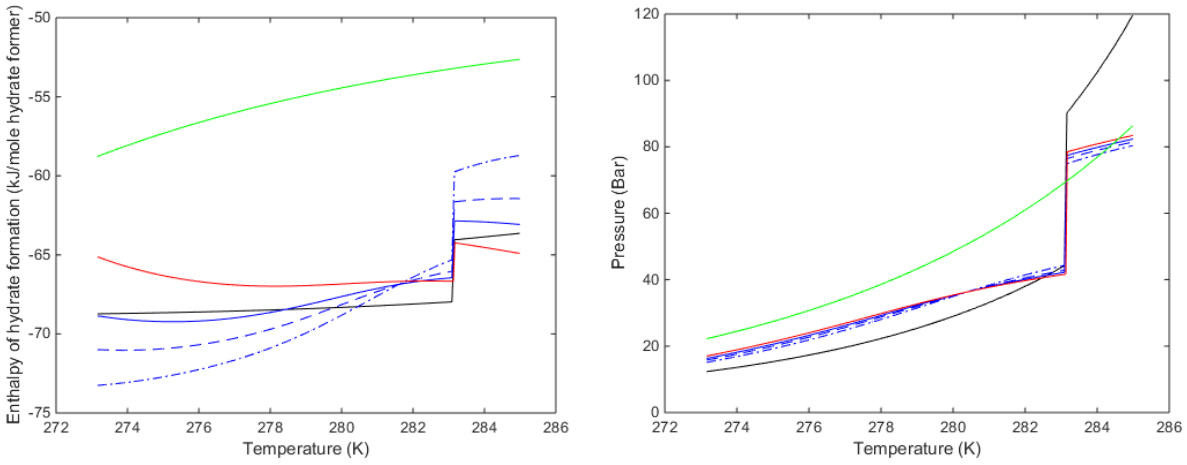

(a) (b)

Figure 3.8 a) Enthalpy of hydrate formation mixtures. Black curve is pure CO_2 hydrate, and red curve is 30 moles% CO_2 and 70 moles% N_2. Solid blue is 5 moles% CH_4 with 27.5 moles% N_2 and 67.5 moles% CO_2. Dashed blue is 10 moles% CH_4 with 25 moles% N_2 and 65 moles% CO_2. Dashed-dot blue is 20

moles% CH_4 with 20 moles% N_2 and 60 moles% CO_2. Solid green curve is pure methane hydrate, b) Equilibrium curves for all mixtures [60].

Figure 3.8 shows that the modelling of enthalpy using the combination of methods described give reasonable indications of the thermodynamic state of hydrates. It is important to note that these calculations are more complete than is typical in standard equilibrium models of hydrate formation (e.g., software from CSM, etc. [13]). While the differences can be small and relatively unimportant when determining gross outcomes like the conditions of hydrate formation in pipelines, they are significant when considering hydrate-based technologies where control of formation and growth rates determines the ultimate value and performance of the technology. In particular, and specifically relevant to the current research, the calculations show that even for 30 moles% CO_2 and 70 moles% N_2 mixture, there is sufficient excess enthalpy, relative to the need for dissociation of in situ CH_4 hydrate if the hydrate is formed in the pores from CO_2/N_2 gas and free pore water. If some methane mixes with the injection gas instead of escaping towards a production well of slightly lower pressure, then this can increase the available hydrate formation enthalpy further. The free energy for the CO_2 hydrate is roughly 2 kJ/mole lower than the free energy for CH_4 hydrate over the entire range of conditions [38,74].

To summarize the main findings of the physical process evaluation and the thermodynamic computations presented in this chapter, the energetics and transport associated with realistic multiphase hydrates show that:

- Nucleation of hydrate is very rapid, and the time required is insignificant relative to the growth time of hydrates which is dominated by transport rates.

- Without care, the rapidly forming hydrate film, which results just after nucleation, can slow down further hydrate formation dramatically by creating a diffusion barrier to further guest molecule penetration.
- The chemical potential driving force is a critical element that must be included in all estimates of hydrate stability limits.
- With proper attention to multi-species effects in hydrates, a mixture of carbon dioxide and nitrogen may provide the ideal combination for occupying a previous methane hydrate with maximum occupancy.
- There is sufficient free energy difference between CO_2 hydrate and CH_4 hydrate to provide the needed thermal energy for hydrate dissociation and methane gas release. The rate of the process depends, however, on transport times.

The points above are identified from theory and calculation. The current research, as described in the next chapter, is to also verify these findings and predictions experimentally.

CHAPTER 4: EXPERIMENT METHODS OF DISSOCIATION AND GROWTH OF GAS HYDRATES

This chapter describes the experimental setup and procedure for CO_2 sequestration from methane hydrate within porous media. The experiment is conducted in a high-pressure chamber, where the methane hydrate is created from liquid water saturated in porous media, and then introducing CO_2 initiates the exchange process. Figure 4.1 illustrates the full experimental setup with various sub-systems for H_2O injection, methane injection, carbon dioxide with/without surfactant injection, and N_2 injection, data acquisition, and gas sample collection. These sub-systems are particularly constructed with a detailed mechanical engineering design and redesign process based on the physical conditions required, particularly temperature, pressure, and fluid mechanics. The details of how each component functions, what it is composed of, and the purpose will be elucidated in this chapter.

4.1 Experimental apparatus

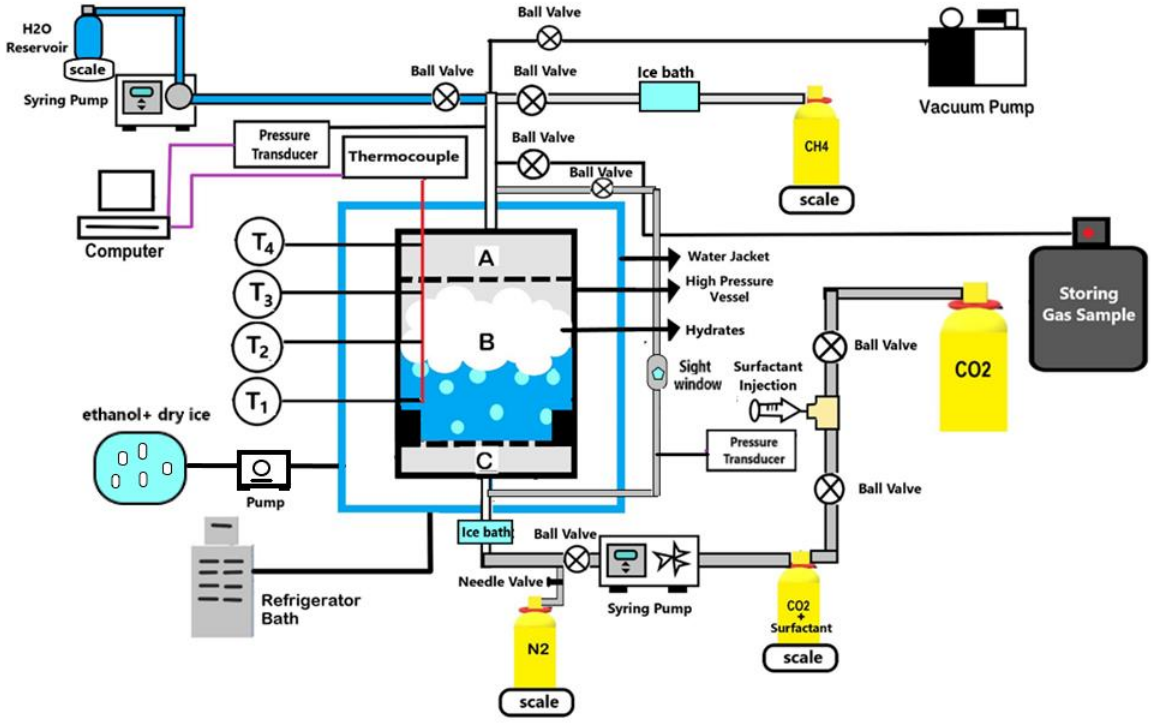

Figure 4.1 Schematic diagram of experiment of CH_4 production by CO_2 substitution.

4.1.1 High-pressure vessel

The high-pressure vessel is built with 316 stainless steel and has 4" inner diameter, and 5.4" internal depth. The vessel is designed to withstand pressure up to 1900 psi and a maximum temperature of 350◦C. There are several ports designed to connect input and output flows or for monitoring purposes, such as for gas and water supply, vacuum pump, H_2O/CO_2 high pressure pumps, data-acquisition probes, and the cooling bath. The details of how these ports are designed for experimental purpose will be explained later. A back-pressure regulator, functioning as a safety valve, is attached to the high-pressure vessel, so that when the pressure reaches over 1900 psi, it will open and release gases from the vessel. The temperature of the vessel is controlled by coolant circulating in a jacketed pipe surrounding the wall of the vessel. The coolant is a 50/50 mixture of distilled water and ethylene glycol. Pressure and temperature are monitored separately by a

pressure transducer and J type thermocouples which are inserted into the vessel at different depths. The gases used for the experiment are analytical-grade methane 99.99% purity, carbon dioxide at 99.99%, and nitrogen gas at 99.99% (Airgas). This high-pressure vessel (Parr-Instrument series 4600, non-stirred pressure vessel) has an internal empty volume of 1000 ml. The removable head assembly, which consists of a top lid with a screw-clamping mechanism (Figure 4.2a), has three pass-through threaded ports for the purpose of (1) an over-pressure 1900 psi burst disk with a back pressure regulator, (2) a thermocouple probe insertion, and (3) a 1/4" diameter stainless steel gas in-out tubing circuit with 1/8” internal H_2O tubing, tube within a tube, that supplies H_2O to the internal vessel for the halo water-drip assembly (as part of the methane hydrate formation mechanism described later, see Figure 4.2b). The lower vessel assembly has a surrounding cooling jacket integrated into the side walls (shown as rectangular blue in Figure 4.1), and the vessel bottom panel has one central threaded through port from which the liquid CO_2 charge is pumped into the hydrate from below around section C. The lower port also has a tube within a tube, with an 1/8” stainless steel tubing stand-pipe that provides a media bed (basket) by-pass circuit. Similarly, this tube within a tube assembly also flows gas in the larger pipe and liquid in the smaller pipe. The gas pipe is for the vacuum procedure which can be pulled from both sides of the vessel, above and below simultaneously, thus minimizing media material (glass beads) disturbance throughout the evacuating process, and another occasion it is to be used for the redundant methane gas that occupies the volume under the hydrate (section C), allowing it to be routed to the upper vessel chamber without being forced into and through the hydrate as liquid CO_2 fills the lower vessel during that stage of the experimental process. The liquid pipe within this by-pass circuit consists of one 1/4" ball-valve, a sight gauge that allows visual verification that the liquid CO_2 has reached the desired level, and pressure transducer (Omega, PX119-1.5KAI) that provides lower

chamber pressure readings. The overall valves designed and installed on the pressure vessel, and their adjustment for control include: (1) 1/4" 3-way ball valve for controlling gas in-out of the upper vessel; (2) 1/8” 3-way valve for CO_2 purging of the CO_2 supply circuit and then controlling the liquid CO_2 flow into the vessel; (3) 1/4” by-pass upper-lower off-on ball valve; and (4) 1/4" vacuum pump off-on ball valve. Pressure readings are supplied by two pressure transducers (one upper chamber and one lower chamber, Omega - PX119-1.5KAI) that report to the data acquisition system board (Omega, OM-CP-OCTPRO), and a digital push-to-read pressure gauge calibrated in bar pressure units that reads the upper chamber pressure. The thermocouple probe is 1/8” in diameter and incorporates 4 “J” type thermocouples along its inserted length. These report temperatures at various locations: T1 deep media bed (basket), T2 upper media bed (basket), T3 just above the media bed (basket) and T4 just below the vessel head. The locations are demonstrated in Figure 4.1.

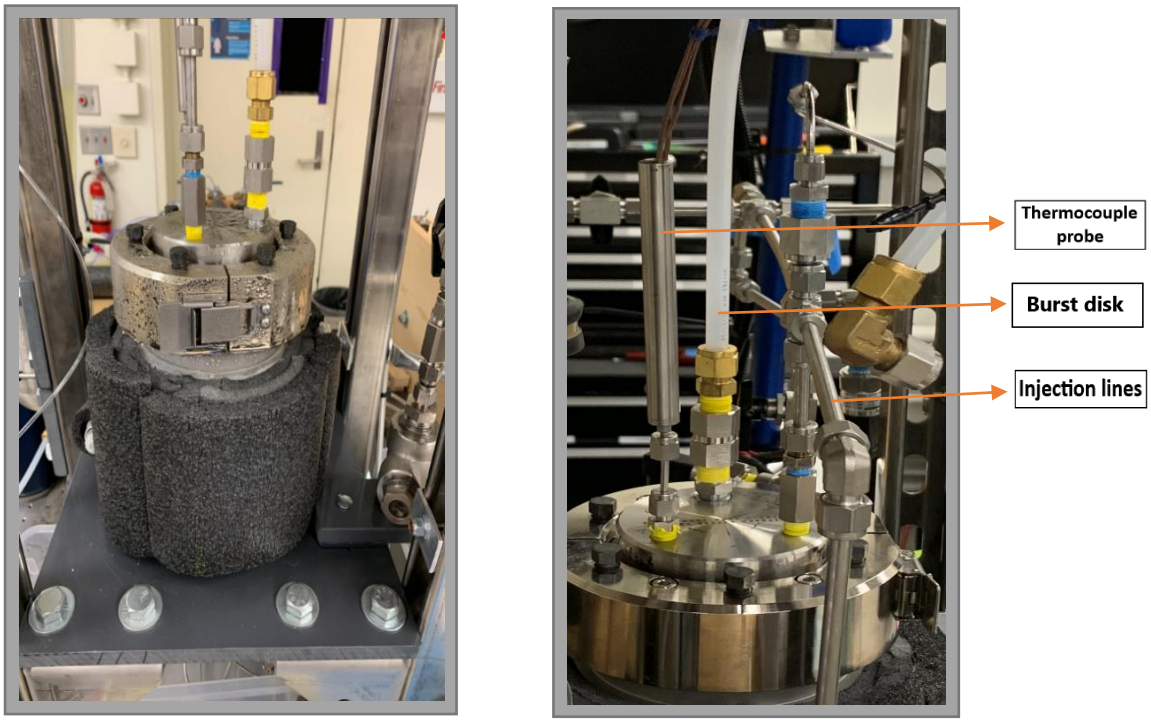

(a) (b)

Figure 4.2 a) High-pressure vessel fully assembled, b) shown all injection lines, burst disk, and thermocouples probe at the top of the vessel.

4.1.2 Test section

The full test section is the total internal volume of the high-pressure vessel, and the hydrate is formed in the middle region of the vessel from a basket holding the hydrate, as shown in section B in Figure 4.1. The basket is the main component which has a 4" OD x 2.5" ID x .75" thick stainless-steel ring that forms the base. The ring is supported off the vessel floor by 6 each .5" OD x .25" ID x .375" long polypropylene unthreaded spacers, as shown in Figure 4.3a). The ring is grooved on its outside face for a 2-342 silicon low temperature O-ring which seals the outside of the ring to the inner wall of the vessel. A pocket is machined into the bottom surface of the ring assembly and tapped for 6 #4-40 button head stainless screws with the screws 60 degrees apart. The screws are used to attached two wire cloth screens from the underside of the ring. A fine 400

x 400 stainless screen disk and a coarse 20 x 20 screen provides support to a fine screen disk across the open center span of the steel ring. In addition, three of the polypropylene spacers are located within the center span area to add screen support while they also serve to locate and hold the stand-pipe director baffle in position.

The upper surface of the basket ring is drilled and tapped for 4 each 1/4"x 20 threaded studs 90 degrees apart. Their purpose is to support the upper basket hardware, to provide convenient lifting points for removing the basket ring for cleaning and reloading of the media material (glass beads, see Figure 4.3b), and to prevent the basket and media material (glass beads) from being lifted by the liquid CO_2 being pumped into the vessel from below. The studs extend to within 1/8" of the vessel head's lower surface. The studs are locked into position by 4 each stainless-steel plain type jam nuts, and 8 each additional nuts are used to locate and hold a single perforated stainless-steel plate mounted 1/4" above the media bed (basket). The perforated plate serves to (1) contain hydrate ice expansion and (2) provide a secure stable mounting point for the halo water drip procedure/assembly. The halo water drip assembly consists of a length of 1/8" Teflon tubing heat formed into a semi-circle and drilled with progressively larger holes toward the end of the tubing that equalizes drip-flow into the media bed (basket), as shown in Figure 4.3d). The semi-circle drilled section is attached firmly to the underside of the perforated plate, while the free end on top of the perforated plate is left with enough length and freedom of motion to allow easy attachment of the Teflon tubing to the H_2O supply line 1/8" steel tubing that extends 3/4" below the lower surface of the head assembly. The media bed material consists of 550 grams of dry 75-microns glass beads average size with distribution of (170-325 mesh size) in Figure 4.3c) into which 132 ml of distilled water is slowly and evenly dripped through an 83 bars methane atmosphere over 20 minutes.

The amount of H_2O introduced is important to monitor as the glass beads in the media bed are super-saturated above 134 ml with H_2O, and the water will then leak from the bed through the screens into the lower open volume under the basket. Undesired hydrate will then form in the lower section and could severely interfere with the passage of fluids later in the process. The fine 400 x 400 wire cloth in the base of the basket ring has .0015" (37.5 micron) openings and it easily contains the glass beads while allowing methane and later liquid CO_2 access into the media bed from below. However, it does not provide a barrier to liquid water. The liquid water is held in the bed by pore surface tension only.

(a) (b) (c) (d)

Figure 4.3 a) Bottom view of basket with 6 spacers, b) basket's structure (fully stands). c) Basket filled with glass beads without lid and water injection, and d) basket with lid and halo water drip line.

4.1.3 Main chilling system

The major chilling system is for maintaining the high-pressure vessel at a constant temperature during methane hydrate formation and during the CO_2 exchange process. The commercial recirculatory (Cole-Parmer Polystat, SKY 1304217), with 17 L/min flow rate, and 500 W cooling capacity is selected. With the capability for cooling ranges from -10°C to +80°C, it

circulates coolant around the experiment pressure vessel and maintains the temperature at 1˚C for 72 hours to allow the methane hydrate and carbon dioxide hydrate formation. All of the chilling pipes carrying fluids flowing in and out of the chiller are well insulated with foam to prevent heat transfer and to ensure an effective process. Figure 4.4a) illustrates the main cooling system, and Figure 4.4b) shows all lines from the main chiller.

(a) (b)

Figure 4.4 a) Main cooling system, b) Inlet and outlet lines from chiller.

4.1.4 Auxiliary chilling system

The secondary cooling system is a liquid-to-liquid open reservoir system. It is designed to have the refrigeration capacity to reduce the temperatures of the pressure vessel and the internal media bed (basket) from the long-term temperatures of 1˚C down to -25 ˚C in 20 minutes or less, and then to hold it at -25 ˚C for up to an hour. The purpose of the auxiliary cooling system is for stabilizing the hydrate once formed so that the excess gases can be released without dissociating the solid phase hydrate. The system consists of a 20-quart insulated polyethylene ice cooler which serves as the cold-bath. The heat exchanger is in-house fabricated from 1/2" copper tubing and

1/2” brass compression fittings. Five each 1/2" brass ball valves and three each 1/2" tee fittings are spliced into the main cooling system as supply and return coolant lines to the pressure vessel. The valves allow the main chilling system fluids (introduced in the previous subsection) to flow normally, and the current chiller is acting as a secondary system to be isolated in a closed-circulation loop until needed. Therefore, the main cooling system can be isolated from the pressure vessel and the secondary system flow can be brought on-line to provide the -25 ˚C cooling on demand. A hand-held 4 channel temperature display (see Figure 4.5a) with K type thermocouples provides simultaneous temperature readouts of ambient, coolant pump fluid, and heat exchanger inlet and outlet flows. Figure 4.5b) demonstrates the auxiliary chilling system with inlet and outlet coolant flows. The liquid cooling bath is a mixture of ethyl alcohol and dry ice.

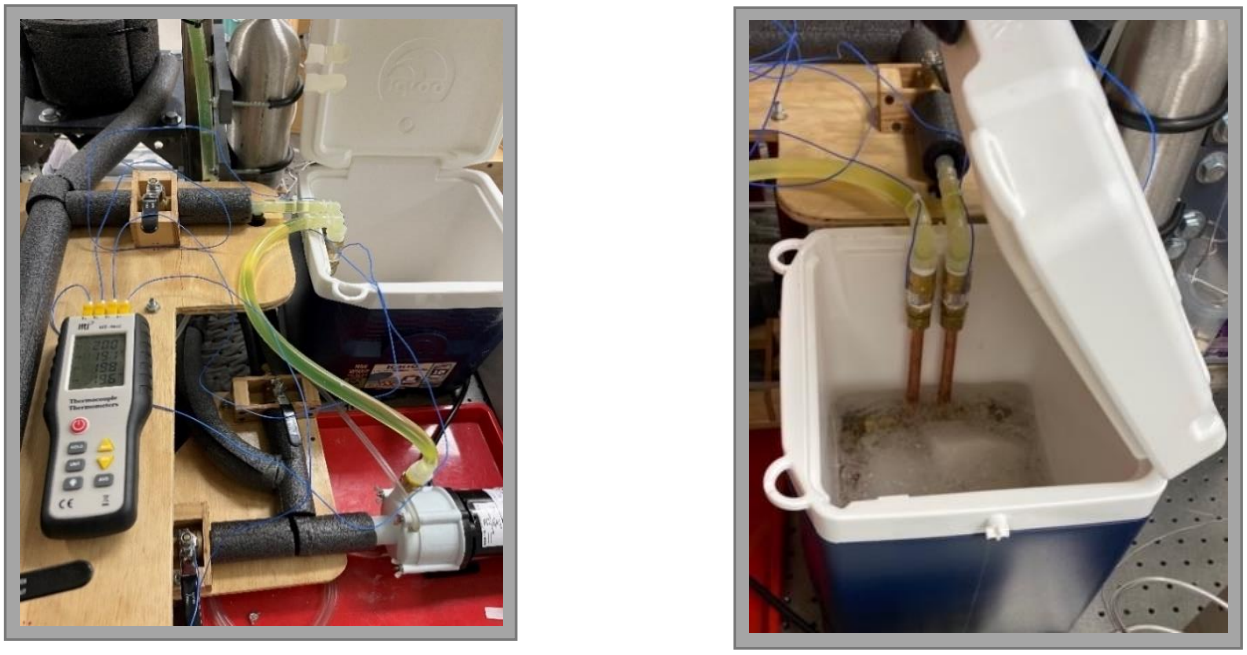

(a) (b)

Figure 4.5 a) A hand-held 4 channel temperature display with K-type thermocouples. b) Auxiliary chilling system.

A 1/3 HP magnetic drive centrifugal water pump from (McMaster-Carr, Type U21, 60 Hz 1.65 Amps with 3000 RPM, 115 V) modified with an automatic air-bleed circuit in the pump housing and a clear section of outlet hose drives the coolant. These modifications provide monitoring for the presence of air or ice in the coolant flow and the purging of trapped air which could stall the pump flow. The transfer coolant is the same 50/50 mixture of distilled water and automotive ethylene glycol used by the main cooling system (shown in Figure 4.6). The liquid cooling bath contains 3 liters of ethyl alcohol which is around 110 grams. Slices of dry ice are introduced as needed to reduce the bath to, and then to maintain, the target temperature -25 ˚C in the pressure vessel and basket. The dry-ice consumption rate is approximately 2.5 kilograms per hour during operation.

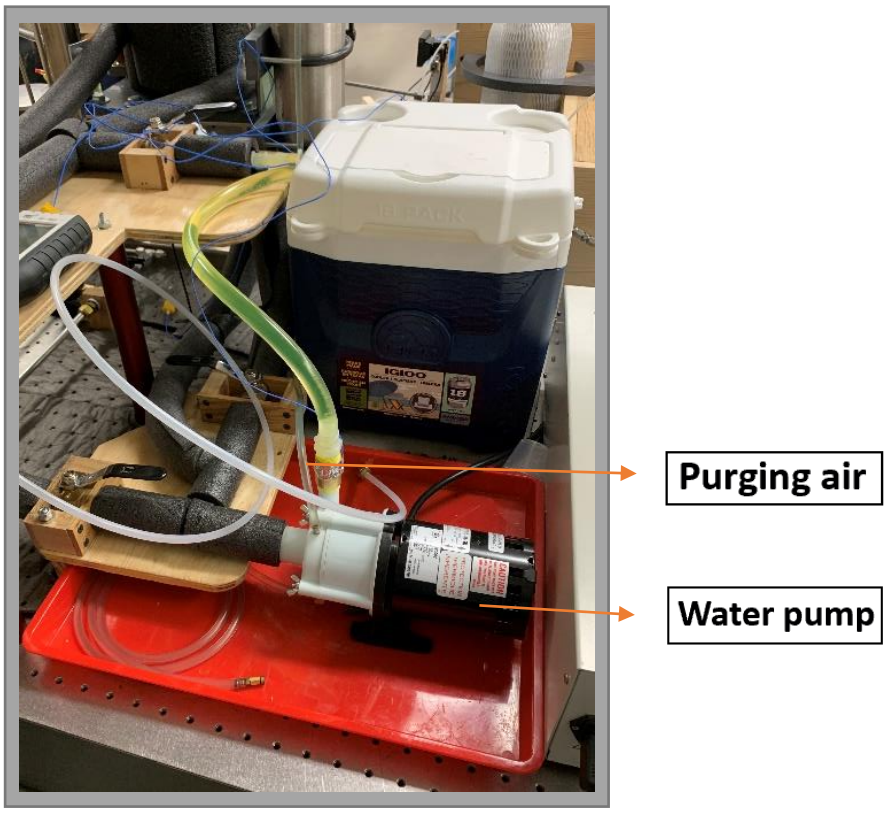

Figure 4.6 Magnetic drive centrifugal water pump and cooling bath.

4.1.5 Vacuum pump

The vacuum pump (Trivac B D4B/D8B Rotary vane, Atex categories 3 I and 3i/0 with mineral oil provided by Hanning Elektro-Werke) is used to reduce the pressure inside the vessel down to 30 inches of mercury before filling the gas and water (shown as in Figure 4.7). It also is used to evacuate all the small reservoir gas tanks (as storage) before filling with the respective gases to be used for the experiment from large gas tanks, and also for evacuating the sample storage tanks that are used to collect samples from the vessel at the end of the experiment. The lines running from the vacuum pump are 3/8” in diameter to 1/4" in diameter to provide the suction flowrate needed. The 3/8” lines are manufactured from aluminum and 1/4" lines are manufactured from 3/16 stainless steel (from McMaster-Carr and Swagelok respectively).

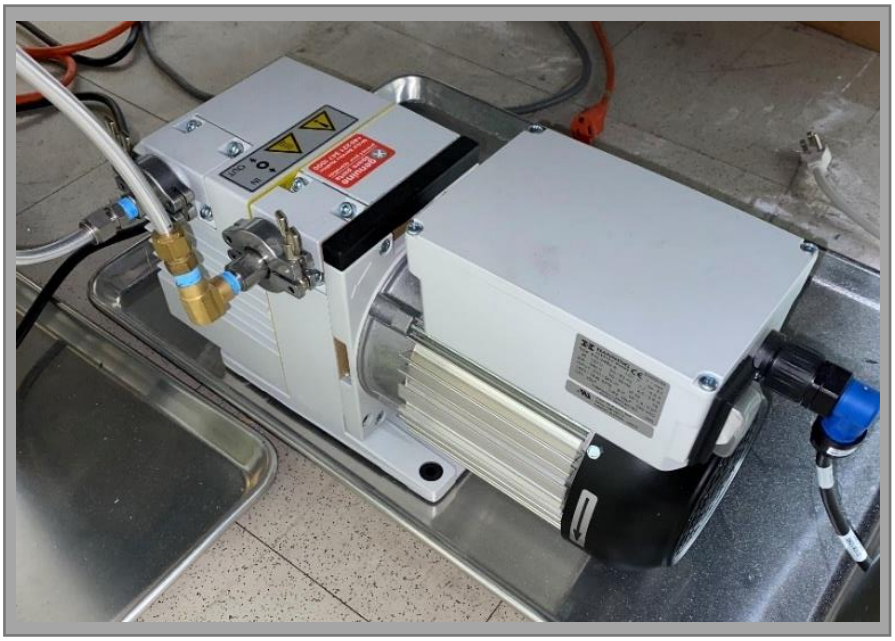

Figure 4.7 Vacuum pump.

4.1.6 Data-acquisition system

A portable data logger from (Omega, OM-CO-OCTPRO) with eight programmable channels is used to record four temperatures and two pressures throughout the course of the

experiment (Figure 4.8b). The four J type thermocouples, integrated in one probe, are inserted into the high-pressure vessel measuring the temperature at the same radial location but at different levels in depth. As described earlier, the temperature is recorded at four different heights: (1) deep media bed as (T1) shown in Figure 4.1, (2) upper media bed (T2), (3) just above the media bed (T3), and (4) just below the vessel head (T4). The detail of the media material (glass beads) within the vessel was described earlier. Two pressure transducers are separately installed at the bottom and top of the vessel to monitor the pressure change and difference within the chamber (see below the Figure 4.8a).

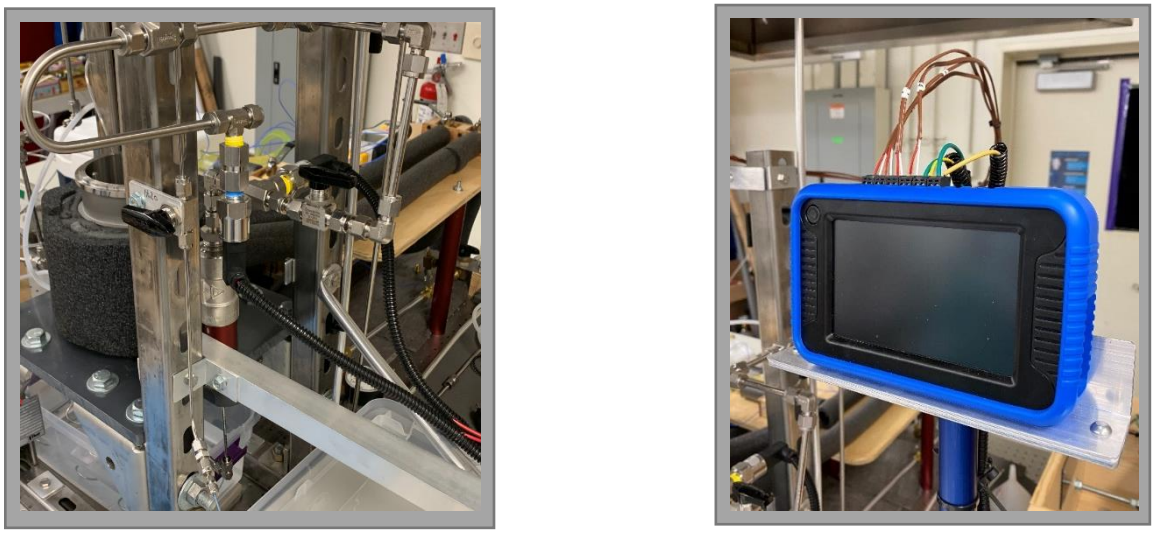

(a) (b)

Figure 4.8 a) Two pressure transducers are located on top and bottom of high-pressure vessel, b) Data acquisition module.

4.1.7 Halo H_2O injection system

A H_2O HPLC pump (SERIES I, Lab Alliance) is used to pump H_2O into the vessel to form the methane hydrate. The pump is rated from 0 - 2,500 psi and has a flow rate of 0 – 10 mL/min. During methane hydrate formation, the pump is set to a flow rate of 5mL/min and it supplies the vessel with about 132 grams of water. The lines running from the HPLC pump are 1/16” in

diameter to 1/8”, and then expanding to 1/4”. The 1/8” and 1/4” lines are manufactured from 316 stainless steel and the 1/16” line is manufactured from high pressure nylon. The 1/8” pump inlet line is made of teflon. This specific pump is used because it must be able to overcome the in-chamber pressures of over 80 bar to effectively pump the water into the vessel. Figure 4.9 illustrates the water injection system and halo water drip line.

(a) (b) (c)

Figure 4.9 a) H_2O HPLC pump, and water reservoir is on the scale, b) Halo water drip line, c) The head of high-pressure vessel with water line that it attached to the halo water drip.

4.1.8 CO_2 injection system

The CO_2 injection with or without surfactant system uses a CO_2 syringe pump is similarly high pressure as is the H_2O pump, shown as in Figure 4.10a). The pump used (Lab Alliance, S10SNX01-SUPERCRITICAL 24,CNST FLOW) is rated from 0 – 10,000 psi along with a flow rate of 0 – 24 mL/min. During the CO_2 hydrate exchange process, the flow rate of the pump is set to 14 mL/min and it pumps around 200 grams of CO_2 into the vessel to substitute for the methane

from the hydrate and create the CO_2 hydrate. The lines running from the syringe pump are 1/8” to the heat exchanger (ice bath) in order to further chill the CO_2 and ensure it remains as condensed liquid and to reduce the heat loss from thermal compression inside the vessel (Figure 4.10b). This line is made from 316 stainless steel. There is one aluminum storage tank in total for the CO_2 injection/exchange process, and that tank hold up to 1.1 kilograms of liquid CO_2.

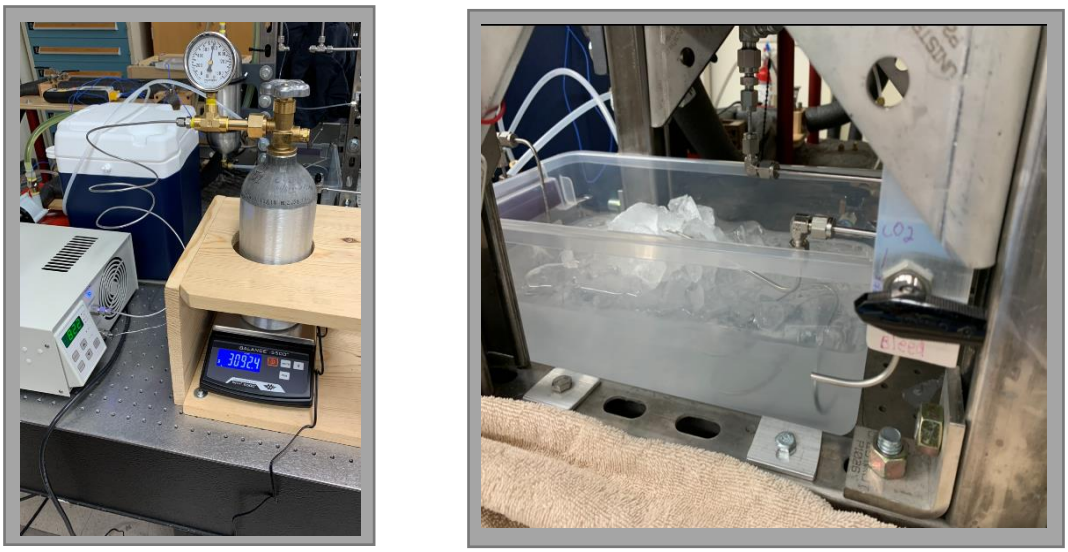

(a) (b)

Figure 4.10 a) CO_2 aluminum storage tank is on the scale and attached to the syringe pump. b) Heat exchanger (ice bath) for CO_2.

4.1.9 CH_4 injection system

The CH_4 injection system consists of a 2.3 kilograms aluminum tank (Figure 4.11a and b). A 1/4" stainless steel line then a 1/8” stainless steel line runs to and then through a heat exchanger (ice bath), and then goes into the pressure vessel (see Figure 4.11c and a). A pump is not necessary to deliver the methane gas for methane hydrate formation because the pressure vessel is always at a lower pressure (83 bar maximum) than the methane supply tank (100 bar minimum) allowing the methane to flow into the vessel while being controlled by the vessel’s inlet ball-valve. From

the methane reservoir tank, CH_4 flows into the 1/8” 316 stainless steel line of the heat exchanger (ice bath) where it is chilled 10 to 15 degrees C below the ambient temperature to reduce the effects of temperature rise due to compression in the test section. When the methane is released into the pressure vessel, it is flowing until the interior reaches a maximum of 83 bar in total.

(a) (b) (c)

Figure 4.11 a) CH_4 injection system, b) CH_4 aluminum storage tank. C) Heat exchanger (ice bath) for CH_4.

4.1.10 N_2 injection system

The nitrogen is held in a 2.3 kilograms aluminum tank (same as the methane tank). The 1/4" 316 stainless steel lines running from the tank go to the digital mass flow meter (Bronkhorst, FG-111B-AAD-22-V). The flow is metered up to 10 ml/min that is injected into the vessel. From this system (Figure 4.12a), the nitrogen is pushed through 1/8” 316 stainless steel line to the vessel. Mixing of N_2 and CO_2 takes place as the CO_2 liquid flows into one leg of a Tee fitting while N_2 gas simultaneously flows into the opposing fitting leg. And then, both fluids merge and turn 90

degrees and exit the central leg of the fitting. While exiting, both fluids are forced through a 0.5 micron stainless steel sintered filter cylinder (Swagelok, SS-4F-K4-05), which breaks up any large N_2 gas bubbles, thus increasing the N_2 surface area to liquid CO_2 interface and improving the mixing of the two fluids. One-way valves in the two fluid circuits ensure that positive flow from both fluid circuits is maintained and that one fluid circuit does not overcome and reverse the flow in the other circuit, shown as Figure 4.12b).

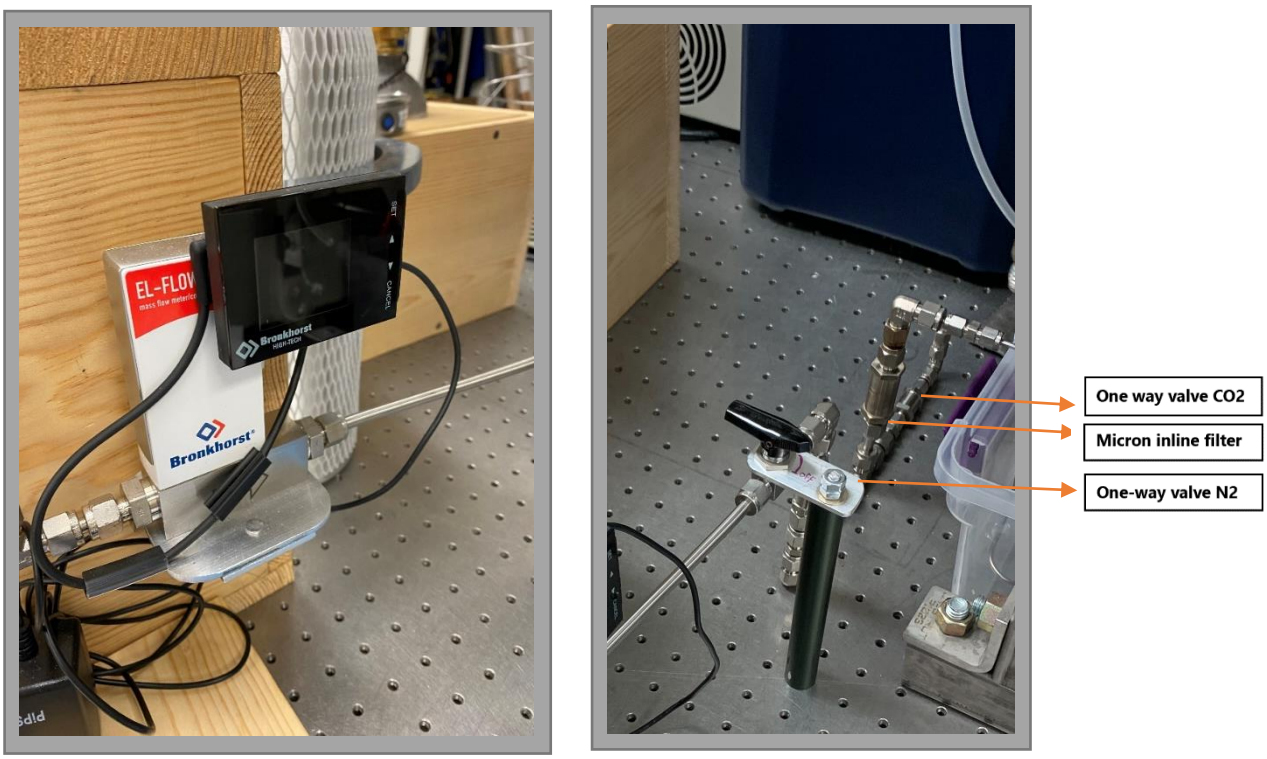

(a) (b)

Figure 4.12 a) Digital mass flow meter, b) Shown mixing nitrogen gas and CO2 at 90 degrees mixture section with include of 0.5 microns stainless steel filter.

4.1.11 Surfactant injection system

Liquid surfactant in loaded into an emptied CO_2 supply cylinder from a stainless-steel plumbing fixture scaled to hold the required amount of surfactant. Compressed CO_2 gas forces the liquid surfactant into the empty pressure cylinder and then, liquid CO_2 charges the aluminum storage tank to the desire fill level (Figure 4.13a). Figure 4.1 demonstrates the mixture tank of CO_2 and surfactant. It sits in a roller fixture (Figure 4.13b), which mixes the tank for 20-30 min in order to dissolve the surfactant into the CO_2 liquid before injection into the high-pressure vessel. During the injection, the tank sits on the magnetic stirrer to make sure that all components are mixing completely together during the process.

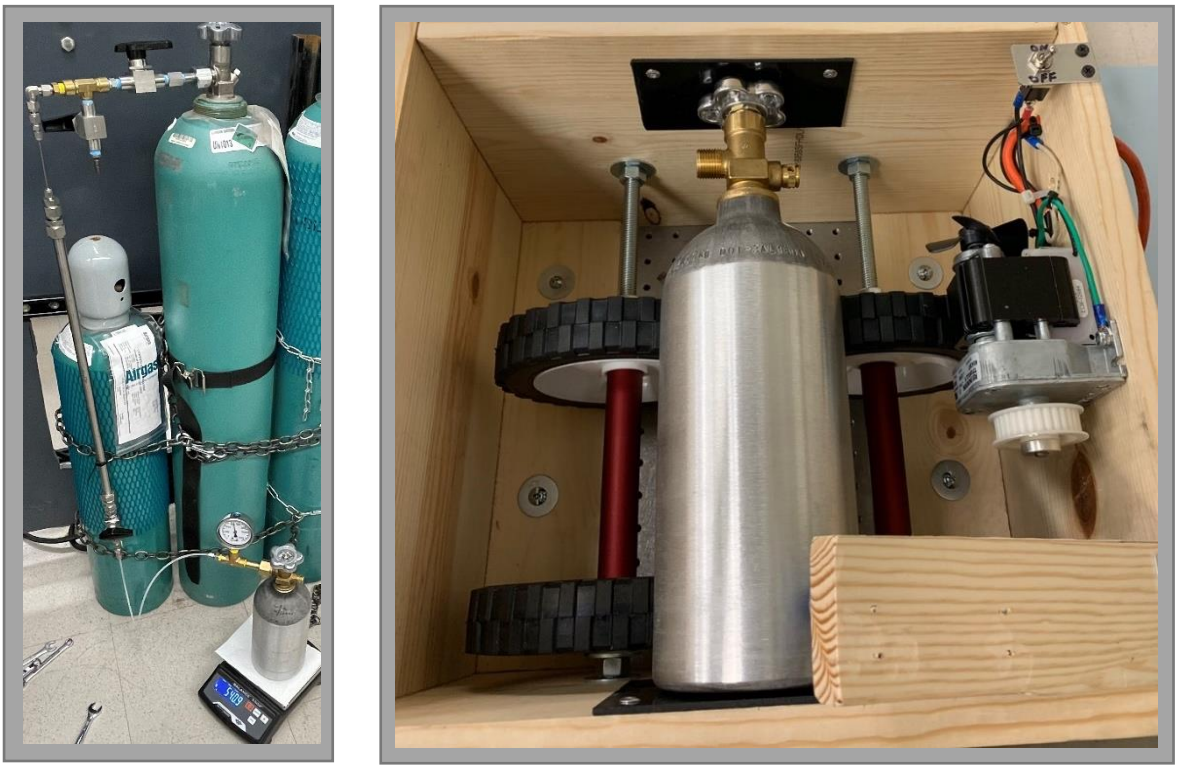

(a) (b)

Figure 4.13 a) Empty CO_2 supply aluminum tank with stainless-steel plumbing fixture scaled to hold the required amount of surfactant. b) Roller system for mixing CO_2 liquid and surfactant.

The experimental design for this research has undergone a substantial effort for following the best practices of the engineering design, including construction and modification of the facility in order to provide a reproducible environment particularly for methane hydrate to be formed in a porous medium and allowing improved control capability for introducing carbon dioxide. The center piece of the experiment design is to manage pressure and temperature of the environment for hydrate formation and substitution carefully. The screened bed design was particularly complicated and represents a novel experiment in hydrate science, where a water-saturated porous bed is used as the base for hydrate formation, followed by exposure of the hydrate to liquid CO_2. The details of the experimental procedure are described next.

4.2 Experimental principal, method and procedures

To achieve the experimental objective of the study, i.e. the influence of the kinetic rate particularly on carbon dioxide hydrate formation and methane hydrate dissociation, the current apparatus is specially designed and carefully refined for (1) the mixture of CO_2 liquid and nitrogen gas (ranges from zero to 30 moles% of N_2) and (2) the possible addition of a small amount of surfactant into the methane hydrate or CO_2 as an aid for the substitution process to enhance methane gas release from hydrate structure.

Because of the physical properties and the sudden nucleation of hydrates discussed in chapter 3, the process of injecting pure carbon dioxide into an existing methane hydrate is not straightforward. The resultant rapid nucleation will form new hydrate with free water in the form of liquid flowing in hydrate pores creating hydrate films. The nucleation process happens on the nanoscale in time and space. This will rapidly lead to blocking of the flow for the exchange process and will result in extremely slow conversion from in situ methane hydrate to CO_2 hydrate. Adding nitrogen gas into the CO_2 injection flow, with the enthalpy prediction model (in chapter3), is

expected to reduce the blocking flow from new hydrate films and increase permeability of N_2/CO_2 into the methane hydrate. Also, additional chemicals (biological or synthetic surfactants) may be needed to keep the water/CO_2 interface hydrate free and increase the kinetic rate of new CO_2 hydrate formation. This section follows the experimental sequence to create methane hydrate first from liquid water, then to conduct the CO_2 exchange process, and finally to collect the resulting gas sample for analysis.

4.2.1 CH_4 hydrate formation process

To create methane hydrates inside the high-pressure vessel, we introduced dried glass beads covering half the volume of the vessel using 170-325 mesh size and 550 grams for creating artificial sediments mimicking the natural environment. Before the experiment starts, the vessel is evacuated to near zero absolute pressure. Then, the valve is opened to flow methane gas at 1500 psi into the vessel until it reaches to 83 bar (1204 psi, which is about 52 grams methane gas). The CH_4 is pre-chilled in the ice-bath heat exchanger before injecting it into the vessel. The injection process will not start until the CH_4 gas pressure inside the vessel is stabilized (without fluctuation at least for 10 min/within ± 0.1 bar/0.12% changes of the total pressure). When the pressure inside the vessel is steady, 132 ml distilled water is injected from the halo assembly at the top of the vessel using the high-pressure syringe pump. The process drips water droplets at a rate of 5 ml/min allowing water to accumulate from the bottom of section B to the top of the same section (Figure 4.1), inside the glass beads. The total pressure inside the vessel will increase throughout the process above 83 bar. At the same time, the main chilling system (as mentioned in section 4.1) is turned on to bring the vessel temperature down from around 20˚C to setpoint 1 ˚C slowly. The procedure for the chiller to bring down the methane/water gas temperature to 1 ˚C takes around 120 min, and the full process requires keeping constant temperature for 48 hours to form the methane hydrate.

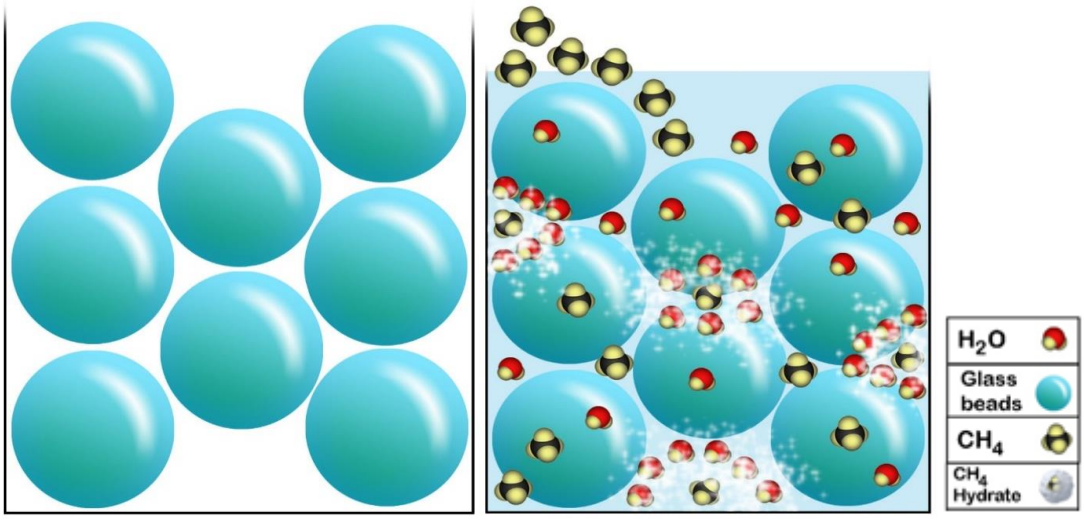

(a) (b)

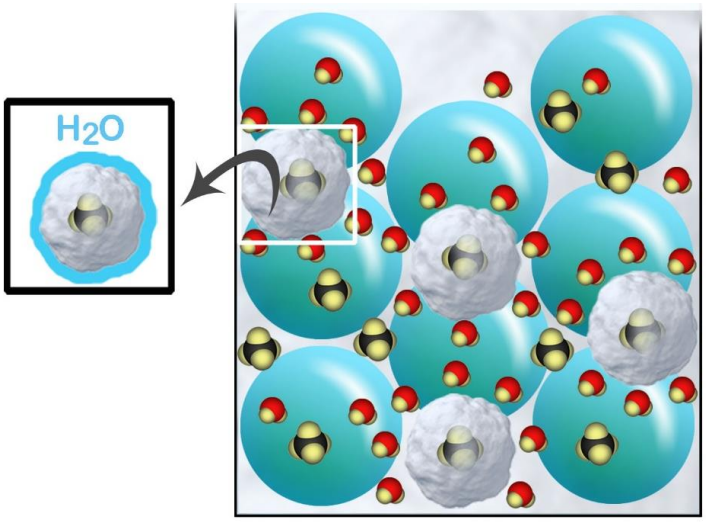

(c)

Figure 4.14 Qualitative illustration of methane hydrate formation in porous media. a) Macroscopic view of dry glass beads representing sediments, b) methane gas and liquid water were introduced inside the glass beads while the temperature is reduced for hydrate formation, c) methane hydrate formed in the porous media after 48 hours [55].

Figure 4.14 shows the schematic of methane hydrate formation in the porous media as a detailed illustration, and Figure 4.14a) shows macroscopic glass beads inside the vessel of section B. Figure

4.14b) illustrates the water and methane molecules surrounded the glass beads with partial hydrate starting to form, and Figure 4.14c) shows the methane hydrate formed in the fine glass beads representing natural sediments.

4.2.2 CO_2 and CH_4 hydrates exchange process

After 48 hours, following the methane hydrate formation around 70 bar at 1 ˚C there is excess methane gas that is not converted to hydrate within the vessel. The remaining methane gas is then released slowly, with a bleeding procedure, from the high-pressure vessel to the exhaust. This will bring the pressure from 70 bar to 48 bar, but the hydrate remains intact for the short duration of this release. CO_2 with/without surfactant, and N_2 are then measured and pre-chilled in the ice-bath heat exchanger at 2-3 ˚C before injection from the bottom of the vessel. The pressure and temperature are kept at 48 bar and 1 ˚C respectively before the injection to ensure that only CO_2 liquid with/without surfactant, and with/without N_2 arrives at the vessel. The full injection process, shown in Figure 4.15a), takes 20 min while the vessel pressure increases. After the CO_2 injection is completed, the vessel sits 24 hours to allow for a complete exchange process, and the pressure will keep increasing throughout the process. This is because methane gas from the hydrate is released during the exothermic exchange as the new CO_2 hydrate forms, see Figure 4.15b). Figure 4.15c) demonstrates that CO_2 hydrate is formed with free liquid water in the porous media and the heat released will cause in situ neighboring CH_4 hydrate to dissociate. The N_2 participation is implied in this figure because it is complicated to show N_2 molecules inside the small cavities of the hydrate structure in this cartoon.

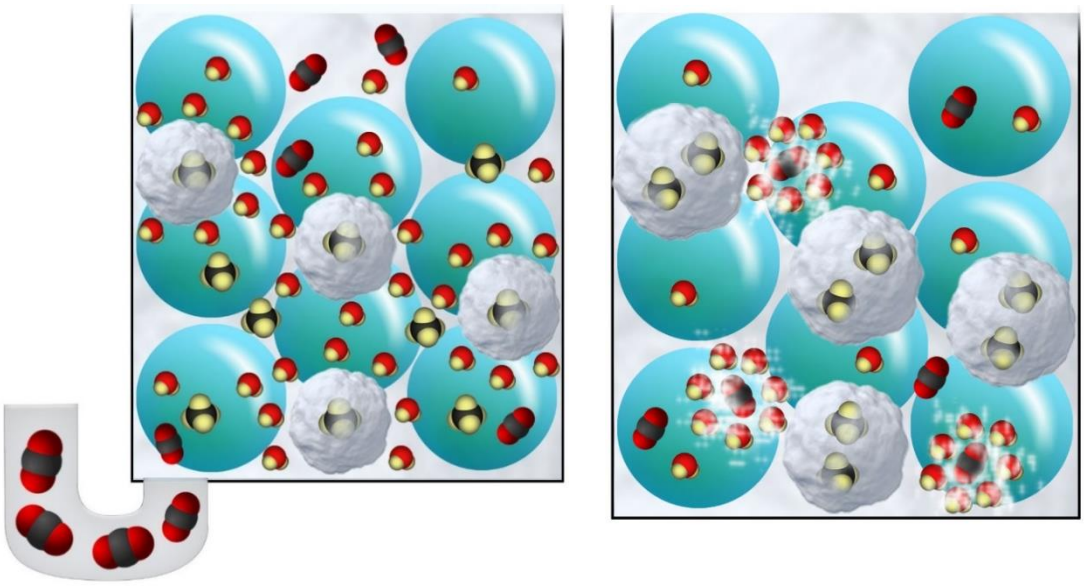

(a) (b)

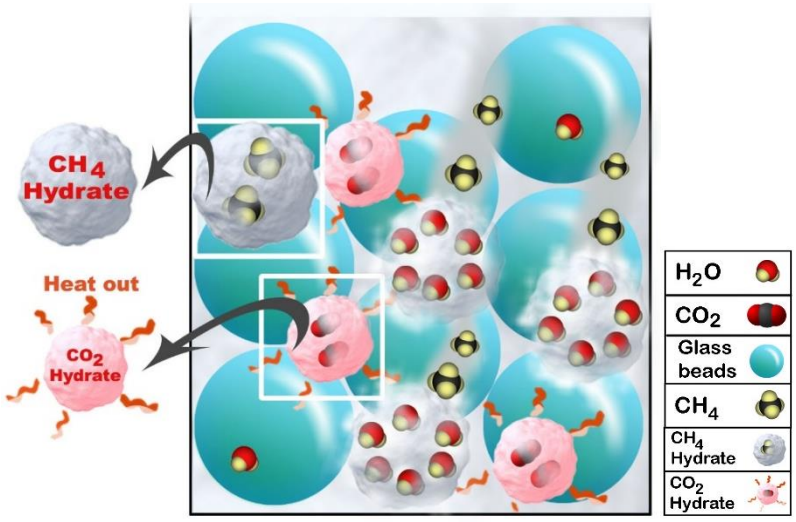

(c)

Figure 4.15 Animated macroscopic CO_2 and CH_4 hydrate exchange process in porous media. a) Injection of CO_2 liquid from the bottom of vessel into the media bed, section B. b) Nuclei CO_2 hydrate with residual water around the methane hydrate. c) New CO_2 hydrate formation in porous media and the heat released will dissociate CH_4 hydrate [55]. (Note: N_2 gas molecules are not illustrated in this figure).

4.2.3 CO_2/CH_4 exchange and sampling

After 24 hours of the CO_2/CH_4 hydrate exchange process, the excess methane gas, CO_2, and N_2 that did not participate in the hydrate sequestration are released. The bleeding process is maintained at approximately 1 bar drop per 10 seconds. The auxiliary chiller system with dry ice and ethanol is operating to cool the high-pressure vessel from 1 ˚C to -25 ˚C. The temperature reaches -25 ˚C in about 35 min (from 1 ˚C), and is maintained at that temperature for 15-20 min. This is because CO_2 hydrate is stable at 1 bar and -20 ˚C [38,47]. After reaching the lowered temperature and steady state for 20 min, the auxiliary chiller is shut off to allow hydrate dissociation. This work uses a calibrated thermodynamic condensation analysis method (with gas chromatography confirmation) for analyzing gas compositions by monitoring gas pressure and temperature. The idea is to provide accurate composition results with an inexpensive method, and

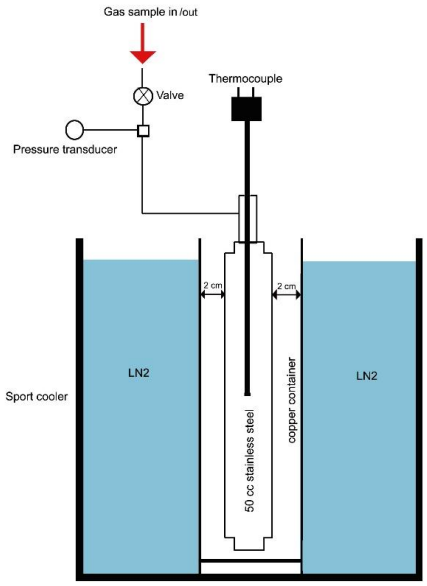

Figure 4.16 The full schematic of the sample gas condensation setup. The 50 ml stainless steel sample bottle with pressure transducer, thermocouple, and a ball valve for receiving gas in and out of the sample bottle.

within an uncertainty of no more than 4% in comparison to what is achievable with a GC (gas chromatography) analysis. The dissociated mixture is collected inside the pre-evacuated 50 ml stainless steel sample bottle. The pressure of the captured gas mixture in the sample bottle is 15 bar absolute pressure at a usual laboratory ambient room temperature between 17 to 20 degrees C. The sample bottle is then centrally suspended in a copper cooling chamber to surround it with a low temperature air environment. The cooling chamber, with sample bottle, is placed inside the 0.5 gallon (cylindrical sport beverage cooler) and submerged with liquid coolant. Liquid nitrogen is slowly poured into the 0.5-gallon cooler until the copper cooling chamber is submerged to within 3 to 5 mm of the top of the copper chamber tube. The sample bottle starts slowly cooling down from room temperature to about -170 degrees C over a period of 50 min. Due to the temperature decrease, carbon dioxide gas converts to liquid/solid phases, which is then followed by phase changes of the methane gas. Finally, nitrogen gas is the last component that begins to transition to liquid phase. Pressure is monitored throughout this process. Figure 4.16 shows the schematic of the sample gas condensation setup for composition analysis.

With the above-described experimental apparatus and procedure, a range of experiments were run to determine the efficacy of carbon dioxide replacement in methane hydrate.

CHAPTER 5: EXPERIMENT RESULTS OF DISSOCIATION AND GROWTH OF GAS HYDRATES

This chapter focuses on the experimental analysis and discussion, particularly on the set of the experiments of methane hydrate substituted with pure CO_2 with/without additional compounds participating in the process. These tests confirm that the experimental approach, the analysis, and the results will produce the information necessary to evaluate the hypotheses proposed in this work.

5.1 Results and discussions

5.1.1 Capillary rise of water in porous media/sediment

In this experiment, first we want to know the maximum distance between the particles to hold water in B section (described in previous chapter) under saturated condition without leaking into the section C. If the methane hydrate forms rapidly in section C as well as in the B section, it will block the CO_2 injection reaching section B. Therefore, the space between the particles (glass beads) is calculated. The calculation assumes that water rises in a capillary tube to a height of 2.930 inch, with angle of contact is 0°, g=9.81 m/s^2, and the density of water is 1000 kg/m^3 with surface tension of water is 0.072 N/m at the room temperature.

$$r = \frac{2.\sigma.\cos\theta}{\rho.g.h} \quad (51)$$

$$r = \frac{2\times 0.072(\frac{N}{m})\times 1}{1000(\frac{kg}{m^3})\times 9.81(\frac{m}{s^2})\times 0.074(m)} \quad (52);\ @\ r = 198 \text{ micrometers}$$

Which means, 198 micrometers are the maximum distance between particles (and also approximately the maximum sediment particle size) that we can use in our experiment. Figure 5.1 shows the capillary rise of water in the tube.

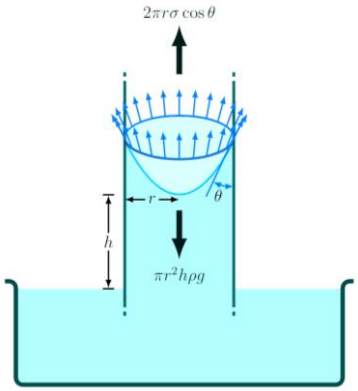

Figure 5.1 Capillary rise [82].

Sediment has different potential effects on hydrate formation:

1) There are different types of hydrate morphologies from sediments [83,86]: a) The gas hydrates become a component of the matrix; b) Hydrate grows everywhere in the sediment (around the particles, pore space, on the surface); c) Hydrates fill into the pore space. Figure 5.2 illustrates these different types of hydrate morphologies in sediment [86].

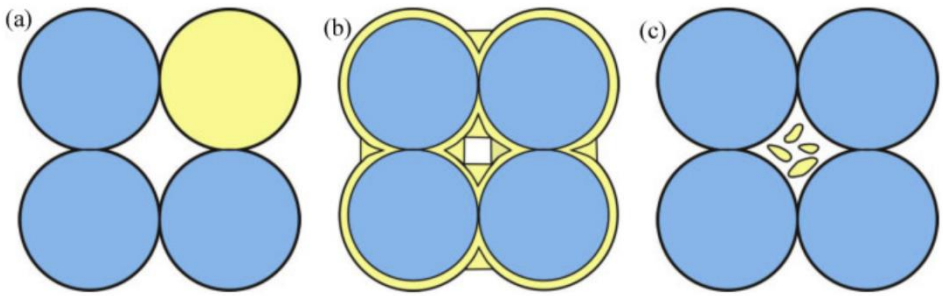

Figure 5.2 Three types of hydrate morphologies. (a) matrix-supporting; (b) Hydrate growth everywhere and (c) pore-filling. (Note: blue spheres represent sediment grains and the yellow refer to hydrates).

2) There is a porosity/channel for water and bulk flow, which means flow can pass through the sediment and react with liquid water in order to form the hydrate. Figure 5.3 illustrates how bulk flow can move easily through the space between the particles and can create multiple nucleation sites for hydrate formation, so the hydrate formation is much faster than with sediment-free bulk solution [87,88].

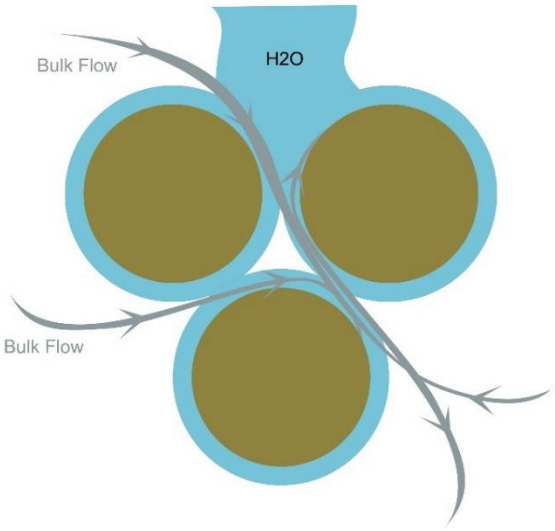

Figure 5.3 Bulk flow (gas molecules) moves through the space between particles and react with liquid water for forming gas hydrate. (Note: brown color represents sediment and blue color is water, gray color is bulk flow).

3) The material of the sediment can affect hydrate formation: mineral surfaces structure can adsorb the water molecules on the surface and promote hydrate nucleation [89].

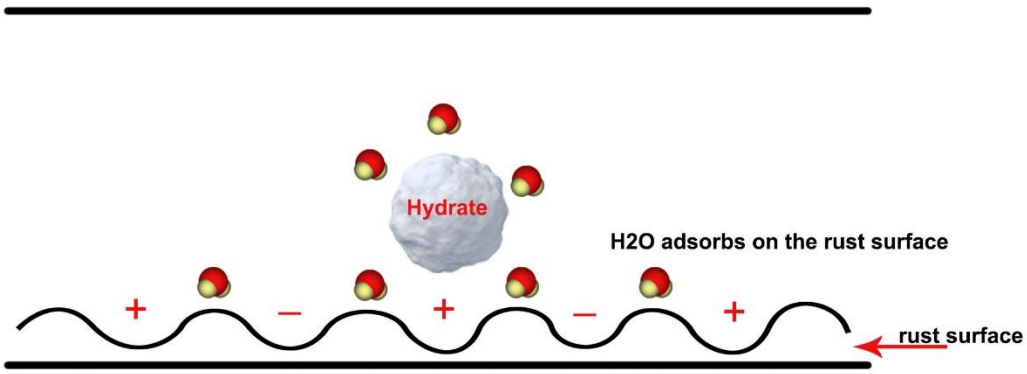

Figure 5.4 Water and slightly polar components adsorb directly on mineral surfaces (rust surface) and generate efficient conditions for hydrate nucleation.

There is no unique answer for the variation and optimization of sediment particle size because all hydrates in nature are different. It appears that the hydrate formation mostly depends on the flow through the sediments. The smaller the particle size of the porous media, the more pronounced the inhibitory effect. Prior research has found that the hydrate formation is largely limited by the mass transfer rate of gas and liquid water in the sediment [90]. The change in properties was similar to the change in the effective thermal conductivity of porous media with particle size [91]. This indicated that the main control factor for hydrate was heat transfer in the sediments. If the tightness of the porous media particles and their size do not allow the easy transfer of the heat, it can prevent the formation of hydrates. Therefore, the larger size of particle is better for transferring the flow and water through the sediment, and heat transfer can then happen more easily during the hydrate formation. This is important because hydrate formation is exothermic. The desirable particle size is usually between 70-1000 microns [92-94]. The sediment particle size

used in the current study is on the low side of this range, 44-88 microns (with average size of 75 microns).

5.1.2 Methane hydrate molar conversion and Z factor

Figure 5.5 a) shows the pressure to temperature plots with stability limits for pure CH_4 hydrate and pure CO_2 hydrate. Note that the temperature and pressure are independent thermodynamic variables, and that thermodynamic stability is reflected in the free energies of the two types of hydrates, as illustrated in figure 5.5 b). There are four temperatures measured at different heights in the vessel with the thermocouple probe. They are, from bottom to top, T_1 and T_2 inside the glass beads of section B, T_3 is right above the glass beads but remains in section B, and T_4 is close to the head of the vessel located in section A as illustrated in Figure 4.1. These temperatures are the raw data directly recorded from the experiment. The methane hydrate is not formed immediately even with the sudden temperature or pressure change in the beginning of the process but rather during the long duration allowing the hydrate induction for hydrate film to establish. Figure 5.5 plots the experimental results in P-T and Gibbs free energy with the theoretical limits which are calculated using the residual energy model [41,47,50]. CO_2 hydrate is more stable than CH_4 hydrate over the complete range of experimental conditions. As for CH_4 hydrate, the stability limit curve for CO_2 hydrate has been verified elsewhere [57,60,75,80]. Since the hydrate free energies along the hydrate stability limit curve in figure 5.5 b) have the same components in other phases, these free energies can be directly compared to free energies of other phases in the system, as for instance the liquid water phase and the adsorbed water phase. In the subsequent discussion, it is assumed that mechanical stability exists, and the pressure is uniform throughout the system.

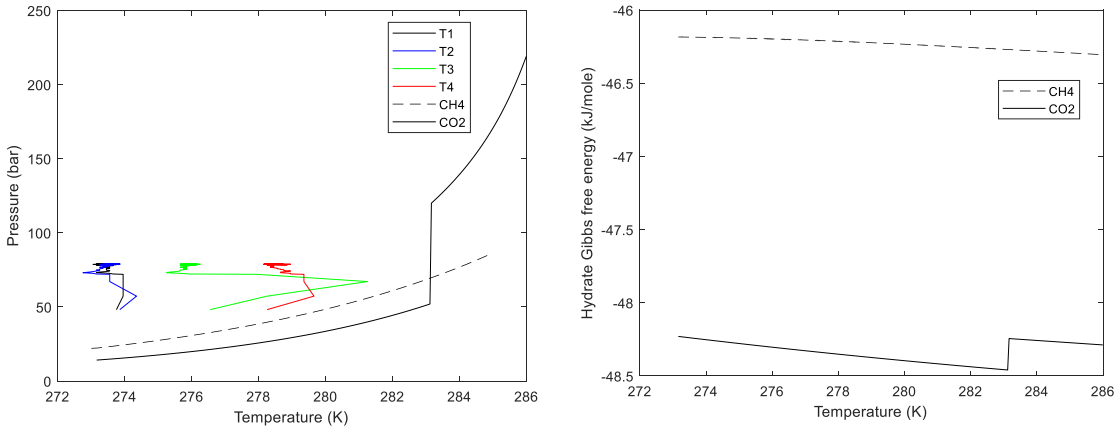

Figure 5.5 a) Simultaneous variations in measured temperatures and pressures as a function of time and compared to CH_4 temperature-pressure hydrate stability limits and CO_2 temperature-pressure hydrate stability limits. The figure shows that the conditions are always inside in the equilibrium hydrate formation domain. b) Free energy of CH_4 hydrate along the pressure-temperature hydrate stability limits. Similar curve for hydrate from pure CO_2 and water.

Table 5.1 shows the experimental injection composition for each condition. The initial weight of CH_4 injected into the system is 51.5 grams, which is equivalent to 3.210 moles. There were 132 grams of liquid water, which is 7.325 moles of H_2O, injected into the sediment filled section B. The water mole-fractions in the hydrate are available from calculated filling fractions. Since a residual thermodynamic model is utilized for the hydrate, these filling fractions are also directly available for conditions of temperature and pressures outside of the stability limits (but remain within the hydrate formation region). Details on the statistical thermodynamic model and the relationship between hydrate cavity partition functions as well as the filling fractions are given elsewhere [41,76] along with equations for conversion to mole-fractions. The calculated mole-fraction of water in the hydrate, based on filling fraction along the pressure temperature stability curve varies within limited ranges. The constant mole-fraction of 0.855 of water in hydrate is used

for the maximum methane conversion, which is 1.243 moles of CH_4 gas to form hydrate. At the end of the 48 hours for methane hydrate formation, we have the following molar balances for CH_4:

$$N^{A}_{(CH_4)} + N^{B}_{(CH_4)} + N^{C}_{(CH_4)} = \frac{(P.V^{A})}{(z^{A}(P^{A},T^{A}).R.T^{A})} + N^{B}_{(CH_4)} + \frac{(P.V^{C})}{(z^{C}(P^{C},T^{C}).R.T^{C})} = N^{total}_{(CH_4)} \approx 3.210 \quad (53)$$

$$N^{(B,H)}_{(CH_4)} + N^{(B,G)}_{(CH_4)} = N^{B}_{(CH_4)} \quad (54)$$

Superscripts A, B and C denote the three different sections of the experimental vessel. Subscript CH_4 denotes methane; H is hydrate and G is gas. Dissolved CH_4 in liquid water is neglected within experimental uncertainties. T^{A} is equal to T_4, and T^{c} is approximately equal to T_1.

$$N^{(B,H)}_{(H_2O)} + N^{(B,W)}_{(H_2O)} = N^{B}_{(H_2O)} \approx N^{total}_{(H_2O)} = 7.325 \quad (55)$$

The low water vapor pressure at hydrate forming conditions justifies the approximation of zero water in the CH_4 gas phase in all three sections. The time at the end of the CH_4 formation is denoted as t_e and the time for starting the injection of CO_2 is denoted as t_0. The difference between these two times for the CH_4 system is that the conditions are changed before the injection of CO_2. The conditions at the end of CH_4 hydrate formation is given for each condition in figure 5.6. T_4 is representative for section A and T_1 is representative for section C. It is approximated that all

sections are in mechanical balance and that pressures in A and C therefore are the same. After the CH_4 hydrate is formed along the temperatures and pressures in the system plotted in Figure 5.5 a) and Figure 5.6, then pressure is reduced to approximately 48 bar (see Table 5.2 for specific conditions). During this change, the additional CH_4 will be converted to hydrate. The composition of this hydrate is different from the initial hydrate formed along the conditions in Figures 5.5 and 5.6. Even during that period, the composition will be slightly different inside section B. But as discussed below, the changes are small enough to be smoothed out to an average value for the finally formed hydrate in B.

In Table 5.2, extracted from experimental results, as an example for cond#1 (the injection compositions are tabulated in Table 5.1), there are 2.315 moles of CH_4 gas in the section A and C (column 1 and 3) inside the vessel and there are a remaining 0.895 moles of CH_4 as the fixed amount of hydrate formed in section B, while the averaged mole-fraction of water in hydrate of these two sections is 0.859. The moles of water in hydrate (section B) before pressure reduction is then:

$$N_{(H_2O)}^{(B,H)} = N_{(CH_4)}^{(B,H)} \times \frac{0.859}{0.141} = 5.440 \quad (56)$$

$$N_{(CH_4)}^{(B,H)(t_0)} - N_{(CH_4)}^{(B,H)(t_e)} = N_{(H_2O)}^{(B,aq)} \times \frac{0.140}{0.861} = 0.304 \quad (57)$$

Table 5.1 Experimental injection composition (mole%)

Condition #	Injection Composition
1	100% CO_2
2	90% CO_2, 10% N_2
3	80% CO_2, 20% N_2
4	70% CO_2, 30% N_2
5	97% CO_2, 3% ethanol
6	77% CO_2, 20% N_2, 3% ethanol
7	76% CO_2, 20% N_2, 4% ethanol
8	79.9% CO_2, 20% N_2, 0.1% ethanol
9	71% CO_2, 20% N_2, 9% ethanol
10	79% CO_2, 20% N_2, 1% ethanol
11	79.99% CO_2, 20% N_2, 0.01% ethanol
12	79% CO_2, 20% N_2, 1% NFM
13	79.99% CO_2, 20% N_2, 0.01% NFM
14	79.9% CO_2, 20% N_2, 0.1% NFM
15	77% CO_2, 20% N_2, 3% NFM
16	99% CO_2, 1% NFM

Table 5.2 Calculated from SRK (Soave-Redlich-Kwong) equation of state (described in 5.1.4 with more details) [95,96] to find the compressibility factor (Z), moles of CH_4 (N_{CH4}), and mole fraction of water in hydrate ($x^H_{H_2O}$) at the end of CH_4 formation under high pressure (t_e) and after pressure reduction prior to CO_2 injection (t_0) for all of the experimental conditions.

Property	Section A (t_e)		Section A (t_0)		Section C (t_e)		Section C (t_0)	
Cond#1	278.95 K	69.44 bar	278.25 K	48.57	273.35 K	69.44 bar	273.75 K	48.57 bar
Z	0.860		0.898		0.848		0.891	
N_{CH4}	2.000		1.334		0.314		0.207	
$x^H_{H_2O}$	0.860		0.863		0.857		0.859	

Property	Section A (t_e)		Section A (t_0)		Section C (t_e)		Section C (t_0)	
Cond#2	278.05 K	74.91 bar	277.15 K	48.57	273.65 K	74.91 bar	273.55 K	48.57 bar
Z	0.850		0.896		0.822		0.890	
N_{CH4}	2.193		1.354		0.349		0.209	
$x^H_{H_2O}$	0.858		0.862		0.857		0.859	

Property	Section A (t_e)		Section A (t_0)		Section C (t_e)		Section C (t_0)	
Cond#3	277.15 K	69.51 bar	278.75 K	48.57	273.75 K	69.51 bar	274.15 K	48.57 bar
Z	0.856		0.898		0.849		0.891	
N_{CH4}	2.025		1.342		0.314		0.209	
$x^H_{H_2O}$	0.859		0.863		0.858		0.860	

Property	Section A (t_e)		Section A (t_0)		Section C (t_e)		Section C (t_0)	
Cond#4	277.75 K	69.53 bar	277.55 K	48.14	273.45 K	69.53 bar	273.55 K	48.14 bar
Z	0.858		0.897		0.848		0.891	
N_{CH4}	2.018		1.338		0.315		0.208	
$x_{H_2O}^H$	0.859		0.862		0.857		0.859	

Property	Section A (t_e)		Section A (t_0)		Section C (t_e)		Section C (t_0)	
Cond#5	278.65 K	71.64 bar	278.85 K	48.41	273.45 K	71.64 bar	273.65 K	48.41 bar
Z	0.857		0.899		0.844		0.891	
N_{CH4}	2.076		1.336		0.326		0.208	
$x_{H_2O}^H$	0.860		0.862		0.857		0.859	

Property	Section A (t_e)		Section A (t_0)		Section C (t_e)		Section C (t_0)	
Cond#6	277.75 K	67.37 bar	277.75 K	48.19	273.45 K	67.37 bar	273.45 K	48.19 bar
Z	0.862		0.897		0.852		0.890	
N_{CH4}	1.946		1.337		0.304		0.208	
$x_{H_2O}^H$	0.861		0.863		0.858		0.860	

Property	Section A (t_e)		Section A (t_0)		Section C (t_e)		Section C (t_0)	
Cond#7	278.65 K	71.52 bar	277.75 K	48.19	273.45 K	71.52 bar	273.45 K	48.19 bar
Z	0.857		0.897		0.844		0.890	
N_{CH4}	2.072		1.337		0.326		0.208	
$x_{H_2O}^H$	0.859		0.862		0.857		0.858	

Property	Section A (t_e)		Section A (t_0)		Section C (t_e)		Section C (t_0)	
Cond#8	277.45 K	69.66 bar	277.35 K	47.96	273.35 K	69.66 bar	273.35 K	47.96 bar
Z	0.857		0.897		0.848		0.891	
N_{CH4}	2.025		1.333		0.316		0.207	
$x_{H_2O}^H$	0.858		0.863		0.858		0.859	

Property	Section A (t_e)		Section A (t_0)		Section C (t_e)		Section C (t_0)	
Cond#9	277.15 K	68.60 bar	277.35 K	48.22	273.25 K	68.60 bar	274.05 K	48.22 bar
Z	0.858		0.897		0.849		0.891	
N_{CH4}	1.994		1.341		0.310		0.208	
$x_{H_2O}^H$	0.859		0.862		0.857		0.859	

Property	Section A (t_e)		Section A (t_0)		Section C (t_e)		Section C (t_0)	
Cond#10	278.05 K	69.62 bar	278.05 K	48.78	273.65 K	69.62 bar	273.75 K	48.78 bar
Z	0.859		0.897		0.848		0.889	
N_{CH4}	2.017		1.353		0.315		0.211	
$x_{H_2O}^H$	0.858		0.861		0.858		0.859	

Property	Section A (t_e)		Section A (t_0)		Section C (t_e)		Section C (t_0)	
Cond#11	277.65 K	69.40 bar	277.85 K	48.38	273.55 K	69.40 bar	273.55 K	48.38 bar
Z	0.858		0.897		0.849		0.890	
N_{CH4}	2.014		1.342		0.314		0.209	
$x_{H_2O}^H$	0.860		0.863		0.859		0.860	

Property Cond#12	Section A (t_e)		Section A (t_0)		Section C (t_e)		Section C (t_0)	
	277.25 K	72.14 bar	278.35 K	48.10	273.35 K	72.14 bar	271.35 K	48.10 bar
Z	0.853		0.898		0.843		0.891	
N_{CH4}	2.110		1.330		0.329		0.207	
$x^H_{H_2O}$	0.859		0.860		0.857		0.858	

Property Cond#13	Section A (t_e)		Section A (t_0)		Section C (t_e)		Section C (t_0)	
	277.45 K	68.53 bar	277.55 K	48.02	273.45 K	68.53 bar	273.65 K	48.02 bar
Z	0.859		0.897		0.850		0.891	
N_{CH4}	1.988		1.333		0.309		0.207	
$x^H_{H_2O}$	0.858		0.859		0.857		0.858	

Property Cond#14	Section A (t_e)		Section A (t_0)		Section C (t_e)		Section C (t_0)	
	277.35 K	70.19 bar	277.15 K	48.37	273.45 K	70.19 bar	273.35 K	48.37 bar
Z	0.856		0.896		0.847		0.890	
N_{CH4}	2.044		1.347		0.319		0.209	
$x^H_{H_2O}$	0.859		0.861		0.858		0.859	

Property Cond#15	Section A (t_e)		Section A (t_0)		Section C (t_e)		Section C (t_0)	
	277.75 K	72.53 bar	277.55 K	48.81	273.75 K	72.53 bar	273.55 K	48.81 bar
Z	0.853		0.896		0.843		0.889	
N_{CH4}	2.117		1.358		0.330		0.211	
$x^H_{H_2O}$	0.859		0.862		0.859		0.860	

Property Cond#16	Section A (t_e)		Section A (t_0)		Section C (t_e)		Section C (t_0)	
	277.45 K	68.67 bar	277.55 K	48.16	273.45 K	68.67 bar	273.65 K	48.16 bar
Z	0.859		0.897		0.849		0.891	
N_{CH4}	1.993		1.338		0.310		0.207	
$x^H_{H_2O}$	0.860		0.863		0.859		0.860	

The mole-fraction of CH_4 in hydrate is 0.140 (see table above the average number for mole-fraction of water). There are 0.304 moles of methane hydrate formed during reduction to 48 bar. Since only water and CH_4 are involved, then (1-mole fraction of water = mole-fraction of methane),

$$x^H_{CH_4} = \frac{(N^H_{CH_4})}{(N^H_{CH_4} + N^H_{H_2O})} \quad (58)$$

$$x^H_{CH_4}(N^H_{CH_4} + N^H_{H_2O}) = N^H_{CH_4} \quad (59)$$

$$x_{CH_4}^{H} N_{H_2O}^{H} = (1 - x_{CH_4}^{H}) N_{CH_4}^{H} \quad (60)$$

$$N_{CH_4}^{H} = \frac{(x_{CH_4}^{H})}{(1 - x_{CH_4}^{H})} N_{H_2O}^{H} \quad (61)$$

According to equations (58-61), this 0.470 moles of CH_4 is extracted from the experimental vessel prior to injection of CO_2 and 1.200 moles of CH_4 is trapped in hydrate in section B for cond#1-16 approximately. Table 5.2 shows the moles of methane and water at different pressure and temperature before CO_2 injection for sixteenth conditions. We did the same calculations for condition 2 through 16 with their own initial and final pressure-temperature conditions for methane hydrate formation before and after pressure reduction prior to CO_2 injection. Also, the initial weight of CH_4 and water injected into the system for all experiments are the same amounts as described above.

5.1.3 Measured P and T with time for methane and exchange hydrates

The temperature and pressure after/before the injection of CO_2 along with time is plotted in Figure 5.6. After the above procedures, 200 grams of CO_2 (4.544 moles) are injected with or without N_2 and surfactants into section C within a 20-minute time window at a rate of 0.0042 moles/second. Mixing of N_2 (10, 20 and 30 moles%) and surfactants (0.01, 0.1, 1, 3 moles%) with CO_2 takes place as both the CO_2 with/without surfactants and nitrogen liquid flow separately into a Tee fitting. They then merge at a 90-degree turn exiting from the center. Both fluids are forced through a 0.5-micron stainless steel filter cylinder at the exit for breaking up larger N_2 gas bubbles, thus increasing the N_2 surface area to liquid CO_2 interface for improving the mixing quality.

Methane hydrate formation

CO_2/CH_4 hydrate exchange

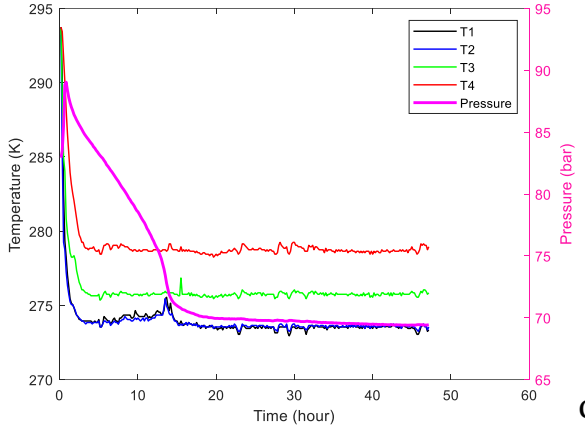

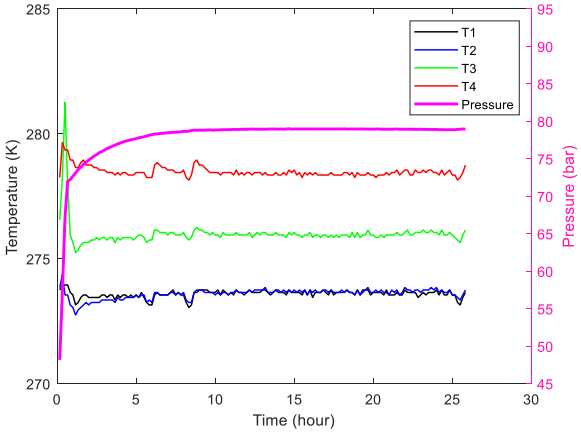

Cond#1

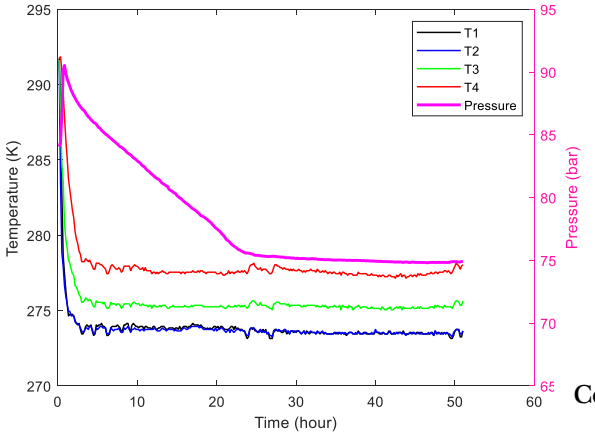

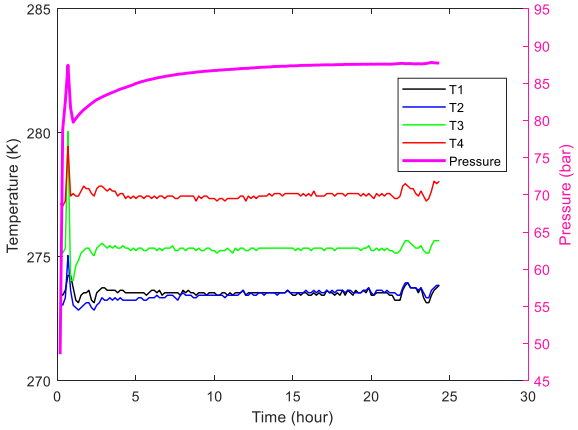

Cond#2

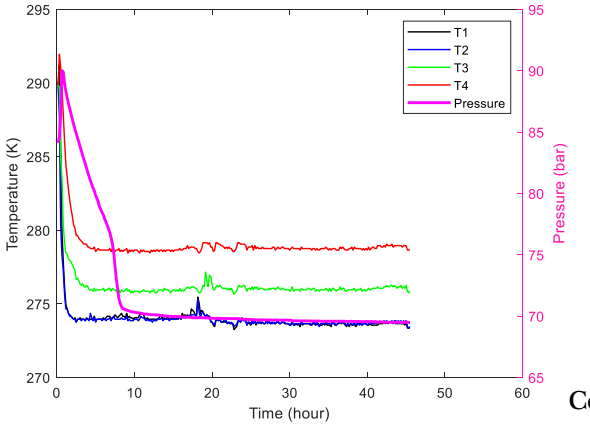

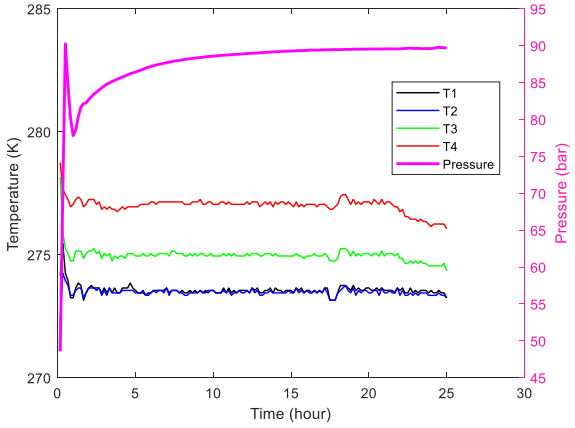

Cond#3

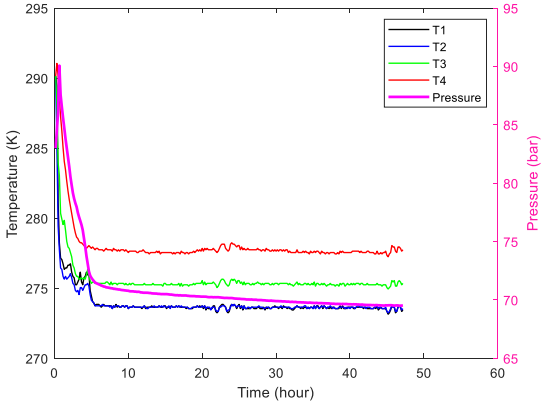

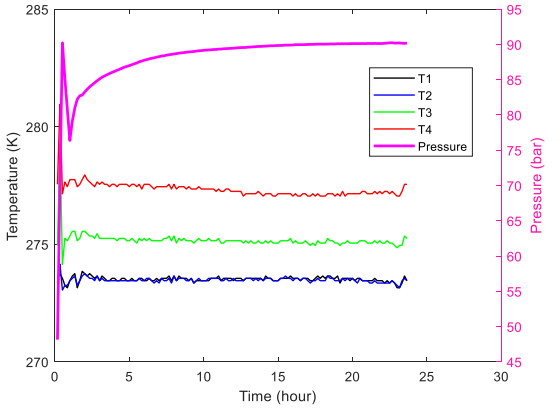

Cond#4

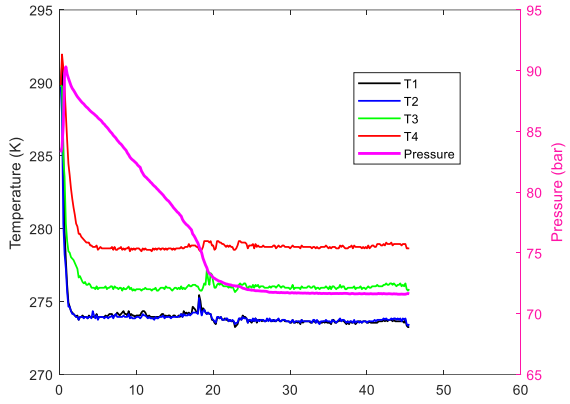

Cond#5

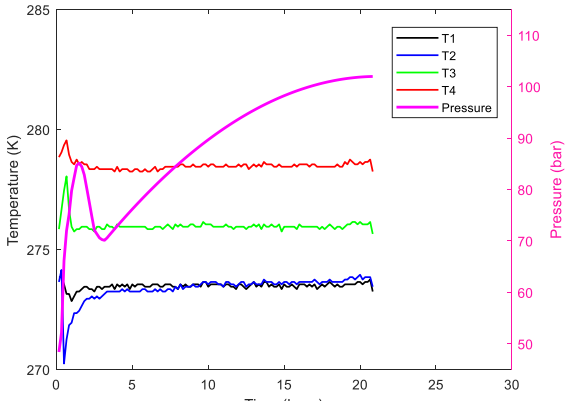

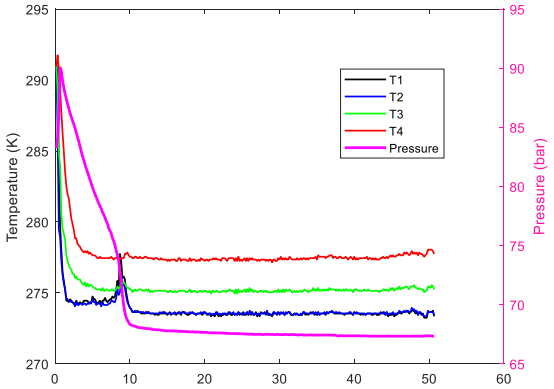

Cond#6

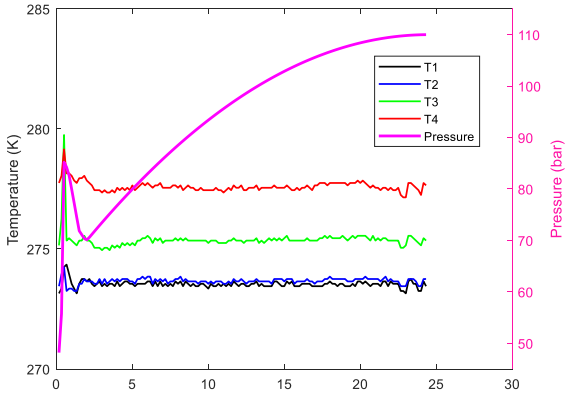

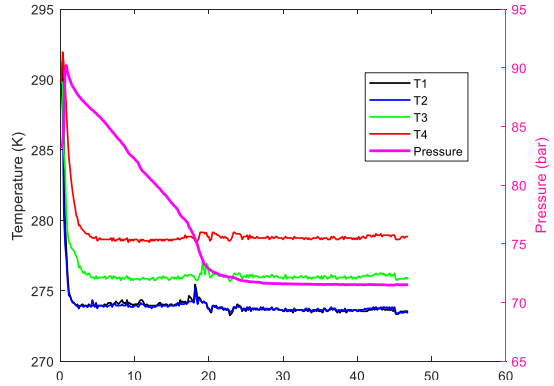

Cond#7

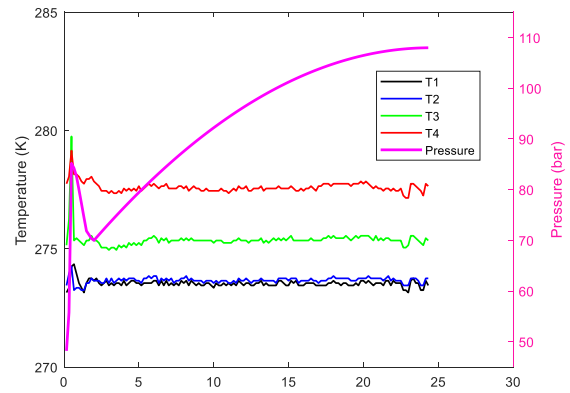

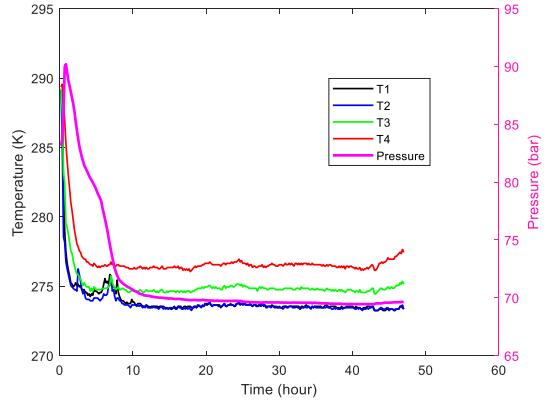

Cond#8

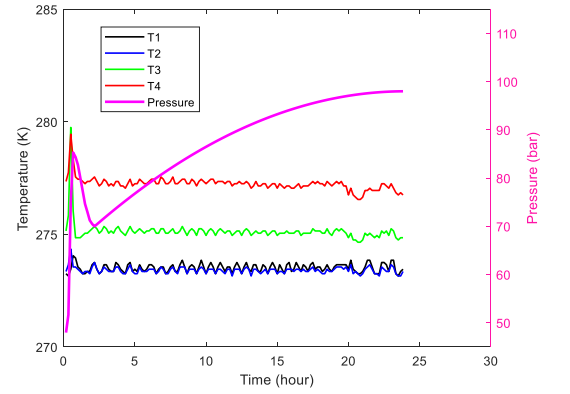

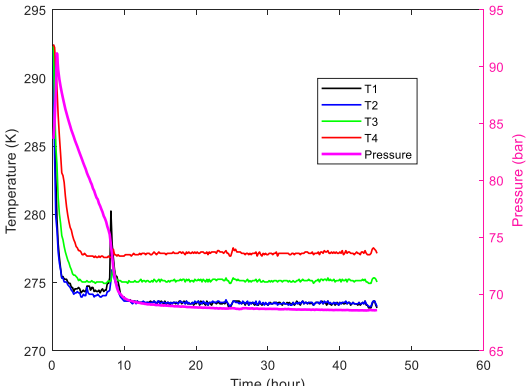

Cond#9

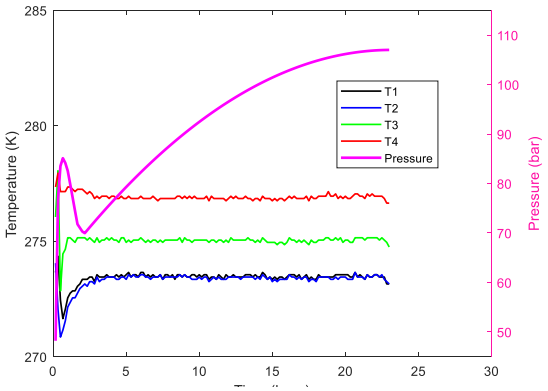

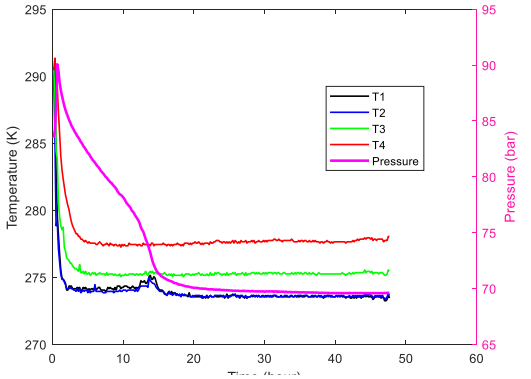

Cond#10

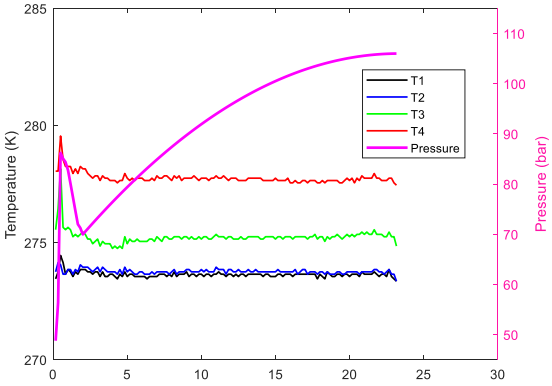

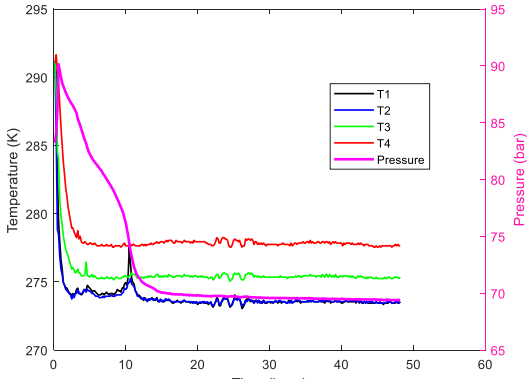

Cond#11

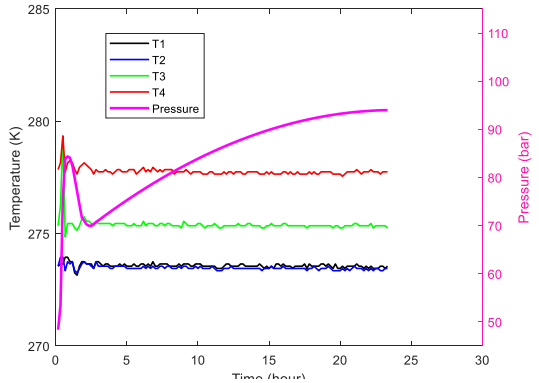

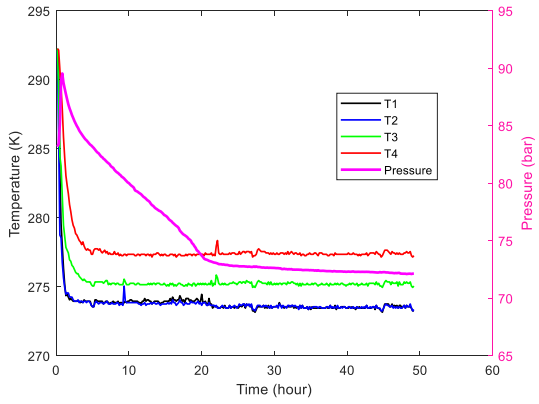

Cond#12

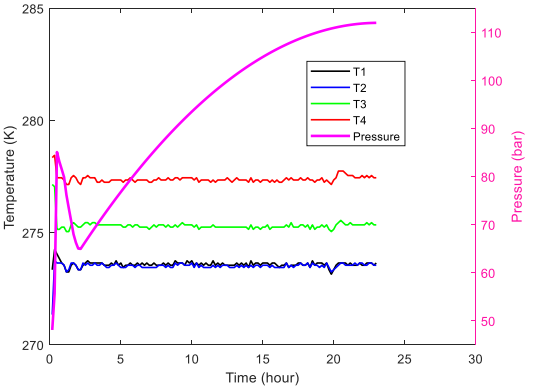

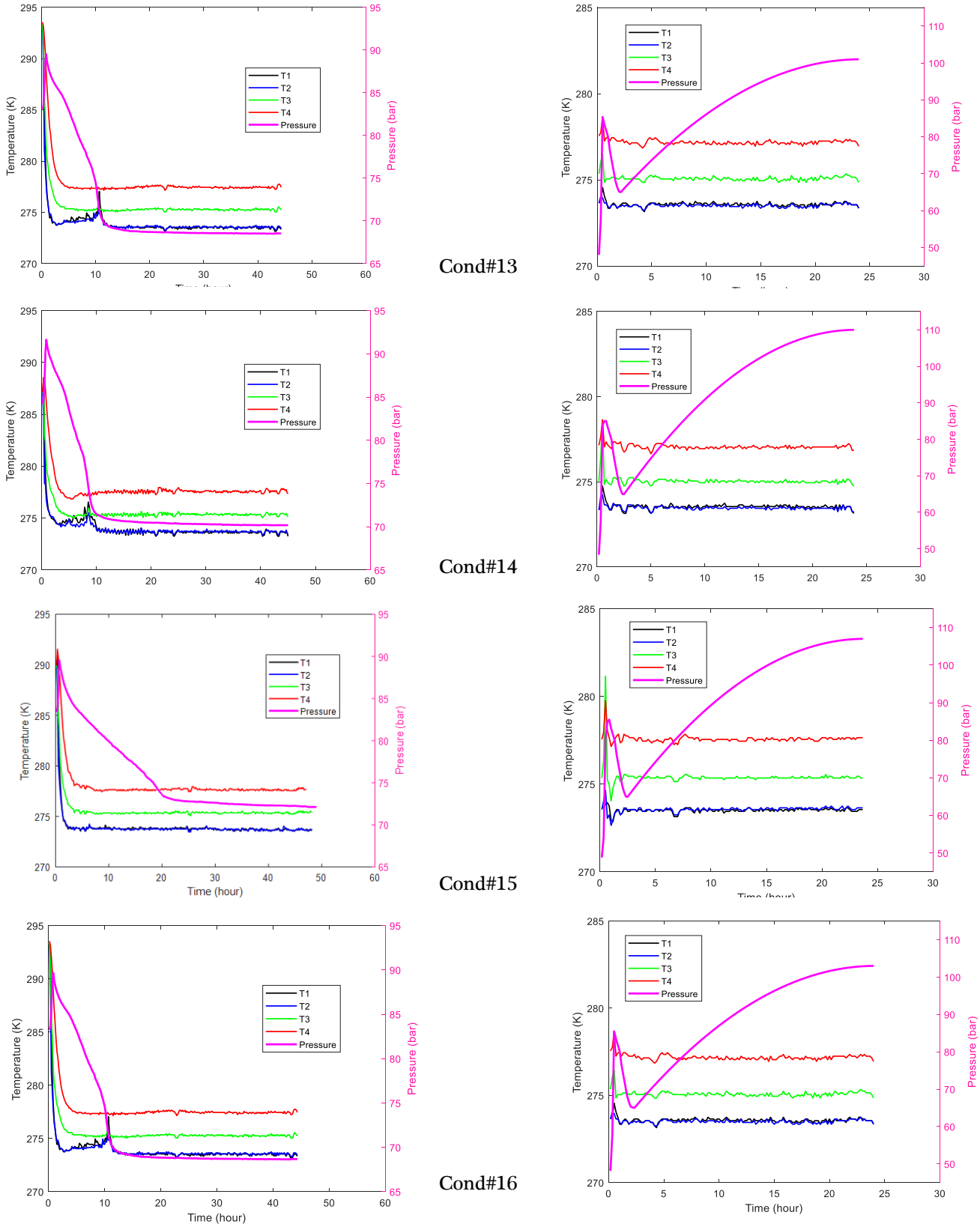

Figure 5.6 Time histories of methane hydrate and CO_2/CH_4 hydrate exchange process.

The initial CH_4 in section C is flushed over to section A through a bypass loop during the first 10 minutes. Figure 5.6. shows the time history of methane hydrate formation and CH_4/CO_2 hydrate exchange process based on pressure and temperature measurements from the experiment.

5.1.4 Kinetic rate of hydrate exchange

The data acquired from the experiment are gas temperature and pressure. The pressure given used the unit of bar. The gas state equation is used to estimate the compressibility factor which depends on pressure and temperature. At zero pressure, the compressibility factor of all gases is equal to 1, which is equal to ideal gas. The compressibility factor (Z) of a gas is defined as the measure of the deviation of the behavior of a real gas from the ideal:

$$Z = \frac{PV}{nRT} \quad (62)$$

For ideal gases in all conditions Z=1, but for real gases Z is not equal to one. The deviation of the Z factor from 1 indicates that the behavior of the gas is out of the ideal state. At very low pressure, all gases have Z=1, and have almost ideal gas behavior. Because this work is conducted at high pressure, the third order correction equation of SRK (Soave-Redlich-Kwong) was used to obtain the methane gas compressibility factor. The Redlich-Kwong equation is an experimental-algebraic equation that relates the temperature, pressure, and volume of gases. It is generally more accurate than the Van der Waals equation and the ideal gas equation at temperatures above the critical temperature. The Redlich-Kwong equation has undergone many revisions to improve its accuracy

in predicting the gas phase properties of compounds as well as in better simulation at lower temperatures, including liquid vapor equilibrium. The equation of state of SRK is below:

$$P = \frac{RT}{V-b} - \frac{a(T)}{V(V+b)} \quad (63)$$

$$a(T) = 0.42748 \frac{R^2 T^2}{P_C} \quad (64)$$

$$b = 0.08664 \frac{RT_C}{P_C} \quad (65)$$

$$\sqrt{\alpha(T)} = 1 + k(1 - \frac{\sqrt{T}}{\sqrt{T_C}}) \quad (66)$$

$$k = 0.0480 + 1.574w - 0.176w^2 \quad (67)$$

The SRK equation based on the compressibility factor (Z) is as follows:

$$Z^3 - Z^2 + (A - B - B^2)Z - AB = 0 \quad (68)$$

Which in this equation A and B are calculated as follows:

$$A = \frac{aP}{(RT)^2} \quad (69)$$

$$B = \frac{bP}{RT} \quad (70)$$

The compressibility factor is a function of temperature, pressure, type of gas and the composition of the percentage of gas components. Because in each test we are faced with the need to calculate a high number of points, determining the compressibility at each point manually is difficult. For this reason, the current research relies on commercial software ProPhyPlus [97] to achieve these calculations for these data. This software has the ability to calculate most of the thermodynamic quantities with minimum input data, to use the equation of state, and to calculate thermodynamic conditions. The obtained results are comparable to the experimental results and have an acceptable error. First, we select methane gas in the software and calculate the compressibility factor for each temperature and pressure in each test. There were, for example around 130 data points acquired in each test, and therefore 130 compressibility factors need to be calculated. Then using the relation:

$$n = \frac{PV}{ZRT} \quad (71)$$

the number of moles is calculated at each point. The molar change during the experiment is then acquired because the initial number of moles of each test conditions varies. N_t is the number of moles of methane at 10 minute intervals, N_0 is the number of moles of methane at the beginning of the process in the high-pressure vessel.

$$\Delta N=N_t-N_0 \quad (72)$$

The changes in the number of moles of each test (condition) in relation to the pressure and temperature changes are shown in Table 5.3 as follows:

Table 5.3 Moles of methane released from hydrate structure by substitution of CO_2 for each condition.

Cond#	P_i (bar)	P_f (bar)	T_i (K)	T_f (k)	N_0	N_{max}	ΔN_{max}	Time (hour)
1	72.003898	78.946748	273.55	273.75	1.312	1.540	0.228	15
2	79.753205	87.711538	273.05	273.85	1.312	1.543	0.231	15
3	77.815751	89.711538	273.25	273.35	1.312	1.673	0.361	15
4	76.387001	90.162275	273.45	273.45	1.312	1.744	0.432	15
5	70.1278	101.98902	273.15	273.45	1.312	2.128	0.816	15
6	71.176406	108.99780	273.65	273.75	1.311	2.353	1.042	15
7	70.551025	107.99791	273.65	273.75	1.311	2.291	0.980	15
8	70.406153	97.998367	273.35	273.45	1.312	2.008	0.696	15
9	70.555444	106.99766	273.05	273.15	1.308	2.232	0.924	15
10	70.520925	105.99120	273.65	273.95	1.312	2.213	0.901	15
11	70.334157	93.986794	273.45	273.45	1.312	1.913	0.601	15
12	65.613545	111.99703	273.55	273.75	1.312	2.512	1.200	15

13	65.523690	100.99793	273.35	273.55	1.312	2.214	0.902	15
14	65.645742	109.99729	273.25	273.25	1.311	2.499	1.188	15
15	65.633997	106.99743	273.55	273.65	1.311	2.475	1.164	15
16	65.568090	102.99778	273.35	273.45	1.311	2.241	0.930	15

The condition#12 has the highest number of moles under the same full experimental process of 15 hours. N_{max} is the maximum number of N_t for each condition. In order to better understand the influence of the role of promoters, nitrogen and NFM, in this research, three conditions are selected to analyze along the experimental time. Figure 5.7a) shows the number of moles of methane released from the hydrate structure after injection of pure CO_2 (Cond#1), CO_2 with 20 moles% N_2 (cond#3), and cond#12 CO_2 with 20 moles% N_2 and 1 mole% NFM (N-formylmorpholine).

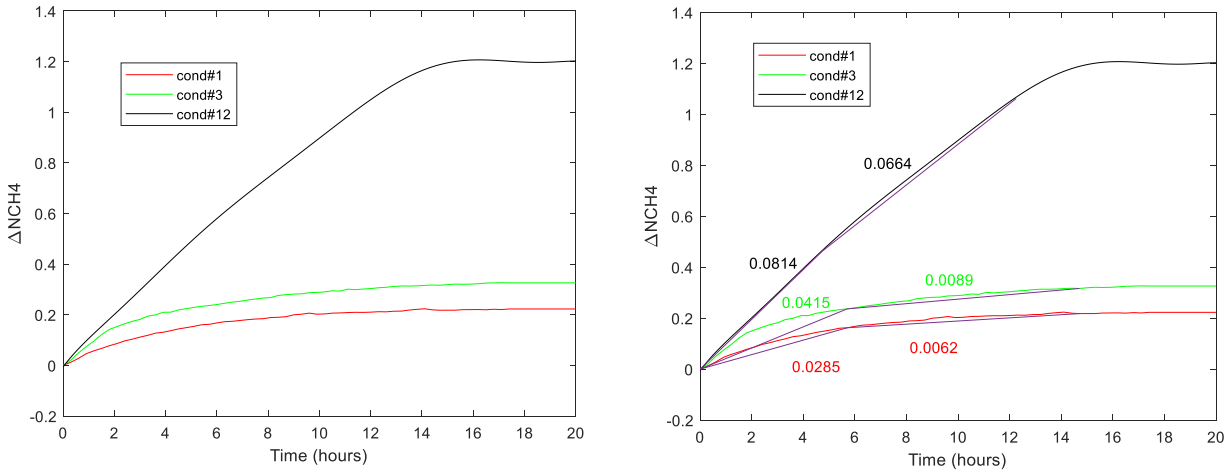

(a) (b)

Figure 5.7 a) Moles of methane released by substitution of CO_2 from lowest to the highest methane hydrate production level. b) Shows the average slope of each condition from 0-6 hours, and 6-15 hours.

Figure 5.7b) includes the approximated curve fitting of the slope locally, and illustrates that when adding nitrogen and surfactant in CO_2 liquid, the kinetic rate of substitution increased by factor of 2 during the first 6 hours, then it increased by factor of 10 after 6 hours. This appears to indicate that after 6 hours more new CO_2 hydrate forms and it creates some blockage of the flow (mass transport limitation). Therefore, introducing surfactant helps to break the hydrate film at the interface. The cond#1 and 3 do not have surfactant, and it is observed that the production of methane stopped at an early stage after less than 10 hours in comparison to cond#12.

Moreover, in Table 5.3, some conditions showing (cond#12,14 and 15) a pressure difference (ΔP) between the initial pressure and the final pressure of the vessel of more than 38 bar. This indicates in addition to the removal methane, other gases are released. The released gas can be nitrogen, CO_2, and methane from section C to section A of the vessel. As a first step, we must obtain exactly the pressure at which methane is completely released from hydrate under the test conditions. In order to do that, we draw a line in the graph for two data points that they have the same temperature. Figure 5.8 shows the pressure versus number of moles at the same temperature in the process to see when the methane gas is completely released from the hydrate structure.

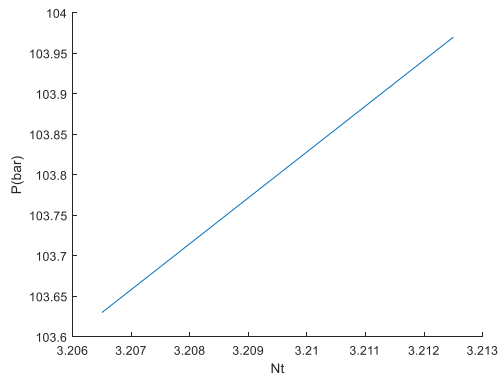

Temperature	Pressure	Z factor	N_t
273.75	103.63	0.7960	3.20660
273.75	103.99	0.7962	3.21235

Figure 5.8 The pressure versus N_t at the constant temperature for cond#12, 14 and15.

For this analysis, because we consider a very small range of pressure changes and the condition that the temperature is constant, the compressibility factor does not change much and reaches only to 0.7962 from 0.7960. By approximating between these two points, the slope of the line method can be used to determine the methane released. The pressure is calculated at a constant temperature, so according to the following pressure relations, we get the total methane gas in the vessel:

$$V = \frac{ZnRT}{P} \quad (73)$$

Because the volume of the vessel is constant, the following relationship is established between the two points after the methane gas is completely released:

$$\frac{Z1nRT1}{P1} = \frac{Z2nRT2}{P2} \quad (74)$$

Therefore,

$$P2\,fCH4 = \frac{Z2nRT2}{Z1nRT1}(P1\,fCH4) \quad (75)$$

This equation provides the pressure at which the methane gas is completely removed so that we can consider any further increase in reservoir pressure comes from the release of other gases. Table 5.4 shows how the number of moles of other gases affects the final pressure of the experiment.

Table 5.4 Number of moles/mole fraction of other gases released during the exchange process.

Condition#	**Mole number of other gases**	**Mole fraction of other gases**
12	0.401	0.250
14	0.312	0.206
15	0.178	0.129

5.1.5 Sample gas condensation and composition analysis

In order to analyze the total final conversion outcome of the hydrate exchange process, the gases trapped are released for composition analysis by sequentially condensing the contents. This method for determining gas composition is straightforward, and requires careful monitoring of pressure alternation with temperature to identify the relevant phase change. The mass of each species is fixed and known at the start of each test. The process is to adjust the composition of gas and liquid phases to provide the best fit over the entire conversion process, and then to report the final CO_2, CH_4 and N_2 compositions and relate those to the conversion level. Figure 5.9. shows the dynamic temperature varying over time (as the pressure changes) for different compositions of hydrate dissociation for all of the experiment conditions.

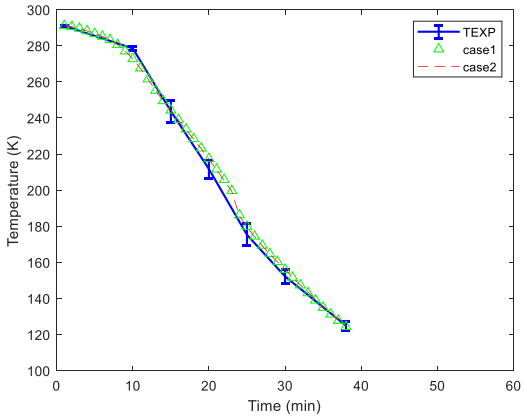

Condition #1: Pure CO_2	%Error
Calculated Composition 1: 26 moles% CO_2 74 moles% CH_4	1.66%
Calculated Composition 2: 25.5 moles% CO_2 74.5 moles% CH_4	1.56%

(a)

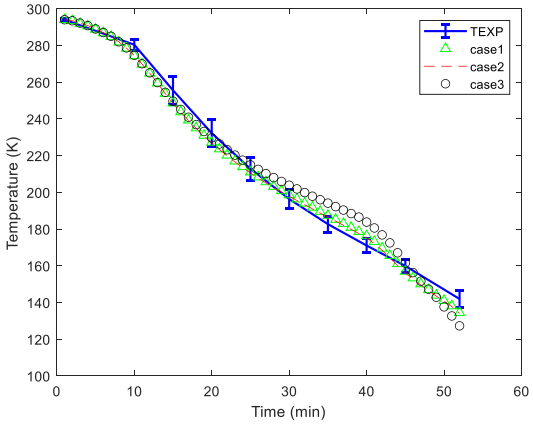

Condition #2: CO_2 with 10% N_2	%Error
Calculated Composition 1: 30 moles% CO_2-68 moles% CH_4 -2 moles% N_2	1.32%
Calculated Composition 2: 29 moles% CO_2-69 moles% CH_4 -2 moles% N_2	1.14%
Calculated Composition 3: 40 moles% CO_2-50 moles% CH_4 -10 moles% N_2	3.51%

(b)

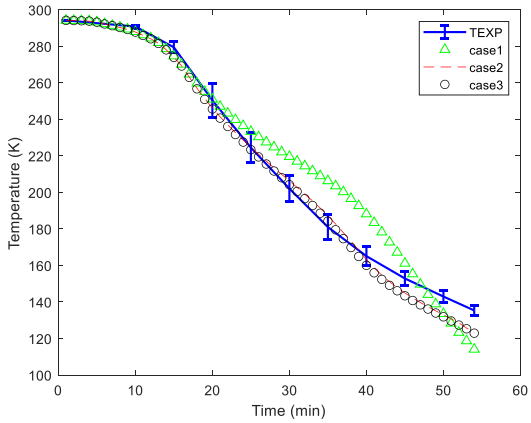

Condition #3: CO_2 with 20% N_2	%Error
Calculated Composition 1: 65 moles% CO_2-30 moles% CH_4 -5 moles% N_2	5.40%
Calculated Composition 2: 33 moles% CO_2-65 moles% CH_4 -2 moles% N_2	1.91%
Calculated Composition 3: 30 moles% CO_2-65 moles% CH_4 -5 moles% N_2	2.58%

(c)

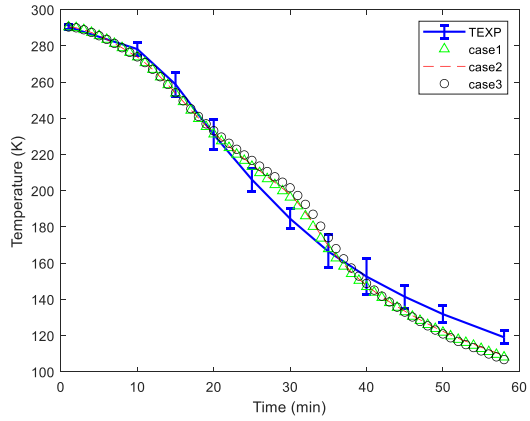

Condition #4: CO_2 with 30% N_2	%Error
Calculated Composition 1: 32 moles% CO_2-66 moles% CH_4 -2 moles% N_2	2.02%
Calculated Composition 2: 34 moles% CO_2-64 moles% CH_4 -2 moles% N_2	1.84%
Calculated Composition 3: 36 moles% CO_2-62 moles% CH_4 -2 moles% N_2	1.93%

(d)

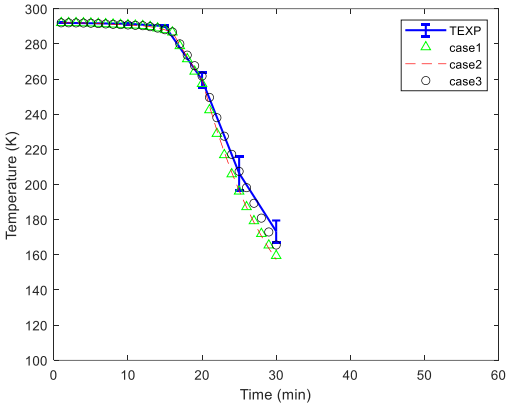

Condition #5: CO_2 with 3% ethanol	%Error
Calculated Composition 1: 49.9 moles% CO_2-50 moles% CH_4 -0.1 moles% C_2H_5OH	2.10%
Calculated Composition 2: 59.9 moles% CO_2-40 moles% CH_4 -0.1 moles% C_2H_5OH	2.06%
Calculated Composition 3: 69.9 moles% CO_2-30 moles% CH_4 -0.1 moles% C_2H_5OH	0.75%

(e)

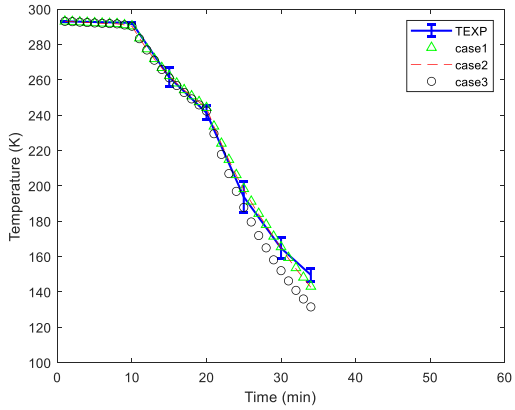

Condition #6: CO_2 with 20% N_2 and 3% ethanol	%Error
Calculated Composition 1: 80moles% CO_2-18 moles% CH_4 -1.85 moles% N_2-0.15 mole% C_2H_5OH	1.07%
Calculated Composition 2: 79.9 moles% CO_2-18 moles% CH_4 -2 moles% N_2-0.1 mole% C_2H_5OH	1.05%
Calculated Composition 3: 73.9 moles% CO_2-24 moles% CH_4 -2 moles% N_2-0.1 mole% C_2H_5OH	2.67%

(f)

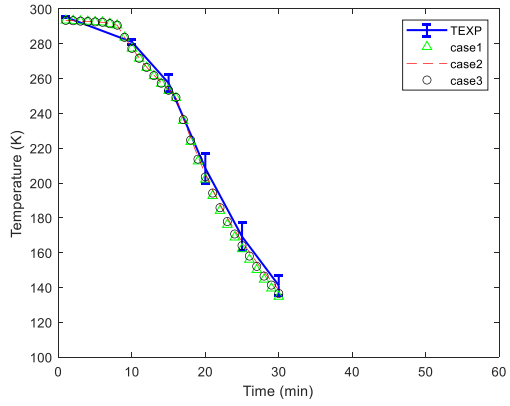

Condition #7: CO_2 with 20% N_2 and 4% ethanol	%Error
Calculated Composition 1: 76.89 moles% CO_2-21 moles% CH_4 -2 moles% N_2-0.11 mole% C_2H_5OH	2.42%
Calculated Composition 2: 78.89 moles% CO_2-19 moles% CH_4 -2 moles% N_2-0.11 mole% C_2H_5OH	1.39%
Calculated Composition 3: 77.89 moles% CO_2-20 moles% CH_4 -2 moles% N_2-0.11 mole% C_2H_5OH	1.94%

(g)

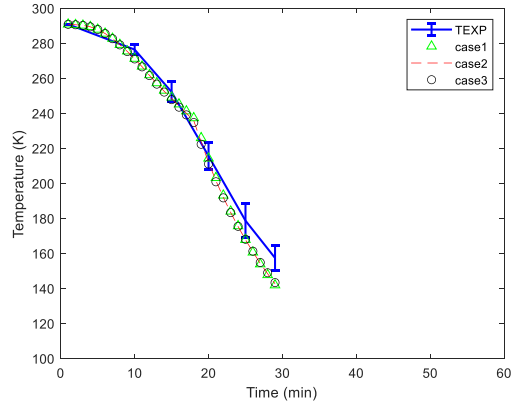

Condition #8: CO_2 with 20% N_2 and 0.1% ethanol	%Error
Calculated Composition 1: 56 moles% CO_2-42 moles% CH_4 -2 moles% N_2-0.05 mole% C_2H_5OH	1.71%
Calculated Composition 2: 50 moles% CO_2-48 moles% CH_4 -2 moles% N_2-0.05 mole% C_2H_5OH	2.55%
Calculated Composition 3: 46 moles% CO_2-52 moles% CH_4 -2 moles% N_2-0.05 mole% C_2H_5OH	2.89%

(h)

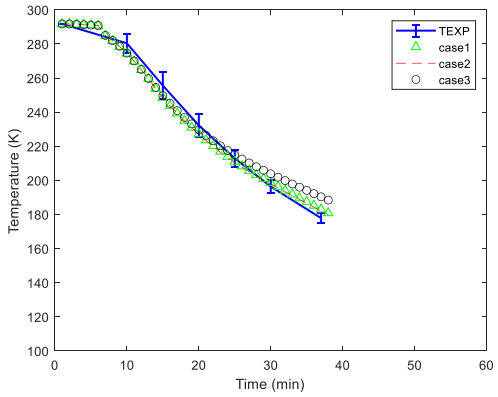

Condition #9: CO_2 with 20% N_2 and 9% ethanol	%Error
Calculated Composition 1: 77.8 moles% CO_2-20 moles% CH_4 -2 moles% N_2-0.2 mole% C_2H_5OH	1.22%
Calculated Composition 2: 74.85 moles% CO_2-23 moles% CH_4 -2 moles% N_2-0.15 mole% C_2H_5OH	1.10%
Calculated Composition 3: 77.9 moles% CO_2-20 moles% CH_4 -2 moles% N_2-0.1 mole% C_2H_5OH	1.23%

(i)

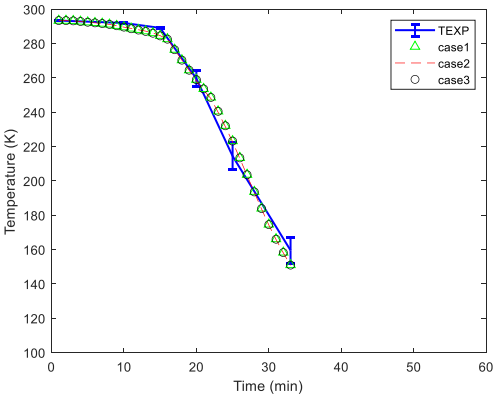

Condition #10: CO_2 with 20% N_2 and 1% ethanol	%Error
Calculated Composition 1: 73 moles% CO_2-24.95 moles% CH_4 -2 moles% N_2-0.05 mole% C_2H_5OH	1.49%
Calculated Composition 2: 72.95 moles% CO_2-25 moles% CH_4 -2 moles% N_2-0.05 mole% C_2H_5OH	1.45%
Calculated Composition 3: 72.8 moles% CO_2-25 moles% CH_4 -2 moles% N_2-0.2 mole% C_2H_5OH	1.50%

(j)

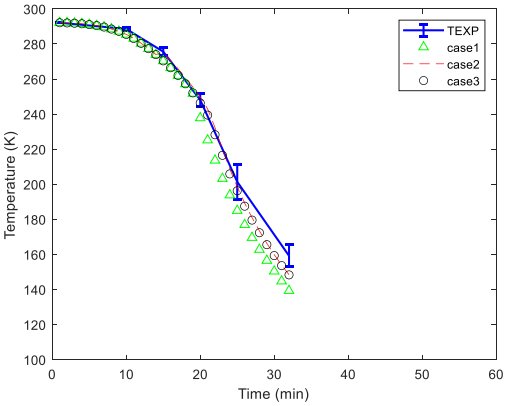

Condition #11: CO_2 with 20% N_2 and 0.01% ethanol	%Error
Calculated Composition 1: 37.99 moles% CO_2-60 moles% CH_4 -2 moles% N_2-0.005 mole% C_2H_5OH	3.20%
Calculated Composition 2: 47.99 moles% CO_2-50 moles% CH_4 -2 moles% N_2-0.005 mole% C_2H_5OH	1.64%
Calculated Composition 3: 41.99 moles% CO_2-56 moles% CH_4 -2 moles% N_2-0.005 mole% C_2H_5OH	2.94%

(k)

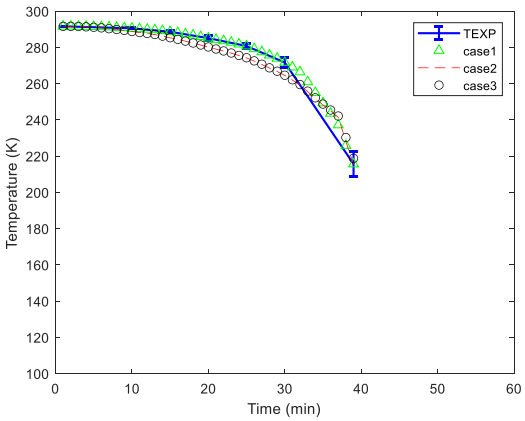

Condition #12: CO_2 with 20% N_2 and 1% NFM	%Error
Calculated Composition 1: 84.8 moles% CO_2-13 moles% CH_4 -2 moles% N_2-0.2 mole% $C_5H_9NO_2$	1.34%
Calculated Composition 2: 87.8 moles% CO_2-10 moles% CH_4 -2 moles% N_2-0.2 mole% $C_5H_9NO_2$	1.23%
Calculated Composition 3: 77.8 moles% CO_2-20 moles% CH_4 -2 moles% N_2-0.2 mole% $C_5H_9NO_2$	2.20%

(l)

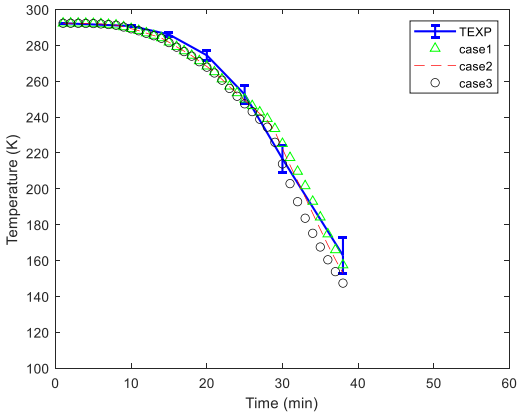

Condition #13: CO_2 with 20% N_2 and 0.01% NFM	%Error
Calculated Composition 1: 76.96 moles% CO_2-21 moles% CH_4 -2 moles% N_2-0.04 mole% $C_5H_9NO_2$	1.55%
Calculated Composition 2: 72.96 moles% CO_2-25 moles% CH_4 -2 moles% N_2-0.04 mole% $C_5H_9NO_2$	1.44%
Calculated Composition 3: 59.96 moles% CO_2-38 moles% CH_4 -2 moles% N_2-0.04 mole% $C_5H_9NO_2$	2.40%

(m)

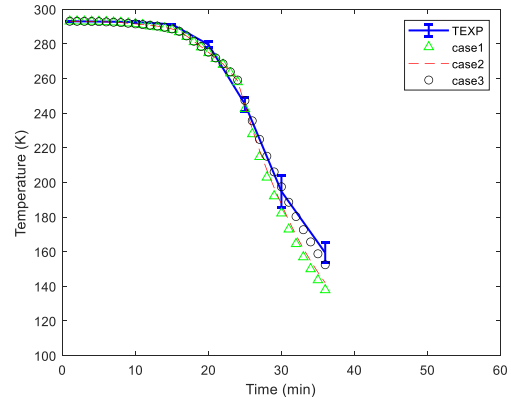

Condition #14: CO_2 with 20% N_2 and 0.1% NFM	%Error
Calculated Composition 1: 77.88 moles% CO_2-20 moles% CH_4 -2 moles% N_2-0.12 mole% $C_5H_9NO_2$	3.16%
Calculated Composition 2: 81.88 moles% CO_2-16 moles% CH_4 -2 moles% N_2-0.12 mole% $C_5H_9NO_2$	2.22%
Calculated Composition 3: 85.88 moles% CO_2-12 moles% CH_4 -2 moles% N_2-0.12 mole% $C_5H_9NO_2$	0.97%

(n)

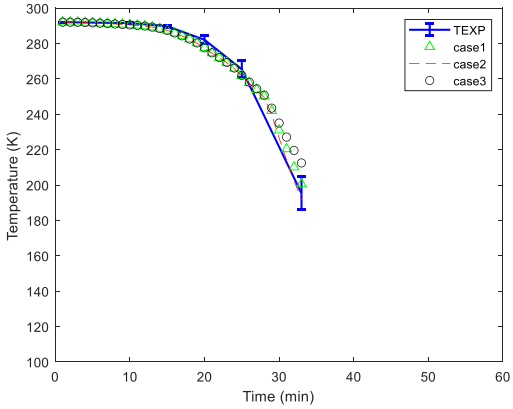

Condition #15: CO_2 with 20% N_2 and 3% NFM	%Error
Calculated Composition 1: 87.88 moles% CO_2-10 moles% CH_4 -2 moles% N_2-0.12 mole% $C_5H_9NO_2$	1.11%
Calculated Composition 2: 83.88 moles% CO_2-14 moles% CH_4 -2 moles% N_2-0.12 mole% $C_5H_9NO_2$	0.85%
Calculated Composition 3: 91.88 moles% CO_2-6 moles% CH_4 -2 moles% N_2-0.12 mole% $C_5H_9NO_2$	1.56%

(o)

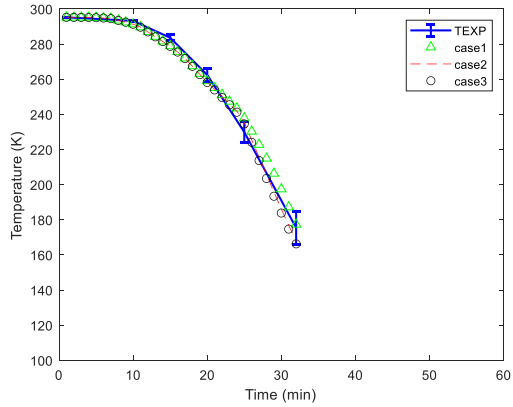

Condition #16: CO_2 with 1% NFM	%Error
Calculated Composition 1: 79.85 moles% CO_2-20 moles% CH_4 -0.15 mole% $C_5H_9NO_2$	1.64%
Calculated Composition 2: 72.85 moles% CO_2-27 moles% CH_4 -0.15 mole% $C_5H_9NO_2$	1.17%
Calculated Composition 3: 70.85 moles% CO_2-29 moles% CH_4 -0.15 mole% $C_5H_9NO_2$	1.20%

(p)

Figure 5.9 The temperature results of the condensation process and the various cases of calculated temperatures along the time (left), and the concluded compositions with the error (right). The standard deviation of experiments is marked (around 4.66 for all the conditions).

After the phase change process starts, the total volume of the mixture is assumed constant with neglecting the local volume change during the phase change of liquid against gas. Though there might be some detailed changes occurring locally even when the volume of liquid and solid is much less than the volume of gas. The error bar shown in the figures represents the variation over the averaged datapoints within the interval from the measurements. The averaged error is approximately 3% while the instrumentation uncertainty (of the pressure and temperature transducers) is approximately $\pm$ 2%.

All possibilities of combining the percentage of mixed gases with an accuracy of 0.05 molar fraction were considered. According to the temperature and phase change pressures [98], one data point was selected approximately every minute (and the temperature and pressure units were converted to Kelvin and bar). These points were examined using ProPhyPlus software [97]. As previously described, the volume of the mixture is considered constant until the end of the reaction. In ProPhyPlus, the volume is defined as the molar volume, meaning the volume of one mole of gas mixture. Since the composition of the mixture is unknown, the molar volume cannot be calculated simply using the full cylinder volume in the experiment (50 ml). The initial conditions of all the input gas components at the beginning of the process is used as the probable percentage for the molar volume of the corresponding composition. Then, the pressure obtained from the experimental results is placed in the software at each point and the temperature corresponding to this composition percentage is calculated. This calculation is performed at one minute per point for each pressure and its corresponding temperature for the hypothetical system.

After the temperature of the desired points were calculated, a smoothing function was used to eliminate the noise. The error in terms of absolute average deviation compared to experiments was calculated using the following equation [99]:

$$Error\% = \sum \left\{ \left(\frac{|T\exp - aTcal|}{aTcal} \right) \right\} \times 100;\ at\ a = 1 \quad (76)$$

Finally, the gas composition percentage combination with the lowest error rate was considered as the most probably actual mixture. The calculated temperature graph is higher than the experimental temperature over time but when the composition of the calculated mixture approaches those of the experiment the calculated temperature aligns with the experimental temperature. The level of compliance is measured by the error function mentioned above. As shown in the Figure 5.9, the highest degree of adaptation is at the beginning of the process because at this temperature and pressure there is no phase change and there is no liquid phase, so the considered volume has the lowest error. As the process progresses, the more phase change occurs, the more liquid volume is produced, and therefore the volume of the gaseous phase is not constant. This causes small errors in calculating the volume, which has a small effect on the final results for gas compositions. Other challenges to calculate the composition of gases in hydrate samples during the pressure reduction (from ~100 bar to 1 bar) and cooling temperature (from 1°C to -25°C) are the possible re-formation of more CH_4 gas into hydrate and solubility of CO_2 into the CH_4 gas phase in the A section (top of the media bed). There are also effects of a possible ice region on that temperature for trapping gases instead of hydrate before the dissociation process. Fortunately,

based on the comparison between calculated and measured temperatures, these potential effects appear to be very small in the experiment, and the results show consistent and reliable outcome.

CHAPTER 6: CONCLUSION AND FUTURE WORK

6.1 Conclusion

The experimental results illustrate that 20 moles% N_2 and 1 mole% NFM with CO_2 liquid injection is more effective for conversion between CO_2/CH_4 hydrate than other conditions, and adding more N_2 beyond 20% reduces conversion effectiveness. Maximum conversion in this study was 88 moles% of CO_2, and 2 moles% N_2 taking the place of methane hydrate in large and small cavities after dissociating the sample of gas hydrates. This work uses a calibrated thermodynamic condensation analysis method (with gas chromatography confirmation) for analyzing gas compositions by monitoring gas pressure and temperature. The idea is to provide accurate composition results with an inexpensive and unique method, and within an uncertainty of 4% in comparison to what is achievable with a GC analysis. The approach of analyzing the contents by monitoring the condensation process is reliable and accurate. The results are encouraging in showing that CO_2 drives the conversion through formation of new hydrate so only a small pressure difference may be needed between the injection well for CO_2 and a producing well capturing the released CH_4.

Adding limited amounts of N_2 increases the dynamics of CO_2/CH_4 hydrate swapping. When we used pure CO_2, there was limited conversion. This appears to be because partial CO_2 hydrate blocks flow channels and there is slow permeability associated with injecting CO_2 into the water wetting sediments. Addition of N_2 (~20 moles%) to the CO_2 has been one way to reduce these problems, but not completely. We need to add a small concentration of surfactants (~1 mole%) to the mixture. The surfactant addition will break the hydrate film from new CO_2 hydrate

at the interface, which increases mass transfer into the hydrate cages and liquid water for forming the new hydrates. Limited concentration of N_2 and surfactants are advantageous since the N_2 can remove the methane gas from small cavities of structure I hydrate, and surfactant can break the hydrate film at the interface to allow CO_2 to penetrate through the large cavities.

As was discussed in chapter 3, the formation of new hydrate from free pore water and incoming CO_2 mixture will release more heat than is needed to dissociate *in situ* CH_4 hydrate. The addition of more than 30 moles% N_2 appears to be less favorable for water to create hydrate in terms of liquid water chemical potential versus hydrate water chemical potential.

6.2 Future work

The experimental results are the beginning of connecting the physical understanding of hydrate formation and the practical potential of increasing hydrate formation and dissociation rates. This dissertation includes the first direct experimental evaluation of these processes, and further study using a similar experiment will be valuable to explore many of the other variables involved in hydrate dynamics.

- There is a need for developing new environmentally friendly surfactants because NFM is not acceptable as a surfactant from an environmental point of view.
- Further understanding of CO_2 hydrate stability in an unsaturated environment (using seawater/supersaline solutions) is needed.
- Additional information regarding the role of mineral surfaces in overall hydrate nucleation rate will be beneficial. In particular, it will be important to understand if added surfactants can decrease the efficiency of hydrate nucleation towards mineral surfaces.

- Exploring the crystal morphology and impact for hydrate growth patterns in sediments with different materials and sizes are important because hydrates in nature form in a wide variety of conditions and regions.

BIBLIOGRAPHY

[1] Makogon, Jurij Fedorovič. *Hydrates of Hydrocarbons*. Pennwell Publ, 1997.

[2] Kinnari, Keijo et al. "Hydrate Plug Formation Prediction Tool – an Increasing Need for Flow Assurance in the Oil Industry". *International Conference on Gas Hydrates (ICGH) (6Th: 2008)*, 2008, Accessed 7 Aug 2021.

[3] Gunn, D. A. et al. "Towards Improved Ground Models for Slope Instability Evaluations Through Better Characterization of Sediment-Hosted Gas-Hydrates". *Terra Nova*, vol 14, no. 6, 2002, pp. 443-451. *Wiley*, doi:10.1046/j.1365-3121.2002.00451. x.

[4] Moridis, G.J. "Numerical Studies of Gas Production from Methane Hydrates". *SPE Journal*, vol 8, no. 04, 2003, pp. 359-370. *Society of Petroleum Engineers (SPE)*, doi:10.2118/87330-pa.

[5] Javanmardi, J. et al. "Economic Evaluation of Natural Gas Hydrate as an Alternative for Natural Gas Transportation". *Applied Thermal Engineering*, vol 25, no. 11-12, 2005, pp. 1708-1723. *Elsevier BV*, doi: 10.1016/j.applthermaleng.2004.10.009.

[6] Sloan, E. Dendy. "Fundamental Principles and Applications of Natural Gas Hydrates". *Nature*, vol 426, no. 6964, 2003, pp. 353-359. *Springer Science and Business Media LLC*, doi:10.1038/nature02135.

[7] Chatti, Imen et al. "Benefits and Drawbacks of Clathrate Hydrates: a Review of Their Areas of Interest". *Energy Conversion and Management*, vol 46, no. 9-10, 2005, pp. 1333-1343. *Elsevier BV*, doi: 10.1016/j.enconman.2004.06.032.

[8] Kwan, Jonathan T, and Charles, E. Taylor. *Advances in the Study of Gas Hydrates*. Kluwer Academic/Plenum, 2004.

[9] Adams, Eric et al. "Letter: International Field Experiment on Ocean Carbon Sequestration". *Environmental Science & Technology*, vol 36, no. 21, 2002, pp. 399A-399A. *American Chemical Society (ACS)*, doi:10.1021/es022442b.

[10] Brewer, Peter G. et al. "Gas Hydrate Formation in the Deep Sea: in situ Experiments with Controlled Release of Methane, Natural Gas, and Carbon Dioxide". *Energy & Fuels*, vol 12, no. 1, 1998, pp. 183-188. *American Chemical Society (ACS)*, doi:10.1021/ef970172q.

[11] Khawaji, Akili D. et al. "Advances in Seawater Desalination Technologies". *Desalination*, vol 221, no. 1-3, 2008, pp. 47-69. *Elsevier BV*, doi: 10.1016/j.desal.2007.01.067.

[12] Kavvadias, K.C., and Khamis, I. "The IAEA DEEP Desalination Economic Model: a Critical Review". *Desalination*, vol 257, no. 1-3, 2010, pp. 150-157. *Elsevier BV*, doi: 10.1016/j.desal.2010.02.032.

[13] Sloan, E. Dendy, and Koh, Carolyn. *Clathrate Hydrates of Natural Gases*. CRC Press, 2008.

[14] Makogon, Y.F. et al. "Natural Gas-Hydrates — a Potential Energy Source for the 21St Century". *Journal of Petroleum Science and Engineering*, vol 56, no. 1-3, 2007, pp. 14-31. *Elsevier BV*, doi: 10.1016/j.petrol.2005.10.009.

[15] "Stability Conditions for Gas Hydrates | GRID-Arendal". *Grida.No*, 2021, https://www.grida.no/resources/6625.

[16] Maslin, Mark et al. "Gas Hydrates: Past and Future Geohazard?". *Philosophical Transactions of the Royal Society A: Mathematical, Physical and Engineering Sciences*, vol 368, no. 1919, 2010, pp. 2369-2393. *The Royal Society*, doi:10.1098/rsta.2010.0065.

[17] Adewumi, Michael. "The Hydrate Problem | PNG 520: Phase Behavior of Natural Gas and Condensate Fluids". *E-Education.Psu.Edu*, 2021, https://www.e-education.psu.edu/png520/m21_p3.html.

[18] Ripmeester, John A. et al. "A New Clathrate Hydrate Structure". *Nature*, vol 325, no. 6100, 1987, pp. 135-136. *Springer Science and Business Media LLC*, doi:10.1038/325135a0.

[19] "Center for gas hydrate research", Herriot-Watt University, Institute of Petroleum Engineering, 2010, http://www.pet.hw.ac.uk/research/hydrate/index.cfm.

[20] Chong, Zheng Rong et al. "Review of Natural Gas Hydrates as an Energy Resource: Prospects and Challenges". *Applied Energy*, vol 162, 2016, pp. 1633-1652. *Elsevier BV*, doi: 10.1016/j.apenergy.2014.12.061.

[21] Aktemur, Cenker. "An Overview of Natural Gas as an Energy Source for Various Purposes". *International Journal of Engineering Technologies IJET*, vol 3, no. 3, 2017, pp. 91-104. *International Journal of Engineering Technologies*, doi:10.19072/ijet.300750.

[22] U.S. Geological Survey. *Natural Gas Hydrates—Vast Resource, Uncertain Future*. 2001, https://pubs.usgs.gov/fs/fs021-01/fs021-01.pdf. Accessed 7 Aug 2021.

[23] Collett, Timothy. "Energy Resource Potential of Natural Gas Hydrates". *AAPG Bulletin*, vol 86, 2002. *American Association of Petroleum Geologists AAPG/Datapages*, doi:10.1306/61eeddd2-173e-11d7-8645000102c1865d.

[24] McIver, Richard. "Abstract: Hydrates of Natural Gas--Important Agent in Geologic Processes". *Archives.Datapages.Com*, 2021, https://archives.datapages.com/data/HGS/vol20/no09/03.htm.

[25] "*Cosmosmagazine*, 2019", https://cosmosmagazine.com/climate/ancient-stores-of-methane-may-not-be-a-threat-study-suggests/. Accessed 7 Aug 2021.

[26] Lelieveld, Jos, and Crutzen, Paul J. "Indirect Chemical Effects of Methane on Climate Warming". *Nature*, vol 355, no. 6358, 1992, pp. 339-342. *Springer Science and Business Media LLC*, doi:10.1038/355339a0.

[27] Riemer, P. "Greenhouse Gas Mitigation Technologies, an Overview of the CO2 Capture, Storage and Future Activities of the IEA Greenhouse Gas R&D Program". *Fuel and Energy Abstracts*, vol 37, no. 3, 1996, p. 222. *Elsevier BV*, doi:10.1016/0140-6701(96)89132-6.

[28] Adams, Eric, and Caldeira, Ken. "Ocean Storage of CO2". *People.Ucsc.Edu*, 2008, https://people.ucsc.edu/~mdmccar/migrated/ocea213/readings/15_GeoEngineer/C_sequestration/adams_2008_Elements_CALDERIA_Ocean_CO2_Storeage.pdf.

[29] Cameron, E et al. "Estimating Carbon Storage Resources in Offshore Geologic Environments"; NETL-TRS-14-2018; NETL Technical Report Series; U.S. Department of Energy, National Energy Technology Laboratory: Albany, OR, 2018; p 32. DOI: 10.18141/1464460.

[30] "Monterey Bay Aquarium Research Institute (Annual Report)". *Mbari.Org*, 2010, https://www.mbari.org/wp-content/uploads/2015/11/2010ann_rpt.pdf.

[31] Teng, Yihua, and Zhang, Dongxiao. "Long-Term Viability of Carbon Sequestration in Deep-Sea Sediments". *Science Advances*, vol 4, no. 7, 2018, p. eaao6588. *American Association for the Advancement of Science (AAAS)*, doi:10.1126/sciadv. aao6588.

[32] Babu, Ponnivalavan et al. "A Review of Clathrate Hydrate Based Desalination to Strengthen Energy–Water Nexus". *ACS Sustainable Chemistry & Engineering*, vol 6, no. 7, 2018, pp. 8093-8107. *American Chemical Society (ACS)*, doi:10.1021/acssuschemeng.8b01616.

[33] Aregbe, Azeez G. "Gas Hydrate—Properties, Formation and Benefits". *Open Journal of Yangtze Oil and Gas*, vol 02, no. 01, 2017, pp. 27-44. *Scientific Research Publishing, Inc*, doi:10.4236/ojogas.2017.21003.

[34] "U.S. Energy Information Administration (EIA) - Ap". *Eia.Gov*, 2019, https://www.eia.gov/environment/emissions/carbon/.

[35] Cui, Yudong et al. "Review of Exploration and Production Technology of Natural Gas Hydrate". *Advances in Geo-Energy Research*, vol 2, no. 1, 2018, pp. 53-62. *Yandy Scientific Press*, doi:10.26804/ager.2018.01.05.

[36] Bazaluk, Oleg et al. "Research into Dissociation Zones of Gas Hydrate Deposits with a Heterogeneous Structure in the Black Sea". *Energies*, vol 14, no. 5, 2021, p. 1345. *MDPI AG*, doi:10.3390/en14051345.

[37] Konno, Yoshihiro et al. "Key Findings of The World's First Offshore Methane Hydrate Production Test Off the Coast of Japan: Toward Future Commercial Production". *Energy & Fuels*, vol 31, no. 3, 2017, pp. 2607-2616. *American Chemical Society (ACS)*, doi: 10.1021/acs.energyfuels.6b03143.

[38] Kvamme, Bjørn et al. "Stages in the Dynamics of Hydrate Formation and Consequences for Design of Experiments for Hydrate Formation in Sediments". *Energies*, vol 12, no. 17, 2019, p. 3399. *MDPI AG*, doi:10.3390/en12173399.

[39] Oyama, Ai, and Masutani, Stephen. "A Review of the Methane Hydrate Program in Japan". *Energies*, vol 10, no. 10, 2017, p. 1447. *MDPI AG*, doi:10.3390/en10101447.

[40] Tenma, Norio. "Recent Status of Methane Hydrate R&D Program in Japan". In Proceedings of the 11th International Methane Hydrate Research and Development, Corpus Christie, TX, USA, 5–8 December 2017.

[41] Kvamme, Bjørn. "Thermodynamic Limitations of the CO2/N2 Mixture Injected into CH4 Hydrate in the Ignik Sikumi Field Trial". *Journal of Chemical & Engineering Data*, vol 61, no. 3, 2016, pp. 1280-1295. *American Chemical Society (ACS)*, doi: 10.1021/acs.jced.5b00930.

[42] Partain, Roy Andrew. *Environmental Hazards from Offshore Methane Hydrate Operations*. Wolters Kluwer, 2017.

[43] Brewer, P. G. "Direct Experiments on the Ocean Disposal of Fossil Fuel CO2". *Science*, vol 284, no. 5416, 1999, pp. 943-945. *American Association for the Advancement of Science (AAAS)*, doi:10.1126/science.284.5416.943.

[44] Eslamimanesh, Ali et al. "Application of Gas Hydrate Formation in Separation Processes: a Review of Experimental Studies". *The Journal of Chemical Thermodynamics*, vol 46, 2012, pp. 62-71. *Elsevier BV*, doi: 10.1016/j.jct.2011.10.006.

[45] Lee, Huen et al. "Recovering Methane from Solid Methane Hydrate with Carbon Dioxide". *Angewandte Chemie International Edition*, vol 42, no. 41, 2003, pp. 5048-5051. *Wiley*, doi:10.1002/anie.200351489.

[46] Yuan, Qing et al. "Recovery of Methane from Hydrate Reservoir with Gaseous Carbon Dioxide Using a Three-Dimensional Middle-Size Reactor". *Energy*, vol 40, no. 1, 2012, pp. 47-58. *Elsevier BV*, doi: 10.1016/j.energy.2012.02.043.

[47] Kvamme, Bjørn. "Environmentally Friendly Production of Methane from Natural Gas Hydrate Using Carbon Dioxide". *Sustainability*, vol 11, no. 7, 2019, p. 1964. *MDPI AG*, doi:10.3390/su11071964.

[48] Nixon, M F, and Grozic, J LH. "Submarine Slope Failure Due to Gas Hydrate Dissociation: a Preliminary Quantification". *Canadian Geotechnical Journal*, vol 44, no. 3, 2007, pp. 314-325. *Canadian Science Publishing*, doi:10.1139/t06-121.

[49] Francisca, F. et al. "Geophysical and Geotechnical Properties of Near-Seafloor Sediments in the Northern Gulf of Mexico Gas Hydrate Province". *Earth and Planetary Science Letters*, vol 237, no. 3-4, 2005, pp. 924-939. *Elsevier BV*, doi: 10.1016/j.epsl.2005.06.050.

[50] Kvamme, Bjørn et al. "Hydrate Nucleation, Growth, and Induction". *ACS Omega*, vol 5, no. 6, 2020, pp. 2603-2619. *American Chemical Society (ACS)*, doi:10.1021/acsomega.9b02865.

[51] Kumar, Asheesh et al. "Role of Surfactants in Promoting Gas Hydrate Formation". *Industrial & Engineering Chemistry Research*, vol 54, no. 49, 2015, pp. 12217-12232. *American Chemical Society (ACS)*, doi: 10.1021/acs.iecr.5b03476.

[52] Kaczorek, Ewa et al. "The Impact of Biosurfactants on Microbial Cell Properties Leading to Hydrocarbon Bioavailability Increase". *Colloids and Interfaces*, vol 2, no. 3, 2018, p. 35. *MDPI AG*, doi:10.3390/colloids2030035.

[53] Selvåg, Juri et al. "Molecular Dynamics Study of Morpholines at Water – Carbon Dioxide Interfaces". *Fluid Phase Equilibria*, vol 485, 2019, pp. 44-60. *Elsevier BV*, doi: 10.1016/j.fluid.2018.12.004.

[54] Schoderbek, David et al. “ConocoPhillips Gas Hydrate Production Test Final Technical Report” https://www.osti.gov/servlets/purl/1123878.

[55] Saeidi, Navid et al. “Experimental Studies on Combined Production of CH_4 and Safe Long-Term Storage of CO_2 in the Form of Solid Hydrate in Sediment”. *Physical Chemistry Chemical Physics*, 2021, **23**, 23313 – 23324, doi: 10.1039/d1cp03239a.

[56] Chien, Yu-Chien, and Dunn-Rankin, Derek. "Combustion Characteristics of Methane Hydrate Flames". *Energies*, vol 12, no. 10, 2019, p. 1939. *MDPI AG*, doi:10.3390/en12101939.

[57] Kvamme, Bjørn, and Tanaka, Hideki. "Thermodynamic Stability of Hydrates for Ethane, Ethylene, and Carbon Dioxide". *The Journal of Physical Chemistry*, vol 99, no. 18, 1995, pp. 7114-7119. *American Chemical Society (ACS)*, doi:10.1021/j100018a052.

[58] Van der Waals, J.H., Platteeuw, J.C., “Clathrate solutions. Adv. Chem. Phys.”, Vol. 2 (ed I. Prigogine), John Wiley & Sons Inc, 1959.

[59] Kvamme, Bjørn et al. "The Influence of Gas-Gas Interactions on the Langmuir Constants for some Natural Gas Hydrates". *Fluid Phase Equilibria*, vol 90, no. 1, 1993, pp. 15-44. *Elsevier BV*, doi:10.1016/0378-3812(93)85002-4.

[60] Kvamme, Bjørn et al. "Consistent Enthalpies of the Hydrate Formation and Dissociation Using Residual Thermodynamics". *Journal of Chemical & Engineering Data*, vol 64, no. 8, 2019, pp. 3493-3504. *American Chemical Society (ACS)*, doi: 10.1021/acs.jced.9b00276.

[61] Kvamme, Bjørn et al. "Why Should We Use Residual Thermodynamics for Calculation of Hydrate Phase Transitions?". *Energies*, vol 13, no. 16, 2020, p. 4135. *MDPI AG*, doi:10.3390/en13164135.

[62] Kvamme, Bjørn. "A Unified Nucleation Theory for the Kinetics of Hydrate Formation". *Annals of the New York Academy of Sciences*, vol 912, no. 1, 2006, pp. 496-501. *Wiley*, doi:10.1111/j.1749-6632.2000.tb06804. x.

[63] Svandal, Atle. "Modeling Hydrate Phase Transitions Using Mean-field Approaches". Ph.D. Thesis, University of Bergen: 2006.

[64] Qorbani, Khadijeh et al. "Utilizing Non-Equilibrium Thermodynamics and Reactive Transport to Model CH4 Production from the Nankai Trough Gas Hydrate Reservoir". *Energies*, vol 10, no. 7, 2017, p. 1064. *MDPI AG*, doi:10.3390/en10071064.

[65] Falenty, A. et al. "Kinetics of CO2-Hydrate Formation from Ice Powders: Data Summary and Modeling Extended to Low Temperatures". *The Journal of Physical Chemistry C*, vol 117, no. 16, 2013, pp. 8443-8457. *American Chemical Society (ACS)*, doi:10.1021/jp310972b.

[66] Kuhs, Werner F. et al. "Formation of Methane Hydrate from Polydisperse Ice Powders". *The Journal of Physical Chemistry B*, vol 110, no. 26, 2006, pp. 13283-13295. *American Chemical Society (ACS)*, doi:10.1021/jp061060f.

[67] Tuckerman, Mark. *Statistical Mechanics and Molecular Simulations*. [Verlag Nicht Ermittelbar], 2007.

[68] Plimpton, Steve. "Fast Parallel Algorithms for Short-Range Molecular Dynamics". *Journal of Computational Physics*, vol 117, no. 1, 1995, pp. 1-19. *Elsevier BV*, doi:10.1006/jcph.1995.1039.

[69] Martínez, L. et al. "PACKMOL: A Package for Building Initial Configurations for Molecular Dynamics Simulations". *Journal of Computational Chemistry*, vol 30, no. 13, 2009, pp. 2157-2164. *Wiley*, doi:10.1002/jcc.21224.

[70] Jorgensen, William L., and Madura, Jeffry D. "Temperature and Size Dependence for Monte Carlo Simulations of TIP4P Water". *Molecular Physics*, vol 56, no. 6, 1985, pp. 1381-1392. *Informa UK Limited*, doi:10.1080/00268978500103111.

[71] Kvamme, Bjørn. "Kinetics of Hydrate Formation, Dissociation and Reformation". *Chemical Thermodynamics and Thermal Analysis*, vol 1-2, 2021, p. 100004. *Elsevier BV*, doi: 10.1016/j.ctta.2021.100004.

[72] Kvamme, Bjørn, and Clarke, Matthew. "Hydrate Phase Transition Kinetic Modeling for Nature and Industry–where are we and where do we go?". *Energies*, vol 14, no. 14, 2021, p. 4149. *MDPI AG*, doi:10.3390/en14144149.

[73] Zarifi, Mojdeh et al. "Modeling Heat Transport in Systems of Hydrate-Filled Sediments Using Residual Thermodynamics and Classical Nucleation Theory". *Applied Sciences*, vol 11, no. 9, 2021, p. 4124. *MDPI AG*, doi:10.3390/app11094124.

[74] Kvamme, Bjørn. "Enthalpies of Hydrate Formation from Hydrate Formers Dissolved in Water". *Energies*, vol 12, no. 6, 2019, p. 1039. *MDPI AG*, doi:10.3390/en12061039.

[75] Tumba, Kaniki et al. "Phase Equilibria of Methane and Carbon Dioxide Clathrate Hydrates in the Presence of Aqueous Solutions of Tributylmethylphosphonium Methylsulfate Ionic Liquid". *Journal of Chemical & Engineering Data*, vol 56, no. 9, 2011, pp. 3620-3629. *American Chemical Society (ACS)*, doi:10.1021/je200462q.

[76] Kvamme, Bjørn et al. "Hydrate—A Mysterious Phase or Just Misunderstood?". *Energies*, vol 13, no. 4, 2020, p. 880. *MDPI AG*, doi:10.3390/en13040880.

[77] Max, Michael D, and Johnson, Arthur H. *Exploration and Production of Oceanic Natural Gas Hydrate*. Springer International Publishing, 2019.

[78] Chejara, Ashok. "Gas Hydrates in Porous Media: CO2 Storage and CH4 Production". Ph.D. Thesis, University of Bergen, 2012.

[79] Jemai, Khaled. "Modeling Hydrate Phase Transitions in Porous Media Using a Reactive Transport Simulator". Ph.D. Thesis, University of Bergen, 2014.

[80] Kvamme, Bjørn et al. "Hydrate Production Philosophy and Thermodynamic Calculations". *Energies*, vol 13, no. 3, 2020, p. 672. *MDPI AG*, doi:10.3390/en13030672.

[81] Qorbani, Khadijeh. "Non-Equilibrium Modelling of Hydrate Phase Transition Kinetics in Sediments". Ph.D. Thesis, University of Bergen, 2017.

[82] Capillary Rise - Surface Tension | Solved Problems (concepts-of-physics.com)

[83] Babu, Ponnivalavan et al. "Morphology of Methane Hydrate Formation in Porous Media". *Energy & Fuels*, vol 27, no. 6, 2013, pp. 3364-3372. *American Chemical Society (ACS)*, https://doi.org/10.1021/ef4004818.

[84] Kowalsky, Michael B., and Moridis, George J. "Comparison of Kinetic and Equilibrium Reaction Models in Simulating Gas Hydrate Behavior in Porous Media". *Energy Conversion and Management*, vol 48, no. 6, 2007, pp. 1850-1863. *Elsevier BV*, https://doi.org/10.1016/j.enconman.2007.01.017.

[85] Li, Bo et al. "Kinetic Studies of Methane Hydrate Formation in Porous Media Based on Experiments in a Pilot-Scale Hydrate Simulator and a New Model". *Chemical Engineering Science*, vol 105, 2014, pp. 220-230. *Elsevier BV*, https://doi.org/10.1016/j.ces.2013.11.016.

[86] Pan, Haojie et al. "Quantification of Gas Hydrate Saturation and Morphology Based on a Generalized Effective Medium Model". *Marine and Petroleum Geology*, vol 113, 2020, p. 104166. *Elsevier BV*, https://doi.org/10.1016/j.marpetgeo.2019.104166.

[87] Nazridoust, Kambiz, and Ahmadi, Goodarz. "Computational Modeling of Methane Hydrate Dissociation in a Sandstone Core". *Chemical Engineering Science*, vol 62, no. 22, 2007, pp. 6155-6177. *Elsevier BV*, https://doi.org/10.1016/j.ces.2007.06.038.

[88] Linga, Praveen et al. "Gas Hydrate Formation in a Variable Volume Bed of Silica Sand Particles". *Energy & Fuels*, vol 23, no. 11, 2009, pp. 5496-5507. *American Chemical Society (ACS)*, https://doi.org/10.1021/ef900542m.

[89] Kvamme, Bjørn et al. "Routes to Hydrate Formation from Water Dissolved in Gas and Impact of Mineral Surfaces". *Petroleum*, vol 7, no. 4, 2021, pp. 385-401. *Elsevier BV*, https://doi.org/10.1016/j.petlm.2021.10.012.

[90] Chong, Zheng Rong et al. "Size Effect of Porous Media on Methane Hydrate Formation and Dissociation in an Excess Gas Environment". *Industrial & Engineering Chemistry Research*, vol 55, no. 29, 2015, pp. 7981-7991. *American Chemical Society (ACS)*, https://doi.org/10.1021/acs.iecr.5b03908.

[91] Chuvilin, Evgeny, and Bukhanov, Boris. "Thermal Conductivity of Frozen Sediments Containing Self-Preserved Pore Gas Hydrates at Atmospheric Pressure: An Experimental Study". *Geosciences*, vol 9, no. 2, 2019, p. 65. *MDPI AG*, https://doi.org/10.3390/geosciences9020065.

[92] Benmesbah, Fatima Doria et al. "Methane Hydrate Formation and Dissociation in Sand Media: Effect of Water Saturation, Gas Flowrate and Particle Size". *Energies*, vol 13, no. 19, 2020, p. 5200. *MDPI AG*, https://doi.org/10.3390/en13195200.

[93] Ge, Bin-Bin et al. "Influence of Water Saturation and Particle Size on Methane Hydrate Formation and Dissociation in a Fixed Bed of Silica Sand". *Energy Procedia*, vol 158, 2019, pp. 5402-5407. *Elsevier BV*, https://doi.org/10.1016/j.egypro.2019.01.623.

[94] Lyu, Xin et al. "Fundamental Characteristics of Gas Hydrate-Bearing Sediments in the Shenhu Area, South China Sea". *Frontiers In Energy*, vol 15, no. 2, 2020, pp. 367-373. *Springer Science And Business Media LLC*, https://doi.org/10.1007/s11708-020-0714-z.

[95] Redlich, Otto., and Kwong, J. N. S. "On the Thermodynamics of Solutions. V. An Equation of State. Fugacities of Gaseous Solutions.". *Chemical Reviews*, vol 44, no. 1, 1949, pp. 233-244. *American Chemical Society (ACS)*, https://doi.org/10.1021/cr60137a013.

[96] Soave, Giorgio. "Equilibrium Constants from a Modified Redlich-Kwong Equation of State". *Chemical Engineering Science*, vol 27, no. 6, 1972, pp. 1197-1203. *Elsevier BV*, https://doi.org/10.1016/0009-2509(72)80096-4.

[97] "Prophyplus Software | Prosim". *Prosim.Net*, 2021, https://www.prosim.net/en/product/prophyplus-thermodynamic-calculations/.

[98] Predel, Bruno. *Phase Diagrams and Heterogeneous Equilibria*. Springer, 2010.

[99] Kader, Gary D. "Means and Mads". *Mathematics Teaching in the Middle School*, vol 4, no. 6, 1999, pp. 398-403. *National Council of Teachers of Mathematics*, https://doi.org/10.5951/mtms.4.6.0398.

APPENDIX A: EXTRA CALCULATIONS

a. Volume for each section of the high-pressure vessel

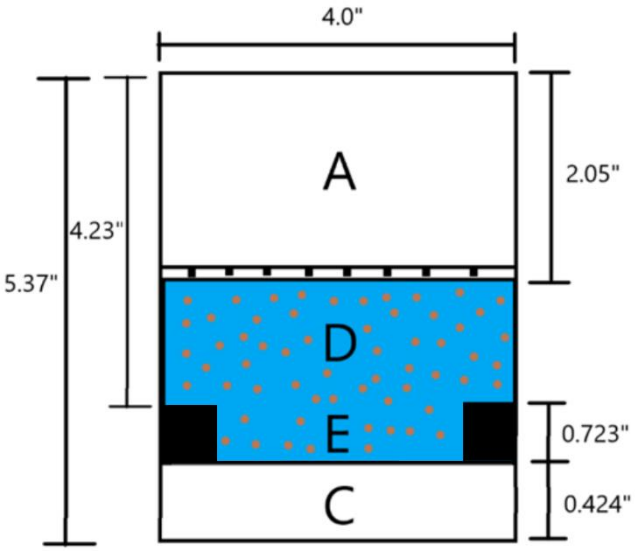

Volume of cylinder: $\pi r^2 h$

$$V_C = \pi \times (5.08cm)^2 \times (1.077cm) = 87.32cm^3$$
$$V_E = \pi \times (3.218cm)^2 \times (1.836cm) = 59.73cm^3$$
$$V_D = \pi \times (5.08cm)^2 \times (3.378cm) = 273.86cm^3$$
$$V_A = \pi \times (5.08cm)^2 \times (7.366cm) = 597.18cm^3$$
$$V_{total} = 1018.1cm^3$$

b. Calculation of mole number of each gas in the experiment

Molar Mass of Methane: $16.04\frac{gr}{mol}$

Density of Methane Gas: $\rho = 0.656\frac{kg}{m^3}$

Number of Moles of Methane: $\frac{51.5gr}{16.09\frac{gr}{mol}} = 3.210moles$

Molar Mass of Water: $18.015\frac{gr}{mol}$

Density of Liquid Water: $\rho = 1.0\frac{gr}{cm^3}$

Number of Moles of Water: $\frac{132gr}{18.01528\frac{gr}{mole}} = 7.325moles$

Molar Mass of Carbon Dioxide: $44.01\frac{gr}{mol}$

Density of Liquid Carbon Dioxide: $0.95\frac{gr}{ml}$

Number of Moles of Carbon Dioxide: $\frac{200gr}{44.01\frac{gr}{mole}} = 4.544moles$

$$\rho = \frac{m}{V} \rightarrow V = \frac{200gr}{0.95\frac{gr}{mL}} = 210.52mL$$

c. RCB/Khuram code for calculating the exchange process from University of Bergen

This part of the results is based on the RCB/Khuram computation code utilized during six-month internship at the University of Bergen as a visiting scholar. It is planned for future publication.

1. Experiment 1. 1 mole per cent NFM, 4.544 mole CO_2, 0.9088 moles N_2 added.

1.1 Creation of CH_4 hydrate

The experimental cell contains of three sections. The gas section on top (A) is 575 cm^3, the water filled section (B) in the middle is 132.18 cm^3 and in the hydrate analysis this section is split in two equal parts in which we denote the upper part as H1 (volume 66.09 cm^3) and characterized by temperature T3. The second part is denoted as H2 (volume 66.09 cm^3) and characterized by temperature T2. The lower section C is 87.32 cm^3 and characterized by temperature T1.

At the end of hydrate formation, the experimental conditions (see Table 1 below) implies high mole numbers of CH_4 in sections A and C. The remaining CH_4 will limit conversions of CH_4 in section B. Based on the hydrate water and liquid water at the end of hydrate formation the hydrate saturation is roughly 64% for this particular case.

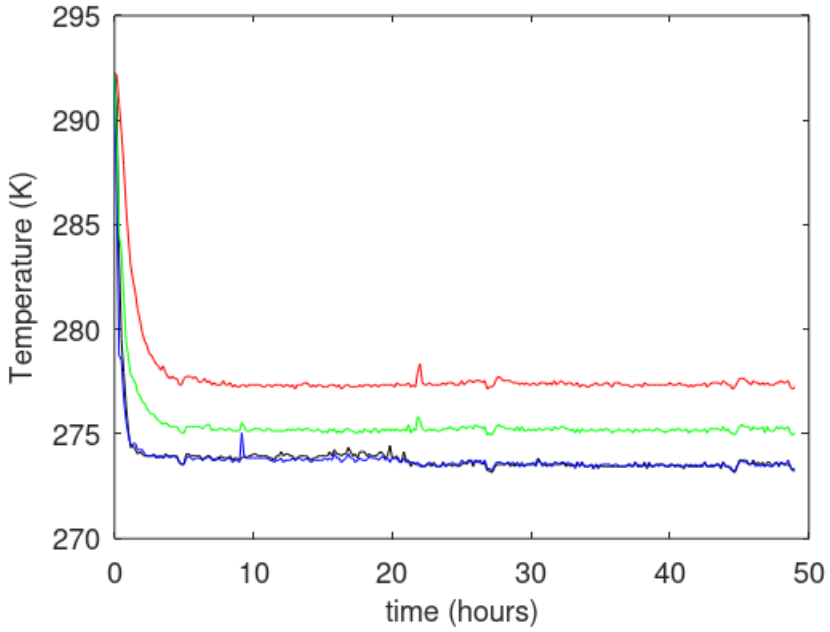

Figure 1. Temperature profiles during formation of CH_4 hydrate as function of experimental time in hours. Mole numbers methane in cell is 3.2102 and mole numbers of water in cell is 7.3252. T1 is black, T2 is blue, T3 is green and T4 is red.

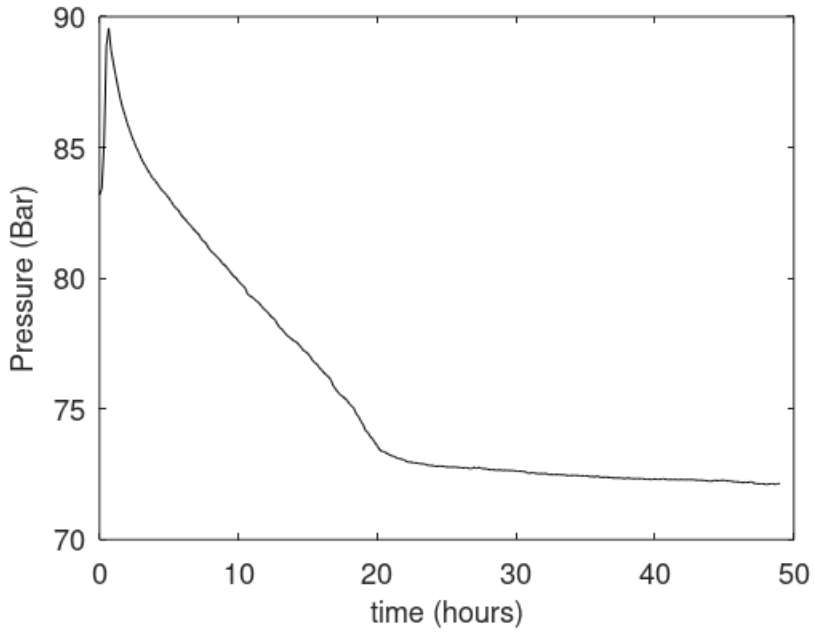

Figure 2. Pressure profile during formation of CH_4 hydrate as function of experimental time in hours. Mole numbers methane in cell is 3.2102 and mole numbers of water in cell is 7.3252.

Table 1. Final balance after formation of CH_4. ΔG^H is Gibbs free energy for hydrate formation in the two sections of B. Z is CH_4 compressibility factor for each of the two gas filled sections. N is mole numbers. Superscript H is hydrate and superscript aq denote liquid water. Subscript H_2O is water and subscript CH_4 is methane.

Sec	T(K)	P(bar)	ΔG^H (kJ/mole)	Z	$x^H_{CH_4}$	ρ^H (mole/m^3)	$N^H_{H_2O}$ (moles)	$N^{aq}_{H_2O}$ (moles)	N_{CH_4} (moles)
A	277.25	72.14		.8526					2.1104
H1	275.05	72.14	-.3545		.1422	51406	2.3188	1.3438	.3845
H2	273.35	72.14	-.4235		.1428	51442	2.3188	1.3438	.3864
C	273.35	72.14		.8432					.3288

Pressure reduction prior to gas injection reduces temperature and gives favorable conditions for further hydrate formation (see table 2). At those conditions water is the limiting component, and it is assumed that remaining liquid water is consumed to CH_4 hydrate. Conditions in the experimental cell prior to injection of CO_2/N_2/NFM are given in table 2. Gibbs free energy is favorable for hydrate formation and during the 20 minutes of extracting CH_4 it is assumed that remaining liquid water from the high-pressure condition in table 1 is converted into hydrate. 0.3636 mole CH_4 is extracted and mole numbers CH_4 as hydrate in section B is 1.1885.

Table 2. Final balance after formation of CH_4. ΔG^H is Gibbs free energy for hydrate formation in the two sections of B. Z is CH_4 compressibility factor for each of the two gas filled sections. N is mole numbers and subscript CH_4 is methane.

Sec	T(K)	P(bar)	ΔG^H (kJ/mole)	Z	$x^H_{CH_4}$	ρ^H (mole/m^3)	N_{CH_4} (moles)
A	278.35	48.10		.8984			1.3302
H1	277.15	48.10	-.1159		.1381	51159	.5869
H2	271.35	48.10	-.3120		.1411	51337	.6017
C	271.35	48.10		.8907			.2075

1.2 Injection of CO_2/N_2/NFM

In figure 3 we plot the measured temperature profiles during the injection of CO_2/N_2/NFM and reformation stage. The associated pressure profile is plotted in figure 4.

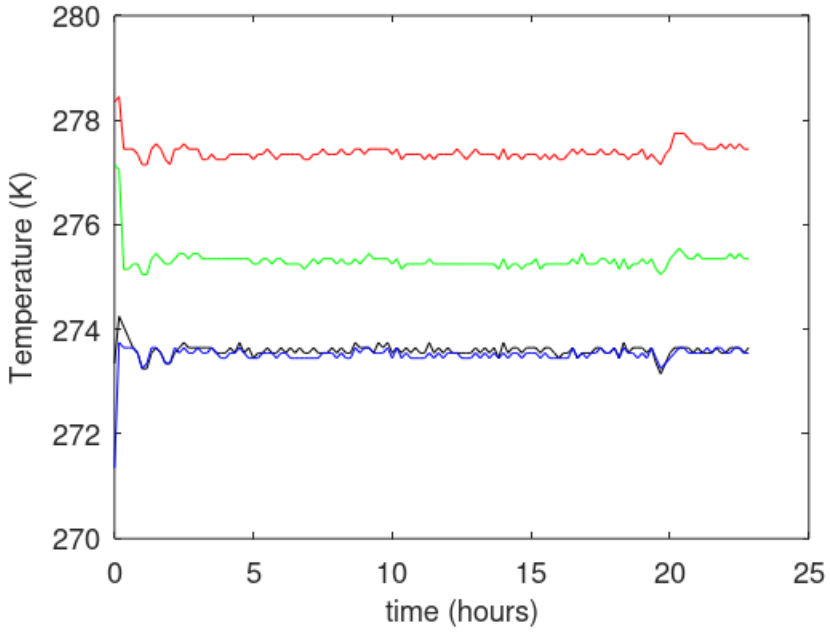

Figure 3. Temperature profiles during injection of CO_2/N_2/NFM and associated reformation processes as function of experimental time in hours. Mole numbers CO_2 injected is 4.544, mole numbers N_2 injected is 0.9088 and 1 mole% NFM injected. Mole numbers of water in cell is 7.3252 and initially in section B since distribution of water in gas is extremely low at experimental conditions.

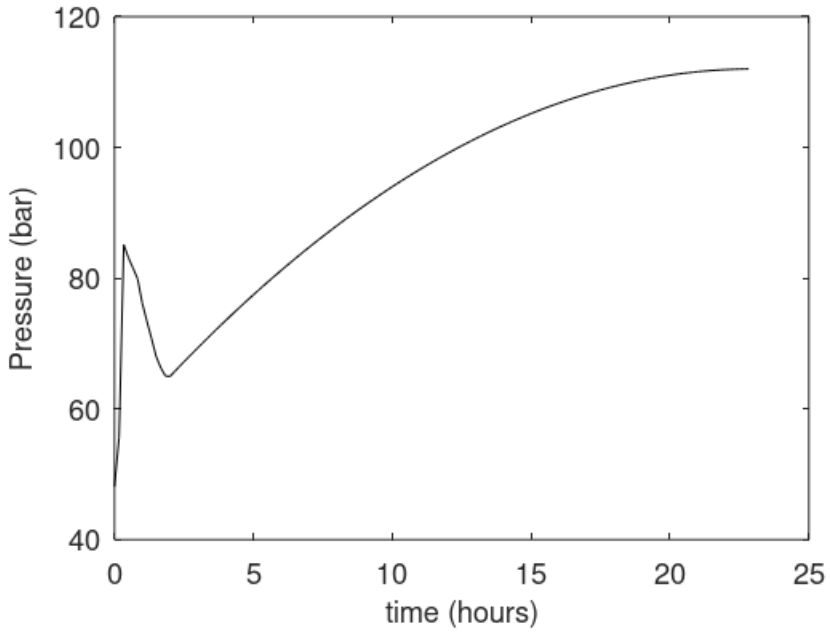

Figure 4. Pressure profile during injection of CO_2/N_2/NFM and associated reformation processes as function of experimental time in hours. Mole numbers CO_2 injected is 4.544, mole numbers N_2 injected is 0.9088 and 1 mole% NFM injected. Mole numbers of water in cell is 7.3252 and initially in section B since distribution of water in gas is extremely low at experimental conditions.

In figure 5 we plot uptake of CO_2 and released CH_4 in the same plot and also in figure 6 we plot released CH_4 per mole CO_2 uptake as a measure of performance. As expected, the performance is almost constant since we expect the NFM to reside on the interface between CO_2 and water and keep the interface free of blocking hydrate as well as ensuring enhanced transport rate across the interface between water and injection gas.

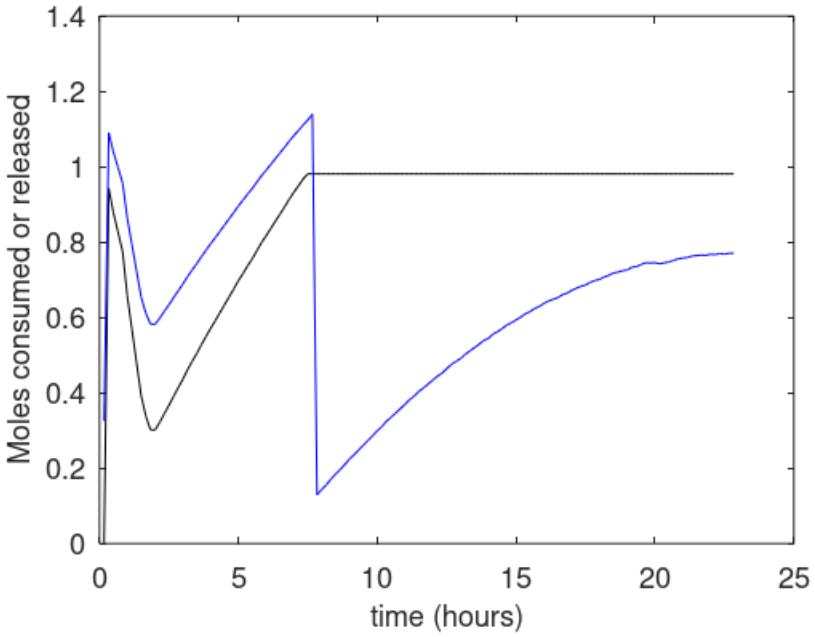

Figure 5. Released CH_4 from CH_4 hydrate is black curve and moles CO_2 consumed to formation of CO_2 hydrate is blue curve.

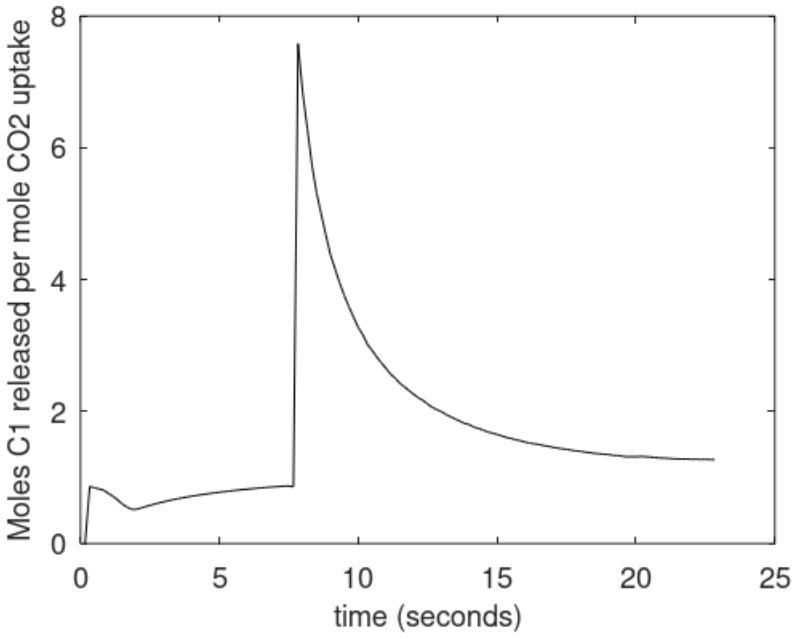

Figure 6. Mole released CH_4 per mole CO_2 uptake.

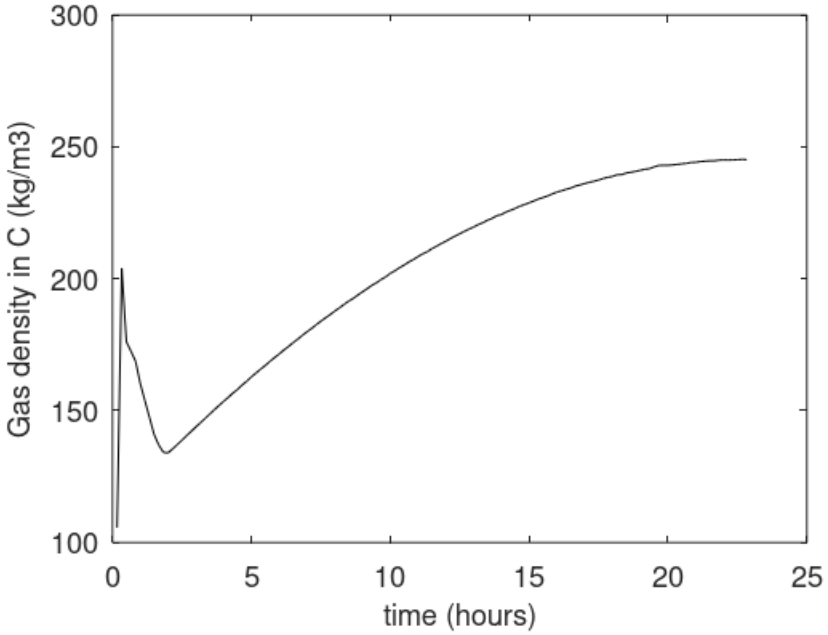

Figure 7. Gas density in section C.

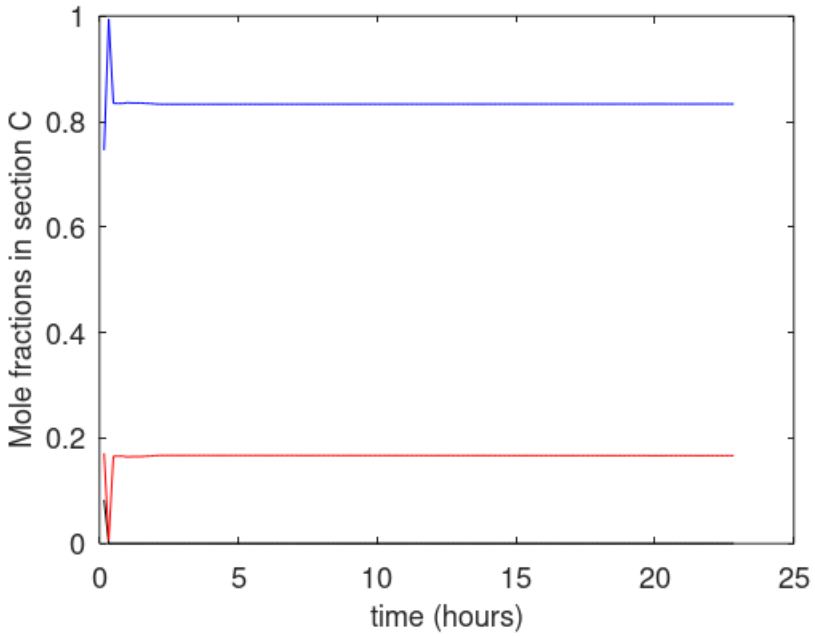

Figure 8. Gas composition in section C in terms of gas mole-fractions. Black is CH_4, blue is CO_2 and red is N_2.

2. Experiment 2. 0.01 mole per cent NFM, 4.544 mole CO_2, 0.9088 moles N_2 added.

2.1 Creation of CH_4 hydrate

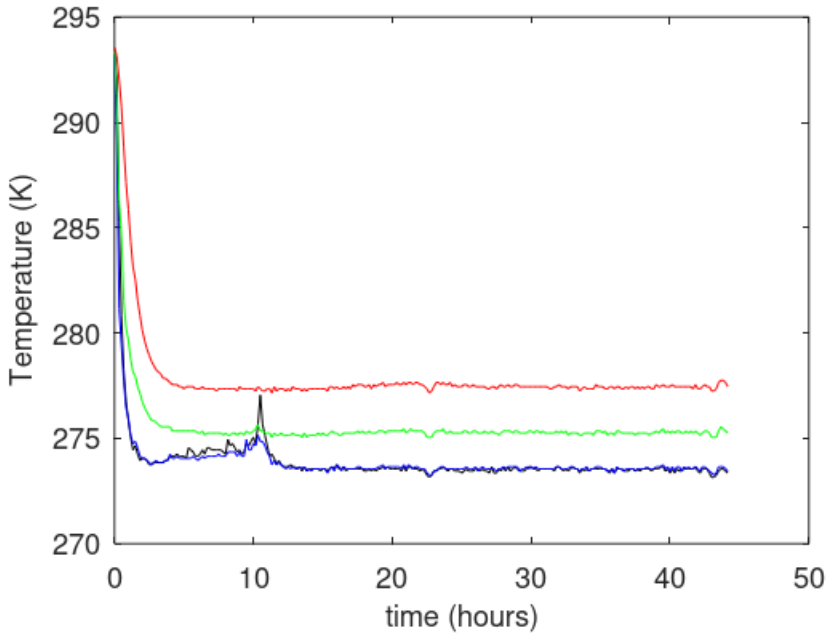

Figure 9. Temperature profiles during formation of CH_4 hydrate as function of experimental time in hours. Mole numbers methane in cell is 3.2102 and mole numbers of water in cell is 7.3252. T1 is black, T2 is blue, T3 is green and T4 is red.

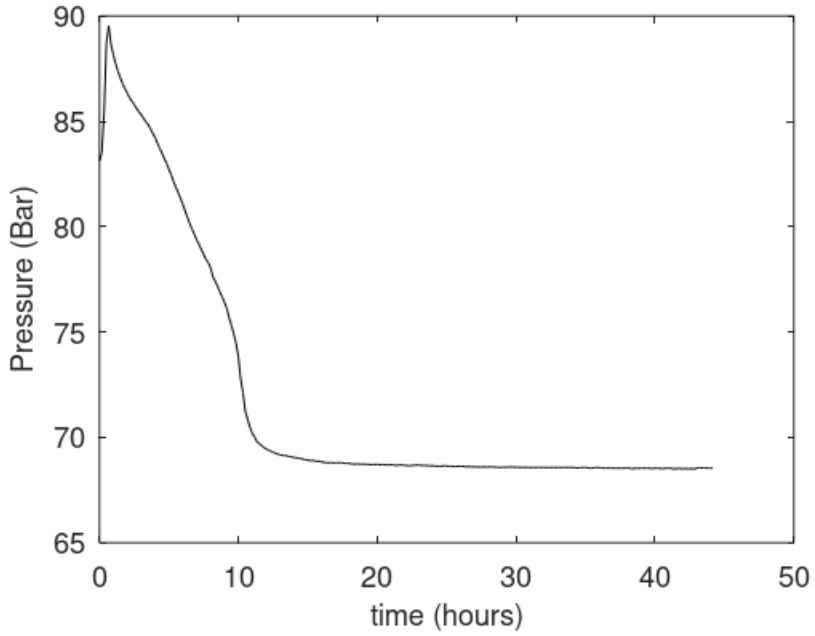

Figure 10. Pressure profile during formation of CH_4 hydrate as function of experimental time in hours. Mole numbers methane in cell is 3.2102 and mole numbers of water in cell is 7.3252.

Table 3. Final balance after formation of CH_4. ΔG^H is Gibbs free energy for hydrate formation in the two sections of B. Z is CH_4 compressibility factor for each of the two gas filled sections. N is mole numbers. Superscript H is hydrate and superscript aq denote liquid water. Subscript H_2O is water and subscript CH_4 is methane.

Sec	T(K)	P(bar)	ΔG^H (kJ/mole)	Z	$x^H_{CH_4}$	ρ^H (mole/m^3)	$N^H_{H_2O}$ (moles)	$N^{aq}_{H_2O}$ (moles)	N_{CH_4} (moles)
A	277.45	68.53	.0000	.8592	.0000	.0000	.0000	.0000	1.9881
H1	275.25	68.53	-.3269	.0000	.1419	51383	2.7517	.9109	.4549
H2	273.45	68.53	-.4001	.0000	.1425	51424	2.7517	.9109	.4574
C	273.45	68.53	.0000	.8500	.0000	.0000	.0000	.0000	.3098

Table 4. Final balance after formation of CH_4. ΔG^H is Gibbs free energy for hydrate formation in the two sections of B. Z is CH_4 compressibility factor for each of the two gas filled sections. N is mole numbers and subscript CH_4 is methane.

Sec	T(K)	P(bar)	ΔG^H (kJ/mole)	Z	$x^H_{CH_4}$	ρ^H (mole/m^3)	N_{CH_4} (moles)
A	277.55	48.02	.0000	.8974	.0000	.0000	1.3334
H1	275.35	48.02	-.1894	.0000	.1393	51229	.5927
H2	273.65	48.02	-.2584	.0000	.1402	51282.	.5971
C	273.65	48.02	.0000	.8913	.0000	.0000	.2068

2.2 Injection of CO_2/N_2/NFM

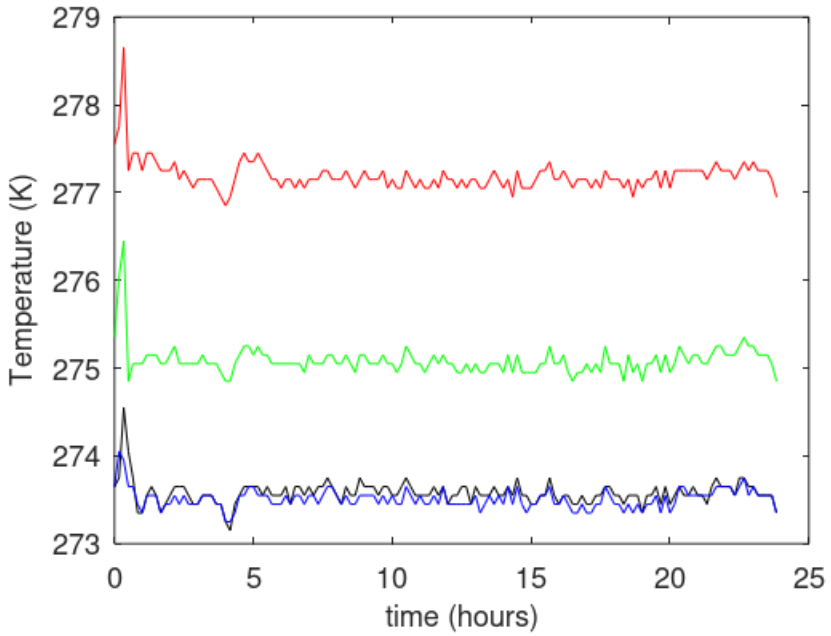

Figure 11. Temperature profiles during injection of CO_2/N_2/NFM and associated reformation processes as function of experimental time in hours. Mole numbers CO_2 injected is 4.544, mole numbers N_2 injected is 0.9088 and 0.01 mole% NFM. Mole numbers of water in cell is 7.3252 and initially in section B since distribution of water in gas is extremely low at experimental conditions.

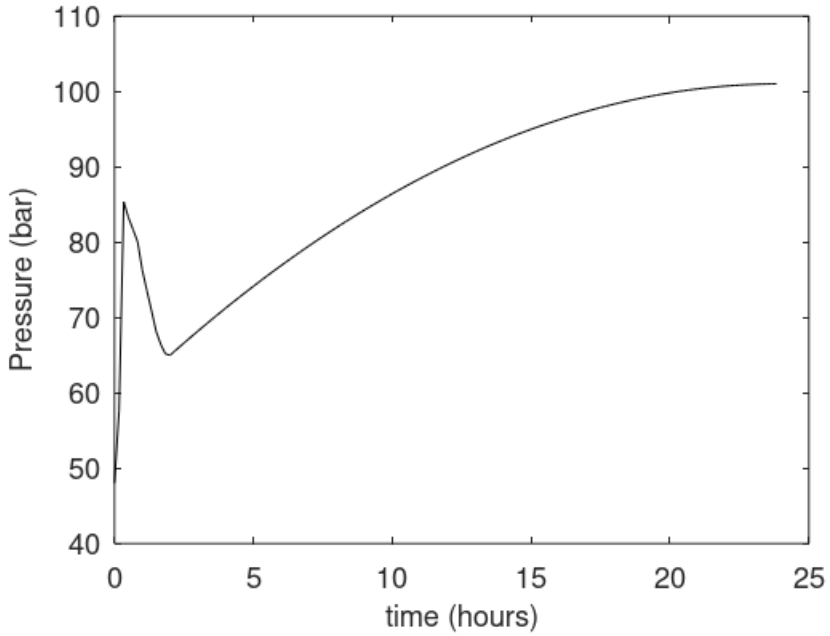

Figure 12. Pressure profile during injection of CO_2/N_2/NFM and associated reformation processes as function of experimental time in hours. Mole numbers CO_2 injected is 4.544, mole numbers N_2 injected is 0.9088 and 0.01 mole% NFM injected. Mole numbers of water in cell is 7.3252 and initially in section B since distribution of water in gas is extremely low at experimental conditions.

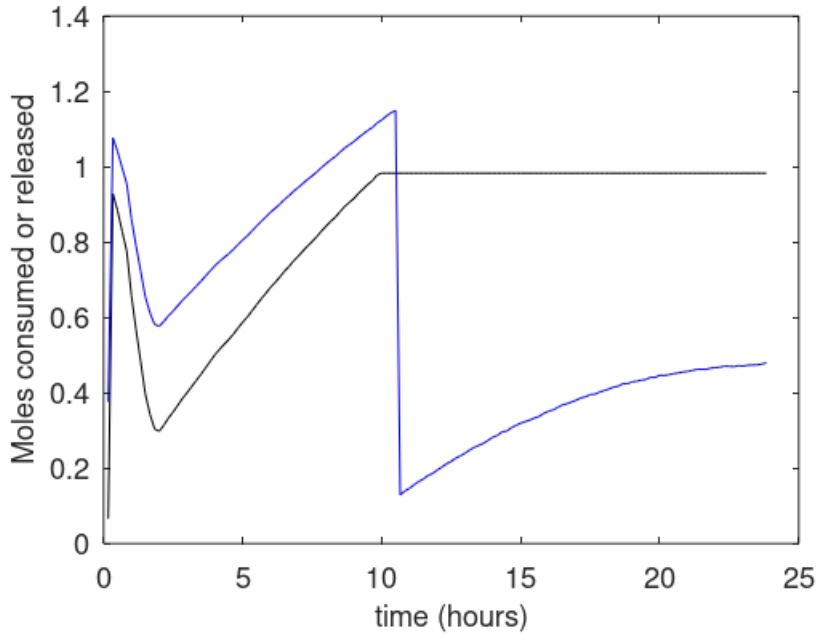

Figure 13. Released CH_4 from CH_4 hydrate is black curve and moles CO_2 consumed to formation of CO_2 hydrate is blue curve.

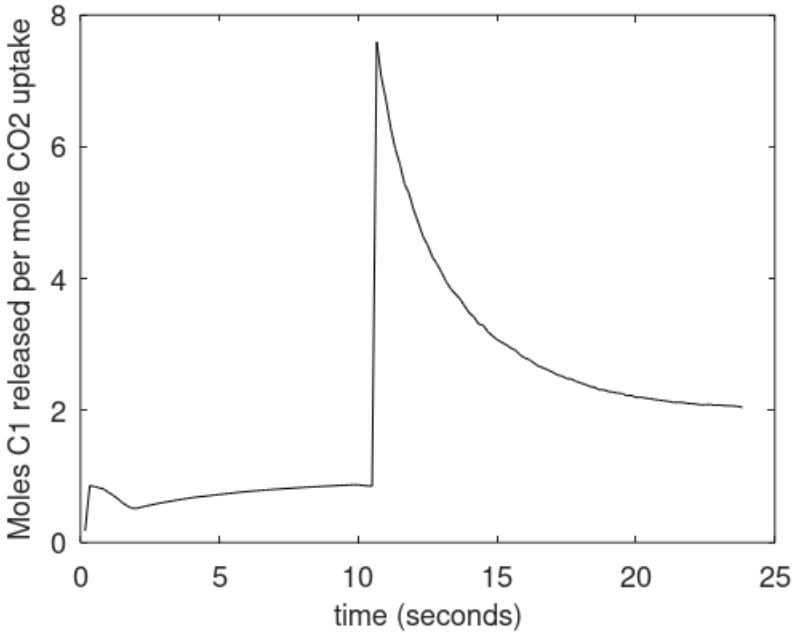

Figure 14. Mole released CH_4 per mole CO_2 uptake.

3. Experiment 3. 0.1 mole per cent NFM, 4.544 mole CO_2, 0.9088 moles N_2 added.

3.1 Creation of CH_4 hydrate

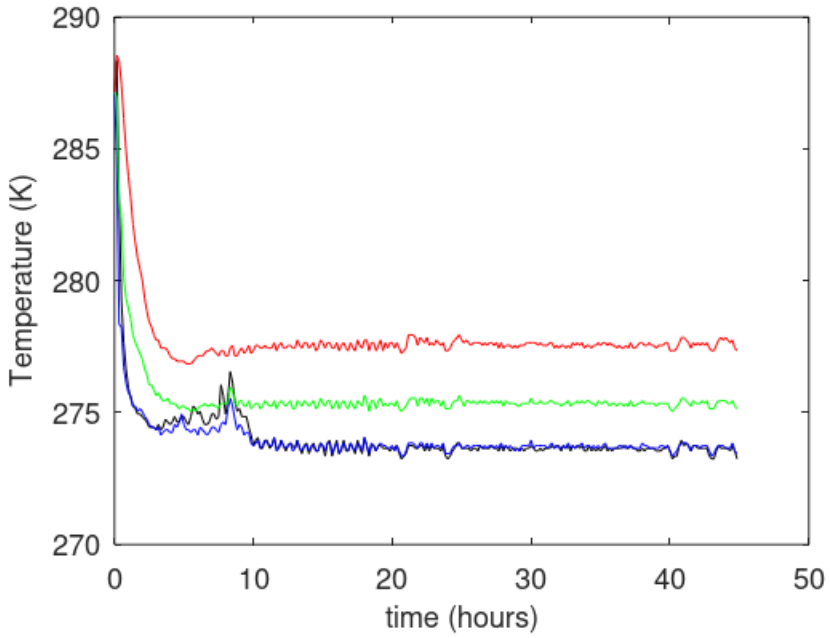

Figure 15. Temperature profiles during formation of CH_4 hydrate as function of experimental time in hours. Mole numbers methane in cell is 3.2102 and mole numbers of water in cell is 7.3252. T1 is black, T2 is blue, T3 is green and T4 is red.

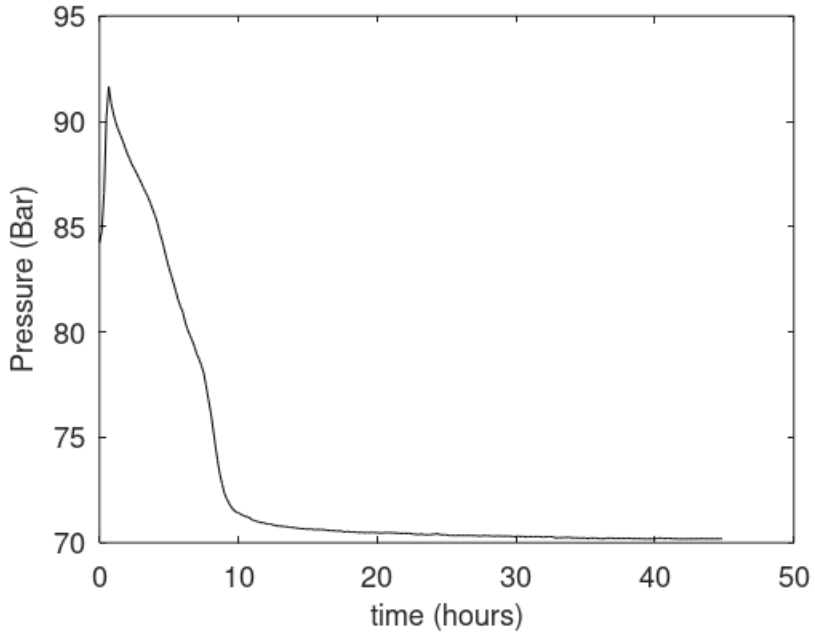

Figure 16. Pressure profile during formation of CH_4 hydrate as function of experimental time in hours. Mole numbers methane in cell is 3.2102 and mole numbers of water in cell is 7.3252.

Table 5. Final balance after formation of CH_4. ΔG^H is Gibbs free energy for hydrate formation in the two sections of B. Z is CH4 compressibility factor for each of the two gas filled sections. N is mole numbers. Superscript H is hydrate and superscript aq denote liquid water. Subscript H_2O is water and subscript CH_4 is methane.

Sec	T(K)	P(bar)	ΔG^H (kJ/mole)	Z	$x^H_{CH_4}$	ρ^H (mole/m^3)	$N^H_{H_2O}$ (moles)	$N^{aq}_{H_2O}$ (moles)	N_{CH_4} (moles)
A	277.35	70.19	.0000	.8562	.0000	.0000	.0000	.0000	2.0442
H1	275.15	70.19	-.3400	.0000	.1420	51394	2.5526	1.1100	.4226
H2	273.45	70.19	-.4091	.0000	.1427	51431	2.5526	1.1100	.4248
C	273.45	70.19	0.	.8467	.0000	.0000	.0000	0.	.3186

Table 6. Final balance after formation of CH_4. ΔG^H is Gibbs free energy for hydrate formation in the two sections of B. Z is CH4 compressibility factor for each of the two gas filled sections. N is mole numbers and subscript CH_4 is methane.

Sec	T(K)	P(bar)	ΔG^H (kJ/mole)	Z	$x^H_{CH_4}$	ρ^H (mole/m^3)	N_{CH_4} (moles)
A	277.15	48.37	.0000	.8961	.0000	.0000	1.3470
H1	275.05	48.37	-.2043	.0000	.1395	51243	.5938
H2	273.35	48.37	-.2732	.0000	.1404	51294	.5980
C	273.35	48.37	.0000	.8901	.0000	.0000	.2088

3.2 Injection of CO_2/N_2/NFM

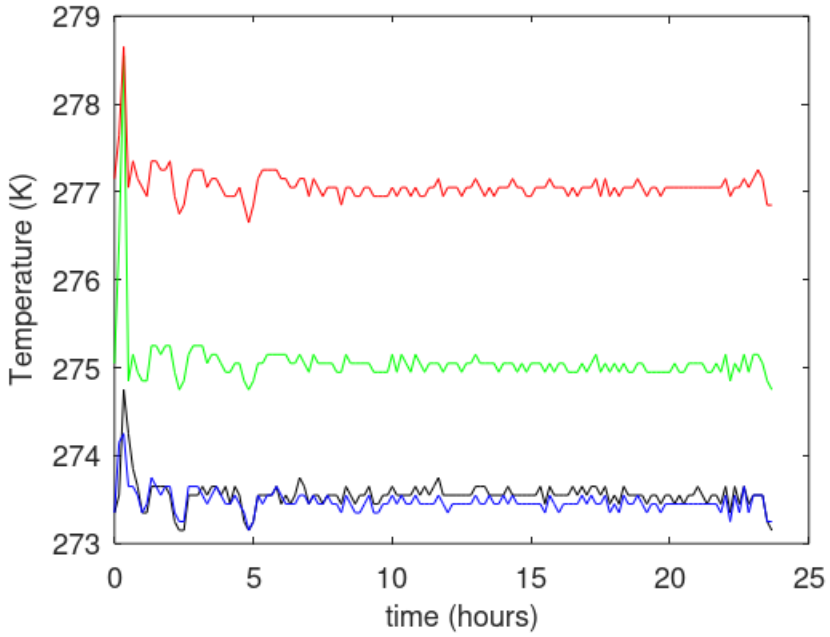

Figure 17. Temperature profiles during injection of CO_2/N_2/NFM and associated reformation processes as function of experimental time in hours. Mole numbers CO_2 injected is 4.544, mole numbers N_2 injected is 0.9088 and 0.1 mole% NFM. Mole numbers of water in cell is 7.3252 and initially in section B since distribution of water in gas is extremely low at experimental conditions.

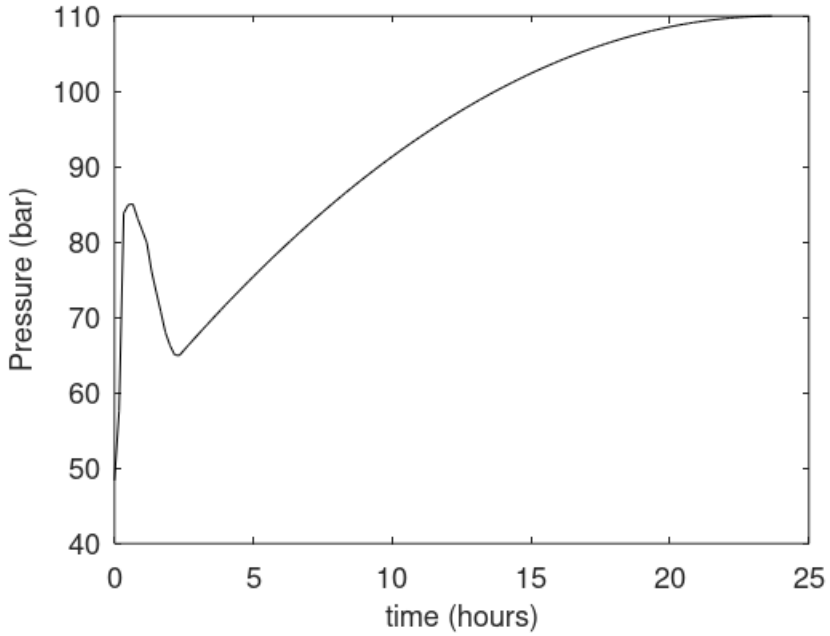

Figure 18. Pressure profile during injection of CO_2/N_2/NFM and associated reformation processes as function of experimental time in hours. Mole numbers CO_2 injected is 4.544, mole numbers N_2 injected is 0.9088 and 0.1 mole% NFM injected. Mole numbers of water in cell is 7.3252 and initially in section B since distribution of water in gas is extremely low at experimental conditions.

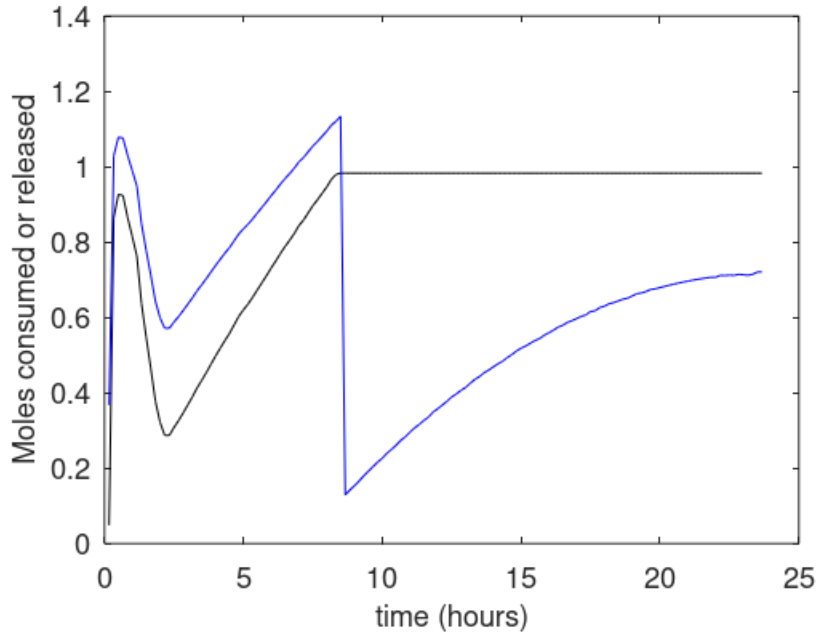

Figure 19. Released CH_4 from CH_4 hydrate is black curve and moles CO_2 consumed to formation of CO_2 hydrate is blue curve.

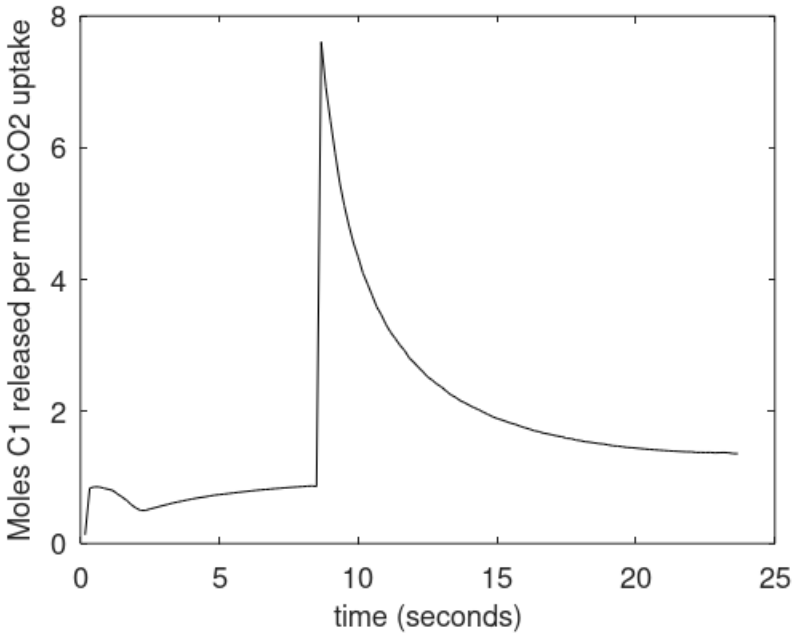

Figure 20. Mole released CH_4 per mole CO_2 uptake.

4. Experiment 4. 3 moles per cent NFM, 4.544 mole CO_2, 0.9088 moles N_2 added.

4.1 Creation of CH_4 hydrate

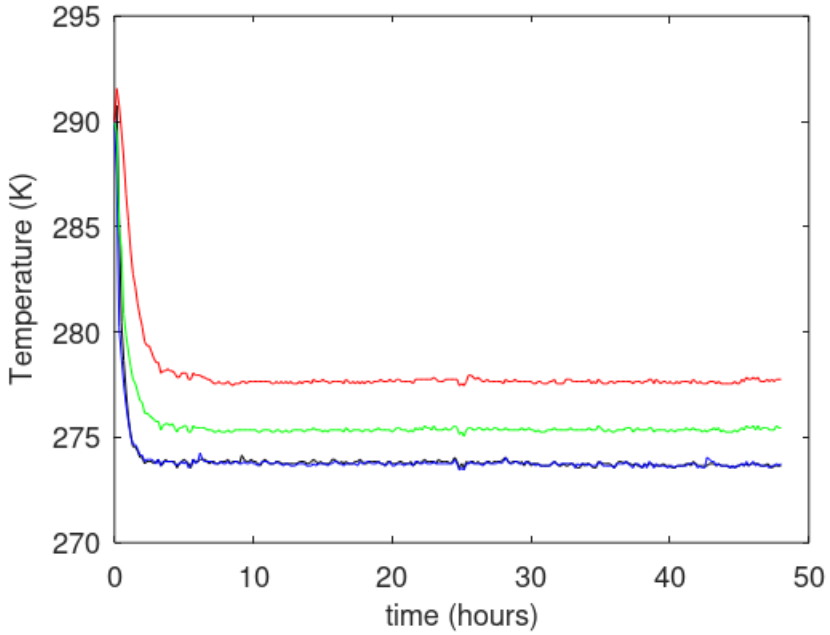

Figure 21. Temperature profiles during formation of CH_4 hydrate as function of experimental time in hours. Mole numbers methane in cell is 3.2102 and mole numbers of water in cell is 7.3252. T1 is black, T2 is blue, T3 is green and T4 is red.

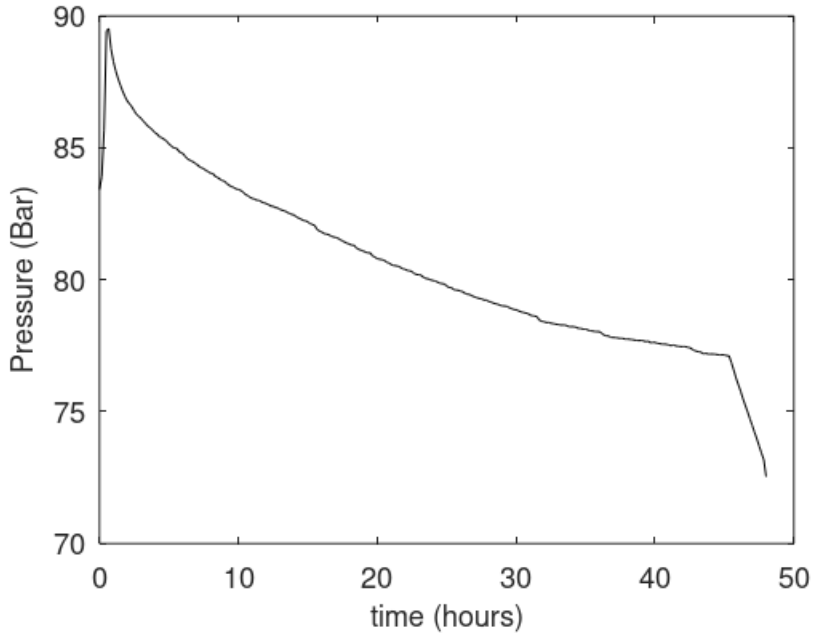

Figure 22. Pressure profile during formation of CH_4 hydrate as function of experimental time in hours. Mole numbers methane in cell is 3.2102 and mole numbers of water in cell is 7.3252.

Table 7. Final balance after formation of CH_4. ΔG^H is Gibbs free energy for hydrate formation in the two sections of B. Z is CH4 compressibility factor for each of the two gas filled sections. N is mole numbers. Superscript H is hydrate and superscript aq denote liquid water. Subscript H_2O is water and subscript CH_4 is methane.

Sec	T(K)	P(bar)	ΔG^H (kJ/mole)	Z	$x^H_{CH_4}$	ρ^H (mole/m^3)	$N^H_{H_2O}$ (moles)	$N^{aq}_{H_2O}$ (moles)	N_{CH_4} (moles)
A	277.75	72.53	.0000	.8531	.0000	.0000	.0000	.0000	2.1170
H1	275.45	72.53	-.3401	.0000	.1421	51398	2.2976	1.3650	.3806
H2	273.75	72.53	-.4094	.0000	.1427	51436	2.2976	1.3650	.3826
C	273.75	72.53	.0000	.8435	.0000	.0000	.0000	.0000	.3300

Table 8. Final balance after formation of CH_4. ΔG^H is Gibbs free energy for hydrate formation in the two sections of B. Z is CH4 compressibility factor for each of the two gas filled sections. N is mole numbers and subscript CH_4 is methane.

Sec	T(K)	P(bar)	ΔG^H (kJ/mole)	Z	$x^H_{CH_4}$	ρ^H (mole/m^3)	N_{CH_4} (moles)
A	277.55	48.81	.0000	.8958	.0000	.0000	1.3577
H1	275.35	48.81	-.1954	.0000	.1394	51237	.5933

H2	273.55	48.81	-.2685	.0000	.1403	51292	.5979
C	273.55	48.81	.0000	.8897	.0000	.0000	.2106

4.2 Injection of CO_2/N_2/NFM

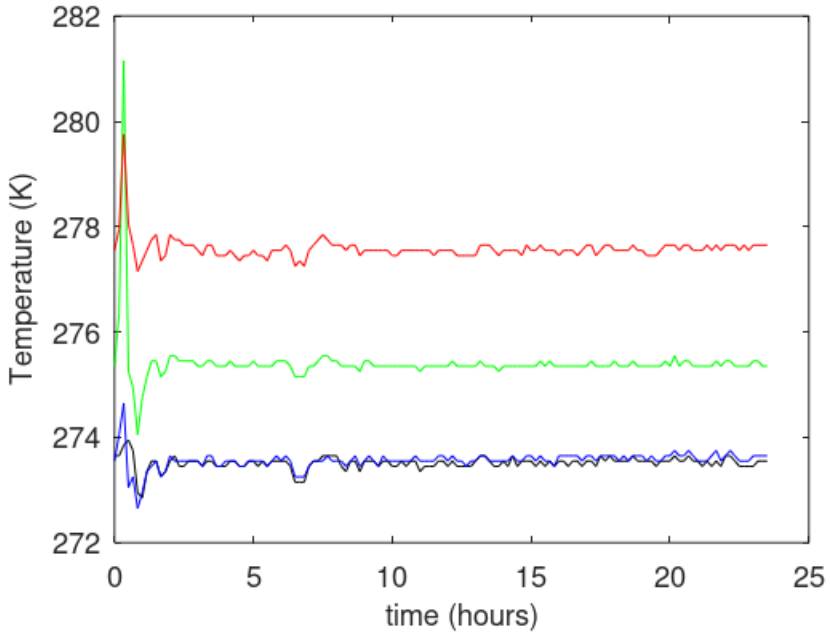

Figure 23. Temperature profiles during injection of CO_2/N_2/NFM and associated reformation processes as function of experimental time in hours. Mole numbers CO_2 injected is 4.544, mole numbers N_2 injected is 0.9088 and 3 moles% NFM. Mole numbers of water in cell is 7.3252 and initially in section B since distribution of water in gas is extremely low at experimental conditions.

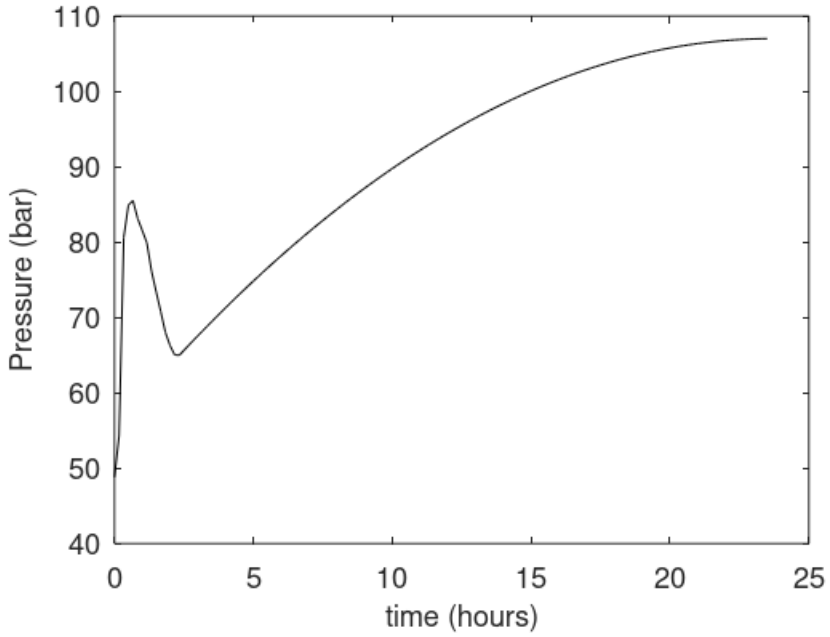

Figure 24. Pressure profile during injection of CO_2/N_2/NFM and associated reformation processes as function of experimental time in hours. Mole numbers CO_2 injected is 4.544, mole numbers N_2 injected is 0.9088 and 3 moles% NFM injected. Mole numbers of water in cell is 7.3252 and initially in section B since distribution of water in gas is extremely low at experimental conditions.

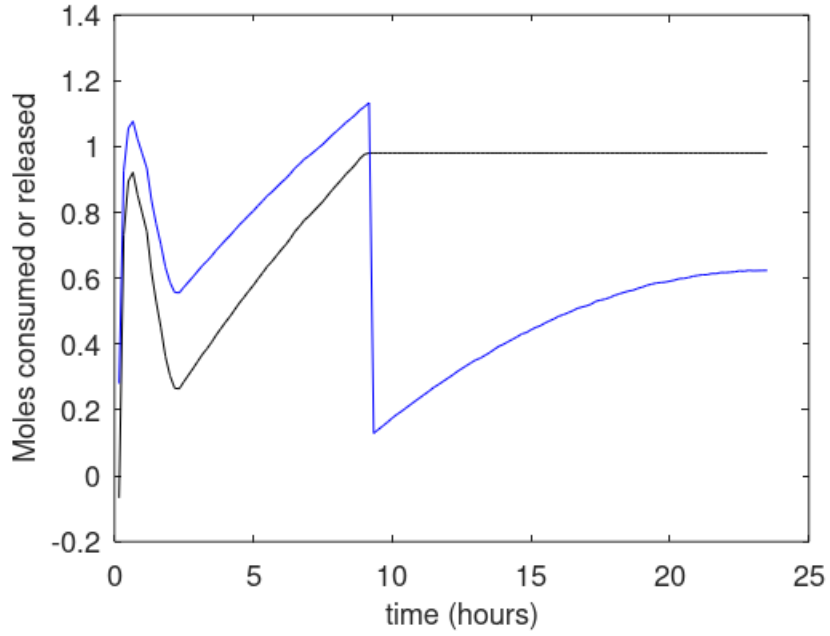

Figure 25. Released CH_4 from CH_4 hydrate is black curve and moles CO_2 consumed to formation of CO_2 hydrate is blue curve.

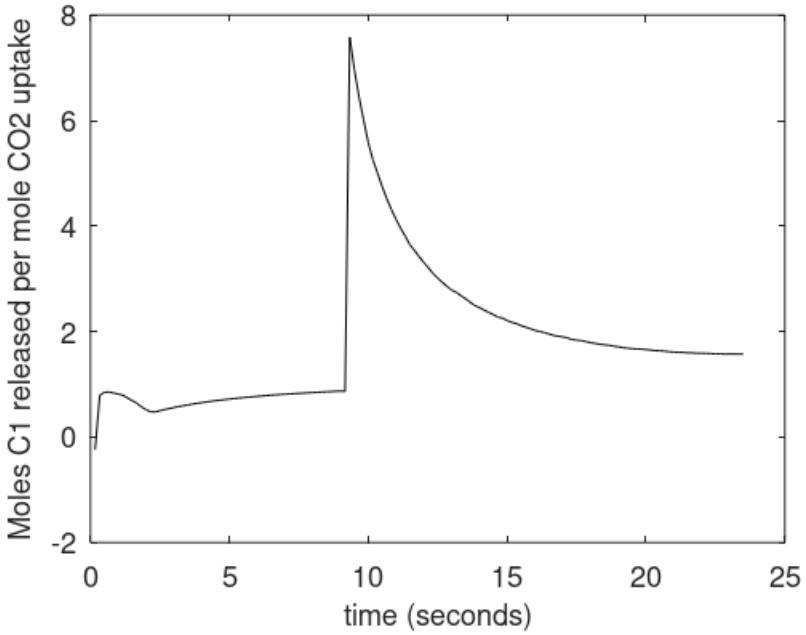

Figure 26. Mole released CH_4 per mole CO_2 uptake.

5. Experiment 5. 1 mole per cent NFM, 4.544 mole CO_2 added.

5.1 Creation of CH_4 hydrate

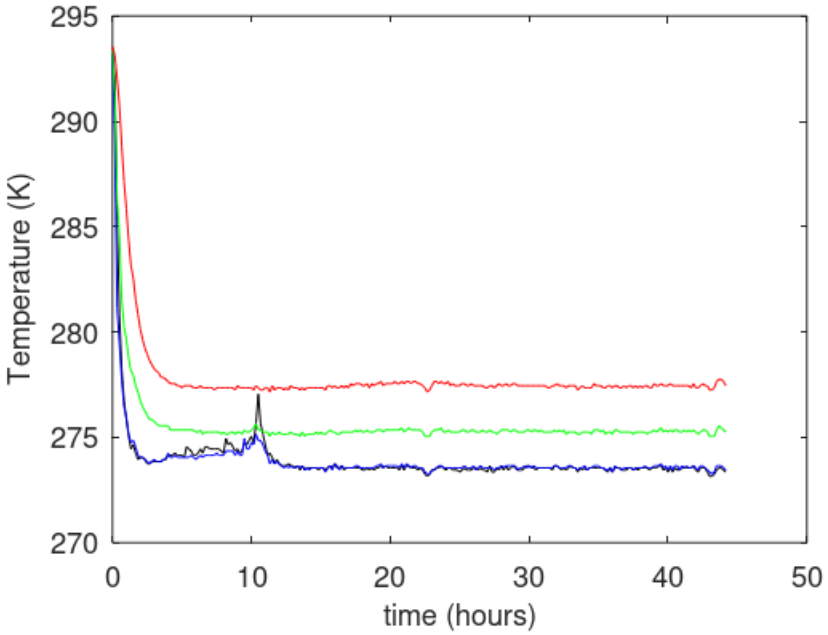

Figure 27. Temperature profiles during formation of CH_4 hydrate as function of experimental time in hours. Mole numbers methane in cell is 3.2102 and mole numbers of water in cell is 7.3252. T1 is black, T2 is blue, T3 is green and T4 is red.

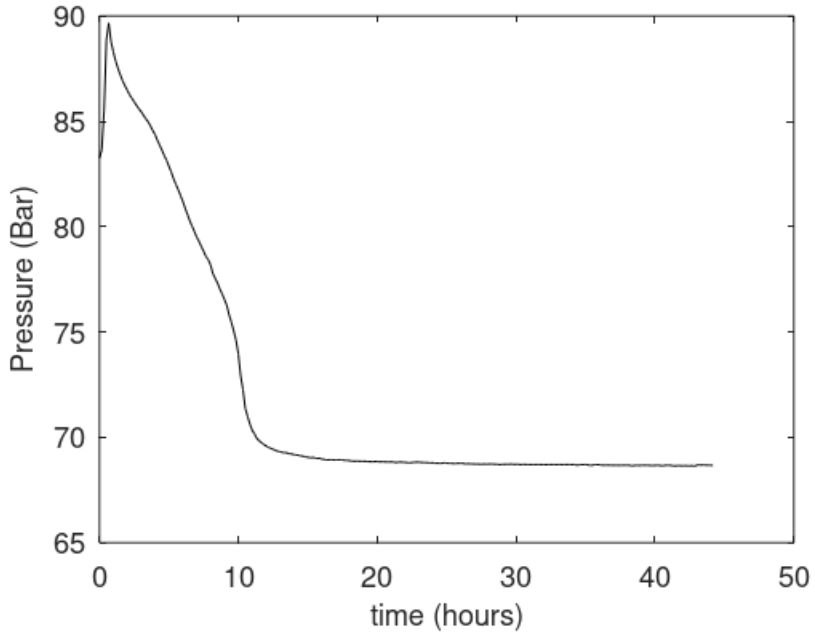

Figure 28. Pressure profile during formation of CH_4 hydrate as function of experimental time in hours. Mole numbers methane in cell is 3.2102 and mole numbers of water in cell is 7.3252.

Table 9. Final balance after formation of CH_4. ΔG^H is Gibbs free energy for hydrate formation in the two sections of B. Z is CH4 compressibility factor for each of the two gas filled sections. N is mole numbers. Superscript H is hydrate and superscript aq denote liquid water. Subscript H_2O is water and subscript CH_4 is methane.

Sec	T(K)	P(bar)	ΔG^H (kJ/mole)	Z	$x^H_{CH_4}$	ρ^H (mole/m^3)	$N^H_{H_2O}$ (moles)	$N^{aq}_{H_2O}$ (moles)	N_{CH_4} (moles)
A	277.45	68.67	.0000	.8590	.0000	.0000	.0000	.0000	1.9926
H1	275.25	68.67	-.3277	.0000	.1419	51384	2.7356	.9270	.4523
H2	273.45	68.67	-.4008	.0000	.1426	51424	2.7356	.9270	.4548
C	273.45	68.67	.0000	.8497	.0000	.0000	.0000	.0000	.3105

Table 10. Final balance after formation of CH_4. ΔG^H is Gibbs free energy for hydrate formation in the two sections of B. Z is CH4 compressibility factor for each of the two gas filled sections. N is mole numbers and subscript CH_4 is methane.

Sec	T(K)	P(bar)	ΔG^H (kJ/mole)	Z	$x^H_{CH_4}$	ρ^H (mole/m^3)	N_{CH_4} (moles)
A	277.55	48.16	.0000	.8971	.0000	.0000	1.3376
H1	275.35	48.16	-.1904	.0000	.1393	51230	.5928
H2	273.65	48.16	-.2595	.0000	.1402	51284	.5972
C	273.65	48.16	.0000	.8910	.0000	.0000	.2074

5.2 Injection of CO_2/N_2/NFM

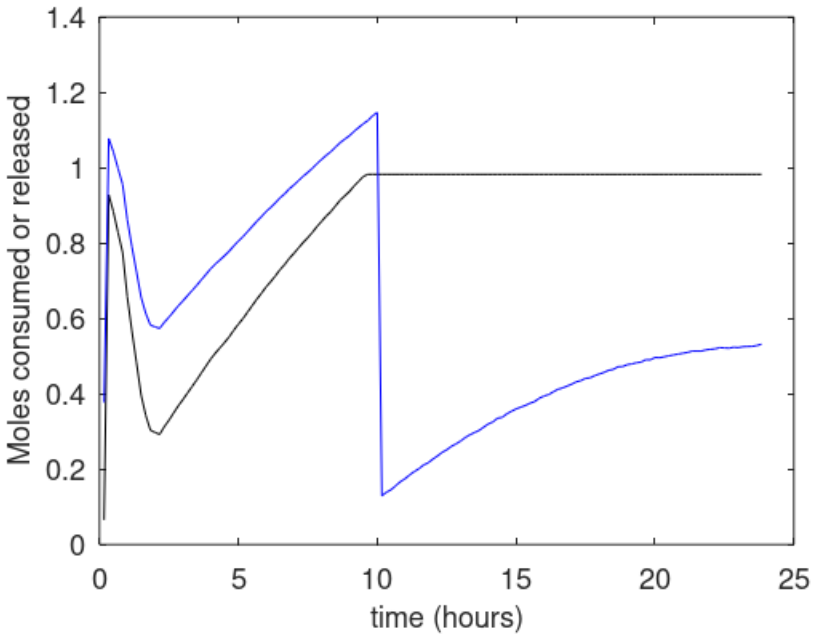

Figure 29. Released CH_4 from CH_4 hydrate is black curve and moles CO_2 consumed to formation of CO_2 hydrate is blue curve.

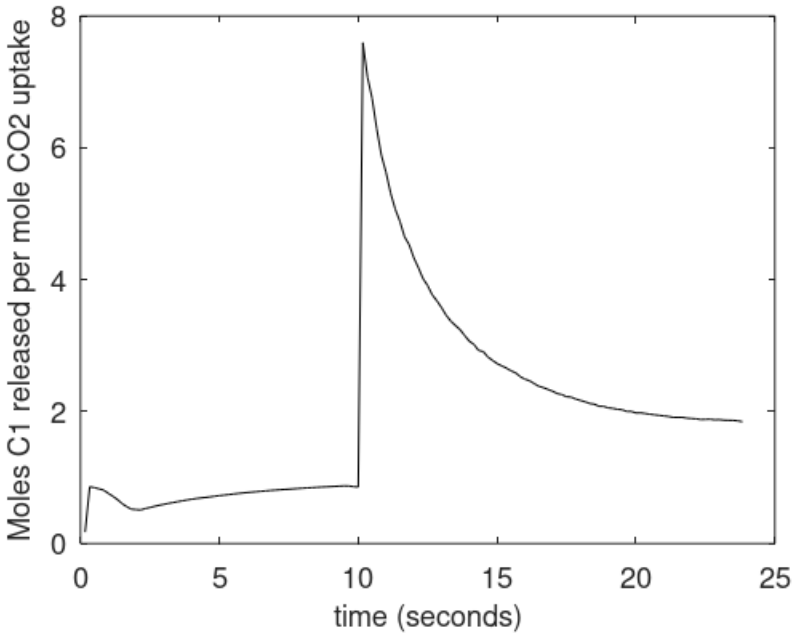

Figure 30. Mole released CH_4 per mole CO_2 uptake.

6. Experiment 6. 3 moles per cent ethanol, 4.544 mole CO_2 added.

6.1 Creation of CH_4 hydrate

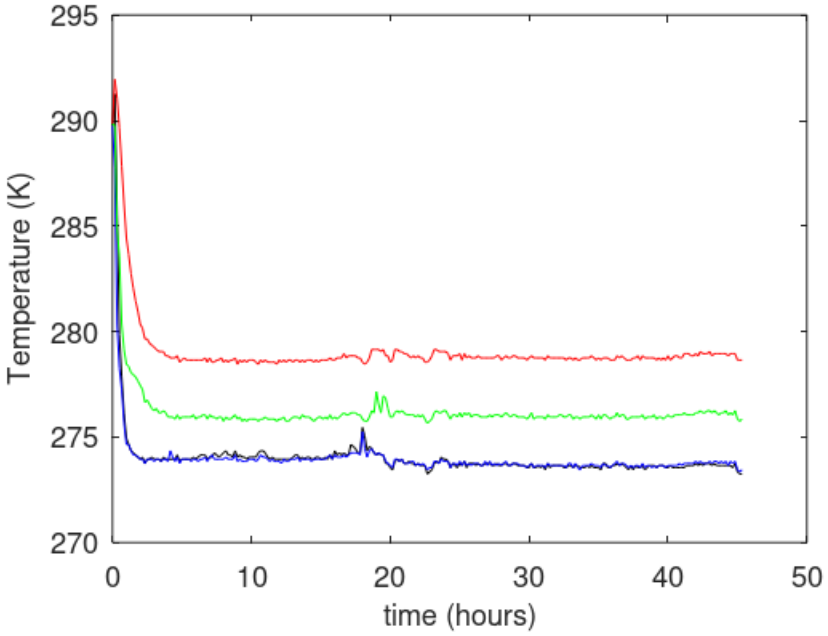

Figure 31. Temperature profiles during formation of CH_4 hydrate as function of experimental time in hours. Mole numbers methane in cell is 3.2102 and mole numbers of water in cell is 7.3252. T1 is black, T2 is blue, T3 is green and T4 is red.

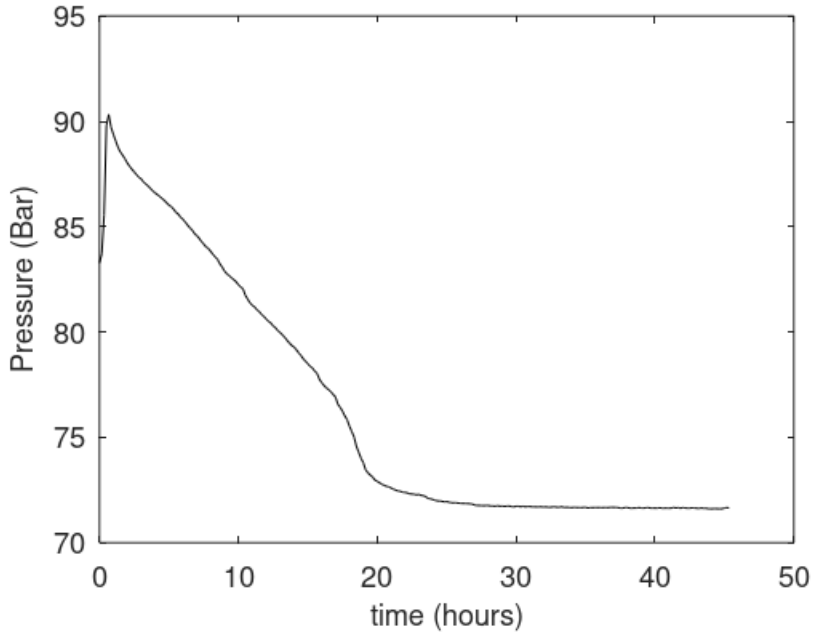

Figure 32. Pressure profile during formation of CH_4 hydrate as function of experimental time in hours. Mole numbers methane in cell is 3.2102 and mole numbers of water in cell is 7.3252.

Table 11. Final balance after formation of CH_4. ΔG^H is Gibbs free energy for hydrate formation in the two sections of B. Z is CH4 compressibility factor for each of the two gas filled sections. N is mole numbers. Superscript H is hydrate and superscript aq denote liquid water. Subscript H_2O is water and subscript CH_4 is methane.

Sec	T(K)	P(bar)	ΔG^H (kJ/mole)	Z	$x^H_{CH_4}$	ρ^H (mole/m^3)	$N^H_{H_2O}$ (moles)	$N^{aq}_{H_2O}$ (moles)	N_{CH_4} (moles)
A	278.65	71.64	.0000	.8566	.0000	.0000	.0000	.0000	2.0757
H1	275.85	71.64	-.3190	.0000	.1419	51384	2.4355	1.2271	.4026
H2	273.45	71.64	-.4168	.0000	.1428	51438	2.4355	1.2271	.4056
C	273.45	71.64	.0000	.8441	.0000	.0000	.0000	.0000	.3262

Table 12. Final balance after formation of CH_4. ΔG^H is Gibbs free energy for hydrate formation in the two sections of B. Z is CH4 compressibility factor for each of the two gas filled sections. N is mole numbers and subscript CH_4 is methane.

Sec	T(K)	P(bar)	ΔG^H (kJ/mole)	Z	$x^H_{CH_4}$	ρ^H (mole/m^3)	N_{CH_4} (moles)
A	278.85	48.41	.0000	.8986	.0000	.0000	1.3361
H1	275.85	48.41	-.1719	.0000	.1390	51215	.5915
H2	273.65	48.41	-.2614	.0000	.1402	51286	.5974
C	273.65	48.41	.0000	.8908	.0000	.0000	.2084

6.2 Injection of CO_2/N_2/ethanol

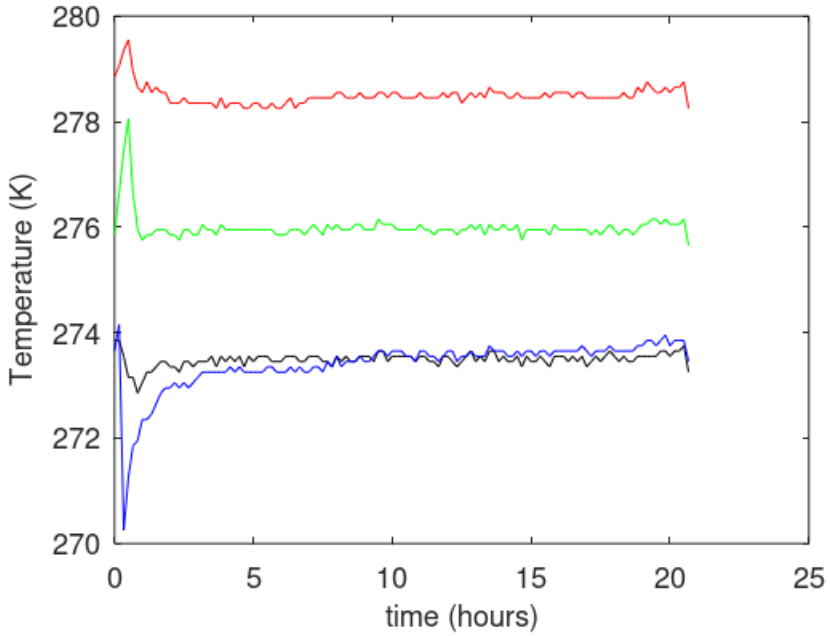

Figure 33. Temperature profiles during injection of CO_2/N_2/ethanol and associated reformation processes as function of experimental time in hours. Mole numbers CO_2 injected is 4.544, 3 moles% ethanol. Mole numbers of water in cell is 7.3252 and initially in section B since distribution of water in gas is extremely low at experimental conditions.

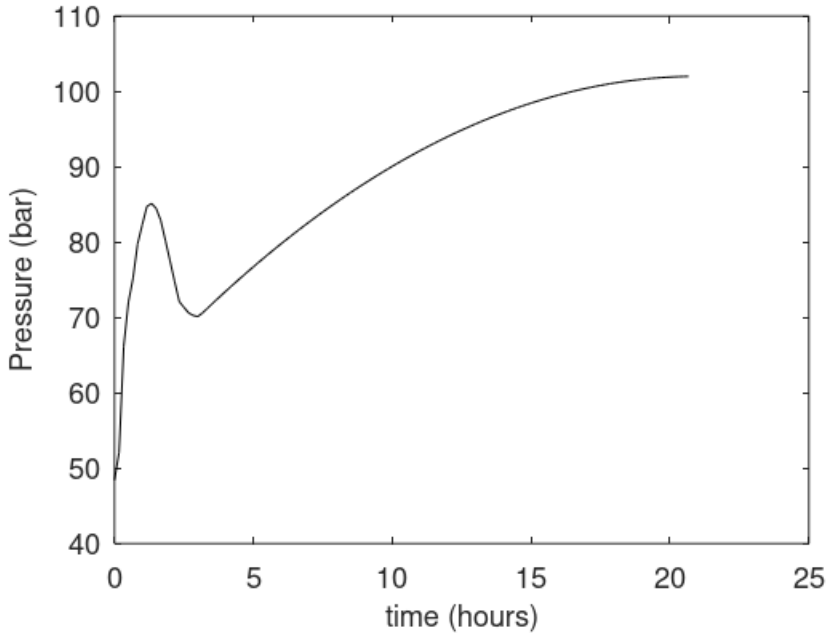

Figure 34. Pressure profile during injection of CO_2/N_2/ethanol and associated reformation processes as function of experimental time in hours. Mole numbers CO_2 injected is 4.544, 3 moles% ethanol injected. Mole numbers of water in cell is 7.3252 and initially in section B since distribution of water in gas is extremely low at experimental conditions.

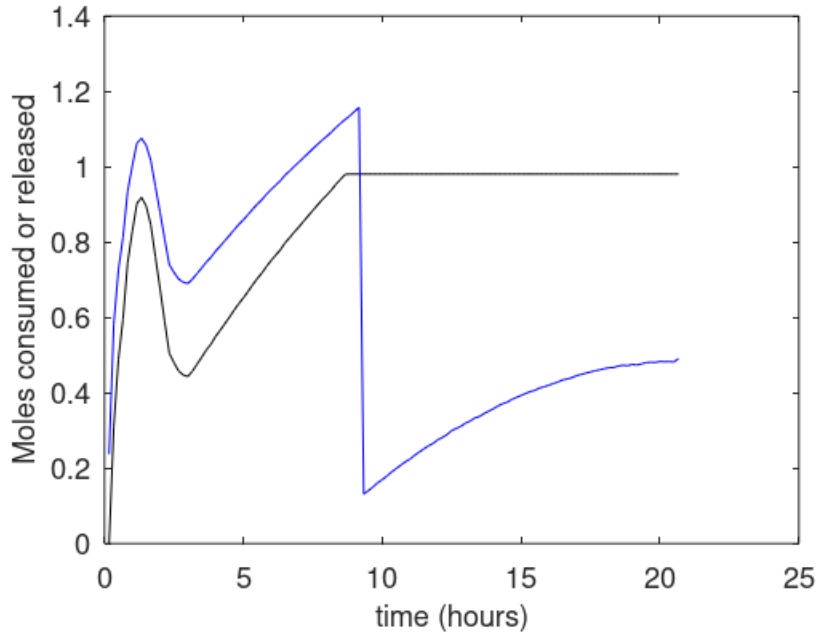

Figure 35. Released CH_4 from CH_4 hydrate is black curve and moles CO_2 consumed to formation of CO_2 hydrate is blue curve.

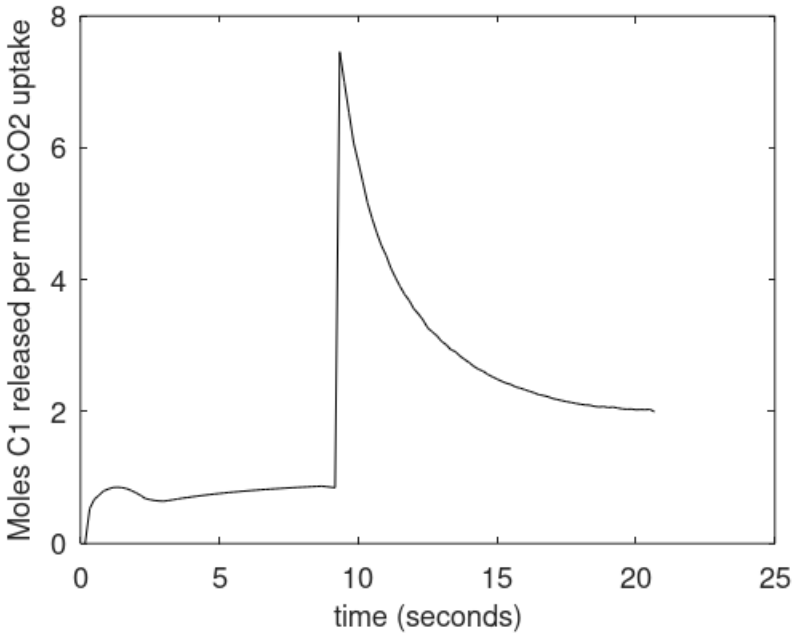

Figure 36. Mole released CH_4 per mole CO_2 uptake.

7. Experiment 7. 3 moles per cent ethanol, 4.544 mole CO_2, 0.9088 moles N_2 added.

7.1 Creation of CH_4 hydrate

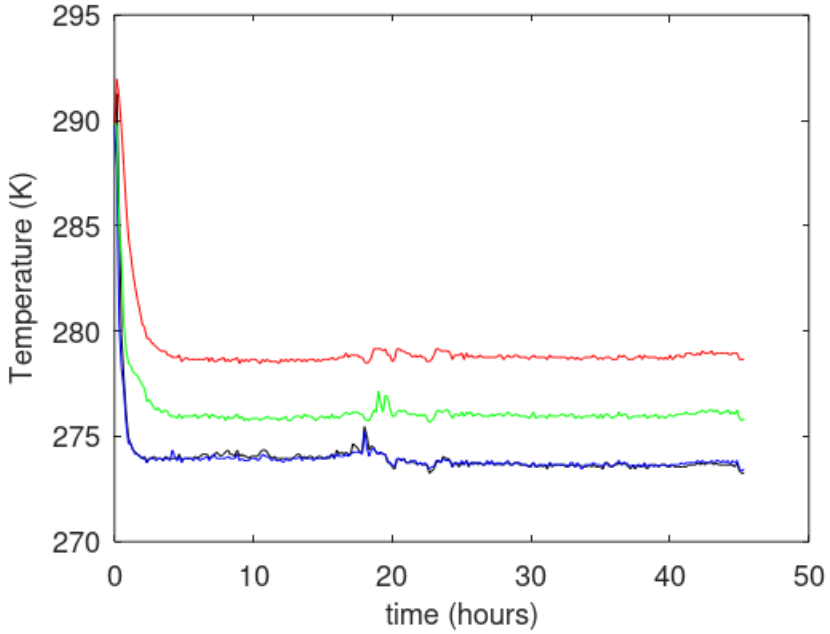

Figure 37. Temperature profiles during formation of CH_4 hydrate as function of experimental time in hours. Mole numbers methane in cell is 3.2102 and mole numbers of water in cell is 7.3252. T1 is black, T2 is blue, T3 is green and T4 is red.

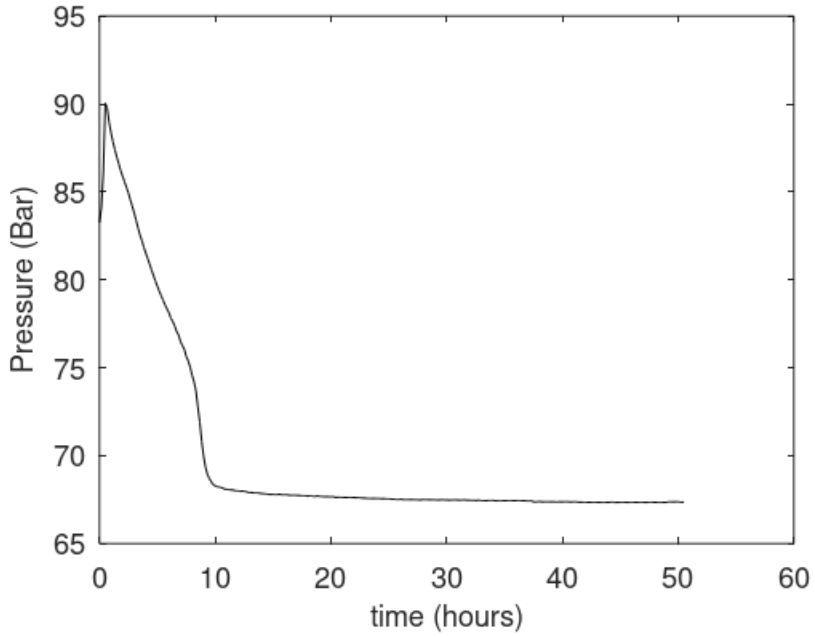

Figure 38. Pressure profile during formation of CH_4 hydrate as function of experimental time in hours. Mole numbers methane in cell is 3.2102 and mole numbers of water in cell is 7.3252.

Table 13. Final balance after formation of CH_4. ΔG^H is Gibbs free energy for hydrate formation in the two sections of B. Z is CH4 compressibility factor for each of the two gas filled sections. N is mole numbers. Superscript H is hydrate and superscript aq denote liquid water. Subscript H_2O is water and subscript CH_4 is methane.

Sec	T(K)	P(bar)	ΔG^H (kJ/mole)	Z	$x^H_{CH_4}$	ρ^H (mole/m^3)	$N^H_{H_2O}$ (moles)	$N^{aq}_{H_2O}$ (moles)	N_{CH_4} (moles)
A	277.75	67.37	.0000	.8618	.0000	.0000	.0000	.0000	1.9464
H1	275.25	67.37	-.3205	.0000	.1418	51377	2.8979	.7647	.4787
H2	273.45	67.37	-.3936	.0000	.1424	51418	2.8979	.7647	.4814
C	273.45	67.37	.0000	.8521	.0000	.0000	.0000	.0000	.3038

Table 14. Final balance after formation of CH_4. ΔG^H is Gibbs free energy for hydrate formation in the two sections of B. Z is CH4 compressibility factor for each of the two gas filled sections. N is mole numbers and subscript CH_4 is methane.

Sec	T(K)	P(bar)	ΔG^H (kJ/mole)	Z	$x^H_{CH_4}$	ρ^H (mole/m^3)	N_{CH_4} (moles)
A	277.75	48.19	.0000	.8974	.0000	.0000	1.3372
H1	275.15	48.19	-.1988	.0000	.1394	51237	.5934

H2	273.45	48.19	-.2678	.0000	.1403	51289	.5977
C	273.45	48.19	.0000	.8901	.0000	.0000	.2082

7.2 Injection of CO_2/N_2/ethanol

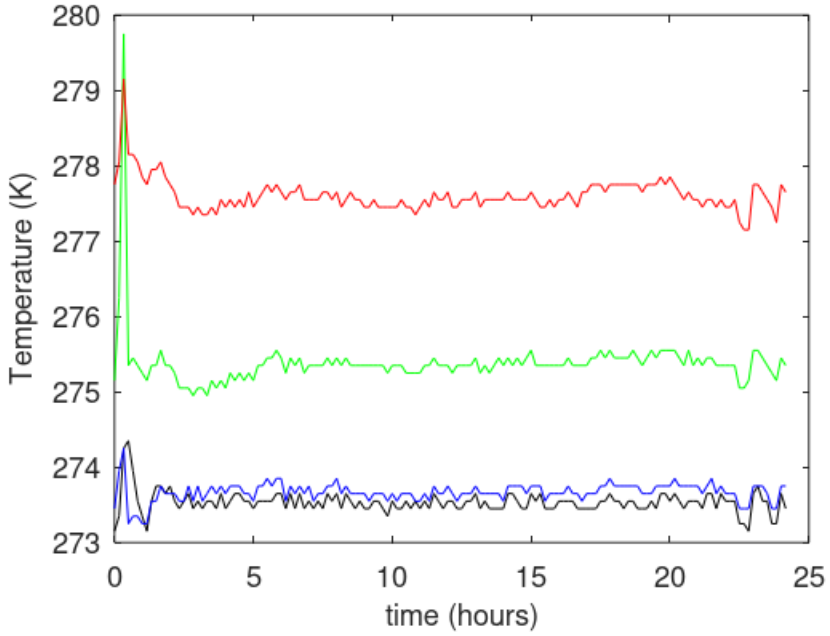

Figure 39. Temperature profiles during injection of CO_2/N_2/ethanol and associated reformation processes as function of experimental time in hours. Mole numbers CO_2 injected is 4.544, mole numbers N_2 injected is 0.9088 and 3 moles% ethanol. Mole numbers of water in cell is 7.3252 and initially in section B since distribution of water in gas is extremely low at experimental conditions.

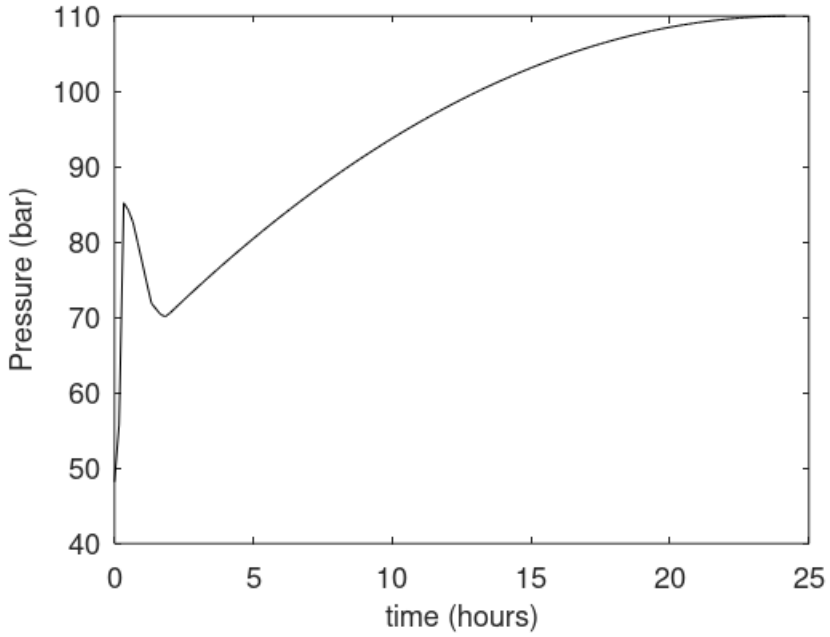

Figure 40. Pressure profile during injection of CO_2/N_2/ethanol and associated reformation processes as function of experimental time in hours. Mole numbers CO_2 injected is 4.544, mole numbers N_2 injected is 0.9088 and 3 moles% ethanol injected. Mole numbers of water in cell is 7.3252 and initially in section B since distribution of water in gas is extremely low at experimental conditions.

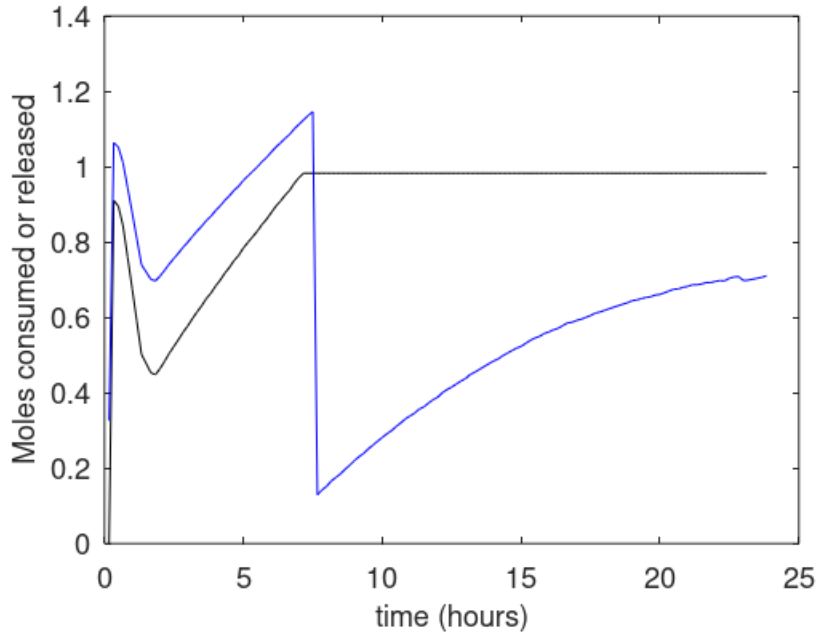

Figure 41. Released CH_4 from CH_4 hydrate is black curve and moles CO_2 consumed to formation of CO_2 hydrate is blue curve.

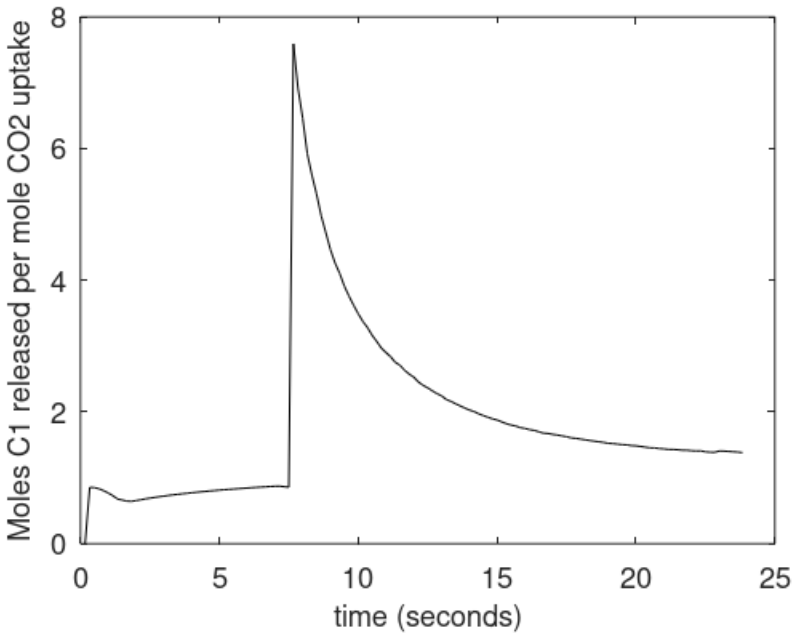

Figure 42. Mole released CH_4 per mole CO_2 uptake.

8. Experiment 8. 4 moles per cent ethanol, 4.544 mole CO_2, 0.9088 moles N_2 added.

8.1 Creation of CH_4 hydrate

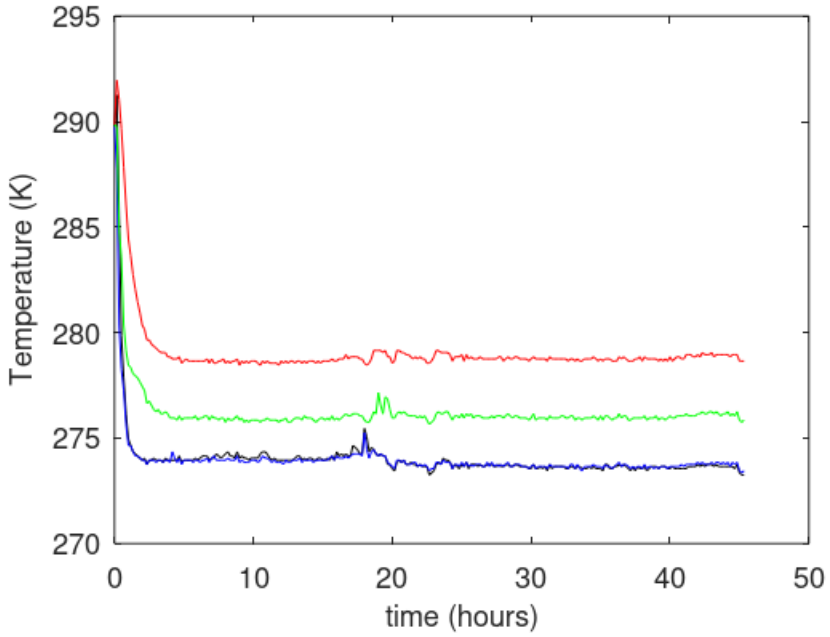

Figure 43. Temperature profiles during formation of CH_4 hydrate as function of experimental time in hours. Mole numbers methane in cell is 3.2102 and mole numbers of water in cell is 7.3252. T1 is black, T2 is blue, T3 is green and T4 is red.

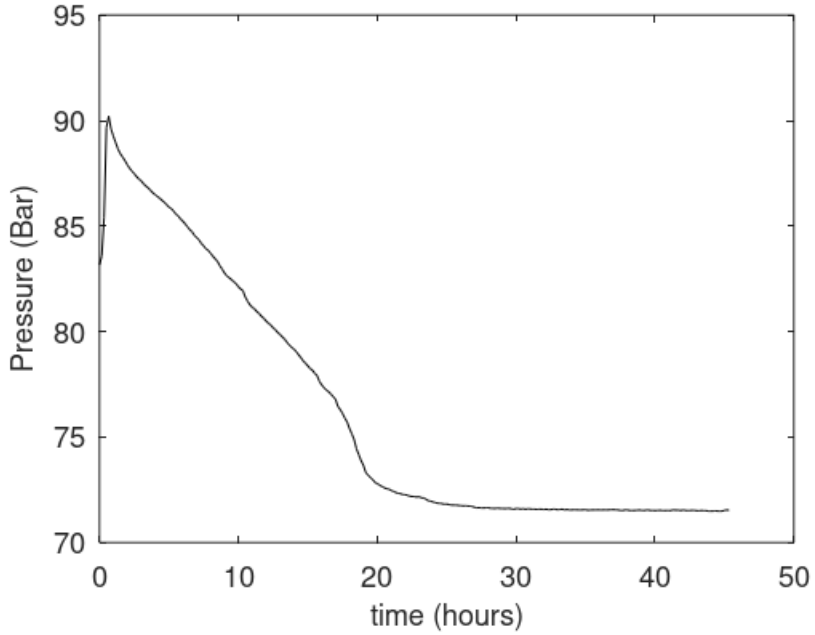

Figure 44. Pressure profile during formation of CH_4 hydrate as function of experimental time in hours. Mole numbers methane in cell is 3.2102 and mole numbers of water in cell is 7.3252.

Table 15. Final balance after formation of CH_4. ΔG^H is Gibbs free energy for hydrate formation in the two sections of B. Z is CH4 compressibility factor for each of the two gas filled sections. N is mole numbers. Superscript H is hydrate and superscript aq denote liquid water. Subscript H_2O is water and subscript CH_4 is methane.

Sec	T(K)	P(bar)	ΔG^H (kJ/mole)	Z	$x^H_{CH_4}$	ρ^H (mole/m^3)	$N^H_{H_2O}$ (moles)	$N^{aq}_{H_2O}$ (moles)	N_{CH_4} (moles)
A	278.65	71.52	.0000	.8568	.0000	.0000	.0000	.0000	2.0717
H1	275.85	71.52	-.3184	.0000	.1419	51383	2.4495	1.2131	.4049
H2	273.45	71.52	-.4162	.0000	.1428	51437	2.4495	1.2131	.4079
C	273.45	71.52	.0000	.8443	.0000	.0000	.0000	.0000	.3256

Table 16. Final balance after formation of CH_4. ΔG^H is Gibbs free energy for hydrate formation in the two sections of B. Z is CH4 compressibility factor for each of the two gas filled sections. N is mole numbers and subscript CH_4 is methane.

Sec	T(K)	P(bar)	ΔG^H (kJ/mole)	Z	$x^H_{CH_4}$	ρ^H (mole/m^3)	N_{CH_4} (moles)
A	277.75	48.19	.0000	.8974	.0000	.0000	1.3372
H1	275.15	48.19	-.1988	.0000	.1394	51237	.5934
H2	273.45	48.19	-.2678	.0000	.1403	51289	.5977
C	273.45	48.19	.0000	.8901	.0000	.0000	.2082

8.2 Injection of CO_2/N_2/ethanol

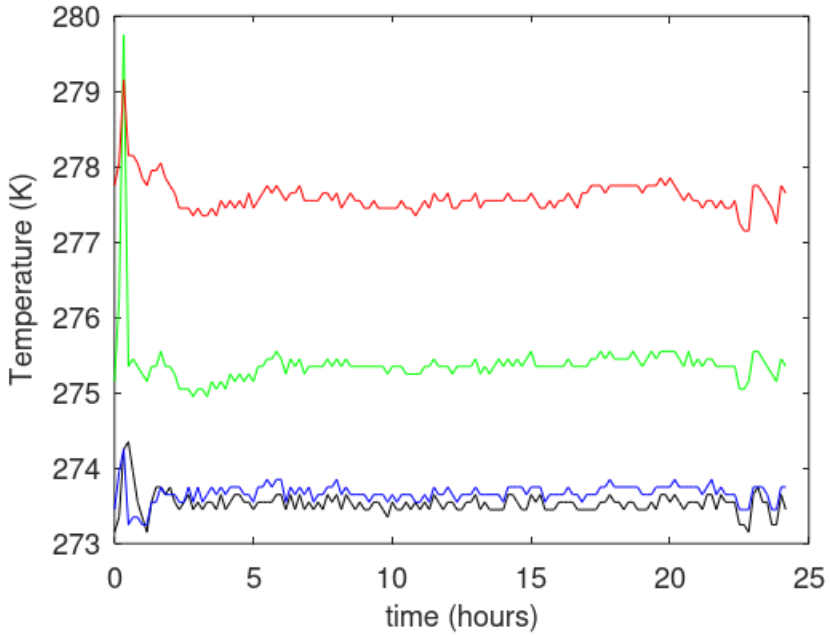

Figure 45. Temperature profiles during injection of CO_2/N_2/ethanol and associated reformation processes as function of experimental time in hours. Mole numbers CO_2 injected is 4.544, mole numbers N_2 injected is 0.9088 and 4 moles% ethanol. Mole numbers of water in cell is 7.3252 and initially in section B since distribution of water in gas is extremely low at experimental conditions.

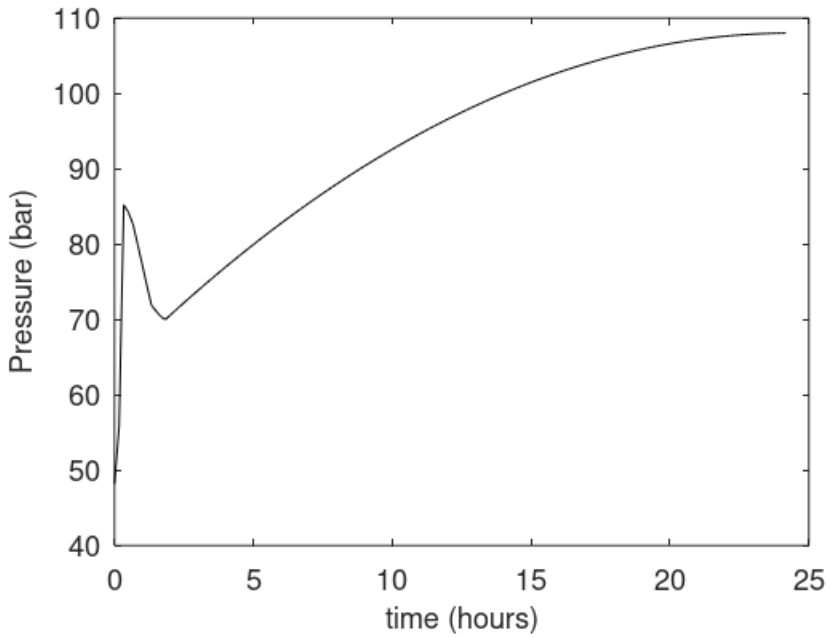

Figure 46. Pressure profile during injection of CO_2/N_2/ethanol and associated reformation processes as function of experimental time in hours. Mole numbers CO_2 injected is 4.544, mole numbers N_2 injected is

0.9088 and 4 moles% ethanol injected. Mole numbers of water in cell is 7.3252 and initially in section B since distribution of water in gas is extremely low at experimental conditions.

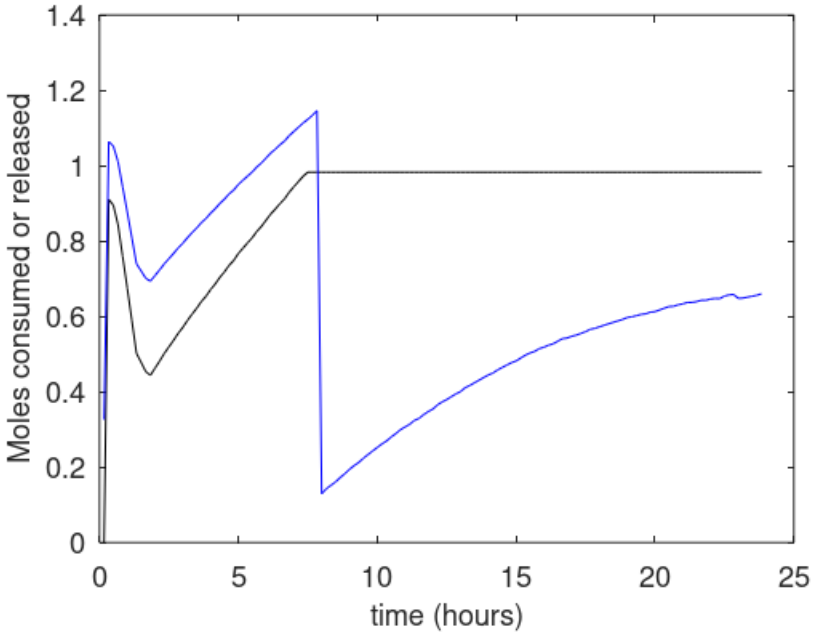

Figure 47. Released CH_4 from CH_4 hydrate is black curve and moles CO_2 consumed to formation of CO_2 hydrate is blue curve.

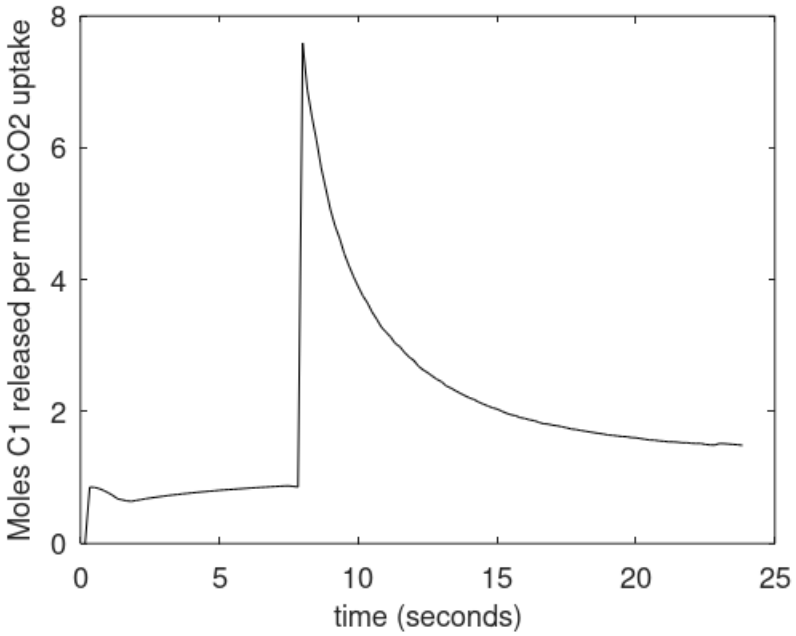

Figure 48. Mole released CH_4 per mole CO_2 uptake.

9. Experiment 9. 0.1 mole per cent ethanol, 4.544 mole CO_2, 0.9088 moles N_2 added.

9.1 Creation of CH_4 hydrate

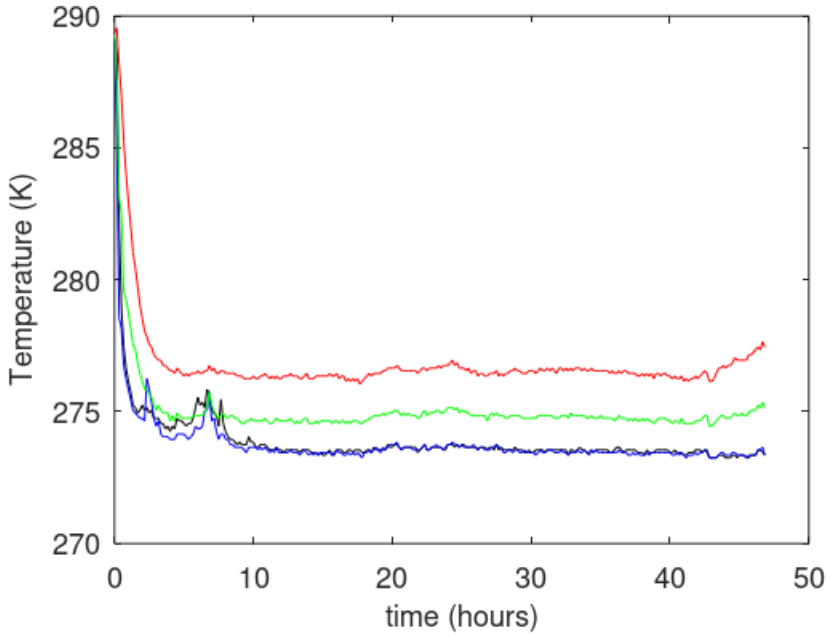

Figure 49. Temperature profiles during formation of CH_4 hydrate as function of experimental time in hours. Mole numbers methane in cell is 3.2102 and mole numbers of water in cell is 7.3252. T1 is black, T2 is blue, T3 is green and T4 is red.

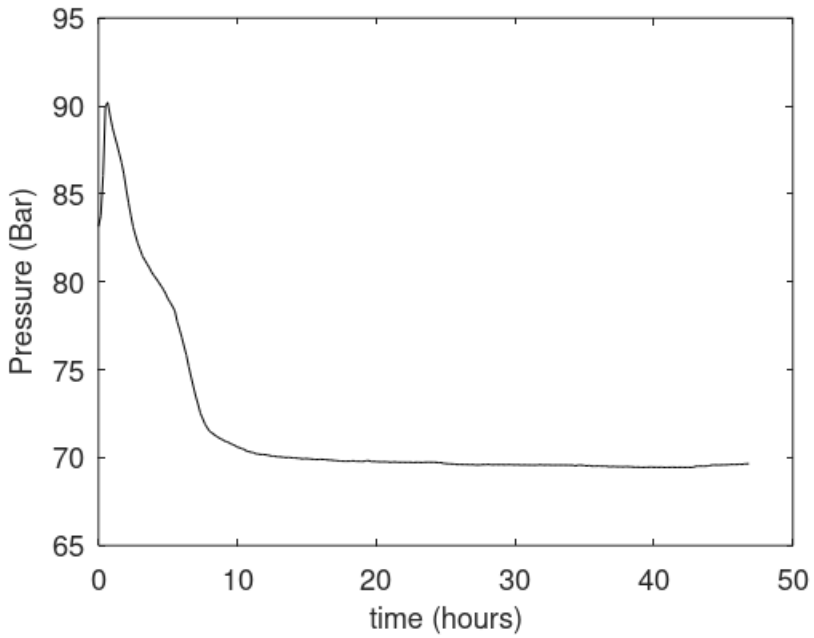

Figure 50. Pressure profile during formation of CH_4 hydrate as function of experimental time in hours. Mole numbers methane in cell is 3.2102 and mole numbers of water in cell is 7.3252.

Table 17. Final balance after formation of CH_4. ΔG^H is Gibbs free energy for hydrate formation in the two sections of B. Z is CH4 compressibility factor for each of the two gas filled sections. N is mole numbers. Superscript H is hydrate and superscript aq denote liquid water. Subscript H_2O is water and subscript CH_4 is methane.

Sec	T(K)	P(bar)	ΔG^H (kJ/mole)	Z	$x^H_{CH_4}$	ρ^H (mole/m^3)	$N^H_{H_2O}$ (moles)	$N^{aq}_{H_2O}$ (moles)	N_{CH_4} (moles)
A	277.45	69.66	.0000	.8573	.0000	.0000	.0000	.0000	2.0255
H1	275.15	69.66	-.3372	.0000	.1420	51392	2.6184	1.0442	.4334
H2	273.35	69.66	-.4103	.0000	.1427	51431	2.6184	1.0442	.4357
C	273.35	69.66	.0000	.8479	.0000	.0000	.0000	.0000	.3157

Table 18. Final balance after formation of CH_4. ΔG^H is Gibbs free energy for hydrate formation in the two sections of B. Z is CH4 compressibility factor for each of the two gas filled sections. N is mole numbers and subscript CH_4 is methane.

Sec	T(K)	P(bar)	ΔG^H (kJ/mole)	Z	$x^H_{CH_4}$	ρ^H (mole/m^3)	N_{CH_4} (moles)
A	277.35	47.96	.0000	.8972	.0000	.0000	1.3328
H1	275.15	47.96	-.1970	.0000	.1394	51235	.5932
H2	273.35	47.96	-.2700	.0000	.1403	51290	.5977
C	273.35	47.96	.0000	.8908	.0000	.0000	.2069

9.2 Injection of CO_2/N_2/ethanol

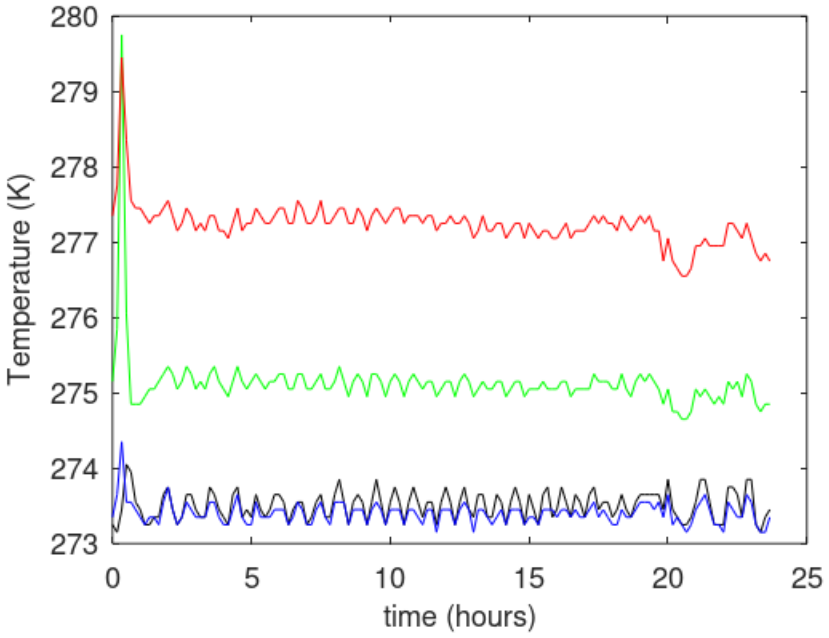

Figure 51. Temperature profiles during injection of CO_2/N_2/ethanol and associated reformation processes as function of experimental time in hours. Mole numbers CO_2 injected is 4.544, mole numbers N_2 injected is 0.9088 and 0.1 mole% ethanol. Mole numbers of water in cell is 7.3252 and initially in section B since distribution of water in gas is extremely low at experimental conditions.

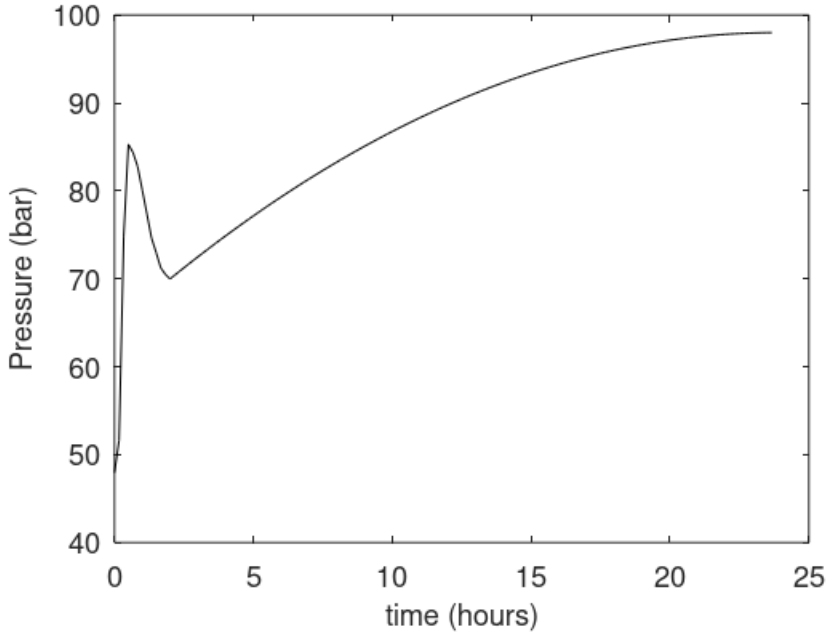

Figure 52. Pressure profile during injection of CO_2/N_2/ethanol and associated reformation processes as function of experimental time in hours. Mole numbers CO_2 injected is 4.544, mole numbers N_2 injected is 0.9088 and 0.1 mole% ethanol injected. Mole numbers of water in cell is 7.3252 and initially in section B since distribution of water in gas is extremely low at experimental conditions.

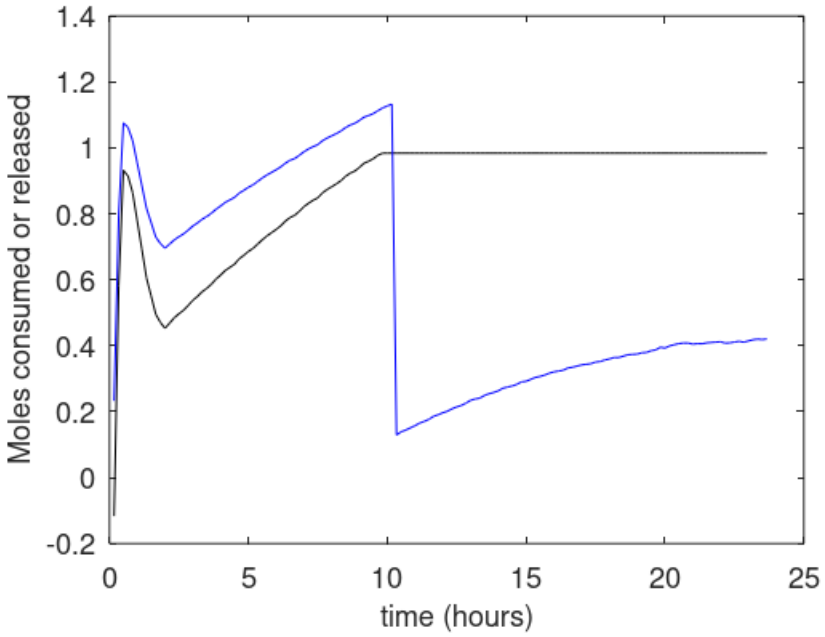

Figure 53. Released CH_4 from CH_4 hydrate is black curve and moles CO_2 consumed to formation of CO_2 hydrate is blue curve.

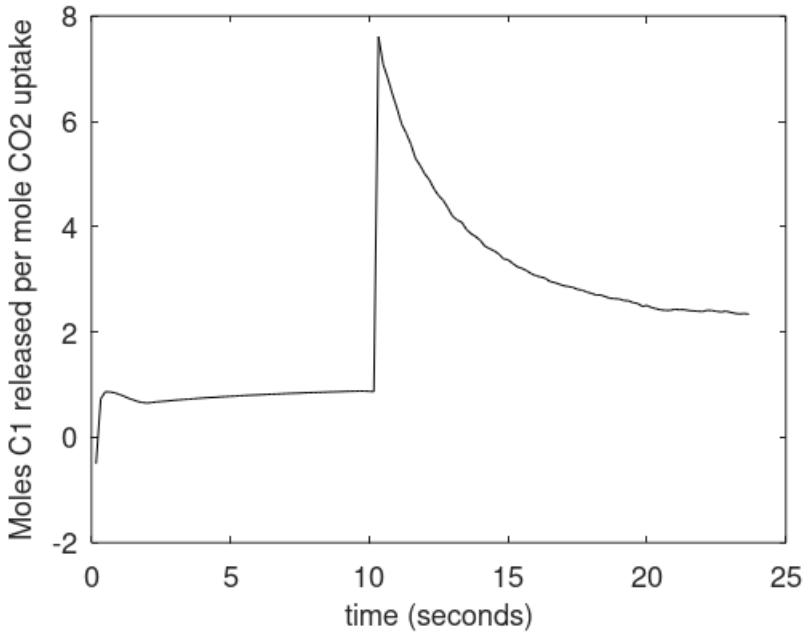

Figure 54. Mole released CH_4 per mole CO_2 uptake.

10. Experiment 10. 9 moles per cent ethanol, 4.544 mole CO_2, 0.9088 moles N_2 added.

10.1 Creation of CH_4 hydrate

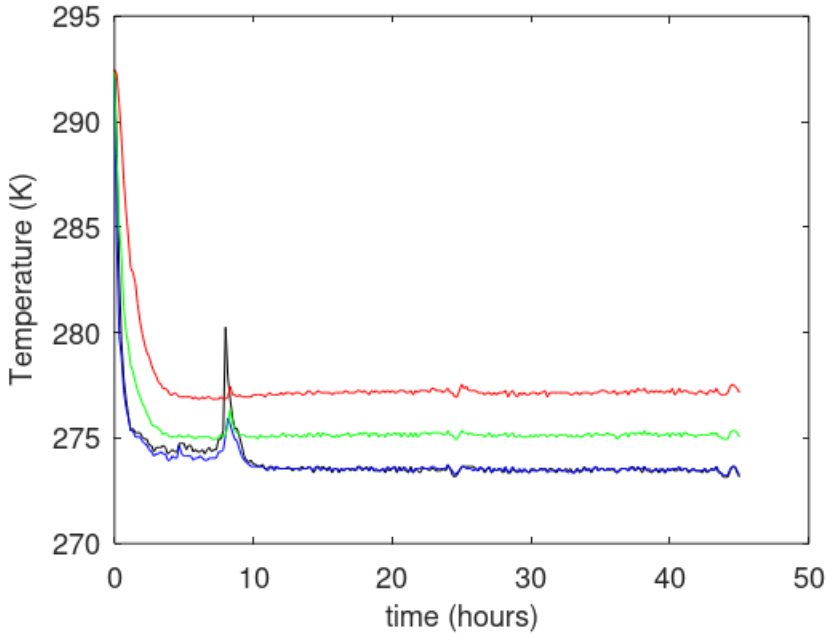

Figure 55. Temperature profiles during formation of CH_4 hydrate as function of experimental time in hours. Mole numbers methane in cell is 3.2102 and mole numbers of water in cell is 7.3252. T1 is black, T2 is blue, T3 is green and T4 is red.

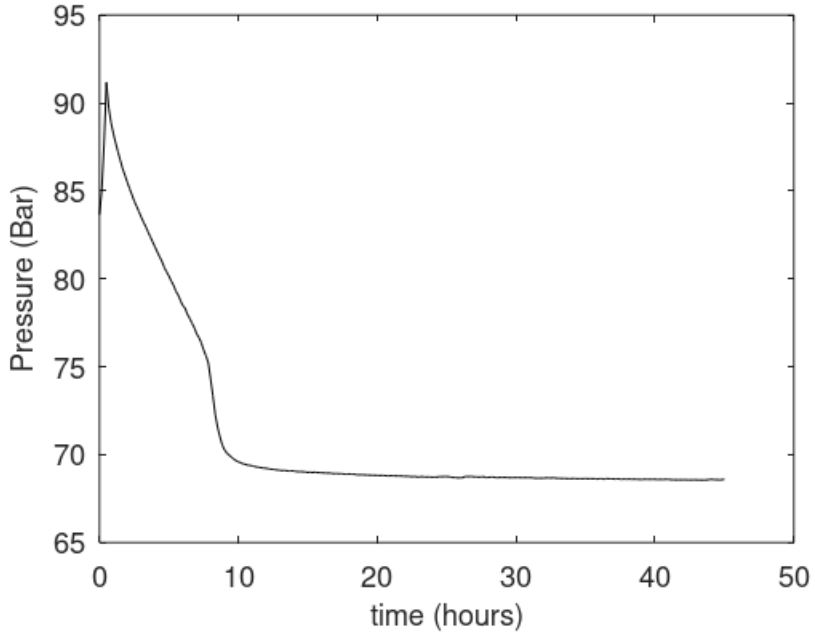

Figure 56. Pressure profile during formation of CH_4 hydrate as function of experimental time in hours. Mole numbers methane in cell is 3.2102 and mole numbers of water in cell is 7.3252.

Table 19. Final balance after formation of CH_4. ΔG^H is Gibbs free energy for hydrate formation in the two sections of B. Z is CH4 compressibility factor for each of the two gas filled sections. N is mole numbers. Superscript H is hydrate and superscript aq denote liquid water. Subscript H_2O is water and subscript CH_4 is methane.

Sec	T(K)	P(bar)	ΔG^H (kJ/mole)	Z	$x^H_{CH_4}$	ρ^H (mole/m^3)	$N^H_{H_2O}$ (moles)	$N^{aq}_{H_2O}$ (moles)	N_{CH_4} (moles)
A	277.15	68.60	.0000	.8584	.0000	.0000	.0000	.0000	1.9941
H1	275.05	68.60	-.3355	.0000	.1420	51389	2.7296	.9330	.4516
H2	273.25	68.60	-.4085	.0000	.1426	51428	2.7296	.9330	.4540
C	273.25	68.60	.0000	.8494	.0000	.0000	.0000	.0000	.3105

Table 20. Final balance after formation of CH_4. ΔG^H is Gibbs free energy for hydrate formation in the two sections of B. Z is CH4 compressibility factor for each of the two gas filled sections. N is mole numbers and subscript CH_4 is methane.

Sec	T(K)	P(bar)	ΔG^H (kJ/mole)	Z	$x^H_{CH_4}$	ρ^H (mole/m^3)	N_{CH_4} (moles)
A	277.35	48.22	.0000	.8967	.0000	.0000	1.3407
H1	276.05	48.22	-.1621	.0000	.1389	51205	.5907
H2	274.05	48.22	-.2437	.0000	.1400	51273	.5963
C	274.05	48.22	.0000	.8909	.0000	.0000	.2077

10.2 Injection of CO_2/N_2/ethanol

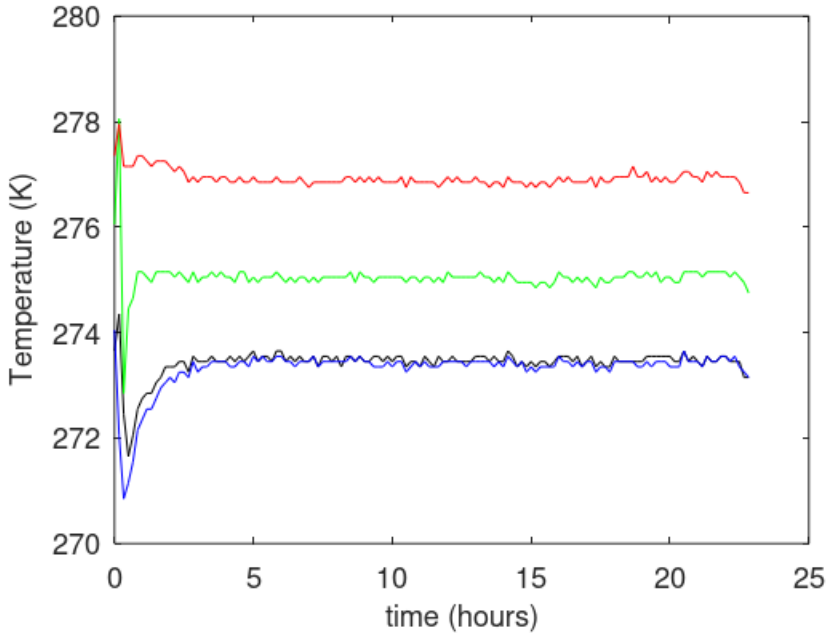

Figure 57. Temperature profiles during injection of CO_2/N_2/ethanol and associated reformation processes as function of experimental time in hours. Mole numbers CO_2 injected is 4.544, mole numbers N_2 injected is 0.9088 and 9 moles% ethanol. Mole numbers of water in cell is 7.3252 and initially in section B since distribution of water in gas is extremely low at experimental conditions.

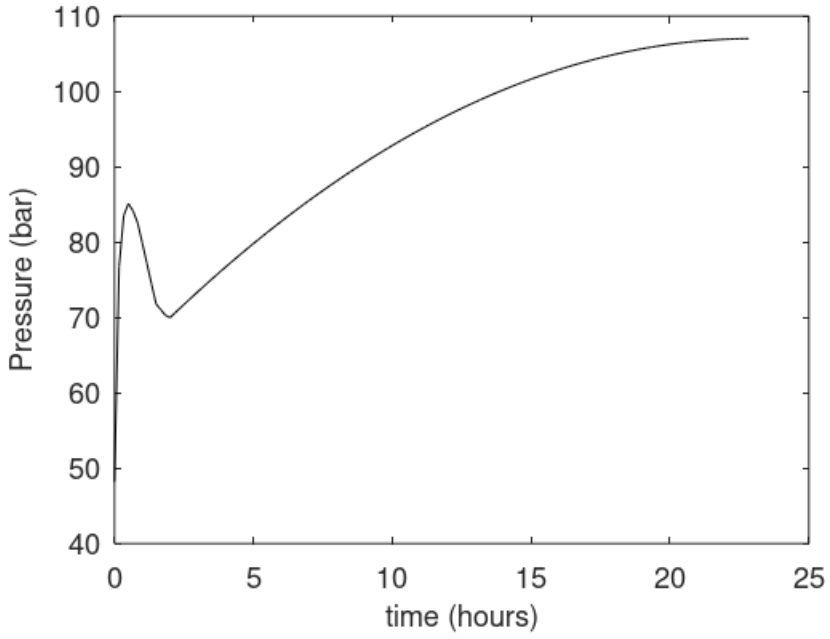

Figure 58. Pressure profile during injection of CO_2/N_2/ethanol and associated reformation processes as function of experimental time in hours. Mole numbers CO_2 injected is 4.544, mole numbers N_2 injected is 0.9088 and 9 moles% ethanol injected. Mole numbers of water in cell is 7.3252 and initially in section B since distribution of water in gas is extremely low at experimental conditions.

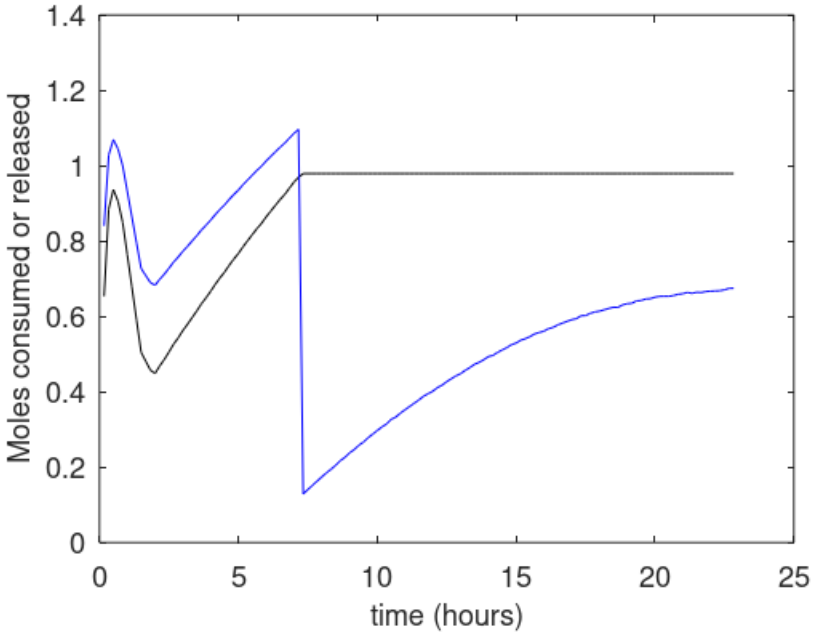

Figure 59. Released CH_4 from CH_4 hydrate is black curve and moles CO_2 consumed to formation of CO_2 hydrate is blue curve.

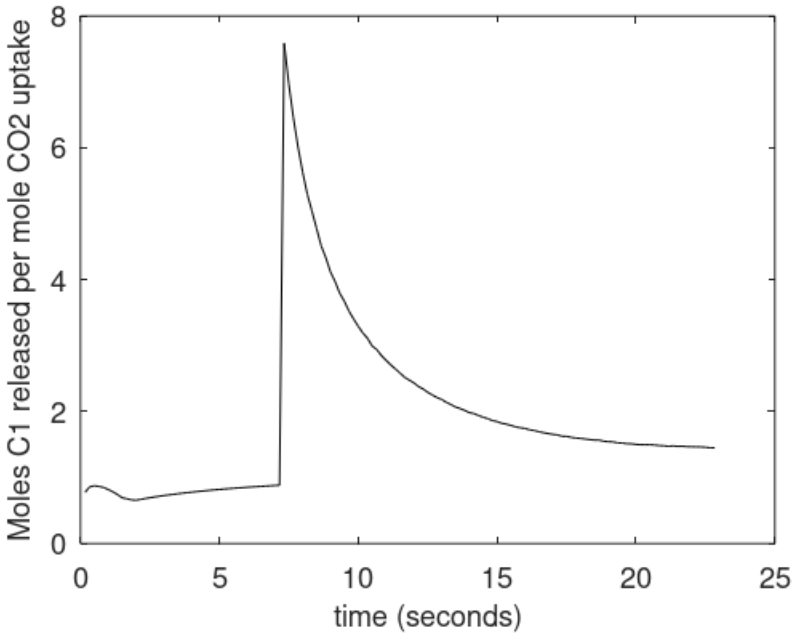

Figure 60. Mole released CH_4 per mole CO_2 uptake.

11. Experiment 11. 1 mole per cent ethanol, 4.544 mole CO_2, 0.9088 moles N_2 added.

11.1 Creation of CH_4 hydrate

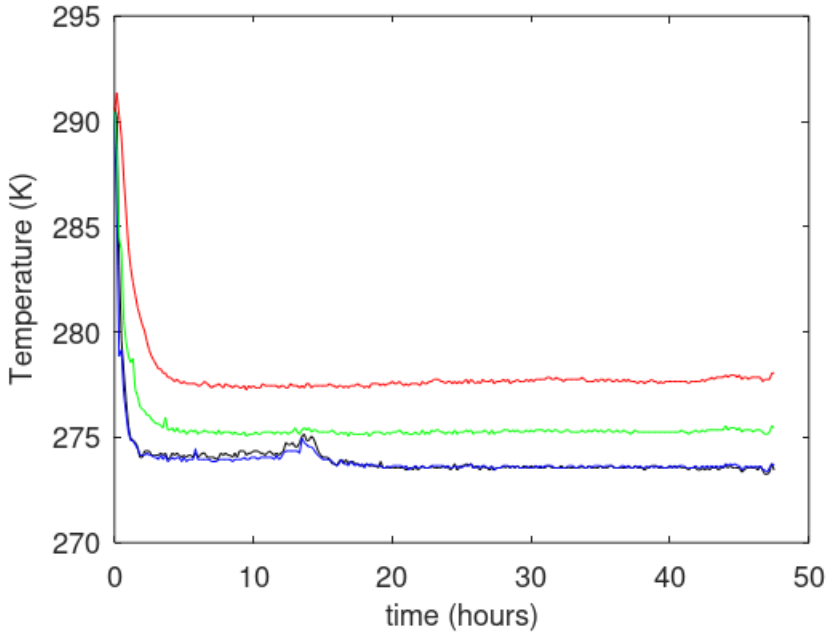

Figure 61. Temperature profiles during formation of CH_4 hydrate as function of experimental time in hours. Mole numbers methane in cell is 3.2102 and mole numbers of water in cell is 7.3252. T1 is black, T2 is blue, T3 is green and T4 is red.

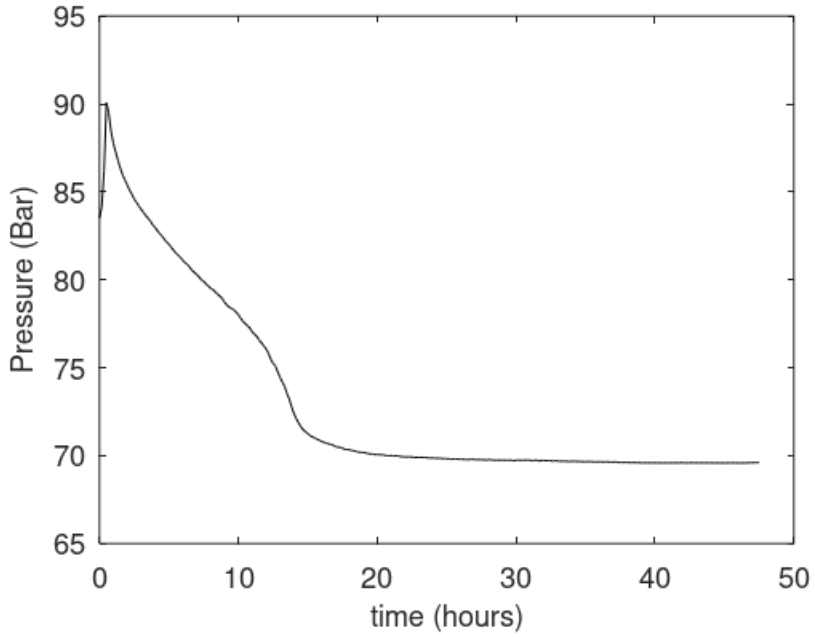

Figure 62. Pressure profile during formation of CH_4 hydrate as function of experimental time in hours. Mole numbers methane in cell is 3.2102 and mole numbers of water in cell is 7.3252.

Table 21. Final balance after formation of CH_4. ΔG^H is Gibbs free energy for hydrate formation in the two sections of B. Z is CH4 compressibility factor for each of the two gas filled sections. N is mole numbers. Superscript H is hydrate and superscript aq denote liquid water. Subscript H_2O is water and subscript CH_4 is methane.

Sec	T(K)	P(bar)	ΔG^H (kJ/mole)	Z	$x^H_{CH_4}$	ρ^H (mole/m^3)	$N^H_{H_2O}$ (moles)	$N^{aq}_{H_2O}$ (moles)	N_{CH_4} (moles)
A	278.05	69.62	.0000	.8587	.0000	.0000	.0000	.0000	2.0166
H1	275.45	69.62	-.3247	.0000	.1419	51384	2.6491	1.0135	.4380
H2	273.65	69.62	-.3980	.0000	.1426	51425	2.6491	1.0135	.4404
C	273.65	69.62	.0000	.8482	.0000	.0000	.0000	.0000	.3152

Table 22. Final balance after formation of CH_4. ΔG^H is Gibbs free energy for hydrate formation in the two sections of B. Z is CH4 compressibility factor for each of the two gas filled sections. N is mole numbers and subscript CH_4 is methane.

Sec	T(K)	P(bar)	ΔG^H (kJ/mole)	Z	$x^H_{CH_4}$	ρ^H (mole/m^3)	N_{CH_4} (moles)
A	278.05	48.78	.0000	.8967	.0000	.0000	1.3530

H1	275.55	48.78	-.1870	.0000	.1393	51229	.5927
H2	273.75	48.78	-.2602	.0000	.1402	51286	.5974
C	273.75	48.78	.0000	.8894	.0000	.0000	.2106

11.2 Injection of CO_2/N_2/ethanol

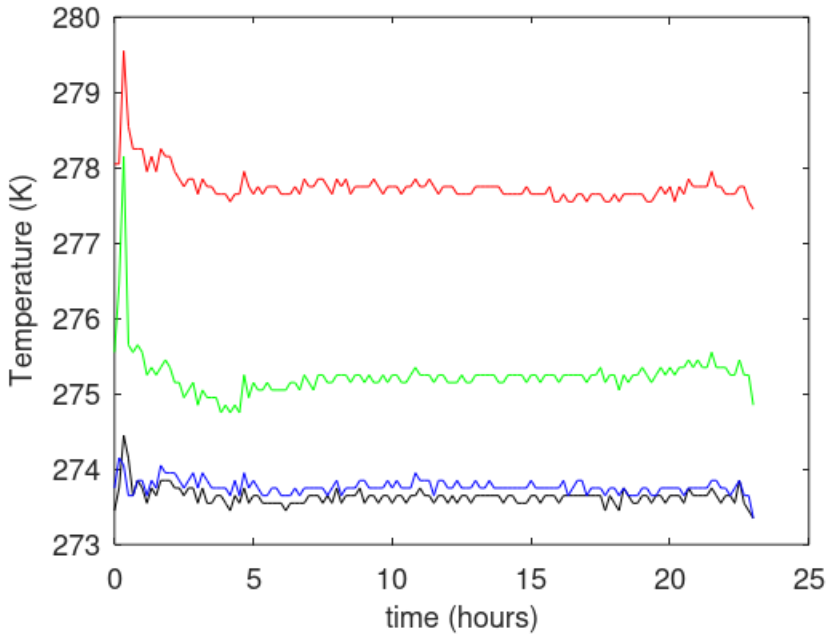

Figure 63. Temperature profiles during injection of CO_2/N_2/ethanol and associated reformation processes as function of experimental time in hours. Mole numbers CO_2 injected is 4.544, mole numbers N_2 injected is 0.9088 and 1 mole% ethanol. Mole numbers of water in cell is 7.3252 and initially in section B since distribution of water in gas is extremely low at experimental conditions.

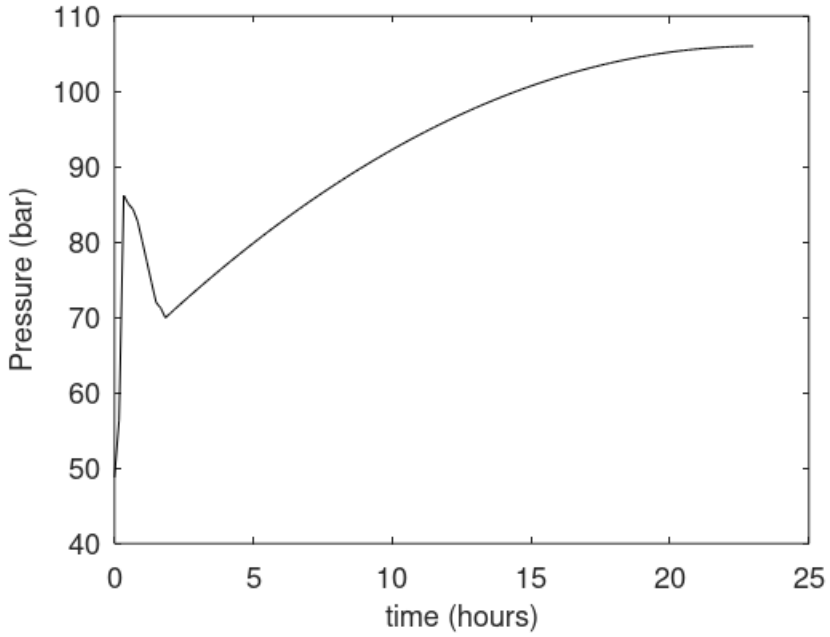

Figure 64. Pressure profile during injection of CO_2/N_2/ethanol and associated reformation processes as function of experimental time in hours. Mole numbers CO_2 injected is 4.544, mole numbers N_2 injected is 0.9088 and 1 mole% ethanol injected. Mole numbers of water in cell is 7.3252 and initially in section B since distribution of water in gas is extremely low at experimental conditions.

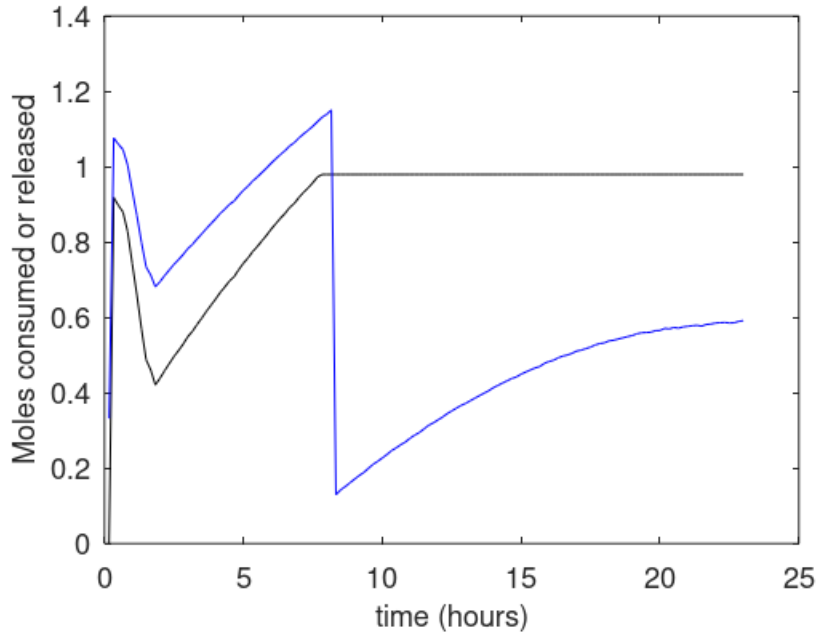

Figure 65. Released CH_4 from CH_4 hydrate is black curve and moles CO_2 consumed to formation of CO_2 hydrate is blue curve.

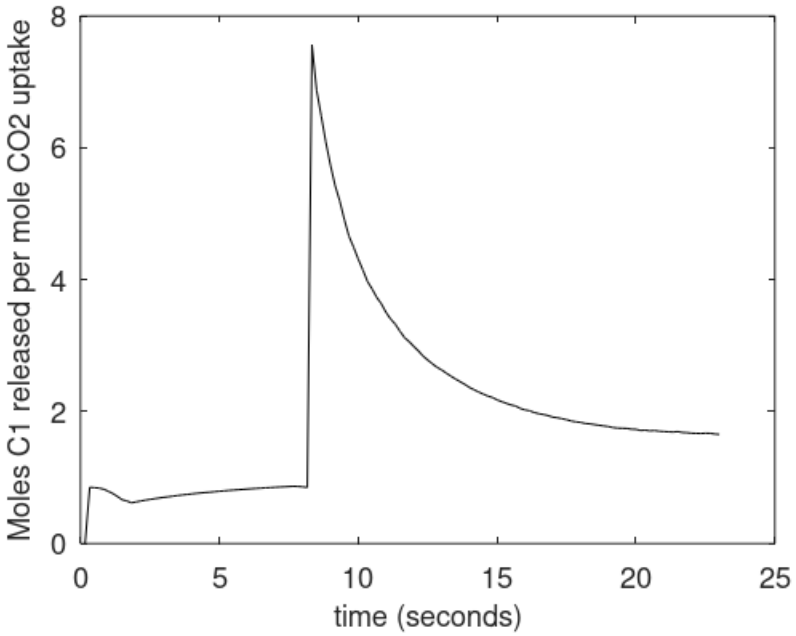

Figure 66. Mole released CH_4 per mole CO_2 uptake.

12. Experiment 12. 0.01 mole per cent ethanol, 4.544 mole CO_2, 0.9088 moles N_2 added.

12.1 Creation of CH_4 hydrate

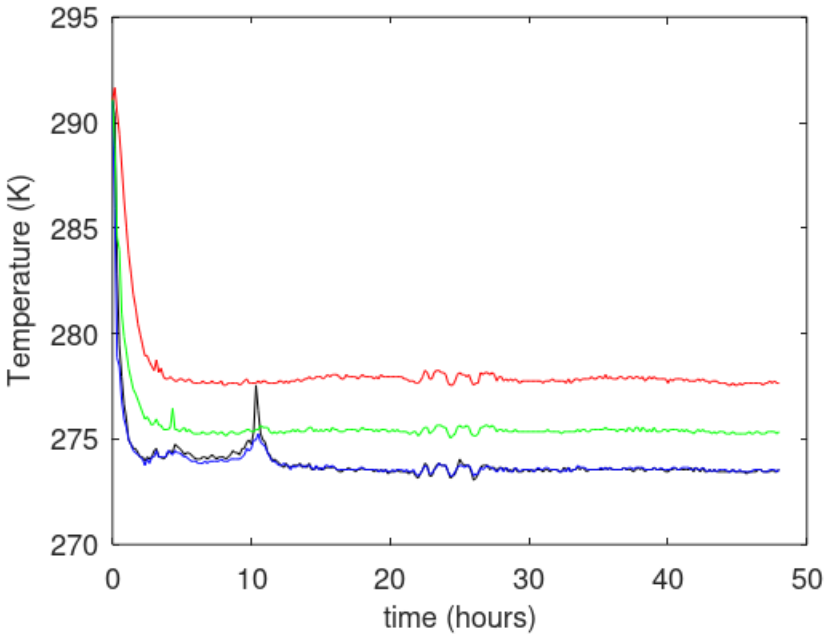

Figure 67. Temperature profiles during formation of CH_4 hydrate as function of experimental time in hours. Mole numbers methane in cell is 3.2102 and mole numbers of water in cell is 7.3252. T1 is black, T2 is blue, T3 is green and T4 is red.

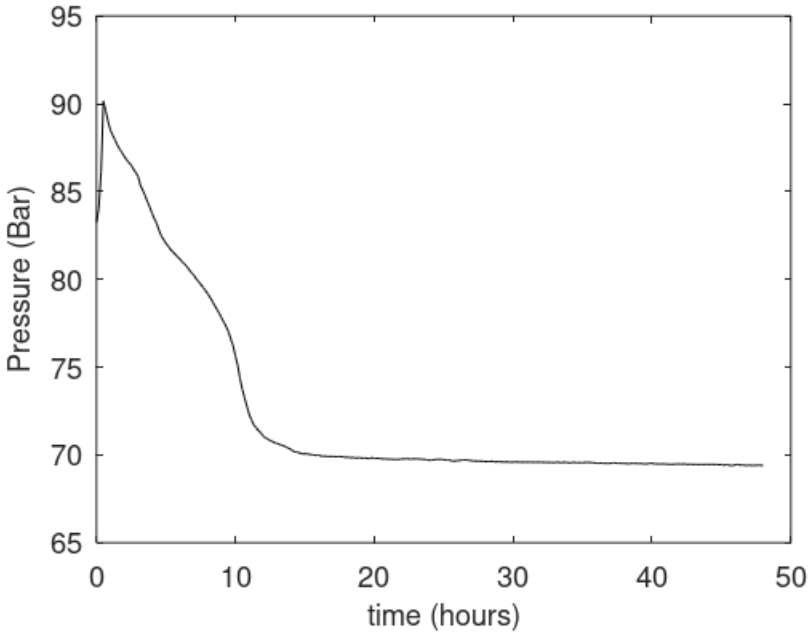

Figure 68. Pressure profile during formation of CH_4 hydrate as function of experimental time in hours. Mole numbers methane in cell is 3.2102 and mole numbers of water in cell is 7.3252.

Table 23. Final balance after formation of CH_4. ΔG^H is Gibbs free energy for hydrate formation in the two sections of B. Z is CH4 compressibility factor for each of the two gas filled sections. N is mole numbers. Superscript H is hydrate and superscript aq denote liquid water. Subscript H_2O is water and subscript CH_4 is methane.

Sec	T(K)	P(bar)	ΔG^H (kJ/mole)	Z	$x^H_{CH_4}$	ρ^H (mole/m^3)	$N^H_{H_2O}$ (moles)	$N^{aq}_{H_2O}$ (moles)	N_{CH_4} (moles)
A	277.65	69.40	.0000	.8582	.0000	.0000	.0000	.0000	2.0143
H1	275.35	69.40	-.3276	.0000	.1419	51385	2.6595	1.0031	.4398
H2	273.55	69.40	-.4008	.0000	.1426	51426	2.6595	1.0031	.4422
C	273.55	69.40	.0000	.8489	.0000	.0000	.0000	.0000	.3139

Table 24. Final balance after formation of CH_4. ΔG^H is Gibbs free energy for hydrate formation in the two sections of B. Z is CH4 compressibility factor for each of the two gas filled sections. N is mole numbers and subscript CH_4 is methane.

Sec	T(K)	P(bar)	ΔG^H (kJ/mole)	Z	$x^H_{CH_4}$	ρ^H (mole/m^3)	N_{CH_4} (moles)
A	277.85	48.38	.0000	.8972	.0000	.0000	1.3421
H1	275.35	48.38	-.1921	.0000	.1393	51232	.5930
H2	273.55	48.38	-.2652	.0000	.1403	51288	.5976
C	273.55	48.38	.0000	.8904	.0000	.0000	.2086

12.2 Injection of CO_2/N_2/ethanol

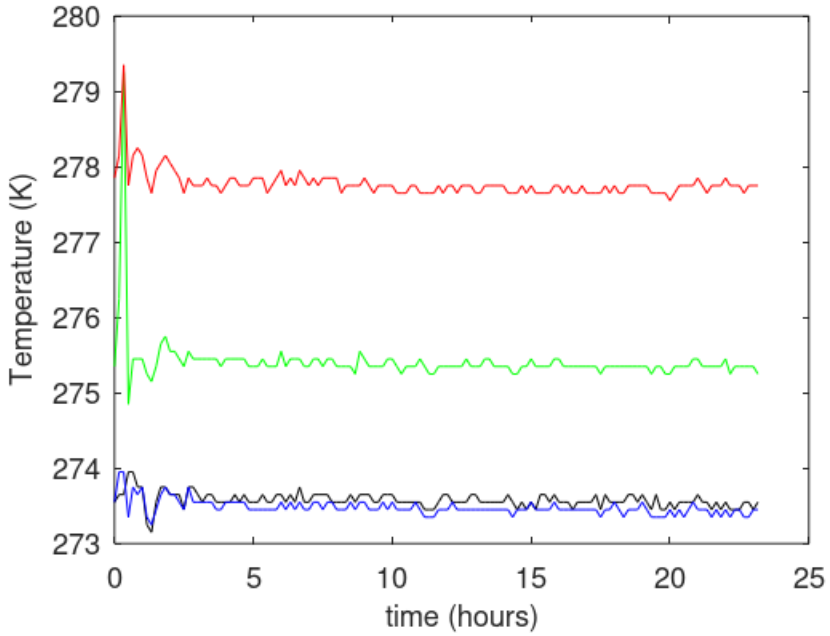

Figure 69. Temperature profiles during injection of CO_2/N_2/ethanol and associated reformation processes as function of experimental time in hours. Mole numbers CO_2 injected is 4.544, mole numbers N_2 injected is 0.9088 and 0.01 mole% ethanol. Mole numbers of water in cell is 7.3252 and initially in section B since distribution of water in gas is extremely low at experimental conditions.

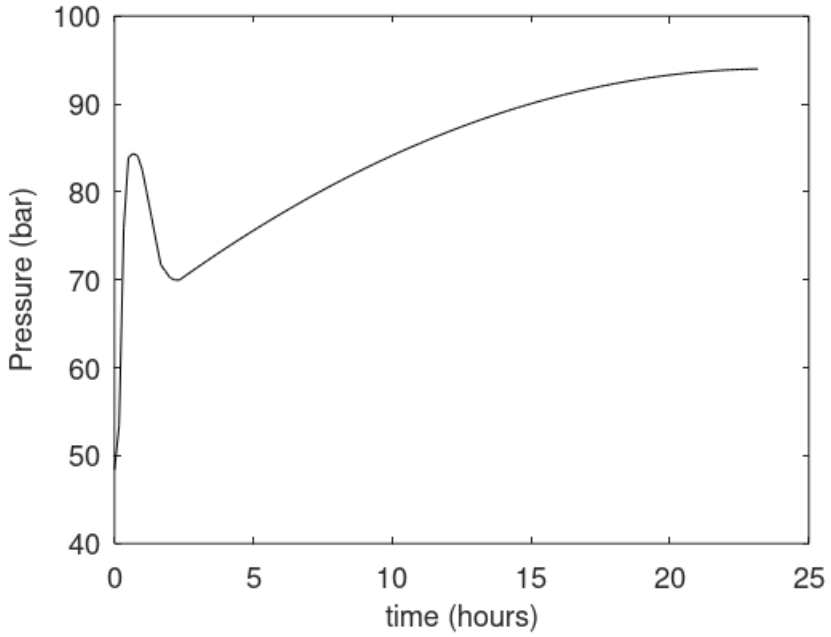

Figure 70. Pressure profile during injection of CO_2/N_2/ethanol and associated reformation processes as function of experimental time in hours. Mole numbers CO_2 injected is 4.544, mole numbers N_2 injected is 0.9088 and 0.01 mole% ethanol injected. Mole numbers of water in cell is 7.3252 and initially in section B since distribution of water in gas is extremely low at experimental conditions.

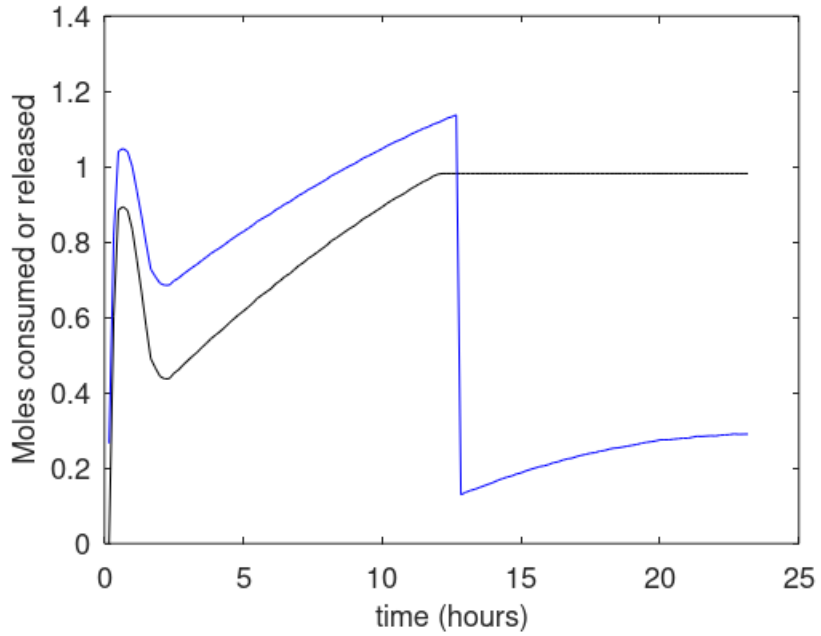

Figure 71. Released CH_4 from CH_4 hydrate is black curve and moles CO_2 consumed to formation of CO_2 hydrate is blue curve.

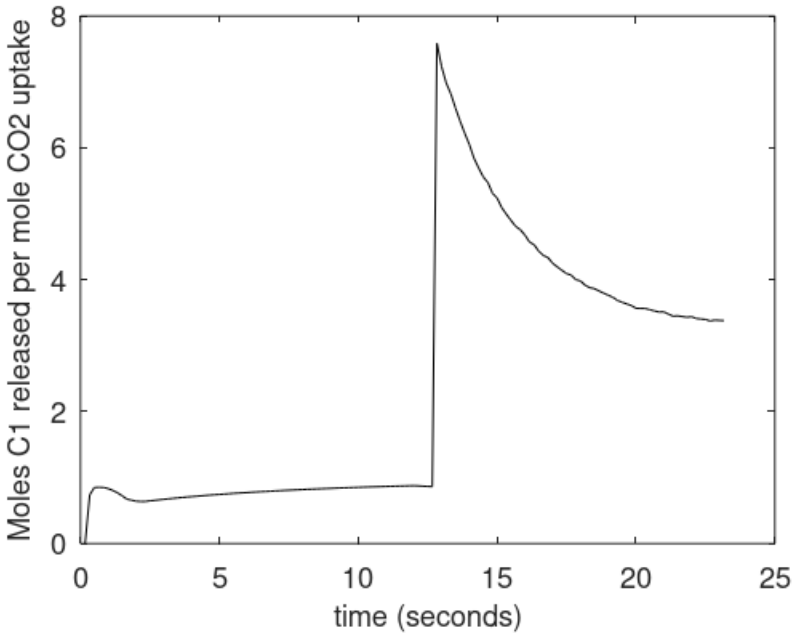

Figure 72. Mole released CH_4 per mole CO_2 uptake.

13. Effects of surfactant on hydrate reformation kinetics

The peak in the performance curves is not actually an indication of high efficiency. It is a transition point where all water is consumed, and very little new CO_2 is consumed. After that point CO_2 is consumed due to rearrangement of hydrate to higher filling during increased pressure. A second transition point is when all CH_4 from B have entered A as can be seen from the flat section of the released CH_4 curve. I.e.: No more CH_4 comes from B after that point. The peak performance in mole number released is higher than any of the systems with up to 30 moles per cent N_2 added but no surfactant. See Figure 73 below.

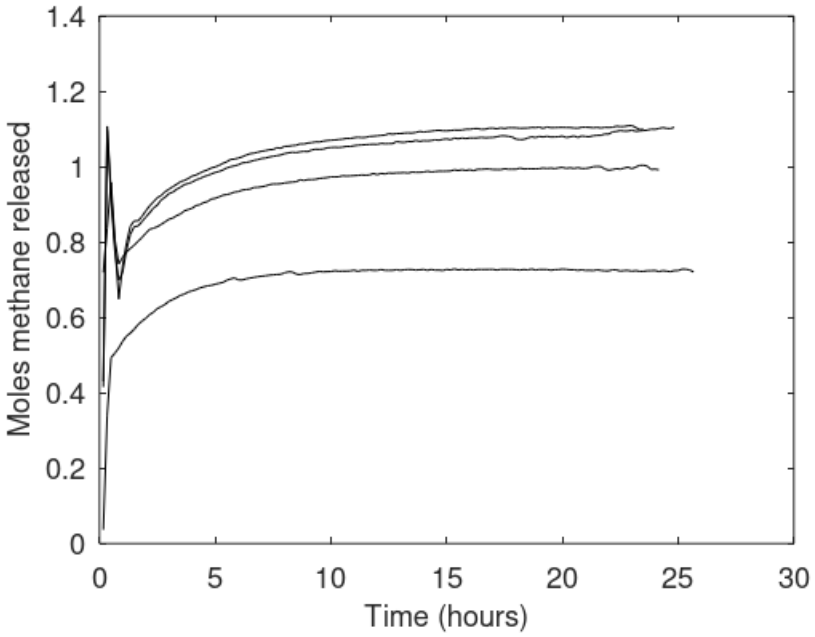

Figure 73. CH_4 released as function of time for injection of CO_2 containing nitrogen, lowest cure is for 0 N_2, then 10 moles per cent N_2 added, the 20 mole per cent N_2 added and upper curve is for 30 mole percent N_2. No surfactant added.

The time when all water is consumed is a good indicator of surfactant performance on hydrate reformation kinetics. NFM is fundamentally different than ethanol as it is expected to stay at the CO_2/water interface. As such there needs to be enough NFM for efficient interface coverage. But NFM in excess amounts might result in a mass transport delay through a relatively thick film of NFM.

Table 25. Time for consumption of all available water in section B for 20 mole % N2 added to CO2 and different mole % NFM added. As reference 0 % N2 added and 1 mole % NFM added results in a measured time of 10.167 hours.

Mole % NFM	Time for water consumption (hr)
0.01	10.667
0.1	8.667
1	7.833

3	10.1667

Table 26. Time for consumption of all available water in section B for 20 moles% N_2 added to CO_2 and different mole% Ethanol added. As reference 0% N_2 added and 3 moles% Ethanol added results in a measured time of 9.333 hours.

Mole % Ethanol	Time for water consumption (hr)
0.01	12.833
0.1	10.333
1	8.333
3	7.667
4	8.000
9	7.333

For Ethanol the difference is limited between 3 and 4 mole per cent added. Some might be due to experimental uncertainty but there is also a small difference in water activity due to dissolved ethanol. See for instance Kvamme for model details and verification towards experimental data.

In Figure 74 we plot temperature pressure stability limits for no ethanol added as well as 3 and 4 moles% added. The corresponding curves for water chemical potential in hydrate as well as Gibbs free energy for hydrate is plotted in Figure 75.

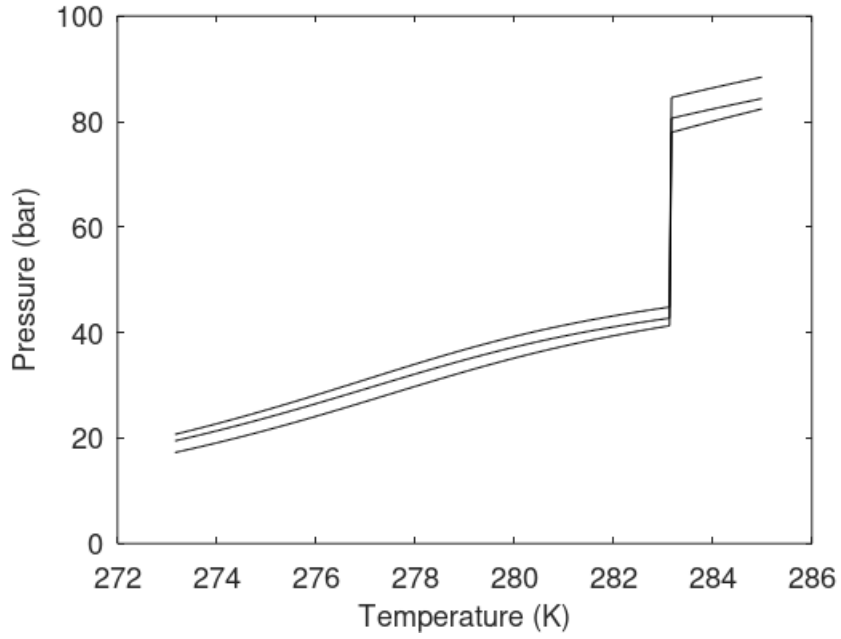

Figure 74. Pressure temperature hydrate stability limits for 80 moles% CO_2 and 20 mole% N_2 with 0 ethanol added (lowest curve), 3 moles% ethanol added (middle curve) and 4 moles% added (upper curve).

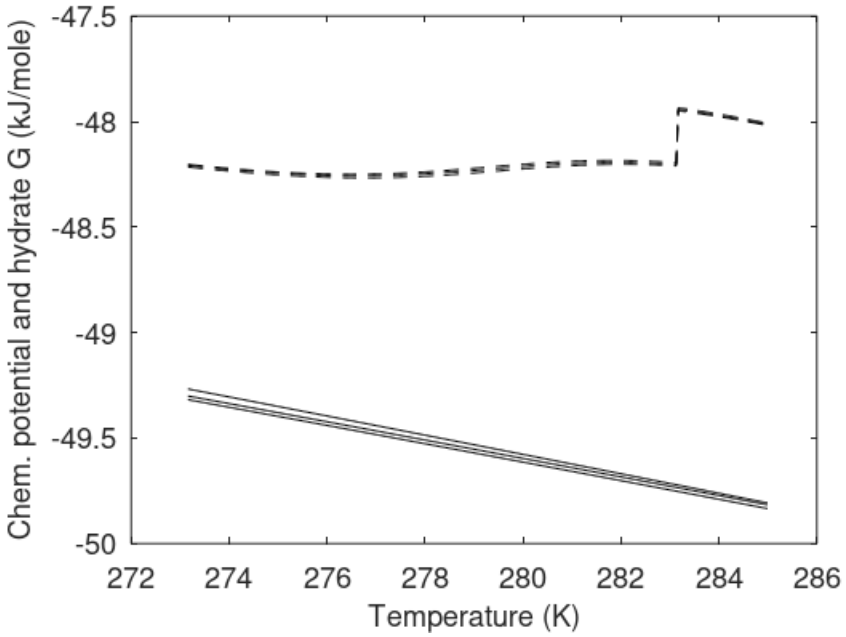

Figure 75. Water Chemical potential in hydrate (solid) and hydrate Gibbs free energy (dashed) for 80 moles% CO_2 and 20 moles% N_2 with 0 ethanol added (lowest curves), 3 moles% ethanol added (middle curves) and 4 moles% added (upper curves).

The primary mechanism is that the injection mixture of CO_2 and N_2 forms a new hydrate from water in the pores. The released heat from this hydrate formation will then dissociate the *in situ* CH_4 hydrate. In Figure 76 we plot enthalpy of hydrate formation for the CO_2/N_2 mixtures and enthalpy of hydrate formation for CH_4 hydrate. It is hard to distinguish the CO_2/N_2 curves and these are therefore plotted separately in Figure 77.

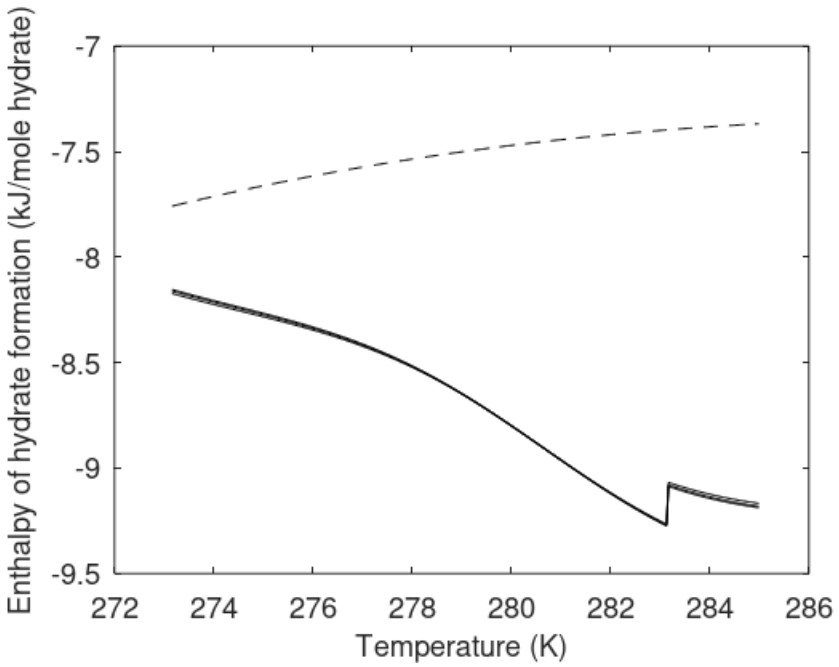

Figure 76. Enthalpy of hydrate formation for hydrate formed from 80 moles% CO_2 and 20 moles% N_2 with 0 ethanol added (lowest solid), 3 moles% ethanol added (middle solid) and 4 moles% added (upper solid). Dashed curve is enthalpy of hydrate formation for hydrate formed from CH_4.

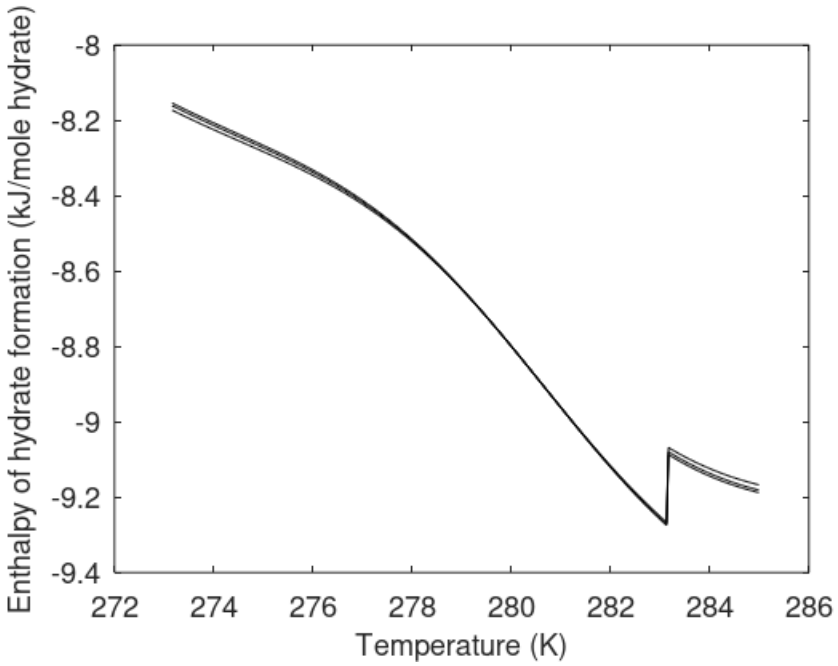

Figure 77. Enthalpy of hydrate formation for hydrate formed from 80 moles% CO_2 and 20 moles% N_2 with 0 ethanol added (lowest solid), 3 moles% ethanol added (middle solid) and 4 mole% added (upper solid).

The differences in water chemical potential and enthalpy of hydrate formation as function of concentration ethanol is limited but then again also the difference in time for consumption of water between 3 and 4 moles% is also limited so the differences that can be seen from Figures 75 and 77 may very well be the reason for the differences in Table 26.

d. ProPhyPlus software

Gases are into two categories: ideal or complete, and non-ideal or real. All gases have four variables are pressure (P), volume (V), temperature (T) and number of moles (n). There must be a relationship between these four variables. The simple law of gases of gases expresses the relationship between two variables when the other two variables are constant.

According to Boyle's law, when the number of moles and the temperature are constant, the pressure changes with the volume inversely proportionally.

The equation of state of an ideal gas expresses the relation between four variables and is a follows:

$$PV = nRT$$

In this equation, R is the ideal gas constant. Any gas that follows this equation is an ideal or perfect gas. But there is a more appropriate definition for ideal gas.

The ideal gas is a gas that:

1- The volume occupied by the gas molecules themselves (insulated volume or excluded volume) can be neglected or in other words zero.

2- Intermolecular forces (including gravitational forces) are zero.

Any factor that brings the gases closer to these two basic conditions brings the gas closer to the ideal state. For example, increasing volume, increasing temperature, decreasing pressure, decreasing density or density of molecules, or concentration all bring gases closer to the ideal state.

Real gas law: Under normal temperature and pressure conditions, real gases follow the rules of ideal gases relatively well. But at low temperature or at high pressure, or both, real gases deviate from the ideal gases. About real gases, there are two types of deviations from the ideal gas:

1- When attractions are important and unavoidable at relatively high pressure.

2- When the repulsion between particles is important and unavoidable at very high pressure. It causes of deviation from the ideal state due to the existence of intermolecular forces and molecular volume of the molecules themselves.

In the kinetic theory of gases, it is assumed that there is no gravitational force between the gas molecules. But there must be such an attraction, because all gases can be liquified. Molecular gravitational forces cause molecules to join together in a liquid state. There are two forces between molecules, the force of gravity and the force of repulsion. If the density or pressure of the gas is high, the distance between the gas molecules is small and the effective factor is the repulsive force between the molecules. If the gas pressure and gas density are low, the distance between the molecules is large and the effective factor is gravity. The factor that shows the deviation from ideal gases well is called the compressibility factor Z.

At high pressure or density, where the repulsive force prevails over the gravitational force, the real gas pressure is higher than the ideal gas pressure, resulting is $Z>1$ and it is more difficult to compress the real gas than the ideal gas. At low pressure and density, the gravitational force prevails over the repulsive force, $Z<1$ and the real gas pressure is lower than the ideal gas pressure, and it is easier to compress the real gas than the ideal gas.

Objective of this experiment: to determine the changes in the number of moles of CH_4 over time method. Our data in this test are gas temperature and pressure. The pressure given are in unit of bar. The temperature obtained from the experimental results are also reported in unit of ˚C, which must be converted to Kelvin. The relationship between kelvin temperature and ˚C is as follows:

Kelvin: ˚C + 273.15

ProPhyPlus software is a unique software for simulating and performing thermodynamic calculations of fluids. This program is an independent and advanced software that you are able to professionally calculate and simulate the various thermodynamic properties of fluids and their various combinations. This simulation takes place in a wide range of thermal processes and under various pressures. This program makes it very easy for us to access molecular thermodynamics and fluid-phase balance. ProPhyPlus software has the following specifications:

1- For calculations require the least input data, because only our data are from experimental results of temperature and pressure.

2- It has valid references.

3- It will be easy and convenient to use.

4- Due to the large number of points in each test, the calculation speed is high.

5- The results are valid.

6- Be able to use the desired equation of state.

7- Be able to calculate the desired thermodynamic conditions.

8- The obtained results are comparable to the experimental results and have an acceptable error.

Finally, ProPhyPlus software was used. This software has the ability to calculate most thermodynamic quantities.

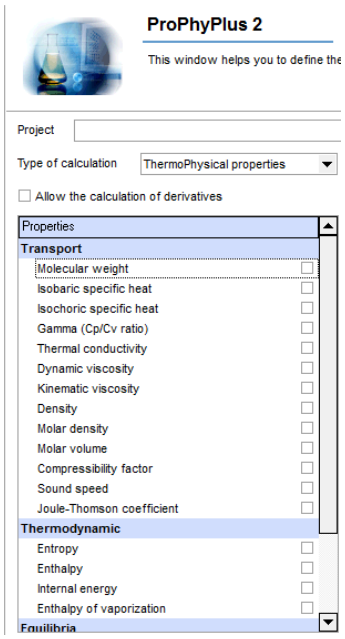

First, we select methane gas in the software and calculate the compressibility factor for each temperature and pressure in each test. That is, if we have 130 points in each test, we must calculate 130 compression factors.

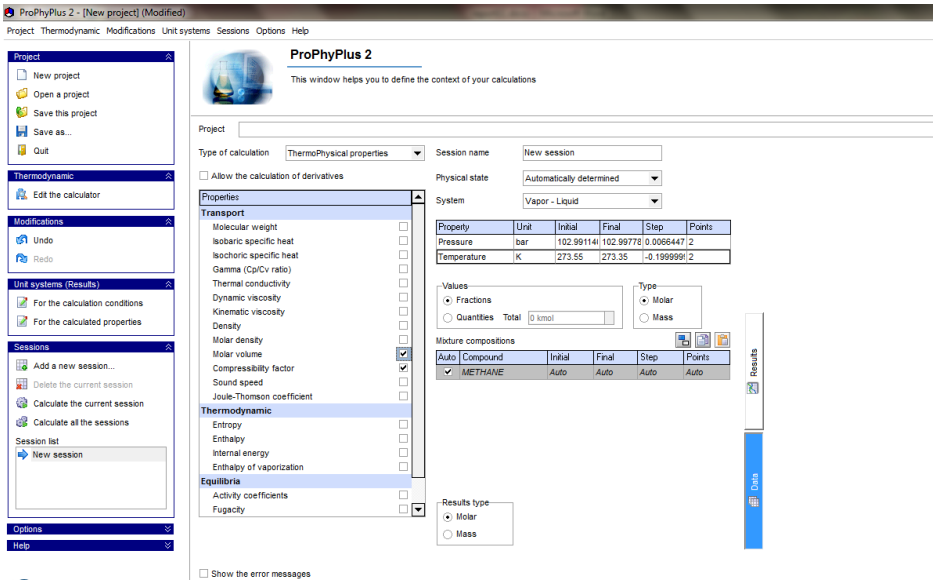

And after each calculation the amount of compressibility factor is calculated.

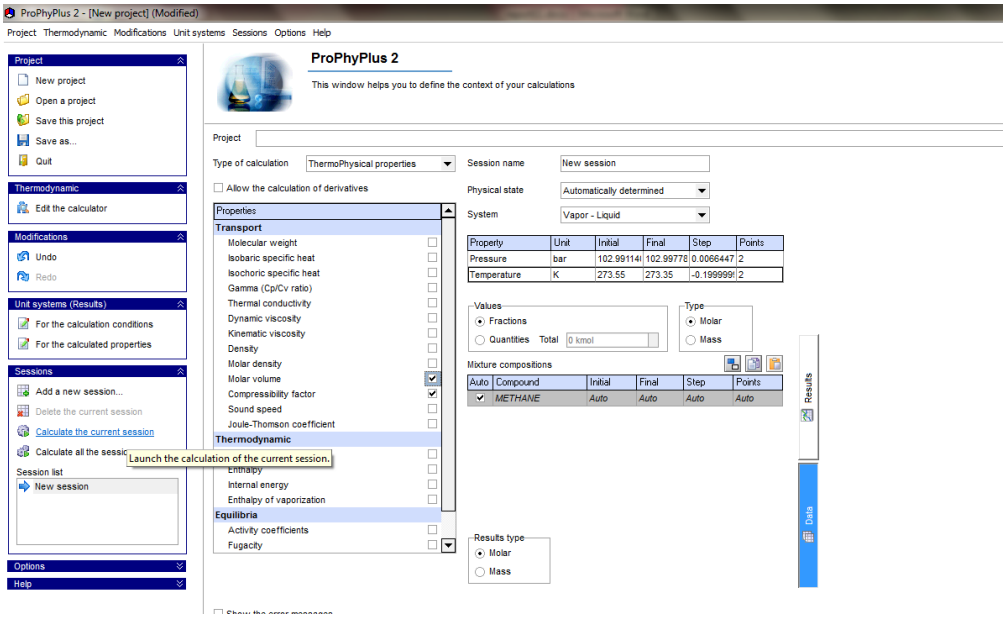
ProPhyPlus 2 - [New project] (Modified)
Project Thermodynamic Modifications Unit systems Sessions Options Help
ProPhyPlus 2
This window helps you to define the context of your calculations
Project
New project
Open a project
Save this project
Save as...
Quit
Thermodynamic
Edit the calculator
Modifications
Undo
Redo
Unit systems (Results)
For the calculation conditions
For the calculated properties
Sessions
Add a new session...
Delete the current session
Calculate the current session
Calculate all the sessic
Launch the calculation of the current session.
Session list
New session
Options
Help
Type of calculation
ThermoPhysical properties
Allow the calculation of derivatives
Session name
New session
Physical state
Automatically determined
System
Vapor - Liquid
Properties
Transport
Molecular weight
Isobaric specific heat
Isochoric specific heat
Gamma (Cp/Cv ratio)
Thermal conductivity
Dynamic viscosity
Kinematic viscosity
Density
Molar density
Molar volume
Compressibility factor
Sound speed
Joule-Thomson coefficient
Thermodynamic
Enthalpy
Internal energy
Enthalpy of vaporization
Equilibria
Activity coefficients
Fugacity
Property Unit Initial Final Step Points
Pressure bar 102.99114 102.99778 0.0066447 2
Temperature K 273.55 273.35 -0.199999 2
Values
Fractions
Quantities Total 0 kmol
Type
Molar
Mass
Mixture compositions
Auto Compound Initial Final Step Points
METHANE Auto Auto Auto Auto
Results type
Molar
Mass
Results
Data

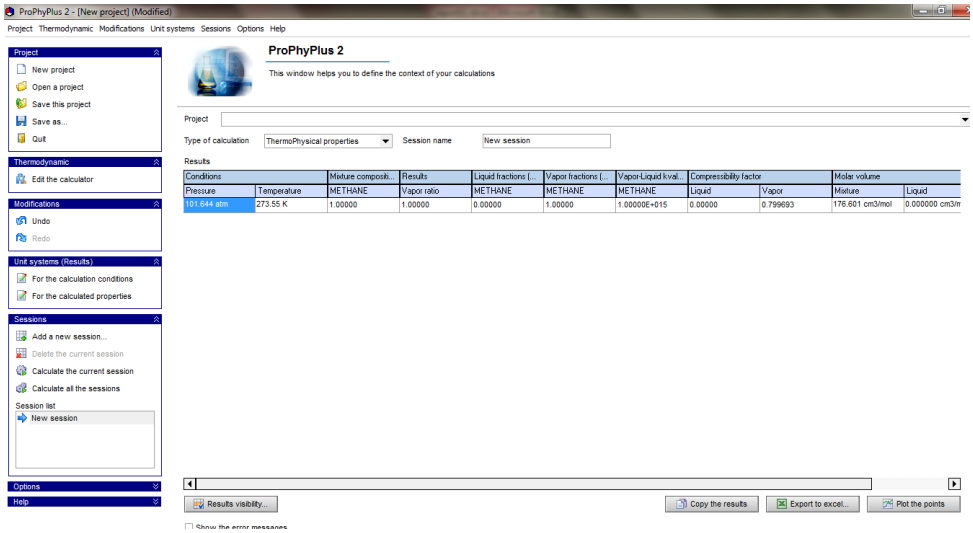
ProPhyPlus 2 - [New project] (Modified)
Project Thermodynamic Modifications Unit systems Sessions Options Help
ProPhyPlus 2
This window helps you to define the context of your calculations
Project
Type of calculation
ThermoPhysical properties
Session name
New session
Results
Conditions Mixture composi... Results Liquid fractions (... Vapor fractions (... Vapor-Liquid k-val... Compressibility factor Molar volume
Pressure Temperature METHANE Vapor ratio METHANE METHANE METHANE Liquid Vapor Mixture Liquid
101.644 atm 273.55 K 1.00000 1.00000 0.00000 1.00000 1.00000E+015 0.00000 0.79693 176.601 cm3/mol 0.000000 cm3/m
Results visibility...
Copy the results
Export to excel...
Plot the points

APPENDIX B: STANDARD OPERATING PROCEDURES

STANDARD OPERATING PROCEDURES

Date: February 2020

Building: Engineering Gateway

Room Number: EG1119

Test: Methane Hydrate Production with CO_2 liquid Injection.

Important Information

1. How to purge gas lines:
   1.1. Connect lines from main tank to secondary tank. Lightly tighten lines to secondary tank
   1.2. Close valve to secondary tank
   1.3. Open main tank
   1.4. Open first gas valve from main tank to fill lines with desired gas

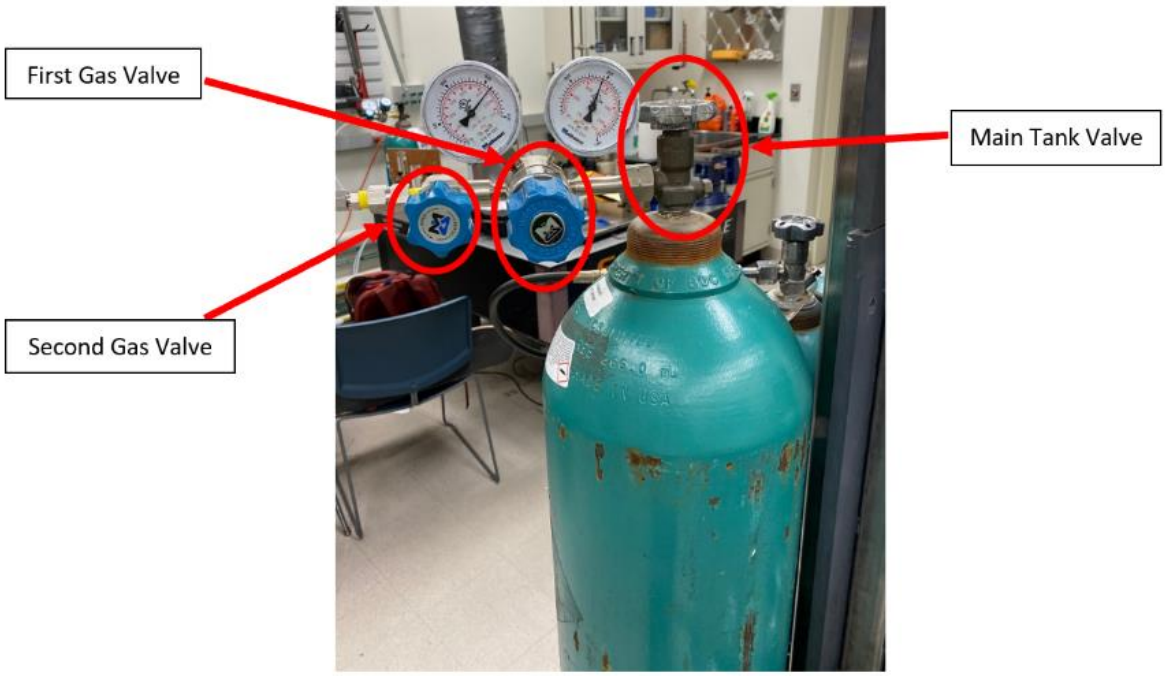

Figure 1: Main Gas Tank

1.5. Lightly open second valve from main tank for 5 seconds then close valve
1.6. Tighten lines on secondary tank

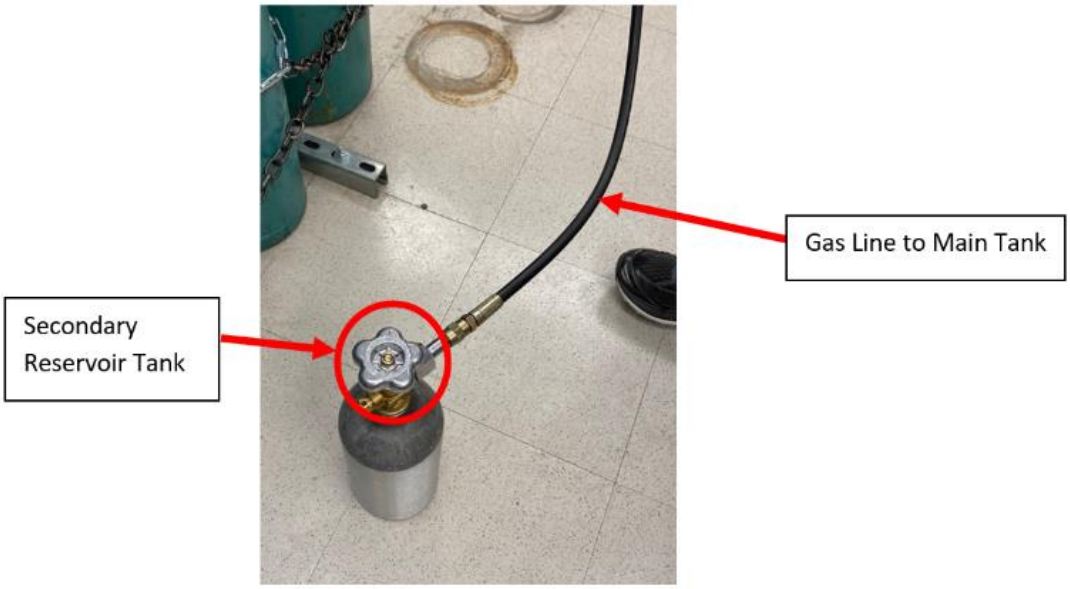

Figure 2: Secondary Reservoir Tank

1.7. Open secondary main tank valve
1.8. Slowly open secondary valve from main tank until valve is all the way open
1.9. Wait until desired pressure in secondary tank
1.10. Close secondary tank
1.11. Close second valve from main tank
1.12. Close first valve from main
1.13. Close main tank
1.14. Disconnect secondary tank from lines
1.15. Slowly open first valve from main tank
1.16. Slowly open second valve from main tank to release pressure in lines
1.17. Close the second valve and the first valve

2. Pressure Vessel

Figure 3: Pressure Vessel Fully Assembled

Figure 4: Pressure Vessel without Insulation

Valve Numbering List and Annotations

Valve Number	Valve Name	Valve Group
1	3 Way Methane Valve	Main Valve
2	3 Way CO_2 Valve	Main Valve
3	H_2O Valve	Main Valve
4	Bypass Loop Valve	Main Valve
5	Inlet Chiller Valve	Main Chiller
6	Outlet Chiller Valve	
7	Main Vacuum Valve	Vacuum System
8	Secondary Vacuum Valve	
9	Auxiliary Vacuum Valve	
10	Vacuum to Vessel	
11	Auxiliary Bypass Valve	Auxiliary Chiller System
12	Auxiliary Refrigeration out to vessel	
13	Auxiliary Refrigeration in from vessel	

Table 1: Valve Number System

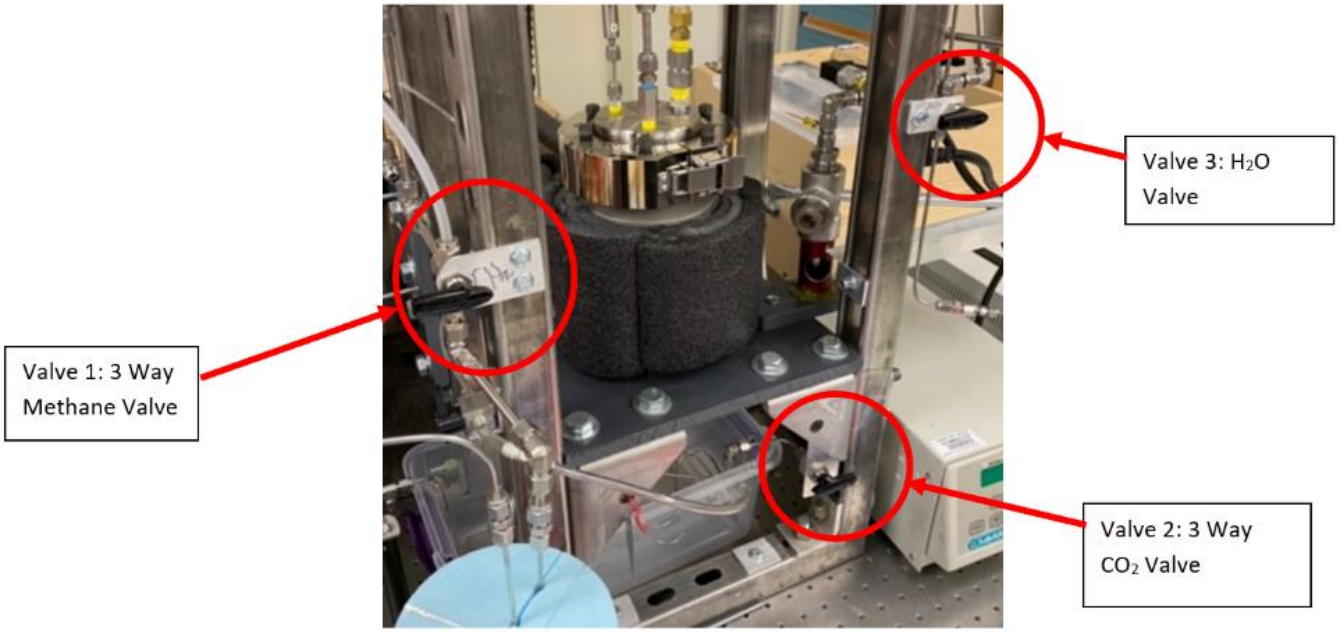

Figure 5: Front View of Vessel

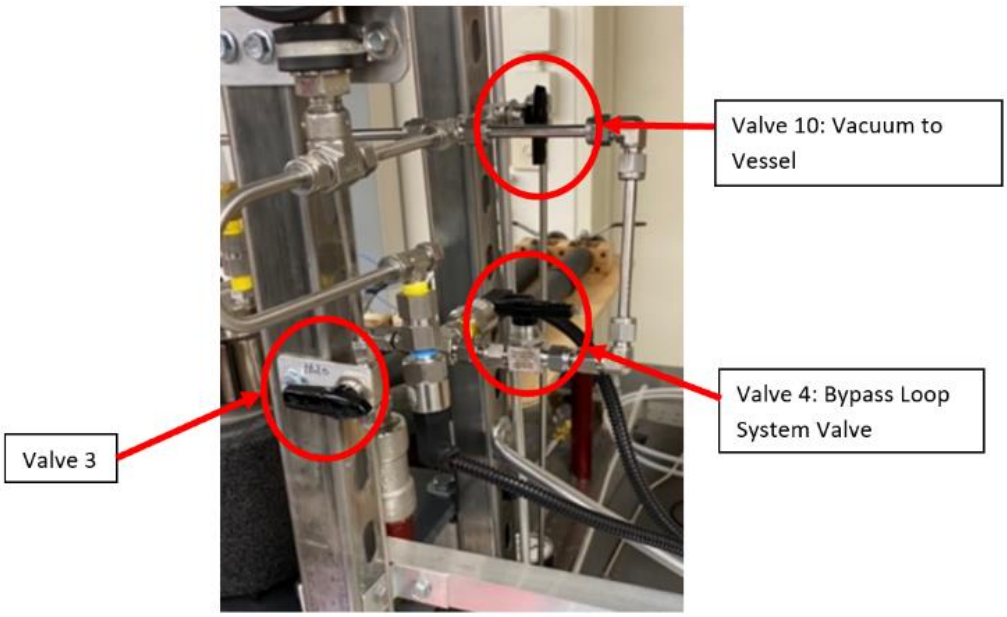

Figure 6: Side View of Vessel

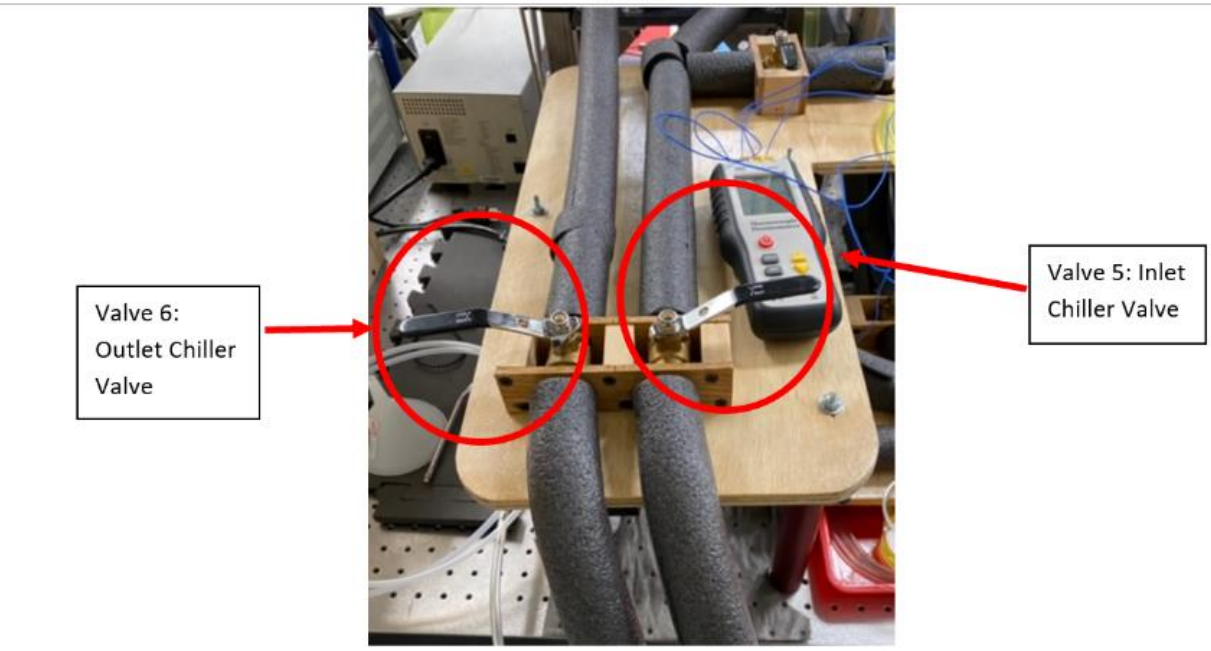

Figure 7: Valves for Chiller

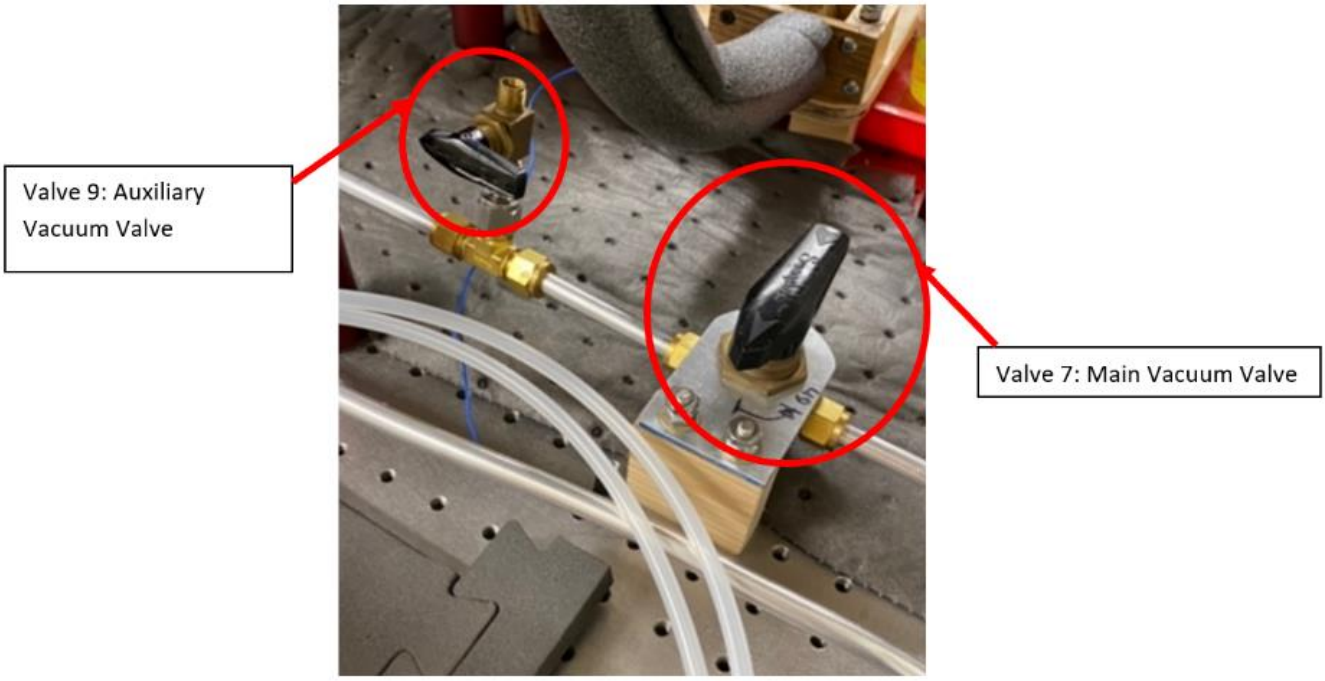

Figure 8: Vacuum Valves

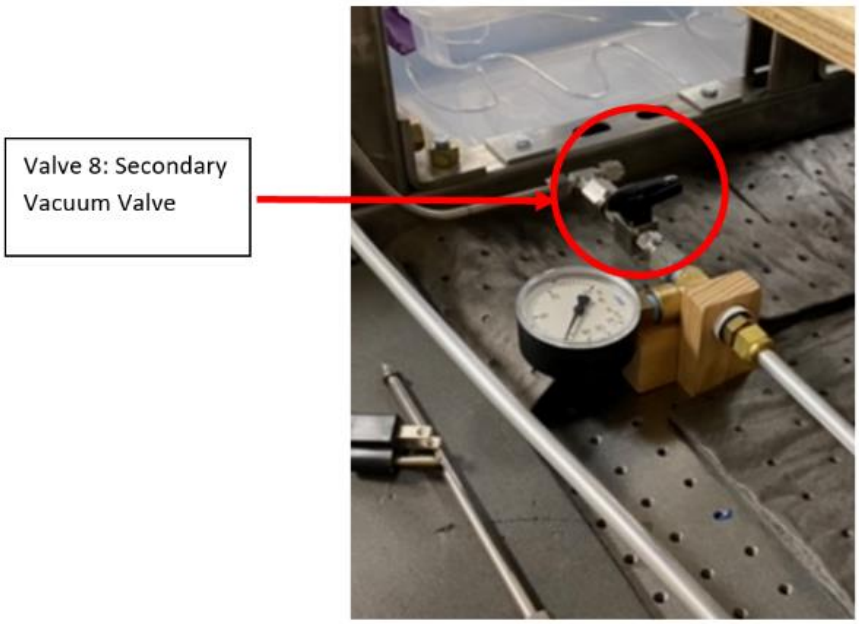

Figure 9: Vacuum Valve System

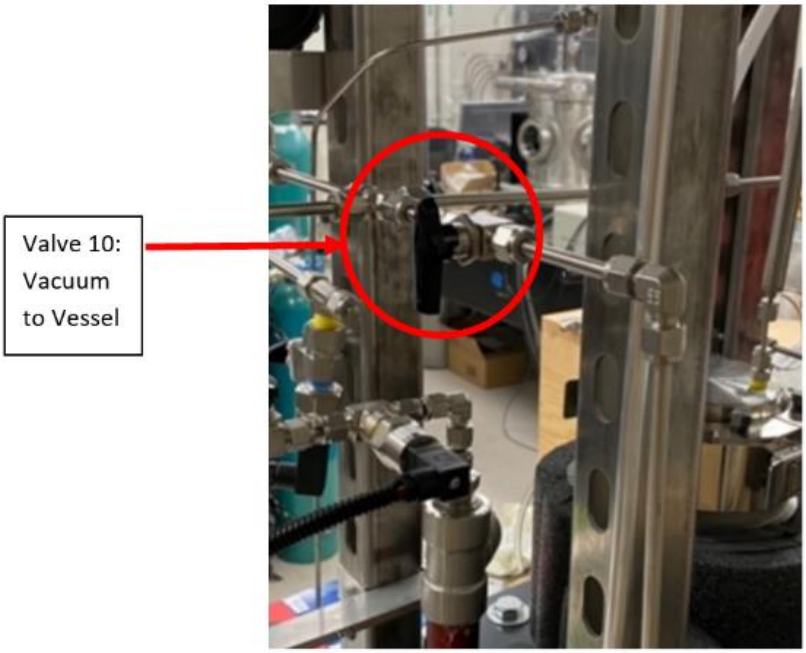

Figure 10: Back View of Vessel

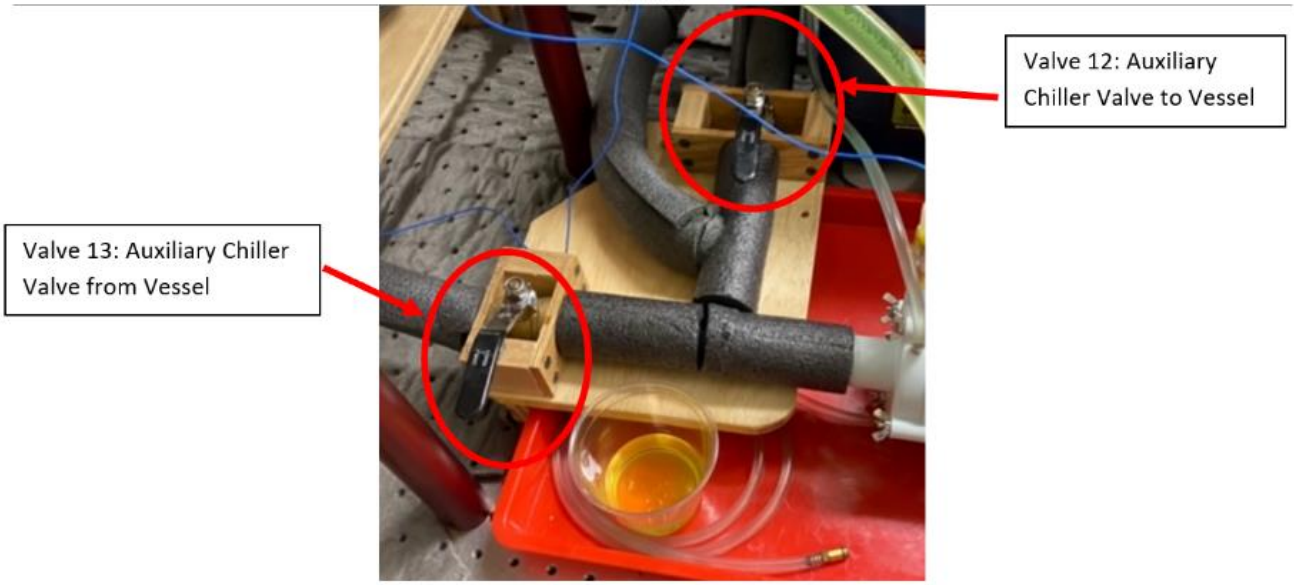

Figure 11: View of Auxiliary Chiller

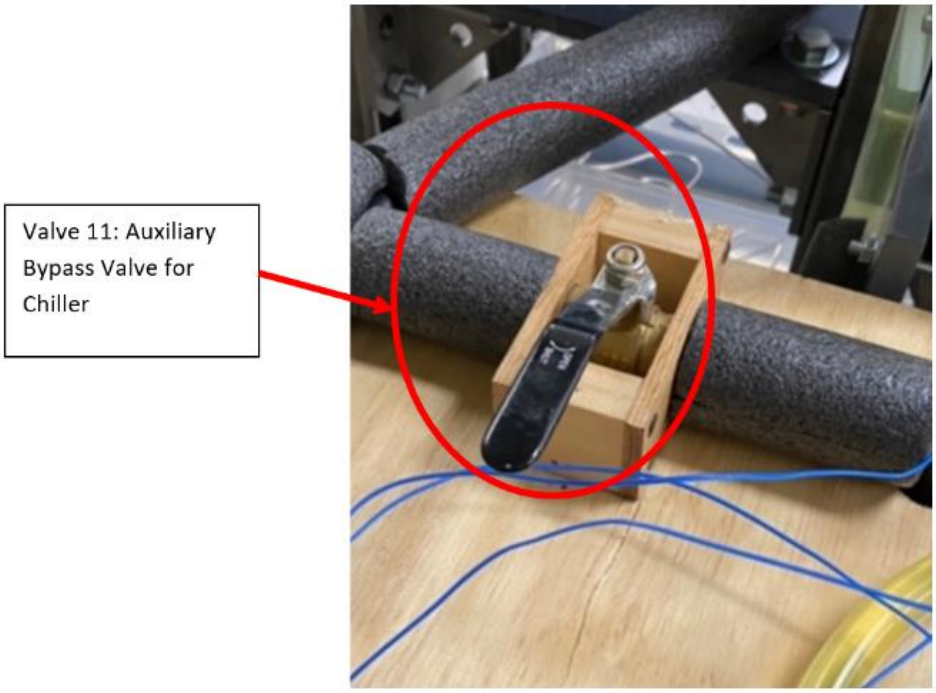

Figure 12: Auxiliary View of Valve System

List of Tools and Items

Table 2: List of items for procedure

Tool/Item/Machine	Type	Part Number	Quantity	Supplier
H_2O Syringe Pump	N/A	A09302	1	LabAlliance
CO_2 Syringe Pump	N/A	S10SNX01	1	LabAlliance
Torque Wrench	N/A	N/A	1	N/A
Wrench	7/16th	N/A	3	N/A
Adjustable Wrench	Small	N/A	2	N/A
Adjustable Wrench	Large	N/A	1	N/A
Vacuum Pump	N/A	E8CD482	1	Hanning
Chiller	N/A		1	Polystat
Auxiliary Chiller	N/A	N/A	1	UCI
Cup	N/A	N/A	1	N/A
Syringe	N/A	N/A	1	N/A
Scale	N/A		1	My Weigh
Balance	N/A		1	Ohaus
Vessel (with internal components)	N/A	Various	1	Various
Snoop	N/A	N/A	1	N/A
Dry Ice	N/A	N/A	10 lbs	N/A
Methane Gas	N/A	N/A	100 grams	N/A
CO_2	N/A	N/A	500 grams	N/A
Distilled Water	N/A	N/A	2 Liters	N/A

Reloading/Recharging Vessel

The recharging phase of the experiment is to be done while vessel is disassembled before the start of the procedure

1. Place basket inside the vessel in correct positioning

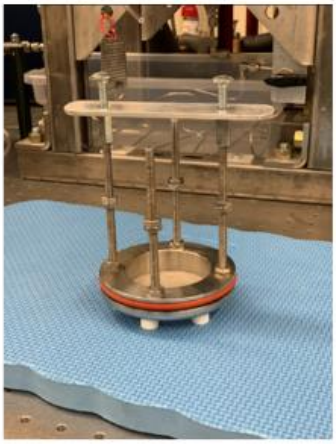

Figure 13: Basket (test section)

Figure 14: Installed Basket inside the vessel

2. Fill the vessel and basket with 535 grams glass beads and put lid on top of the glass beads.

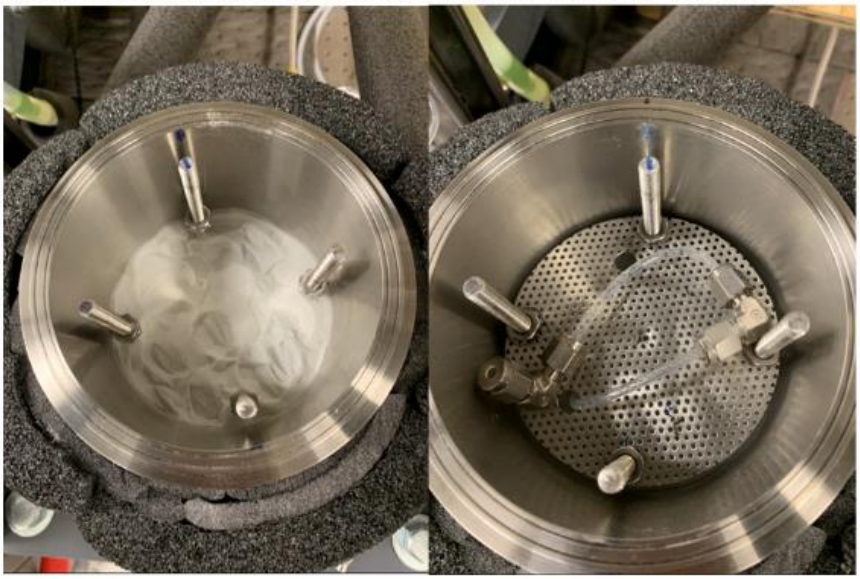

Figure 15. Basket with glass beads and perforated plate (lid) with halo water drip line

3. Screw in 4 bolts on threaded rods to secure basket lid on
4. Clean grooves of vessel lid with brush and damp cloth
5. Attach water line to lid and tighten
6. Connect line A
7. Connect line B
8. Connect emergency line
9. Connect thermocouple
10. Attach ring and clasp closed
11. Tighten bolts on ring in a crisscross manner
    - 11.1. Hand tighten all bolts on ring
    - 11.2. Use torque wrench set to 15 lb · ft on all bolts
    - 11.3. Retighten bolts with torque wrench set to 18 lb · ft
    - 11.4. Retighten bolts with torque wrench set to 22 lb · ft
    - 11.5. Wait 10 minutes and retighten bolts with torque wrench set to 23 lb · ft
12. Attach nitrogen tank to vessel and raise pressure to 60 bar
13. Let the vessel sit for 24 hours to check for leaks

Preparations

1. Ice Water Heat Exchanger Chamber

1.1. Fill heat exchanger chamber with enough water and ice to fill pickup points inside

Figure 16: Heat Exchanger for Methane Gas

NOTE: this should be done 30 min prior to starting the procedures

Main Procedure

1. Vacuuming Vessel and Lines

1.1. Close lines leading to vessel

1.2. Plug in and turn on vacuum pump

1.2.1. The button must be firmly pressed to ensure the vacuum pump stays on

1.3. Slowly open valve 7, valve 8, and valve 10

1.4. Wait 15 min using TIMER. Pressure on gauge should read -30 inch * Hg after the 15 min

Figure 17: Pressure Gauge from Vacuum Lines

1.5. Slowly close valve 10, valve 8, and valve 7
1.6. Turn off vacuum pump and unplug

2. Charging Small Methane Reservoir

2.1. Close valve to small methane reservoir
2.2. Open main methane supply tank
2.3. Purge lines to fill prefill lines with methane and to expel atmospheric pressure
2.4. Slowly open valve lines to small methane tank. The pressure should slowly rise to not increase temperature of methane.
2.5. Wait until small methane tank reaches 1500 psi
2.6. Close small methane reservoir valve
2.7. Close main methane supply tank valve
2.8. Purge lines to expel methane
2.9. Weigh small methane reservoir and record captured methane weight

3. Cooling Methane to Vessel

3.1. Close valve 1
3.2. Connect small methane reservoir to ice water heat exchanger
3.3. Open small methane reservoir valve and purge lines
3.4. Check for leaks in lines by applying Snoop to the connecting points from the lines to the valves
3.4.1. There should be 8 points that are checked along the lines

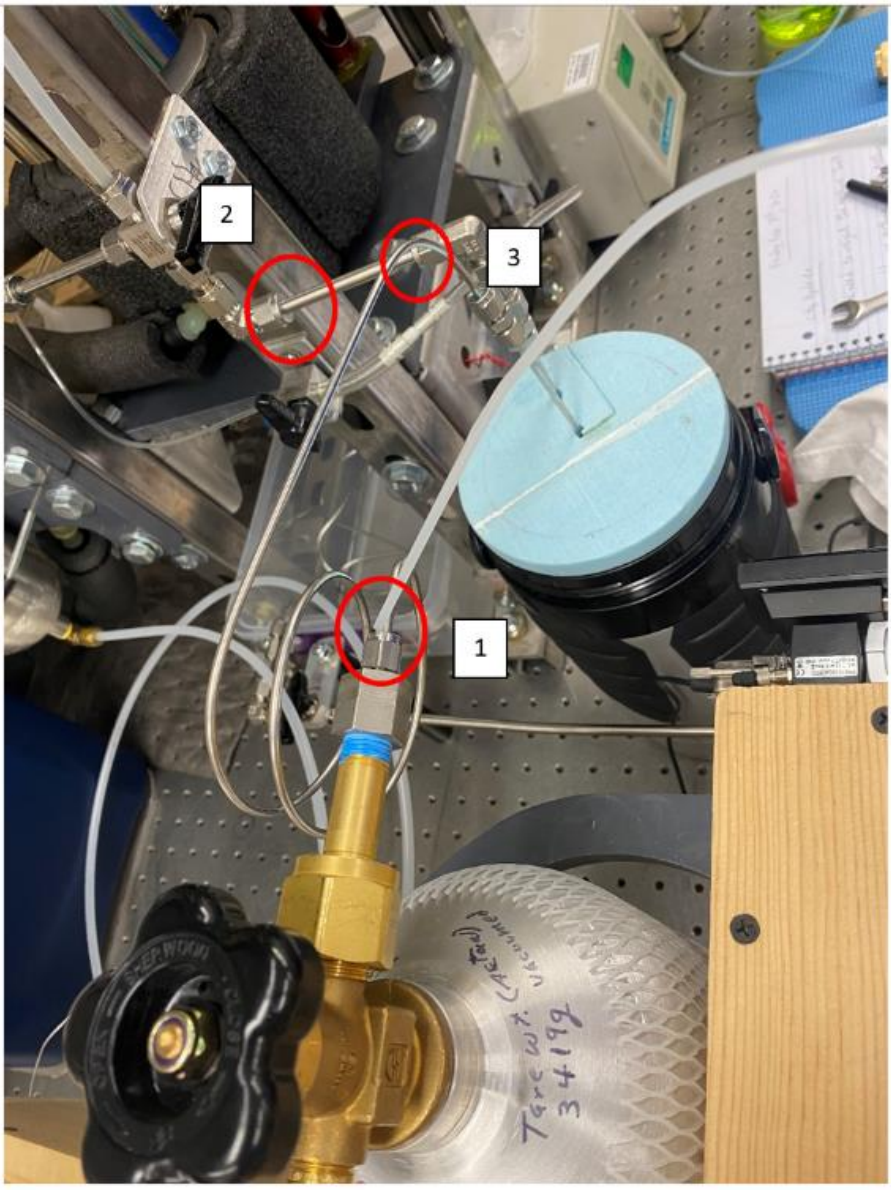

Figure 18: Reference for Leak Points

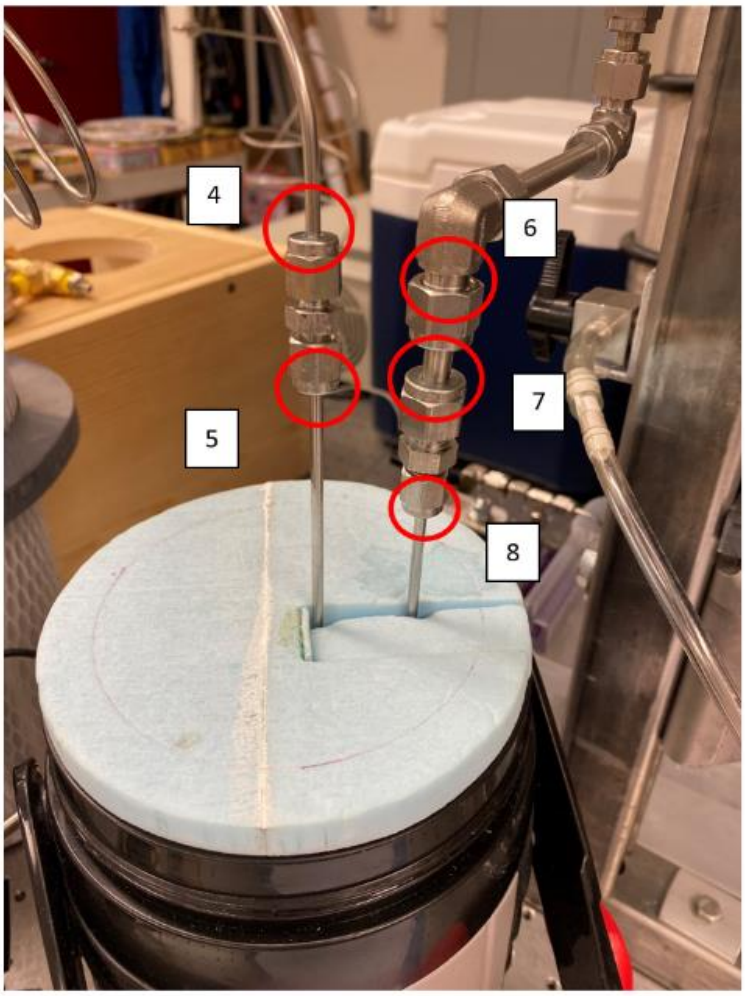

Figure 19: Reference for Leak Points

3.4.2. If there are leaks, close small methane tank valve and disassemble the lines that had leaks

3.4.3. Clean connecting points with a cotton swab Q-tip that is dipped in soap and water mixture

Figure 20: Cleaning Connection Lines

3.4.4.Apply Three Bond Liquid Gasket sealant to connecting points on gas line

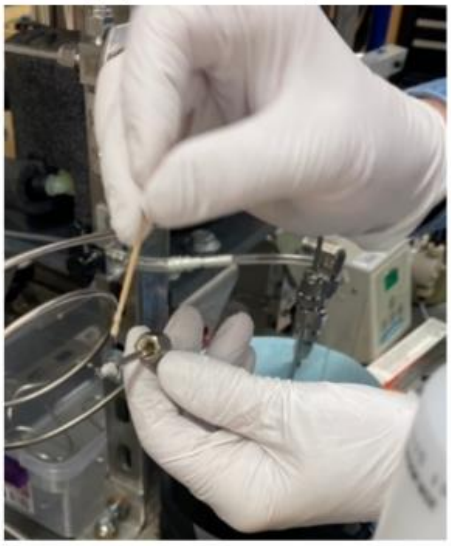

Figure 21: Applying Threebond Sealant

3.4.5. Reweigh small methane tank before reassembling onto heat exchanger and record measured weight.

3.4.6. Recheck gas lines for leaks

4. Charging Vessel with Methane Gas

4.1. While checking pressure gauge on vessel, slowly open valve 1.

4.1.1. Pressure inside the vessel should be rising about 1 bar every 5 to 10 seconds to reduce compression heating and reduce turbulence

4.1.2. Wait till pressure reaches about 83 bars and close valve 1. Set timer for 35 min and wait till tank stabilizes at ~ 83 bars.

4.1.3. If vessel goes below 83 bars, start process over and add more methane and wait till vessel stabilizes at 83 bars

4.2. Disconnect small methane tank and record weight.

5. Charging Water Reservoir

5.1. Clean a cup with soap and water to ensure no dirt particles get inside system

5.2. Fill cleaned cup with Distilled Water

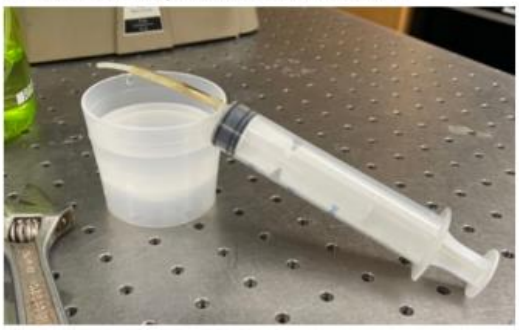

Figure 22: DI water cup and Syringe

5.3. Fill water reservoir to 400 mL

5.3.1. Use syringe to inject distilled water into water reservoir to reduce air bubbles inside of water

Figure 23: Water Syringed into Water Reservoir

5.4. Turn on H_2O syringe pump
5.5. Set flow rate to 5 mL
5.6. Close valve 3
5.7. Bleed lines to get rid of air bubbles in lines
5.8. Place reservoir on balance and use weights to match. Remove 110 grams from the opposite side. This is the amount that will go into the vessel.

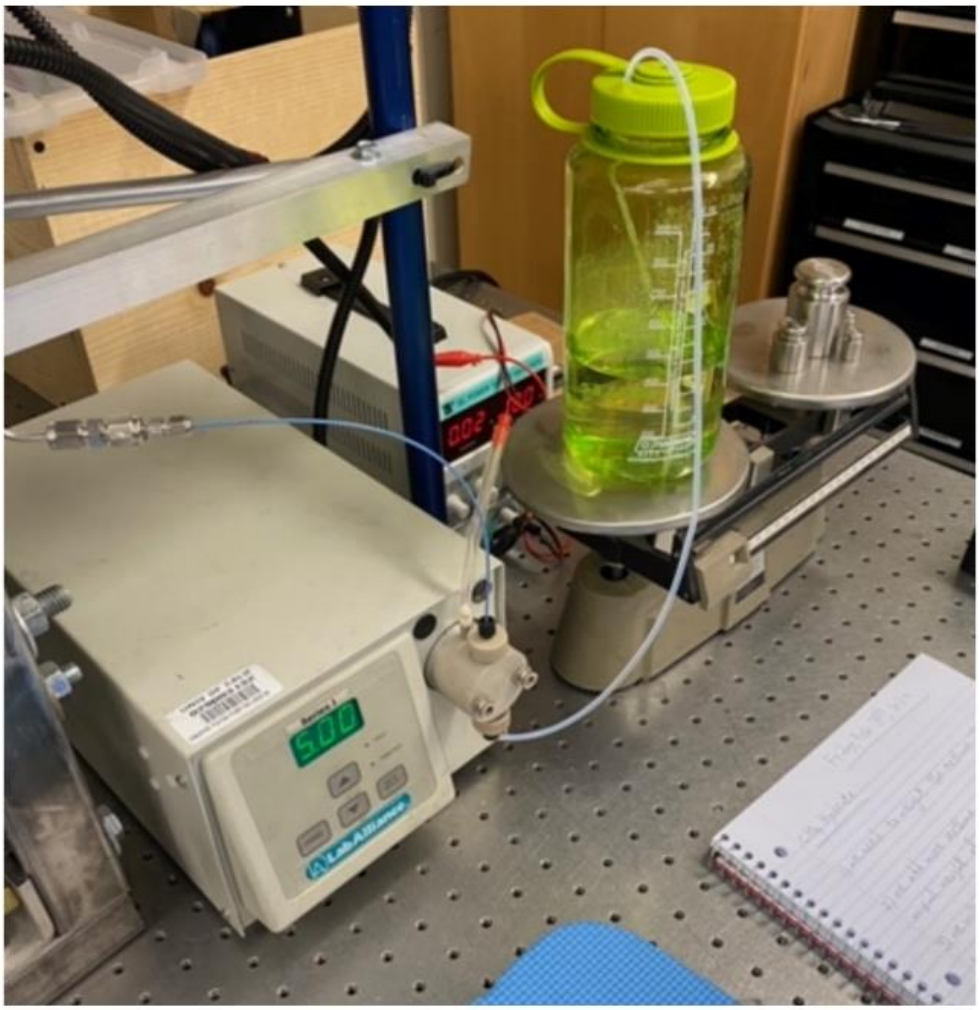

Figure 24: H2O Syringe Pump, Water Reservoir, and Balance with Weights for Controlling Water Input into the System

5.9. Simultaneously open valve 3 at the same time the syringe pump is turned on.

5.10. Start timer for 24 min
5.11. After 5 min, turn on chiller. Chiller should be set to 1 °C
5.12. Wait till compressor in chiller turns on. It should take around 30 seconds
5.13. Once compressor is on, open valves 5 and 6
5.14. Place rag on vessel to remove condensation so vessel cools more efficiently
5.15. After 24 min, balance should be level showing that about 110 grams of water are injected into vessel
5.16. Close valve 3
5.17. Shut off syringe pump
5.18. Wait 48 hours

6. Charging Vessel with Carbon Dioxide

PREPARATIONS FOR CARBON DIOXIDE: Fill tub with ice water until lines are completely submerged AT LEAST 30 min before starting the carbon dioxide step

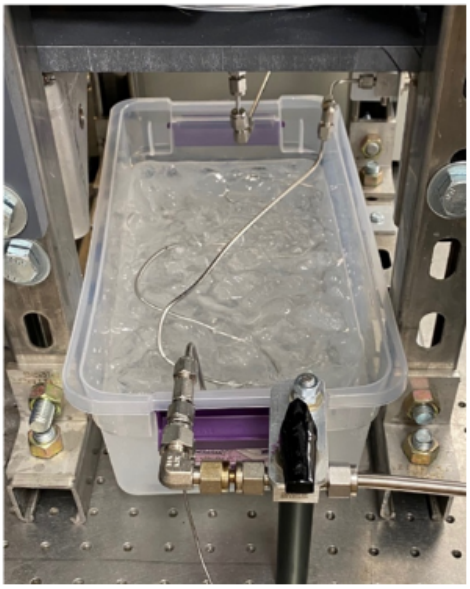

Figure 25: Ice Bath for bypass lines

6.1. Slowly open valve 1 to exhaust to release methane from chamber
  6.1.1. Once the pressure reaches 48 bars, close valve 1
  6.1.2. Wait 15 min for vessel to equalize
6.2. Place empty CO_2 reservoir in freezer for 5 min to chill
6.3. Connect CO_2 reservoir to main tank and purge lines
6.4. Fill CO_2 reservoir with CO_2 for about 2-3 min and close valves
6.5. Weigh CO_2 reservoir and record weight

6.5.1. Tank should have at least 500 grams of CO_2 inside

6.6. Fill secondary CO_2 tank by using the same process without chilling the tank

6.7. Connect CO_2 reservoir to CO_2 syringe pump.

6.7.1. Place CO_2 reservoir on a scale to control the amount of CO_2 that is put into the vessel

Figure 26: CO2 Reservoir Setup

6.8. Open CO2 reservoir main tank valve to check lines for leaks using snoop around connection points

6.8.1.There should be 3 places to check

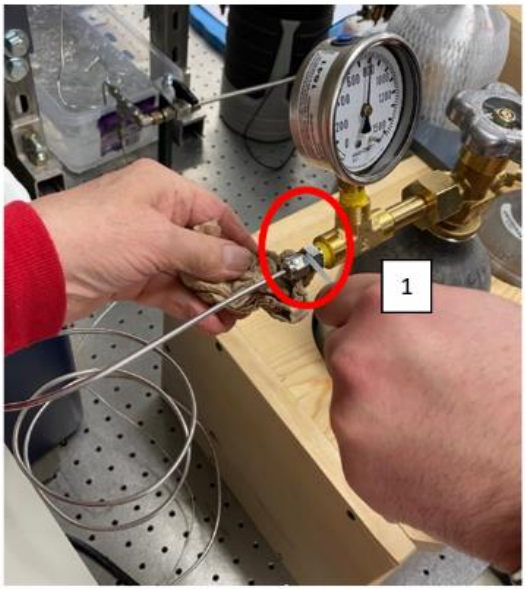

Figure 27: Leak Points for CO_2

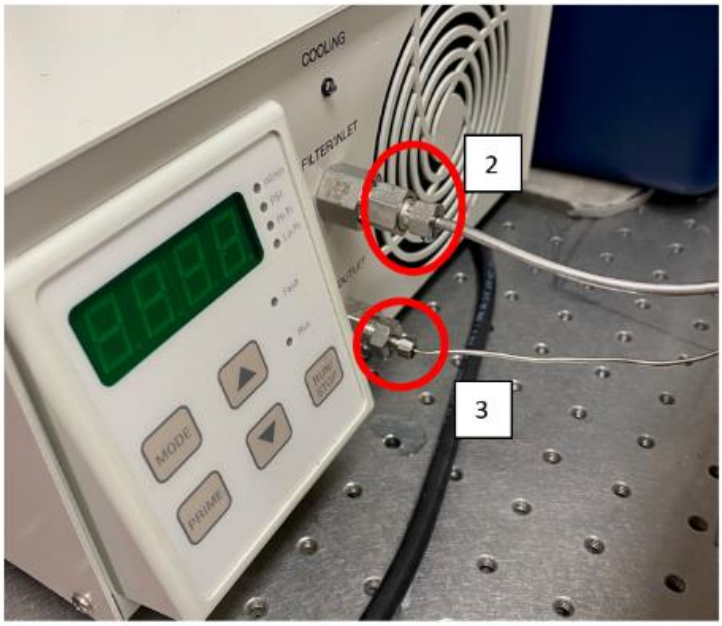

Figure 28: Leak Points for CO_2

6.9. Connect secondary CO_2 tank to valve 2

Figure 29: Secondary Tank Setup

6.10. Open secondary CO_2 tank.

6.11. Open valve 2 to circulate through lines to convert the CO_2 gas to liquid inside of the pipes before injecting into vessel.

6.12. Turn on syringe pump set to 14 mL/min and let run for 2 minutes using stopwatch

6.13. After the 2 min, the line from the syringe pump should be shaking

6.13.1. Open valve 2 to vessel and valve 4

6.13.2. If line is not shaking, wait until it starts to quiver, before to close the secondary CO_2 tank.

6.14. Close the secondary CO_2 tank

6.15. Disconnect lines and weigh secondary tank. Record weight of secondary CO_2 tank

6.16. Record weight of CO_2 reservoir on scale in its setup

6.16.1. Take recorded weight from step 6.16 and subtract 260 grams

6.17. Watch glass view and wait until CO_2 is visible in view

6.17.1. Once liquid goes up halfway on glass view close valve 4

Figure 30: Glass view of CO_2

6.18. Wait until CO_2 reservoir reaches desired weight recorded in step 6.16.1 and desired pressure in vessel

6.19. Close valve 2

6.20. Close CO_2 reservoir

6.21.Turn off pump

6.22. Take off fittings and weigh CO_2 reservoir and weigh

6.22.1. If less than 200 grams have been lost, repeat process to inject more CO_2 into vessel

6.23. Let sit for 24 hours

7. -25 °C below Cooling Cycle

7.1. Fill auxiliary heat exchanger with about 2 ½ L of ethanol

7.2. Turn off main chiller and close valve 5 and 6

7.3. Open valve 11, 12 and 13

7.4. Gradually add about 6 – 7 lbs of dry ice to auxiliary heat exchanger.

Figure 32: Adding Dry Ice to Auxiliary Chiller

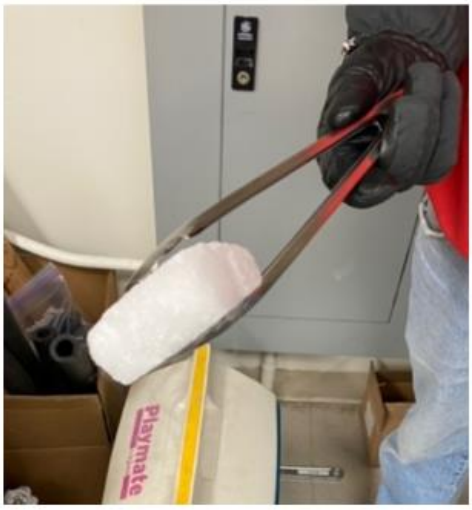

Figure 31: Average Size of Dry ice

Figure 33: Auxiliary Chiller with Dry Ice

7.5. Open valve 1 to exterior and outlet needle valve to drop pressure and release residual gas

7.6. Open valve 4

7.7. Pressure should be slowly dropping to 1 bar while the temperature should be dropping to at least -20 °C

7.8. Close valve 1

7.9. Close heat exchanger valves 11, 12, and 13.

7.10. Turn off the pump.

7.11. Take off rags surrounding vessel

7.12. Let vessel naturally warm for 24 hours

7.13. Remove coolant and dry ice from auxiliary heat exchanger

8. Collecting Sample from Vessel for Testing

Steps 8.1 to step 8.9 is to vacuum seal the sample tank

Figure 34: Sample Tank setup to Vacuum

Figure 35: Sample Tank Connected to Vacuum

8.1. Attach fittings to empty tank and open tank
8.2. Secure fittings to vacuum pump
8.3. Turn on pump
8.4. Slowly open valve 7
8.5. Slowly open valve 9 and wait 6 minutes using a timer
8.6. Close Sample tank
8.7. Close valve 9
8.8. Close valve 7
8.9. Turn off pump
8.10. Weigh sample tank to get weight of empty vessel and record data as tare weight.
8.11. Attach fittings from sample tank to vessel

Figure 36: Sample Tank Setup

8.12. Bleed lines using valve 1
8.13. Open sample tank to collect contents of vessel
8.14. Wait till pressure in sample tank and vessel equalize

8.15. Close sample tank
8.16. Close valve 1
8.17. Take off fittings
8.18. Weigh sample tank and record data
8.19. Dump remains of vessel by reconnecting lines to valve 1 to run outside
8.20. Slowly open valve 1.
8.21. Release all residual gases from the vessel to outside.

9. Cleaning Procedure

9.1. Take fittings off from vessel
  9.1.1. Unscrew line B
  9.1.2. Unscrew line A
  9.1.3. Unscrew water line
  9.1.4. Unscrew thermocouple
9.2. Unplug thermocouple and take out from vessel
9.3. Loosen bolts in crisscross manner
  9.3.1. This should take several passes. Bolts should be loosened gradually to prevent the lid to be unpressurized on one side
9.4. Release latches and remove rings

Figure 37: Vessel After Rings have been removed

9.5. Unscrew water line and remove lid

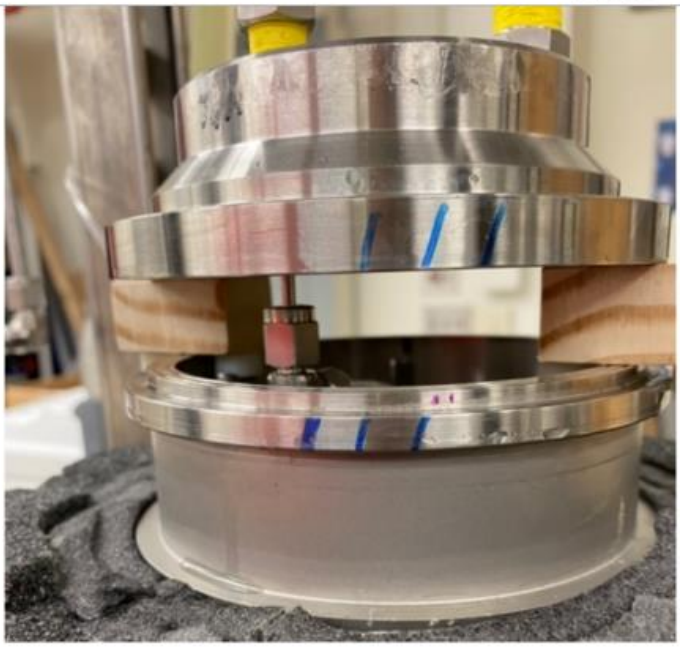

Figure 38: Unscrewing Water Line inside of Vessel

9.6. Remove nuts from threaded rods on basket

9.7. Remove lid of basket

Figure 39: Wire Mesh is Lid of Basket. This should be removed

9.8. Use spoon to remove glass beads from vessel

9.9. Vacuum remaining glass beads. Use brush to help clean inside of vessel

9.10. Rinse all internal parts taken out of vessel

9.11. Wipe down inside of vessel with damp cloth

Figure 40: Inside view of Vessel after Glass Beads have been removed

Condensation/separation process (main procedure)

1. There are two valves (inlet and outlet), one pressure transducer and one K-type thermocouple probe for measuring pressure and temperature respectively

2. Thermocouple stands to the center of the 50 mL sample vessel

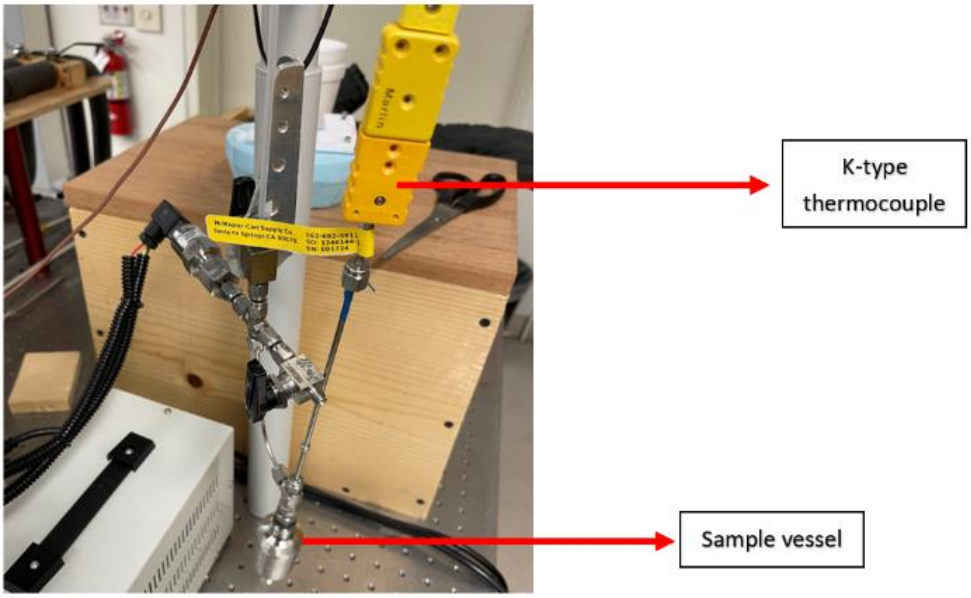

Figure 41: K-type thermocouple inside the sample vessel

3. Evacuate the vessel and pipelines with vacuum pump for 10-15 min

4. Closed inlet valve and isolated vessel and stays isolated until the experimental run is finished, and we take the sample

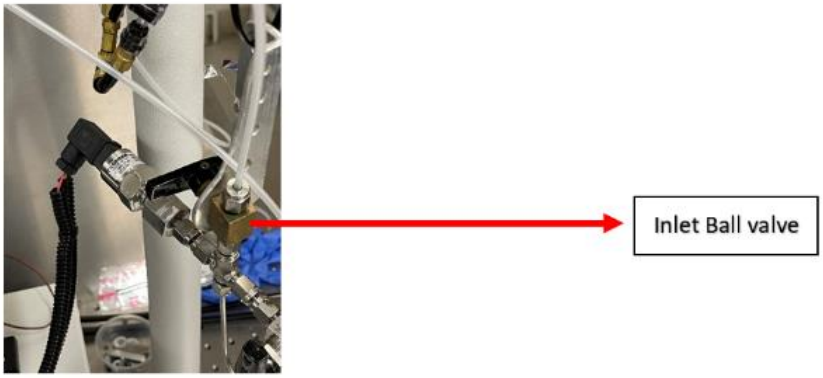

Figure 42: inlet ball-valve for transferring gas from experiment to the sample vessel

5. We monitored the pressure which should be zero absolute pressure

6. If the pressure is not zero, then system can be evacuated through the exit valve again, which is not disturb the main system

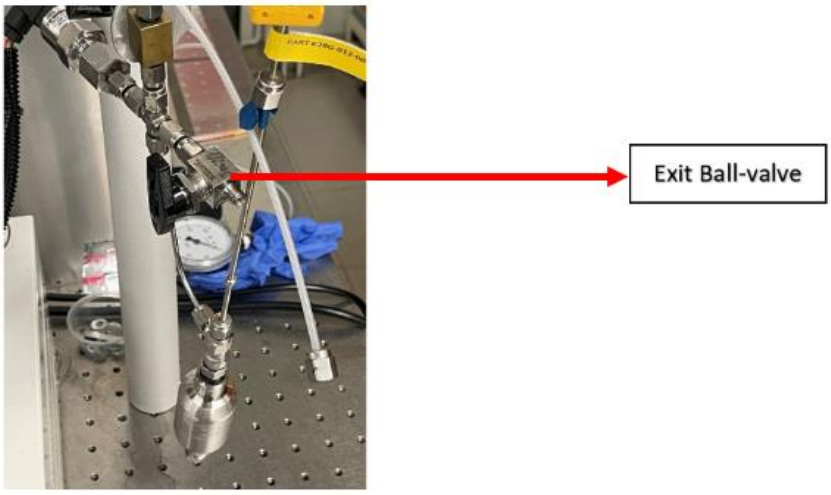

Figure 43: exit valve for vacuum the sample vessel

7. Bleed the main system through the exit valves down to 25 bar

8. Then, slowly open inlet valve to the sample vessel and bring the sample pressure vessel up to 15 bar at room temperature. Then, close the inlet valve

9. 3-point stand-off plate, it purposes to support the copper tubing by holding it up of the insulated LN2 cooler floor

Figure 44: 3-point is located inside the cooler floor

10. Put the sample vessel inside the copper tube

Figure 45: sample vessel inside the copper tube

11. Put the Teflon cap plate on the copper tube for preventing LN2 inside the copper tube

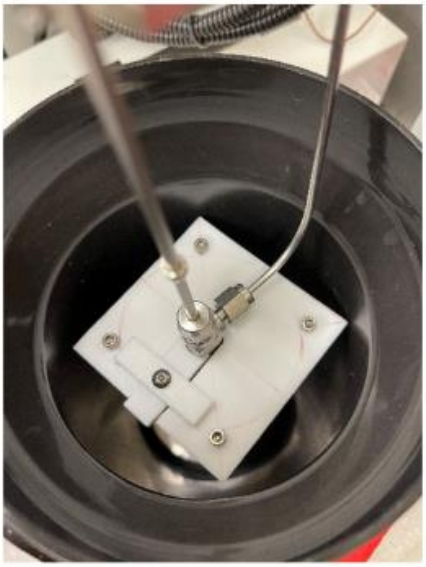

Figure 46: Cap plate is on the copper tube

12. Turn on recording data acquisition

13. Start introducing LN2 into the insulated cooler (Note: Being careful not to pore LN2 inside the copper tube)

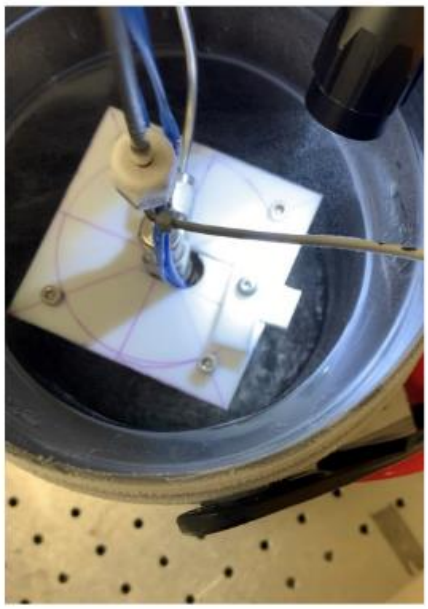

Figure 47: LN2 inside the cooler

14. LN2 is always between insulated cooler wall and outside the copper tube

15. Bring the level of LN2 to the 4-5mm of the top of the copper tube

16. Keep replenishing to 4-5mm near to the top of the copper tube (every 5-10min)

17. Put the foam cover on the top of the cooler for preventing vaporize the LN2

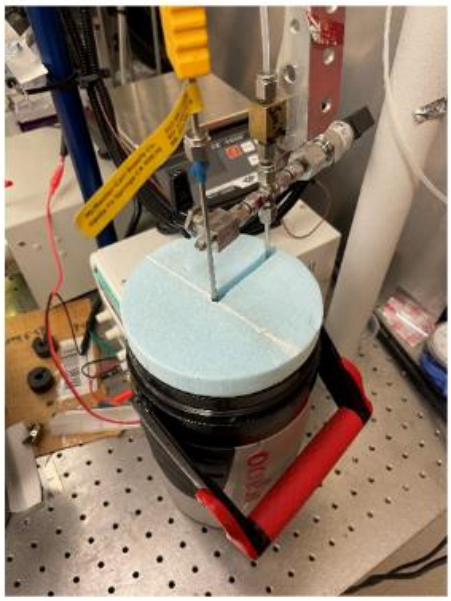

Figure 48: whole setup with foam covers the insulated cooler

18. After that, turn off the recording and remove the sample vessel from the cooler

Figure 49: sample vessel is out from the cooler after procedure

19. Also, remove the copper tube and then, we pore the remaining LN2 back to the storage tank

Figure 50: storage tank for LN2

Figure 51: Fully experimental setup for CH_4/CO_2 hydrates exchange process